



**UNIVERSIDAD DE CHILE  
FACULTAD DE CIENCIAS FÍSICAS Y MATEMÁTICAS  
DEPARTAMENTO DE ASTRONOMÍA**

**IONIZED JETS AND MOLECULAR OUTFLOWS IN  
HIGH-MASS YOUNG STELLAR OBJECTS**

**TESIS PARA OPTAR AL GRADO DE DOCTOR EN  
CIENCIAS, MENCIÓN ASTRONOMÍA**

**ANDRÉS ERNESTO GUZMÁN FERNÁNDEZ**

**SANTIAGO DE CHILE  
ENERO 2012**



**UNIVERSIDAD DE CHILE  
FACULTAD DE CIENCIAS FÍSICAS Y MATEMÁTICAS  
DEPARTAMENTO DE ASTRONOMÍA**

**IONIZED JETS AND MOLECULAR OUTFLOWS IN  
HIGH-MASS YOUNG STELLAR OBJECTS**

**TESIS PARA OPTAR AL GRADO DE DOCTOR EN  
CIENCIAS, MENCIÓN ASTRONOMÍA**

**ANDRÉS ERNESTO GUZMÁN FERNÁNDEZ**

PROFESOR GUÍA:  
GUIDO GARAY BRIGNARDELLO  
PROFESOR CO-GUÍA:  
KATE J. BROOKS

MIEMBROS DE LA COMISIÓN:  
DIEGO MARDONES PÉREZ  
ANDRÉS ESCALA ASTORQUIZA  
THOMAS L. WILSON

SANTIAGO DE CHILE  
ENERO 2012

# Resumen

Uno de los problemas claves en el estudio de la formación de estrellas es determinar si acaso el paradigma de formación de estrellas de baja masa, específicamente, contracción gravitacional y la posterior presencia de un disco de acreción y chorros altamente colimados, se extiende a las estrellas de alta masa. En esta tesis se lleva a cabo una búsqueda sistemática de chorros ionizados hacia objetos estelares jóvenes de alta masa. La presencia de estos chorros entrega evidencia que sostiene dos importantes nociones astrofísicas: que las estrellas de alta masa pasan por una fase de eyección de chorros y acreción desde un disco, y que además estos chorros serían la fuente de energía de los flujos moleculares masivos. Para la búsqueda de chorros se utilizó interferometría en el radio continuo centimétrico. Como sub-producto de esta búsqueda, se presenta también una lista de objetos estelares jóvenes de alta masa candidatos a albergar un chorro ionizado. Para el estudio del gas molecular y los flujos bipolares se utilizan telescopios sub-milimétricos ubicados en el Norte Grande de Chile. Analizando la incidencia y las características de estos chorros y de los flujos moleculares asociados, se extraerán conclusiones respecto al proceso de formación de estrellas de alta masa, la pertinencia de los chorros en este proceso, y algunas características físicas de éstos.

# Abstract

One of the key problems in the study of star formation is to determine whether or not the paradigm of low-mass star formation, specifically, gravitational contraction and the ensuing accretion disk and highly collimated jet, is applicable to the formation of high-mass stars. In this thesis, we carry out a systematic search for ionized jets toward high-mass young stellar objects. The presence of these jets forms strong evidence for two important astrophysical ideas: that a high-mass star have a disk accretion and jet ejection phase during its formation, and that these jets are the driving sources of the massive molecular outflows. The search for jets is done using interferometric observations in radio continuum at centimetric wavelengths. As a by-product of this search, we present a list of high-mass young stellar objects candidate to harbor an ionized jet. The study of the molecular gas and the molecular bipolar outflows is carried out using sub-millimeter telescopes located in the Norte Grande, Chile. By analyzing the incidence, the characteristics of these jets and their associated molecular outflows, we extract important conclusions about the formation of high-mass stars, the pertinence of these jets in the high-mass star formation process, and some of the jet physical characteristics.

# Agradecimientos

Agradezco a todos quienes me han acompañado en mi proceso de doctorado, en especial a todos mis compañeros, a mis profesores guía y co-guía, Guido Garay y Kate Brooks respectivamente, y a todos los profesores y funcionarios del departamento. Agradezco en especial a dos actores fundamentales en mi formación como astrónomo: mis compañeros y mi profesor guía Guido Garay. Mis compañeros del departamento han sido sin lugar a dudas a quienes he tenido más cerca durante todo mi proceso de aprendizaje, en las discusiones científicas y académicas. Guido, por otro lado, es la persona que ha influido de manera más relevante en mi carácter como investigador científico. A mis compañeros y profesor guía debo el científico que soy. Agradezco a todos los funcionarios no-académicos y académicos del departamento, y a la Universidad de Chile, cuyo ideal de universidad pública y estatal imprime una motivación especial por mi trabajo científico. Es tarea de todos nosotros aumentar la coherencia entre este ideal y la labor universitaria efectiva.

Agradezco de manera personal a Valeria y a mi familia. Valeria es mi compañera de vida, y en todo cuanto hago, amo y me motiva, está ella. Me siento infinitamente afortunado de tenerla compartiendo esta relevante parte de mi vida, como es la astronomía y la ciencia, junto a mi. Agradezco también el apoyo y amor de mi familia: su presencia es permanente alegría y motivación para mi.

Finalmente, agradezco a CONICYT el financiamiento otorgado a través de su programa de becas nacionales de doctorado durante la mayor parte de mis estudios. Agradezco también al programa FONDAP por su apoyo en el financiamiento de publicaciones, viajes, estadías de observación e inscripciones para congresos internacionales.

# Note on units convention

Unless explicitly stated otherwise, the following convention apply to the entire thesis:

- CGS-Gaussian units.
- Reference date for equatorial coordinates: J2000.
- IAU standards: Galactocentric Sun distance:  $R_{\odot} = 8.5$  kpc, Local Standard of Rest Velocity:  $220 \text{ km s}^{-1}$ .

# Contents

<b>1</b>	<b>Introduction</b>	<b>1</b>
<b>2</b>	<b>Search for jets using radio centimetric observations</b>	<b>4</b>
2.1	Source Selection . . . . .	5
2.2	Observations . . . . .	10
2.3	Results . . . . .	12
2.3.1	Jet candidates . . . . .	15
2.3.2	Other sources of interest . . . . .	29
2.4	Summary . . . . .	47
<b>3</b>	<b>Molecular outflows toward ionized jet candidates</b>	<b>48</b>
3.1	Observations . . . . .	49
3.1.1	Observational strategy and calibration . . . . .	49
3.2	Results . . . . .	53
3.2.1	Jet candidates . . . . .	56
3.2.2	Other HMYSO candidates . . . . .	71
3.3	Derived parameters . . . . .	78
3.3.1	Basic relations . . . . .	78
3.3.2	Outflow parameters . . . . .	80
3.3.3	Core parameters . . . . .	81
3.4	Conclusions . . . . .	87
<b>4</b>	<b>A collimated jet toward G345.4938+01.4677</b>	<b>89</b>

4.1	Introduction . . . . .	90
4.2	Observations . . . . .	91
4.3	Results . . . . .	91
4.4	Discussion . . . . .	92
4.4.1	The nature of the radio sources . . . . .	92
4.4.2	Characteristics of the exciting source and its environment . . . . .	93
4.4.3	Jet and Shock parameters . . . . .	96
4.5	Summary . . . . .	97
<b>5</b>	<b>A hot molecular outflow driven by the ionized jet associated with G345.4938+01.4677</b>	<b>103</b>
5.1	Introduction . . . . .	104
5.2	Observations . . . . .	104
5.3	Results . . . . .	106
5.4	Analysis and discussion . . . . .	107
5.4.1	K <sub>s</sub> -band evidence of shocked H <sub>2</sub> . . . . .	107
5.4.2	Parameters of the outflows . . . . .	108
5.4.3	Further tracers of shocks . . . . .	111
5.4.4	Infall of molecular core . . . . .	112
5.5	Summary . . . . .	113
<b>6</b>	<b>Discussion and analysis</b>	<b>120</b>
6.1	Ionized jets in high-mass star formation . . . . .	120
6.1.1	Lifetime of jets in HMYSOs . . . . .	120
6.1.2	Ionized jets as the driving sources of molecular outflows . . . . .	121
6.1.3	Collimation mechanism . . . . .	129
<b>7</b>	<b>Summary</b>	<b>130</b>
7.1	Main Conclusions . . . . .	130
7.2	Outlook . . . . .	131

<b>Appendix</b>	<b>132</b>
<b>A Spherical, power-law density ionized regions</b>	<b>132</b>
A.1 Behavior of the spectrum . . . . .	133
A.2 Recombination equilibrium . . . . .	135
<b>Bibliography</b>	<b>137</b>

# Chapter 1

## Introduction

The determination of whether high-mass stars ( $M > 8 M_{\odot}$ ) are formed by an accretion process similar to that inferred for low-mass stars, with an accreting disk (Shu et al. 1987), or via another processes (e.g. merging, Bonnell et al. 1998) is one of the main observational challenges in the field of star formation. This problem sets the general context of the work presented in this thesis.

One of the most striking features related to low-mass star formation is the generation of highly collimated jets during the disk accretion phase. It is rather paradoxical that just when we expect to observe the infall, the signatures of outflow prevail (Smith 2004). Our current understanding of the formation process of low-mass stars can be summarized in four phases, presented in Shu et al. (1987): i) Fragmentation of a molecular cloud in dense cores, which slowly contract gravitationally and become centrally condensed; ii) Inside-out collapse of these cores, accretion onto a central object and formation of a disk. The disk and protostar are deeply embedded within the infalling envelope. iii) A well developed outflow breaks out from the core through the polar regions. The disk accretes from the envelope, and the protostar from the disk. iv) Much of the envelope is now been accreted or dispersed. The central protostar becomes visible as a T-Tauri or a Herbig Ae/Be star.

Only at the end of these four stages the central protostar starts to burn hydrogen and reaches the main sequence, becoming a zero-age main sequence (ZAMS) star. Planets and debris condense from the remanent material of the disk.

Is this schematic picture applicable to high-mass stars? It seems clear that it cannot be applied strictly by scaling the mass, that is, high-mass star formation is not a “mere scaled-up” version of the low-mass star formation process (Zinnecker & Yorke 2007).

One very important difference, compared to a low-mass protostar, is that it takes a very small amount of time to a high-mass protostar to contract and reach the ZAMS. This time is given by the Kelvin-Helmholtz timescale:

$$t_{\text{K-H}} = \frac{GM^2}{RL} \approx 3.1 \times 10^7 \left( \frac{M}{M_{\odot}} \right)^2 \frac{R_{\odot} L_{\odot}}{R L} \text{ yr},$$

where  $M$  is the protostar mass,  $L$  its luminosity and  $R$  its radius. For an O star, this timescale

is about  $10^4$  yr, shorter than the free-fall time

$$t_{\text{ff}} = \sqrt{\frac{3\pi}{32G\rho}} \approx \frac{44 \times 10^6}{\sqrt{n_{\text{H}_2} [\text{cm}^{-3}]}} \text{ yr}$$

associated to a cloud of density  $10^5 \text{ cm}^{-3}$ , typical for high-mass star forming cores. The importance of  $t_{\text{K-H}} < t_{\text{ff}}$  is that  $t_{\text{ff}}$  is a lower limit for the accretion timescale, therefore, a high mass protostar reaches the ZAMS while still accreting. When a high-mass star contracts and starts to fuse hydrogen, it emits copious amount of radiation and ionizing photons. The radiation pressure and the thermal pressure produced by the developing photoionized gas ( $T \sim 10^4$  K) could halt the accretion process. The photoionized region will later become a ultracompact H II region, disrupting and dispersing the parental cloud. These facts had been used as arguments for the inadequacy of accretion as the mechanism through which high-mass stars gain a significant fraction of their masses. Particularly, Stahler et al. (1997) and Bonnell et al. (1998) have proposed that high-mass stars form by the coalescence of low-mass protostars.

Another important difference of high-mass star formation is that high-mass stars appear only in the center of the very massive and dense cores and clusters, and they tend to be gregarious by nature (Garay & Lizano 1999). The role of the formation environment is a rich subject, and since high-mass stars form in dense environments, is particularly pertinent the debate of whether stars accrete most of their mass from gravitational core collapse (Shu et al. 1987, Larson 2005), or competing with each other for the material, growing from stellar “seeds” (Bonnell et al. 2001, Bate & Bonnell 2005). The debate is, however, outside the focus of this thesis. We can consider the coalescence scenario as an extreme situation, where violent interactions play the fundamental role in the formation of high-mass stars.

There has been much theoretical work pointing out that accretion does indeed happen during massive star formation. Large mass inflow rates rates can suppress the development of a H II region (Wolfire & Cassinelli 1987), and radiation pressure does not seems to effectively halt the accretion (Krumholz et al. 2005).

One specific type of accretion, namely, accretion from a disk, is particularly relevant for this work. Disk accretion has been proposed as an effective mechanism to overcome the radiation pressure problem (Kuiper et al. 2010), and it is also intimately related to collimated jets. Jets are thought to allow the disk material to get rid of the angular momentum and fall onto the protostar. If massive O-type stars are formed, or gain a significative fraction of their mass by such a disk-mediated accretion process, we would expect jets and disks in their earliest stages of evolution. On the other hand, if they are formed via merging of lower-mass stars then neither accretion disks nor jets are expected (Bally & Zinnecker 2005).

High mass young stellar objects (HMYSOs) are also frequently associated with massive molecular outflows (Beuther et al. 2002b, Shepherd 2005, Kim & Kurtz 2006). These outflows usually display a bipolar morphology, but most of them are poorly collimated. Their masses range between a few hundredth to several tens of solar masses, and their velocities are typically from 10 up to 100  $\text{km s}^{-1}$ . There exist good evidence, in the low-mass star formation case, that these outflows are entrained and swept up material driven by collimated jets, but similar evidence for the high-mass regime is scant.

The study of the incidence of jets in HMYSOs helps us to evaluate the pertinence of

this phenomenon in the high-mass star formation process, and allows us to identify the dominating formation mechanism. As remarked, their presence is a strong argument in favor of disk-mediated accretion. Jets also have been a natural candidate for being the driving source of molecular outflows (Anglada 1996). If the energy and momentum of the molecular flows are consistent with them being delivered by an ionized jet, then the ubiquity of the outflow phenomena can be reasonably interpreted as ubiquity of jets.

There exists evidence that stars with masses up to  $\sim 10 M_{\odot}$  (or early B-type star) are formed in a disk accretion scenario (e.g., Garay & Lizano 1999, Patel et al. 2005, Chini et al. 2006), and there is growing observational evidence of a disk-mediated accretion for even more massive objects (Cesaroni et al. 2007, Kraus et al. 2010, Preibisch et al. 2011). The evidence for jets from massive YSOs is rather scarce, however. To date there are only a handful of HMYSOs known to be associated with highly collimated jets and/or Herbig-Haro (HH) objects (see Guzmán et al. 2010). Most of them have bolometric luminosities smaller than  $2 \times 10^4 L_{\odot}$  corresponding to that of a B0 zero-age main sequence (ZAMS) star. There is only one O-type YSO with bolometric luminosity  $L > 5 \times 10^4 L_{\odot}$  that is associated with a collimated jet: IRAS 16547–4247, ( $L \sim 6.2 \times 10^4 L_{\odot}$ ; Garay et al. 2003; Brooks et al. 2007). It is not clear whether the lack of young massive stars with spectral types earlier than B0 associated with jets and/or disks is an intrinsic property of the most massive stars or due to observational disadvantages. Massive stars are rarer and their evolutionary time scales are much shorter than those of low mass stars. With the currently available small sample, made from a collection of individual serendipitous studies, it is difficult to characterize the jet phenomena in high-mass star formation.

In order to assess this issue, we carry out multi-frequency radio continuum observations to systematically search for collimated ionized jets towards high-mass YSOs. We present such observations in Chapter 2, made with the Australia Telescope Compact Array (ATCA) and the Very Large Array (VLA) toward 8 source. We also present in this Chapter a list of HMYSOs, candidates to be associated with an ionized jet. Chapter 3 presents CO line observations toward 8 jet candidates, seven of which have radio-continuum data. We mainly study the presence of high-velocity gas, indicative of outflow activity.

Chapters 4 and 5 are devoted to one of the best examples of a jet associated to a HMYSO: G345.4938+01.4677 (IRAS 16562–3959). In Chapter 4 studies we present the radio data and the physical characteristics of the ionized jet. In Chapter 5 we analyze the molecular outflow detected toward this source, and its link with the ionized jet. The work described in these chapters was published in Guzmán et al. (2010) and Guzmán et al. (2011).

In Chapter 6 we analyze the results of the jet search described in Chapter 2. We conclude that jets are an important phase in the process of high-mass star formation, and derive a lifetime of the phenomenon based on its incidence. In this Chapter we also study the pertinence of HMYSO-jets as the driving sources of high-mass molecular outflows. Chapter 7 summarizes the results and main conclusions obtained from this thesis.

## Chapter 2

# Search for jets using radio centimetric observations

We present the first results of a systematic search for collimated ionized jets toward southern high-mass young stellar objects (HMYSOs). Determining the presence of a jet associated to a HMYSO provides clear evidence supporting a disk-mediated accretion scenario in the high-mass star formation process.

Based on published radio and infrared catalogs, we define a candidate selection criteria and compiled a list of 33 jet candidate radio sources. The criteria was mainly based on the luminosity of the HMYSO ( $L > 2 \times 10^4 L_{\odot}$ ) and positive radio spectral index. This Chapter presents the results of ATCA observations at four frequencies between 1.4 and 8.6 GHz, made toward 7 of these candidates; and of VLA observations toward one additional candidate made at four frequencies between 1.4 and 22.5 GHz. In total, 8 jet candidates were observed in radio-centimetric continuum at 4 frequencies, with angular resolutions of typically  $7''$ ,  $4''$ ,  $2''$ , and  $\lesssim 1''$ . We discovered two jets within the observed subset. We conclude that jets are a regular part of the high-mass star formation process and they appear before the hyper and ultracompact H II region phases. One of the two jets discovered, G345.4938+01.4677, corresponds to one of the most luminous and clearest examples of an HMYSO associated with a jet ( $L \sim 7.0 \times 10^4 L_{\odot}$ ). Derived from this study, we also presents ATCA observations toward 5 more fields associated to HMYSOs and 5 newly found southern hypercompact H II regions.

In §2.1 we describe the criteria adopted to build a sample of jet candidates selected from two catalogs of radio sources associated with either HMYSOs or ultracompact H II regions (UCH II). In §2.2 we describe the ATCA and VLA observations and present the results obtained toward eight of the jet candidates. In §2.3 we report the results of observations obtained toward a sample of five radio sources which were selected in an early stage of this study. Three of them are radio sources associated to young high-mass stars, but they do not fulfill the selection criteria. Finally, in §2.4 we summarize the results of the search.

## 2.1 Source Selection

In order to carry out a systematic search, the first step is to compile a list of high-mass young stellar objects candidate to harbor a jet. In this section we describe the steps followed to build such a list. Three requirements were imposed in selecting the targets:

- *Positive radio continuum spectral indices.* First, and as expected for thermal jets (Reynolds 1986), we considered radio sources in the literature with positive spectral indices at radio wavelengths.
- *Association with luminous infrared sources.* Since we are searching for jets associated with high-mass young stellar objects, we expect the driving sources to be luminous and still be enshrouded in a dense cloud of gas and dust. Thus, most of their luminosity should be re-emitted in the infrared and far-infrared (FIR). A second requisite to be fulfilled by our targets is that they be associated with luminous IRAS sources.
- *Underluminous radio objects.* We expect radio jets to be only visible in a very early stage of evolution prior to the ultracompact H II region phase. In such an early stage the UV photons from the central protostar are likely to be trapped by the infalling gas and therefore quench the development of an UCH II region (Yorke 1986, Wolfire & Cassinelli 1987). Thus the third requisite is that the radio luminosity of the targets be considerable lower than that predicted from the bolometric luminosity.

As a starting point to build up our target list, we considered two catalogs of radio sources: Urquhart et al. (2007a) and Walsh et al. (1998). Urquhart et al. reported radio continuum observations, at 4.8 and 8.6 GHz using ATCA, toward 826 Red MSX Sources (RMS) (Urquhart et al. 2008a). RMS sources are HMYSO candidates selected by their colors (Lumsden et al. 2002) in the *Midcourse Space Experiment* (MSX) and 2-MASS bands (Skrutskie et al. 2006). We considered all the radio sources that are within  $18''$  (MSX beam) from the peak position of the associated MSX source, which amounted to 239 objects. Walsh et al. (1998) reported radio continuum observations at 6.7 and 8.6 GHz, using ATCA, towards IRAS sources with colors of UCH II regions (Wood & Churchwell 1989) and associated with methanol masers. They reported emission at 8.6 GHz from 177 ultracompact H II regions.

To be in accordance with the first requirement, we selected from the above radio sources those which exhibit positive radio continuum spectral index between the two observed frequencies (Reynolds 1986). We find that approximately a 40% of the radio sources from both catalogs fulfill this first requirement. We considered sources with upper limits (or non-detections) at the lower frequency. In the case of Urquhart et al. (2007a) the sensitivity in the two observed bands is similar, hence a non-detection in the lower frequency band implies a true positive spectral index. In the case of Walsh et al. (1998) the observations at 6.7 GHz were made with a bandwidth of 4 MHz, much smaller than that used for at 8.6 GHz (128 MHz), and therefore are considerably less sensitive than those at the high frequency. In this case, a non detection does not necessarily implies a truly positive spectral index.

To comply with the second requirement, we then selected from the above sub-sample of radio sources those that are associated — angular separation no larger than  $25''$  — with an IRAS source. As distances we adopted the kinematical distances reported by Bronfman et al.

(1996) and Faúndez et al. (2004) (derived from observations of the CS(2→1) transition) or by Urquhart et al. (2007b, 2008b) (derived from observations of the  $^{13}\text{CO}(2\rightarrow 1)$  line). In the cases when both lines were detected, their velocities are consistent within  $1 \text{ km s}^{-1}$  in 90% of the cases. If the discrepancy is larger, we take the  $v_{LSR}$  of the CS line. In these works, the near-far distance ambiguity for sources located inside the solar circle ( $R_{\odot} = 8.5 \text{ kpc}$ ) has been resolved for several sources. For the sources in which the ambiguity remains, we adopted the *near* distance. From the IRAS fluxes and the distance, we estimated the bolometric luminosity using the expression (Casoli et al. 1986)

$$L_{IRAS} = 5.44 (F_{12}/0.79 + F_{25}/2 + F_{60}/3.9 + F_{100}/9.9) \left( \frac{D}{\text{kpc}} \right)^2 L_{\odot}, \quad (2.1)$$

where  $L_{IRAS}$  is the IRAS FIR luminosity,  $D$  is the distance and  $F_{12}$ ,  $F_{25}$ ,  $F_{60}$ , and  $F_{100}$  correspond to the IRAS fluxes in Jy measured at the 12, 25, 60, and 100  $\mu\text{m}$  bands, respectively. From the sources with positive radio spectral index, we selected approximately a 37% which has molecular line observations and their FIR luminosity fulfills  $L_{IRAS} > 2 \times 10^4 L_{\odot}$ .

To comply with the third requirement, we computed the monochromatic radio luminosity,  $4\pi D^2 F_{\nu}$ , expected from an homogeneous, optically thin H II region that is excited by a single star with a bolometric luminosity,  $L_{IRAS}$ , using the expression (Spitzer 1998)

$$\left( \frac{4\pi D^2 F_{\nu}}{\text{Jy kpc}^2} \right) = 0.12 \left( \frac{N_{*}}{10^{45} \text{ s}^{-1}} \right) \left( \frac{\nu}{8.6 \text{ GHz}} \right)^{-0.11} \left( \frac{T}{8000\text{K}} \right)^{0.38}, \quad (2.2)$$

where  $N_{*}$  is the rate of ionizing continuum photons emitted by a ZAMS star with that luminosity taken from standard stellar atmospheres models (e.g., Panagia 1973). Then we selected those radio sources for which the observed radio luminosity is smaller than that predicted from equation (2.2) by a factor of at least 10. Note that Eq. (2.2) implicitly assumes that all the ionizing photons are absorbed by the plasma.

While we argue that the third requirement is needed to select ionized jets, there are other explanations for the radio under-luminosity: (i) The radio emission at the observed frequency may arise from an optically thick H II region, in which case the radio luminosity is not proportional to the number of ionizing photons; (ii) Dust within the H II region absorbs an important fraction of the ionizing photons, (iii) The distance to the source is overestimated, (iv) The FIR luminosity is due to multiple unresolved stars, and (v) The ionizing photon flux may not be related to the star bolometric luminosity through standard stellar atmospheres models. For instance, it has been found that high accretion rates ( $\dot{M} \sim 10^{-3} - 10^{-4} M_{\odot} \text{ yr}^{-1}$ ), implies large radius and low effective temperatures associated with the accreting protostar (Hosokawa & Omukai 2009). High-mass protostars may produce little if any ionizing photons in their earliest stages. This explanation has recently been considered to account of the lack of ionized gas towards high-mass protostellar objects in the RMS sample (Mottram et al. 2011b).

Table 2.1 presents our sample of 33 jet candidates associated with high-mass young stars that fulfill the three main requisites. Columns (2) and (3) give the right ascension and declination of the radio source, respectively; cols. (4) and (5) the observed flux densities at the low and 8.6 GHz frequencies, respectively; col. (6) the spectral index; col. (7) the kinematic distance; cols. (8) and (9) the name and estimated FIR luminosity of the associated IRAS source, respectively; and col. (10) the reference. Interestingly, one of the selected jet

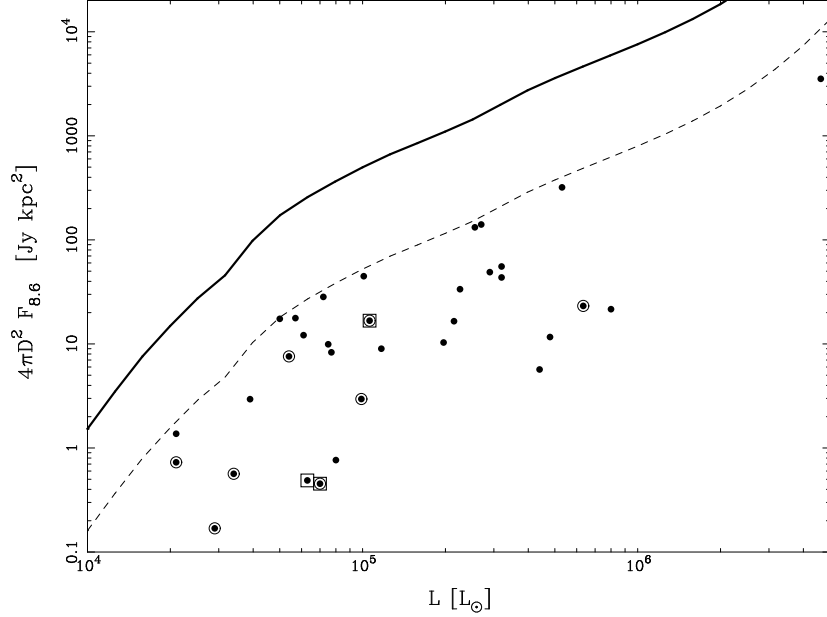


Figure 2.1 Radio luminosity at 8.6 GHz versus bolometric luminosity for all jet candidates in Table 2.1. The continuous line indicates the expected radio luminosity of an optically thin H II region ionized by a ZAMS star with luminosity  $L$  (Panagia 1973). The dashed line marks the selection criterion. The observed sources are enclosed in circles. Squares mark objects G343.1262–00.0620, G345.4938+01.4677, and G337.4032–00.4037.

candidate corresponds to G343.1262–00.0620 (IRAS 16547–4247), the most luminous source known to be associated with a jet (Garay et al. 2003, Brooks et al. 2003, Rodríguez et al. 2005). The list of 33 jet candidates is one result of this first systematic search for jets toward HMYSOs, and the analysis of the sub-sample presented in this work forms the basis of the work presented in this thesis. Table 2.1 is also useful as a selection of sources representative of the youngest phase of radio emitting HMYSOs.

Figure 2.1 presents a plot of the radio luminosity versus the bolometric luminosity for all sources in our sample. The continuous line shows the relation between these quantities for an optically thin H II region ionized by a ZAMS star (Panagia 1973). This figure clearly illustrates that our sources are underluminous in radio continuum emission compared to that expected for a uniform optically thin H II region.

Table 2.1. Jet candidates

Source Name	$\alpha$ (J2000)	$\delta$ (J2000)	$F_{\nu \text{ low}}$ (mJy)	$F_{8.6\text{GHz}}$ (mJy)	S.I.	D (kpc)	IRAS	Lum. ( $10^4 L_{\odot}$ )	Ref.
(1)	(2)	(3)	(4)	(5)	(6)	(7)	(8)	(9)	(10)
G240.3160+00.0714	07 <sup>h</sup> 44 <sup>m</sup> 52 <sup>s</sup> .04	-24°07'42".4	<18	12.4	u	7.3	07427-2400	7.7	(2)
G274.0649-01.1460	09 24 42.13	-52 02 00.8	28.9	36.1	0.44	6.9	09230-5148	80.	(1)
G289.9446-00.8909	11 01 09.00	-60 56 56.3	< 0.7	12.4	$\geq 2$	10.3	10591-6040	21.5	(1)
G293.9633-00.9776	11 32 36.14	-62 28 08.3	24.8	28.9	0.3	11.1	11303-6211	10.1	(1)
G298.2234-00.3393	12 10 01.16	-62 49 53.9	1350.	2200.	0.96	11.3	12073-6233	463.	(1)
G300.9674+01.1499	12 34 53.23	-61 39 40.1	102.	138.	0.6	4.4	12320-6122	22.6	(1)
G301.1364-00.2249A	12 35 35.13	-63 02 31.7	83.8	228.	2.	4.4	12326-6245	32.	(1)
G301.1364-00.2249B	12 35 35.19	-63 02 24.0	126.	179.	0.68	4.4	12326-6245	32.	(1)
G305.7984-00.2416	13 16 42.62	-62 58 21.2	<10	5.	u	3.	13134-6242	3.4	(2)
G308.9176+00.1231	13 43 01.72	-62 08 56.1	247.	374.	0.81	5.3	13395-6153	25.6	(1)
G309.9196+00.4791	13 50 41.89	-61 35 11.5	377.	384.	0.072	5.4	13471-6120	27.	(2)
G311.1359-00.2372	14 02 09.93	-61 58 37.9	3.0	3.5	0.3	14.3	13585-6144	11.7	(1)
G317.4298-00.5612	14 51 37.60	-60 00 19.4	6.6	8.2	0.42	15.0	14477-5947	63.4	(1)
G317.8908-00.0578A	14 53 06.19	-59 20 56.7	< 0.7	3.6	$\geq 2$	15.1	14492-5908	19.7	(1)
G326.4477-00.7485	15 49 18.67	-55 16 52.5	4.7	5.9	0.39	4.3	15454-5507	2.1	(1)
G328.5759-00.5285B	15 59 38.15	-53 45 27.9	326	381	0.27	3.2	15557-5337	29.0	(1)
G331.4181-00.3546	16 12 50.24	-51 43 28.6	80.7	83.9	0.07	4.1	16090-5135	5.7	(1)
G333.0162+00.7615	16 15 18.70	-49 48 52.8	46.9	88.8	1.2	3.3	16115-4941	6.1	(1)
G336.9842-00.1835	16 36 12.42	-47 37 58.0	18.	34.3	1.3	4.8	16325-4731	7.5	(1)
G337.4032-00.4037	16 38 50.45	-47 28 02.7	90.3	130.	0.71	3.2	16351-4722	10.6	(1)
G337.7051-00.0575	16 38 29.63	-47 00 35.3	76.3	171.	1.6	12.2	16348-4654	53.1	(1)
G337.8442-00.3748	16 40 26.67	-47 07 13.1	11.1	24.4	1.5	3.1	16367-4701	3.9	(1)
G340.0708+00.9267	16 43 15.69	-44 35 16.0	48.8	93.8	1.1	4.9	16396-4429	7.2	(1)
G340.2768-00.2104	16 48 53.30	-45 10 22.3	< 1	4.7	$\geq 2$	3.6	16452-4504	8.0	(1)
G343.1262-00.0620	16 58 17.21	-42 52 07.1	<7.3	4.62	u	2.9	16547-4247	6.3	(2)
G345.0061+01.7944	16 56 47.59	-40 14 25.8	127.	209.	0.98	1.7	16533-4009	5.4	(1)
G345.4938+01.4677	16 59 41.61	-40 03 43.4	4.8	12.5	1.9	1.7	16562-3959	7.0	(1)
G352.5173-00.1549	17 27 11.32	-35 19 32.8	<14	7.5	u	5.6	17238-3516	9.9	(2)

Table 2.1 (cont'd)

Source Name	$\alpha$ (J2000)	$\delta$ (J2000)	$F_{\nu \text{ low}}$ (mJy)	$F_{8.6\text{GHz}}$ (mJy)	S.I.	D (kpc)	IRAS	Lum. ( $10^4 L_{\odot}$ )	Ref.
(1)	(2)	(3)	(4)	(5)	(6)	(7)	(8)	(9)	(10)
G000.3138-00.2000	17 47 09.66	-28 46 27.7	8.3	14.5	2.2	8.	17439-2845	48.	(2)
G009.9937-00.0299	18 07 52.84	-20 18 29.3	<10	2.32	u	5.	18048-2019	2.1	(2)
G010.8403-02.5913	18 19 12.10	-20 47 30.7	<21	4.8	u	17.	18162-2048	5.	(2)
G024.4673+00.4910	18 34 08.12	-07 18 18.2	<28	13	u	5.9	18314-0720	44.	(2)
G025.6469+01.0534	18 34 20.91	-05 59 39.3	<7	1.4	u	3.1	18316-0602	2.9	(2)

References. — (1):Urquhart et al. (2007a), (2): Walsh et al. (1998).

## 2.2 Observations

The observations were made using the Australia Telescope Compact Array (ATCA)<sup>1</sup> and were taken between 2008 June and 2009 February. We combined 1.5 and 6.0 km array configurations, utilizing all six antennas and covering east-west baselines from 30 m to 5.9 km. Observations were made at four frequencies: 1.384, 2.368, 4.800, and 8.640 GHz, each with a bandwidth of 128 MHz, full Stokes. Throughout this work we will refer to these frequencies as 1.4, 2.4, 4.8 and 8.6 GHz, respectively. The total integration time at each frequency was between 60 and 240 minutes depending on each source, obtained from 10-minute scans taken over the maximum range of hour angles to provide good (u,v) coverage. The phase calibrators were observed for 3 min. before and after every on-source scan in order to correct the amplitude and phase of the interferometer data for atmospheric and instrumental effects.

The flux density was calibrated by observing 1934–638 (3C84) for which values of 14.95, 11.59, 5.83, and 2.84 Jy were adopted at 1.4, 2.4, 4.8, and 8.6 GHz, respectively. Standard calibration and data reduction were performed using MIRIAD (Sault et al. 1995). Maps were made by Fourier transformation of the robust-weighted visibilities (Robust parameter= 0, see Briggs 1995), obtaining synthesized beams of typical FWHM of  $1.6'' \times 1.0''$ ,  $3.2'' \times 1.8''$ ,  $6.6'' \times 3.5''$ , and  $10'' \times 5.0''$  at 1.4, 2.4, 4.8, and 8.6 GHz, respectively. The noise levels attained in the deconvolved maps at 8.6 GHz were typically 0.1–0.2 mJy beam<sup>-1</sup>, which is less than that of the RMS and Walsh et al. (1998) samples by factors of about 3 and 5, respectively. Table 2.2 gives the phase tracking center, the on-source total integration times, the FWHM axes of the synthesized beam obtained at each frequency, and the deconvolved map noise levels for each observed field.

---

<sup>1</sup>The Australia Telescope Compact Array is funded by the Commonwealth of Australia for operation as a National Facility managed by CSIRO

Table 2.2. Observational parameters

Source	Phase Tracking Center		Time (mins.)	Synthesized Beam				Noise (mJy beam <sup>-1</sup> )			
	$\alpha$ (J2000)	$\delta$ (J2000)		1.4GHz	2.4GHz	4.8GHz	8.6GHz	1.4GHz	2.4GHz	4.8GHz	8.6GHz
(1)	(2)	(3)	(4)	( $''$ )	( $''$ )	( $''$ )	( $''$ )	(mJy)	(mJy)	(mJy)	(mJy)
				(5)	(6)	(7)	(8)	(9)	(10)	(11)	(12)
G263.7759-00.4281	08 <sup>h</sup> 46 <sup>m</sup> 34 <sup>s</sup> .85	-43°54'29".8	60	14.0 × 5.0	9.0 × 3.3	4.6 × 1.9	2.5 × 1.0	0.1	0.1	0.07	0.08
G268.6162-00.7389	09 03 09.51	-47 48 27.3	60	13.0 × 4.4	9.2 × 3.2	4.7 × 1.9	2.6 × 1.0	0.3	0.1	0.06	0.07
G305.7984-00.2416	13 16 42.62	-62 58 21.2	90	6.6 × 6.3	4.4 × 3.9	2.2 × 1.7	1.1 × 0.9	0.2	0.2	0.07	0.08
G317.4298-00.5612	14 51 37.60	-60 00 19.8	110	9.9 × 5.4	6.8 × 3.8	2.8 × 1.7	2.1 × 1.1	0.2	0.2	0.1	0.08
G327.1307+00.5259	15 47 32.47	-53 51 30.9	180	7.2 × 6.3	4.9 × 4.2	2.3 × 1.9	1.2 × 1.0	0.2	0.1	0.09	0.07
G333.1306-00.4275	16 21 02.95	-50 35 12.3	60	12.1 × 4.4	7.0 × 2.7	4.9 × 1.5	2.8 × 0.8	3.1	1.8	2.1	3.4
G337.4032-00.4037	16 38 50.45	-47 28 02.7	240	8.1 × 6.0	5.4 × 3.9	2.2 × 1.7	1.1 × 0.9	0.4	0.2	0.08	0.09
G345.0061+01.7944	16 56 47.59	-40 14 25.8	180	8.7 × 5.9	5.6 × 4.0	2.6 × 2.0	1.4 × 1.0	0.3	0.3	0.1	0.2
G345.3768+01.3926	16 59 37.75	-40 12 03.5	170	9.0 × 5.6	5.7 × 3.7	2.6 × 2.0	1.4 × 1.0	0.1	0.1	0.08	0.08
G345.4938+01.4677	16 59 41.63	-40 03 43.6	180	10.2 × 5.7	6.0 × 3.3	2.8 × 1.8	1.6 × 1.0	0.4	0.2	0.1	0.07
G352.5173-00.1549	17 27 11.32	-35 19 32.8	120	10.1 × 5.6	6.4 × 3.7	3.1 × 2.0	1.7 × 1.0	0.2	0.2	0.2	0.1
G009.9937-00.0299	18 07 52.84	-20 18 29.3	110	20.1 × 5.1	12.5 × 3.0	5.9 × 1.7	3.2 × 0.9	0.2	0.1	0.06	0.05

VLA observations											
Source	Phase tracking center		Time mins.	Synthesized Beam				Noise			
	$\alpha$ (J2000)	$\delta$ (J2000)		L band	C band	X band	K band	L band	C band	X band	K band
				( $''$ )	( $''$ )	( $''$ )	( $''$ )	(mJy)	(mJy)	(mJy)	(mJy)
G025.6469+01.0534	18 34 19.80	-05 59 44.0	15	14.2 × 6.3	4.3 × 2.1	3.2 × 1.1	0.9 × 0.42	0.15	0.09	0.06	0.14

Note. — Units of right ascension are hours, minutes, and seconds. Units of declination are degrees, arcminutes, and arcseconds.

In addition, we present the observations made during 2009, June, using the Very Large Array (VLA) toward the jet candidate G025.6469+01.0534. The observations were made using 27 antennas in the CnB configuration, at bands L (1425.3 MHz), C (4860.1 MHz), X (8460.1 MHz), and K (22460.1 MHz), in both circular polarizations and with a bandwidth of 100 MHz. The observational strategy for the L, C, and X bands was similar to the one used with the ATCA, that is, 8-10 minutes of on-source integration bracketed between observations of the phase calibrator. At K band, the atmospheric decorrelation becomes important compared to that at lower frequencies. Therefore, we observed only 7 minutes on-source scans and performed pointing calibrations at regular intervals. As flux calibrators we observed 3C48 and 3C286, which were calibrated using the source models included in the reduction and analysis software CASA (Reid 2010). This same software was employed for the reduction and deconvolution, using the same weighting scheme as for the ATCA data. The parameters of this observation are displayed in the last row of Table 2.2.

## 2.3 Results

In this section we present the results of the observations towards eight of the 33 jet candidates presented in Table 1 as well as towards five sources selected in an early phase of this work, which are in the radio catalogs, but do not fulfill the jet candidate selection criteria. The observed parameters of all the radio sources detected in  $80'' \times 80''$  fields centered on the target source are given in Table 2.3. Columns (2) and (3) give the peak position, cols. (4-7) the flux densities, and cols. (8-11) the deconvolved angular sizes.

We also present the derived characteristics of the radio emission from each of the jet candidates and from the other radio sources detected in the maps. Usually the spectra are well fitted by the theoretical spectrum from an uniform source of free-free emission. The free-free flux  $F_\nu$  at a frequency  $\nu$  expected from a homogeneous ionized region is given by

$$F_\nu = \Omega B_\nu(T_e) (1 - \exp(-\tau_\nu)) \quad (2.3)$$

$$\tau_\nu = 0.33 \left( \frac{\nu}{\text{GHz}} \right)^{-2.1} \left( \frac{\text{EM}}{10^6 \text{cm}^{-6} \text{pc}} \right) \left( \frac{T_e}{10^4 \text{K}} \right)^{-1.35} \quad (2.4)$$

where  $\Omega$ ,  $B_\nu$ ,  $T_e$ , and EM are the angular size, Planck function, electronic temperature, and emission measure, respectively. The ionizing photon flux  $N_H$  required to maintain a certain homogeneous H II region of volume  $V$  is given by

$$\begin{aligned} N_H &= \int_V \alpha_2 n_e^2 dV = \alpha_2 \Omega D^2 \text{EM} \\ &\approx 2.1 \times 10^{44} \left( \frac{\Omega}{\text{arcsec}^2} \right) \left( \frac{D}{\text{kpc}} \right)^2 \left( \frac{\text{EM}}{10^6 \text{cm}^{-6} \text{pc}} \right) \text{ s}^{-1} \end{aligned} \quad (2.5)$$

where  $D$  is the distance to the source, assumed to be much larger than the size of the region. The term  $\alpha_2$  is the hydrogen recombination coefficient to the second quantum level. It takes the value  $\alpha_2 \approx 3.1 \times 10^{-13} \text{ cm}^3 \text{ s}^{-1}$  at 8000 K (Spitzer 1998). We assume that each UV photon produces a single ionization.

The derived parameters, obtained from model fits of homogeneous H II regions to the spectra, are presented in Table 2.4 for all sources except G327.1307+00.5259, which we suggest

has an extragalactic origin (see §2.3.2). Columns (2) and (3) gives, respectively, the assumed distance to the source and the electron temperature used in the fit to the spectra. Columns (4) and (5) gives, respectively, the emission measure and angular size derived directly from the fit. Column (6) gives the rate of ionizing photons needed to excite the H II region ( $N_i$ ); col. (7) the physical diameter, col. (8) the mean electron density, and col. (9) the type of each radio source.

Table 2.3. Parameters of radio sources

Source (1)	Peak Position		Flux density				Deconvolved Sizes			
	R.A.	Dec.	1.4 GHz	2.4 GHz	4.8 GHz	8.6 GHz	1.4 GHz	2.4 GHz	4.8 GHz	8.6 GHz
	(J2000) (2)	(J2000) (3)	(mJy) (4)	(mJy) (5)	(mJy) (6)	(mJy) (7)	( $''$ ) (8)	( $''$ ) (9)	( $''$ ) (10)	( $''$ ) (11)
<b>Jet candidates</b>										
G305.7984−00.2416 A	13 <sup>h</sup> 16 <sup>m</sup> 42 <sup>s</sup> .626	−62°58′20″.90	10.4	11.2	11.2	9.3	U	1.4	1.4	1.4
G317.4298−00.5612 A	14 51 37.625	−60 00 20.20	...	...	11.0	19.7	...	...	U	0.36
G337.4032−00.4037 A	16 38 50.474	−47 28 03.06	27.8	56.7	110.3	139.5	1.6	1.2	0.5	0.8
G345.0061+01.7944 B	16 59 37.764	−40 12 03.76	12.2	44.4	152.5	271.8	1.3	U	0.7	0.7
G345.4938+01.4677	16 59 41.630	−40 03 43.61	2.0	4.2	8.1	12.1	U	U	U	U
G352.5173−00.1549 A	17 27 11.316	−35 19 32.19	4.4	14.1	40.5	66.0	U	U	0.9	0.4
G009.9937−00.0299	18 07 52.824	−20 18 28.88	3.4	3.5	3.2	2.3	U	U	U	U
<b>Other sources of interest</b>										
G263.7759−00.4281	08 46 34.848	−43 54 30.27	2.0	3.2	2.7	2.4	U	U	U	U
G268.6162−00.7389	09 03 09.499	−47 48 27.66	8.6	9.1	10.0	9.2	U	1.6	1.1	0.7
G327.1307+00.5259	15 47 32.472	−53 51 31.58	20.0	22.5	19.5	13.3	U	0.9	U	0.36
G333.1306−00.4275 B	16 21 02.921	−50 35 12.92	186	604	1100	2000	U	U	5.9	3.3
G345.3768+01.3926 <sup>b</sup>	...	...	...	...	...	...	...	...	...	...
<b>Additional sources detected in the field</b>										
G305.7984−00.2416 B	13 16 42.974	−62 58 28.74	...	...	0.7	1.0	...	...	U	U
G305.7984−00.2416 C	13 16 42.895	−62 58 32.82	1.2	2.2	1.8	2.0	U	U	U	0.9
G305.7984−00.2416 D <sup>a</sup>	13 16 43.474	−62 58 54.72	32.6	27.6	24.2	35.0	8.0	10	10	10
G317.4298−00.5612 B <sup>a</sup>	14 51 38.363	−60 00 24.41	41.6	48.9	5.7	...	7.9	7.1	7	...
G333.1306−00.4275 A	16 21 00.304	−50 35 08.30	1100	1589	1348	1664		~ 25		
G337.4032−00.4037 B <sup>a</sup>	16 38 51.131	−47 28 14.76	5.0	5.1	6.5	4.7	U	U	2.6	~ 2
G345.0061+01.7944 A <sup>a</sup>	16 56 45.970	−40 14 38.14	91.4	99.1	83.0	72	7.1	8.1	~ 8	~ 8
G352.5173−00.1549 B <sup>a</sup>	17 27 11.910	−35 19 35.53	2.8	1.6	...	...	U	U	...	...
<b>VLA Jet candidate</b>										
Source	Peak Position		Flux density				Deconvolved Sizes			
	R.A. (J2000)	Dec. (J2000)	L band (mJy)	C band (mJy)	X band (mJy)	K band (mJy)	L band ( $''$ )	C band ( $''$ )	X band ( $''$ )	K band ( $''$ )
G025.6469+01.0534	18 34 20.89	−05 59 41.9	1.32	2.85	3.2	2.92	U	U	0.64	0.85

Note. — Units of R.A. are hours, minutes and seconds. Units of declination are degrees, arcminutes and arcseconds. All sources in the the first block of the table were observed using ATCA.

<sup>a</sup>The peak positions for these sources was obtained from the 1.4 GHz images.

<sup>b</sup>This source was not detected in our observations.

### 2.3.1 Jet candidates

Maps of the radio continuum emission at the four frequencies, from regions of  $80'' \times 80''$  in size centered at the position of the jet candidates, are shown for each source. In each radio map the cross indicates the position of the target radio object as reported in the catalogs of Urquhart et al. (2007a) or Walsh et al. (1998). The contour levels are in a geometric progression with base between 1 and 2, the value chosen so each radio map displays the most important resolved and unresolved features. The noise and beam size for each of these maps are listed in Table 2.2. Squares in the 1.4 GHz maps indicate the peak position of the MSX sources in the field. Radio continuum spectra of the jet candidates are presented in Fig. 2.18. The spectra of the other sources detected in these maps are presented in Fig. 2.25, except those in the G345.4938+01.4677 field which are analyzed in Chapter 4. We also searched the literature for the presence of water (23.2 GHz) and methanol (6.7 GHz) masers, though to trace young stellar environments. We used the catalogs of water masers presented in Valdetaro et al. (2001), Urquhart et al. (2009) and Forster & Caswell (1999); and the methanol maser catalogs of Pestalozzi et al. (2005), Walsh et al. (1997) and Walsh et al. (1998). In the cases when a reliable position can be assigned to the maser emission (via interferometer observations) we indicate it in the radio maps.

**G305.7984–00.2416.**– This jet candidate, taken from the Walsh et al. survey, is associated with IRAS 13134–6342, although it is located  $\sim 24''$  north of the peak position of the IRAS object. There are four radio objects within the  $80'' \times 80''$  region shown in Fig. 2.2: three compact components (labeled A, B, and C) and an extended source, labeled D, located about  $35''$  south of component A. Components A, C and D were detected at all frequencies, whereas component B was only detected at the two higher frequencies. Components B and C are unresolved at all frequencies.

In order to better determine the nature and evolutionary stage of these radio sources we present in the top panel of Figure 2.3 a three color image made from the 3.6, 4.5 and  $8.0 \mu\text{m}$  emission as seen by the *Spitzer*-GLIMPSE survey. In the bottom panel, we show an image of the MIPS  $24 \mu\text{m}$  emission, together with 4.8 GHz contours. A comparison between the radio and MIR images shows that component A is associated with an extended MIR feature which is prominent at  $8.0 \mu\text{m}$ , components B and C are associated with compact MIR objects, GLIMPSE G305.7996–00.2438 and G305.7991–00.2447, respectively, and that component D is associated with an extended envelope of diffuse emission most prominent at  $8.0 \mu\text{m}$ , thought to arise from a photon dominated (or photo-dissociation) region (PDR).

The jet candidate corresponds to component A, which at 8.6 GHz exhibits a cometary-like structure with a head toward the north and a tail trailing to the south. Its radio continuum spectrum (see Figure 2.18) is well fitted by that of a uniform density H II region (Eqs. 2.3 and 2.4) with an emission measure of  $2.3 \times 10^6 \text{ pc cm}^{-6}$  and an angular size of  $1.4''$ . From Eq. (2.5) the ionizing photon flux needed to excite this H II region is  $9.6 \times 10^{45} \text{ photons s}^{-1}$ . We conclude that component A corresponds to a cometary UCH II excited by a B1-B0.5 ZAMS star. Methanol maser activity has been detected toward this field (Pestalozzi et al. 2005), although it was not possible to discern its precise location.

The radio continuum spectra of components B, C and D are shown in Figure 2.25. The spectra of source B shows that its flux density is rising with frequency, suggesting that it

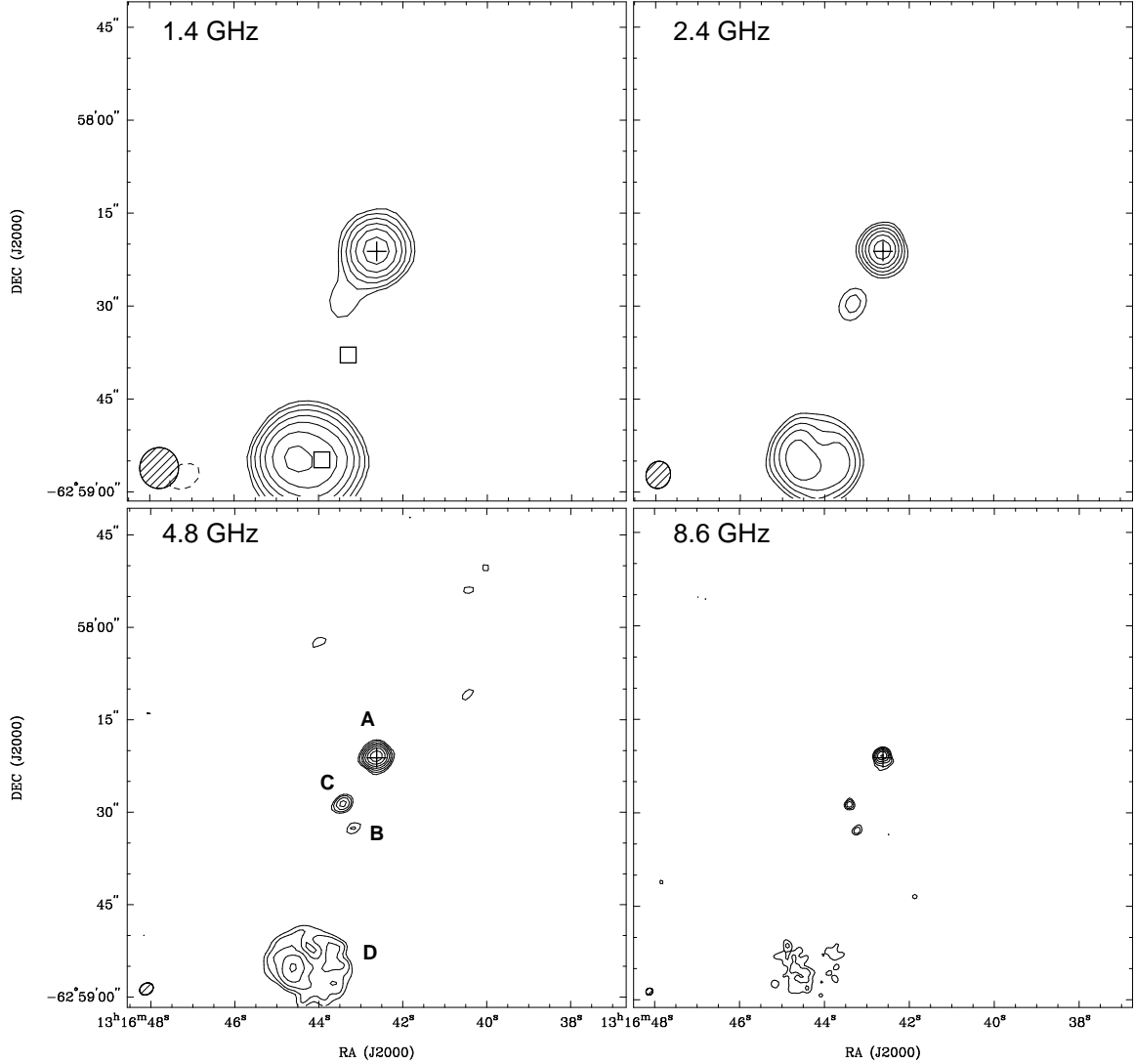


Figure 2.2 ATCA maps of the radio continuum emission toward G305.7984–00.2416. The cross marks the position of the radio source reported by Walsh et al. (1998). Beams are shown in the lower left corner of each panel. Top left: 1.4 GHz map. The squares mark the peak position of two MSX 21  $\mu$ m sources in the field. Top right: 2.4 GHz map. Bottom left: 4.8 GHz map. Labeled are the four radio sources detected in this field. Bottom right: 8.6 GHz map. Contour levels are  $-5, 5, 8, 13, 20, 30, 46,$  and  $70$  times  $0.16 \text{ mJy beam}^{-1}$  for the 1.4 and 2.4 GHz maps, and  $0.07 \text{ mJy beam}^{-1}$  for the 4.8 and 8.6 GHz maps.

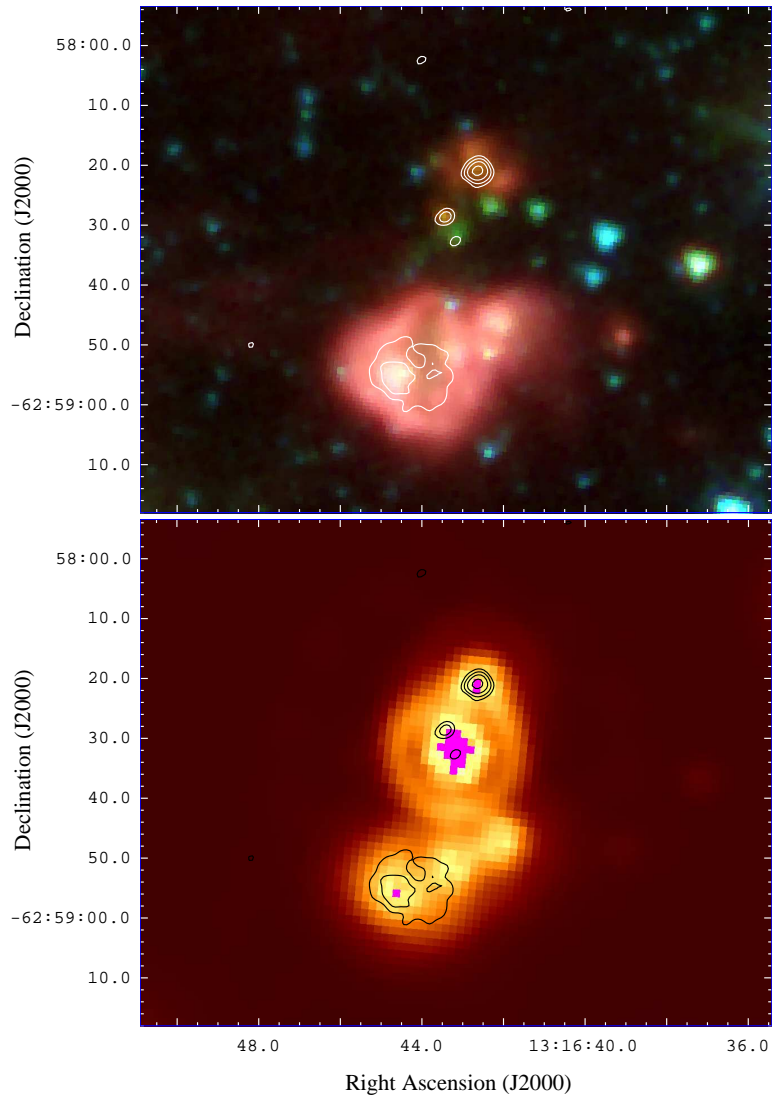


Figure 2.3 Comparison between the radio and IR images for G305.7984–00.2416. The white and black contours in both panels represent 4.8 GHz data. Top panel: 3 color IRAC image using 8.0, 4.5, and 3.6  $\mu\text{m}$  data from GLIMPSE. Bottom panel: 24  $\mu\text{m}$  MIPS image from MIPS GAL. Saturated pixels are shown in magenta.

corresponds to an optically thick H II region. A fit with a uniform density H II region model gives an emission measure of  $1.3 \times 10^8 \text{ pc cm}^{-6}$  and an angular size of  $0.066''$ . For component C we derived an emission measure of  $1.0 \times 10^6 \text{ pc cm}^{-6}$  and an angular size of  $0.9''$ . The ionizing photon rate needed to excite this H II region is  $N_i \sim 2 \times 10^{45} \text{ s}^{-1}$ , which can be provided by a B1 ZAMS star. For component D we derived an emission measure of  $2.0 \times 10^5 \text{ pc cm}^{-6}$  and an angular size of  $8.1''$ . The ionizing photon rate needed to excite this extended and diffuse H II region is  $N_i \sim 3 \times 10^{46} \text{ s}^{-1}$ , which can be provided by a B0.5 ZAMS star.

The G305.7984–00.2416 region may be representative of what is expected to be seen within the maternities of high-mass stars: multiple young stars clustered and in different evolutionary stages. We find that the target radio source in the field is not a jet but an UC H II. The weakest radio source detected in the region (Component B) is particularly striking because, as shown in Fig. 2.3, it is associated with a green object in the three color Spitzer image, possibly indicating shock activity. Extended green objects (EGOs, Chambers et al. 2009, Cyganowski et al. 2008) are thought to probe shocked gas regions associated with HMYSOs, although vibrational CO and hydrogen Br $\alpha$  contribution cannot be ruled out (Qiu et al. 2011).

The position of Component B is consistent with the peak of the emission in the MSX band E ( $21.34 \mu\text{m}$ ) image (marked with a square in Fig. 2.2), and it also seems to be the brightest source in the  $24 \mu\text{m}$  MIPS image (Fig. 2.3), despite the saturation of the central pixels. This evidence suggests that component B is actually the most embedded, and possibly the youngest, object in the region. Using the GLIMPSE flux densities and assuming that the MSX E band flux arises entirely from this source, the YSO SED model fitter of Robitaille et al. (2007) gives a total luminosity of  $3.3 \pm 0.9 \times 10^3 L_{\odot}$ , equivalent to that of a B2 ZAMS star. The ratio between the ionizing photon flux derived from the radio SED fitting ( $\log N_i \sim 45.09$ ) and that inferred from the total luminosity ( $\log N_{\star} \sim 44.8$ ) is 1.9, implying that this radio source is slightly under-luminous in radio. Given its characteristics, particularly the association to green fuzzy emission, we suggest that component B could represent the transition phase as an early B-type star grows onto an O-type star. The excess emission at  $4.5 \mu\text{m}$  may arise from shocks produced in the infalling gas.

**G317.4298-00.5612.** – This RMS jet candidate is associated with IRAS 14477–5947. Water maser activity has been detected toward this source (Urquhart et al. 2009), supporting its identification as a HMYSO. The kinematical distance of the object is 15 kpc, with no ambiguity ( $v_{LSR} = 27.4 \text{ km s}^{-1}$  in the CS(2→1) line, Bronfman et al. 1996) and assuming a flat rotation curve ( $\Theta = 220 \text{ km s}^{-1}$ ). From the bolometric flux given by Mottram et al. (2011a) we estimate a total luminosity of  $L \sim 3.2 \times 10^5 L_{\odot}$ , equivalent to that of a ZAMS star with an spectral type between O6 and O5.5.

There are two radio objects within the  $80'' \times 80''$  region shown in Fig. 2.4: a compact component (labeled A), seen only at 4.8 and 8.6 GHz, and an extended component (labeled B) mainly seen at 1.2 and 2.4 GHz and completely resolved out at 8.6 GHz.

Component A corresponds to the jet candidate. At 1.4 and 2.4 GHz this object is immersed within the more extended component so we could not measure its flux densities. In the frequency range between 4.8 and 8.6 GHz, the flux density rises with frequency. Since the source is unresolved, from these data it is not possible to discern whether this object is a jet or an optically thick H II region. If an H II region, then a fit to the radio continuum spectrum

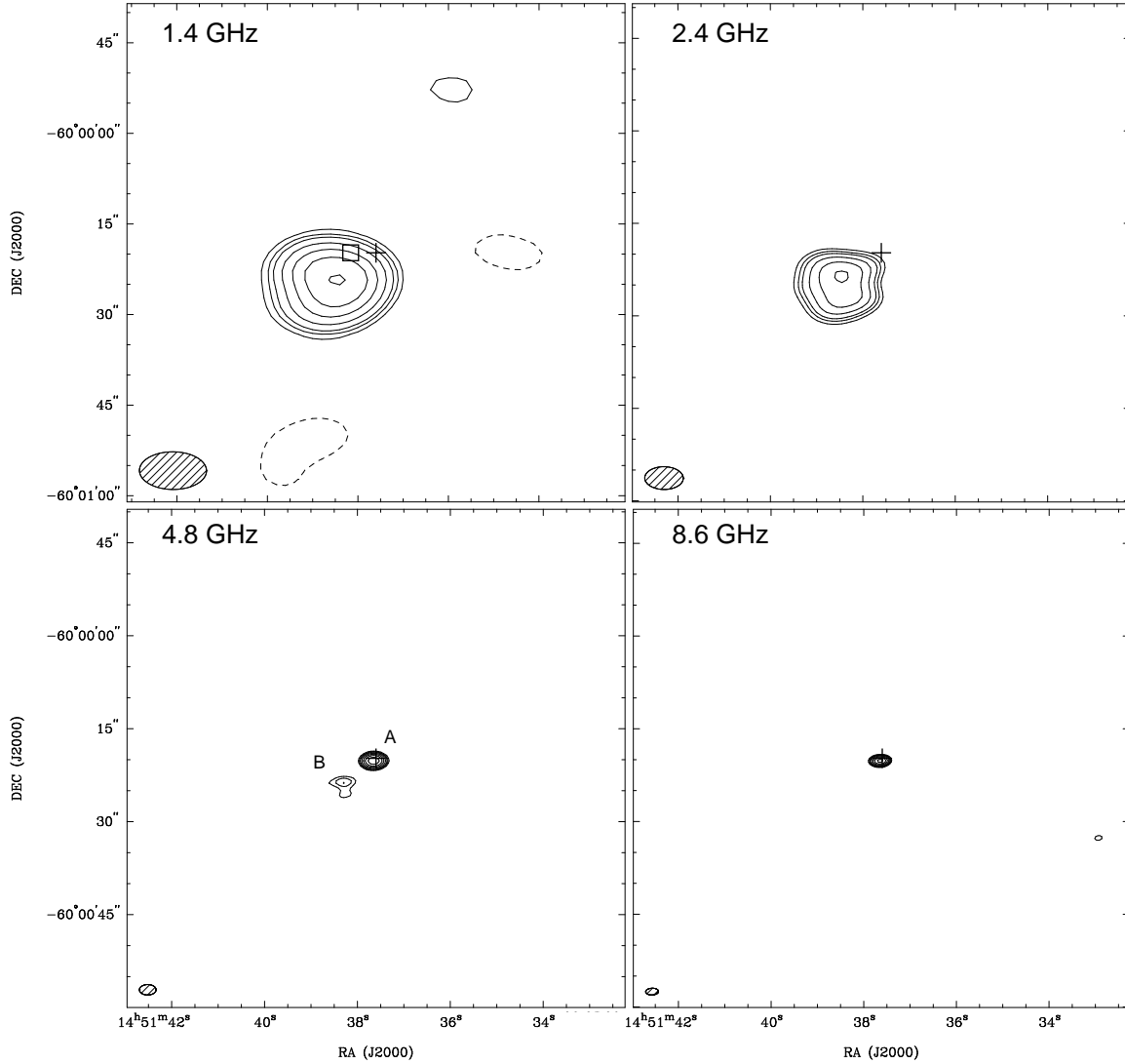


Figure 2.4 ATCA maps of the radio continuum emission toward G317.4298–00.5612. The cross marks the position of the radio source reported by Urquhart et al. (2007a). Beams are shown in the lower left corner of each panel. Top left: 1.4 GHz map. The square marks the peak position of the MSX source detected at  $21 \mu\text{m}$ . Top right: 2.4 GHz map. Bottom left: 4.8 GHz map. The two radio sources detected in this field are labeled A and B. Bottom right: 8.6 GHz map. Contour levels are  $-5, 5, 7, 9, 13, 19, 27,$  and  $40$  times  $0.5, 0.5, 0.2,$  and  $0.4 \text{ mJy beam}^{-1}$  for the 1.4, 2.4, 4.8, and 8.6 GHz images, respectively.

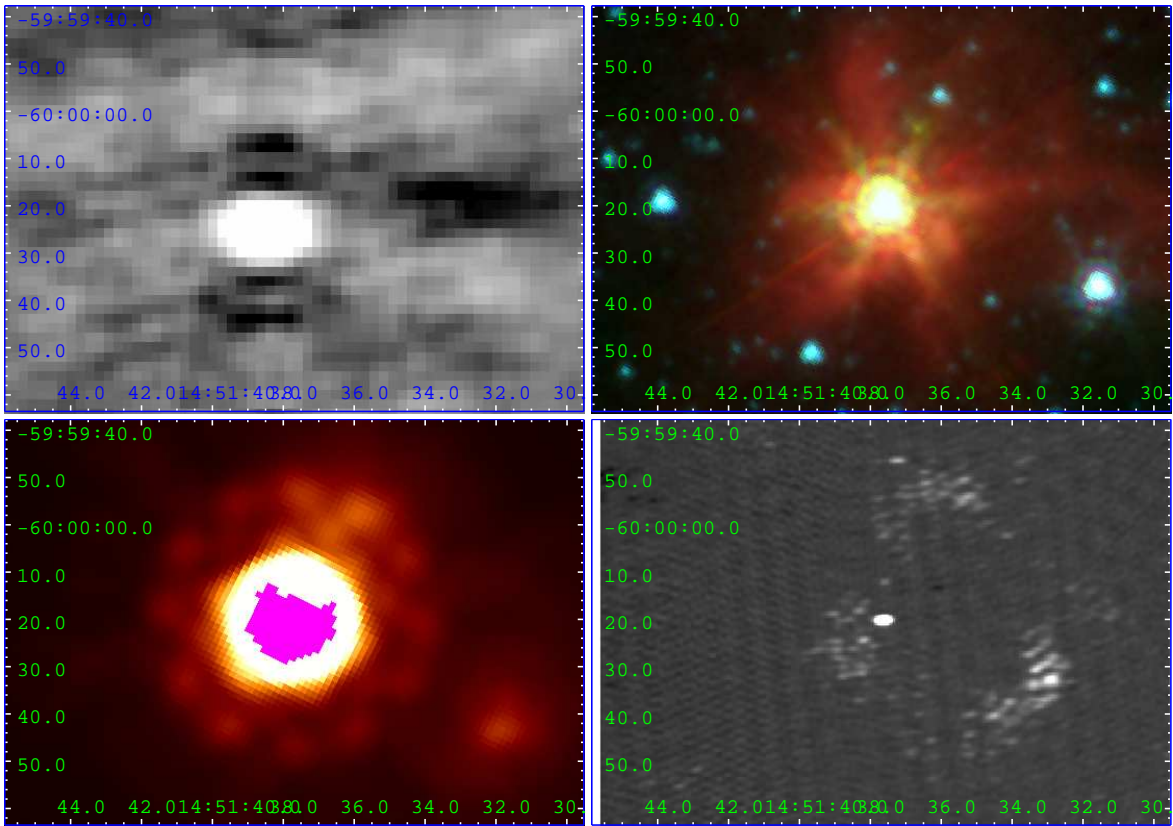


Figure 2.5 Comparison between the radio and IR images for G317.4298–00.5612. Top left panel: 2.4 GHz image. Top right: 3 color IRAC image using 8.0, 4.5, and 3.6  $\mu\text{m}$  data from GLIMPSE. Bottom left: 24  $\mu\text{m}$  MIPS image from MIPS GAL. Bottom right: 8.6 GHz image.

with an uniform density model (see Fig. 2.18) indicates an emission measure of  $1.9 \times 10^8$  pc cm<sup>-6</sup> and an angular size of 0.27". The rate of ionizing photons required to excite this region of ionized gas is  $7.2 \times 10^{47}$  s<sup>-1</sup>, which can be provided by a O9.5 ZAMS star.

The radio continuum spectrum of component B (see Figure 2.25) suggests it corresponds to an extended optically thin H II region. A fit with a theoretical spectra of an homogeneous constant density H II region, gives an emission measure of  $3.5 \times 10^5$  pc cm<sup>-6</sup> and an angular size of 7.6". The rate of ionizing photons required to excite the H II region is  $9.3 \times 10^{47}$  s<sup>-1</sup>, which can be provided by a O9.5 ZAMS star.

The sum of the luminosities of the ZAMS stars exciting components A and B is  $8 \times 10^4 L_{\odot}$ , about 4 times smaller than the bolometric luminosity of the whole region. This discrepancy may be solved if component A is not an H II region but an ionized jet, and thus the exciting source could have a larger luminosity than that implied from the observed radio flux. This hypothesis finds support in the detection of an unresolved, high velocity CO outflow (see Chapter 3). Further observations are needed to confirm this interpretation. The MIR images shown in Fig. 2.5 show a compact intense central component in IRAC bands, and a highly saturated image at 24  $\mu$ m. Although this last images is rather un-usable, it stills shows that the compact radio component A is associated with the "center" and peak of the emission in this band. We could not distinguish a clear MIR counterpart of component B.

**G337.4032–00.4037.**– This jet candidate is an RMS source associated with IRAS 16351–4722. There are two radio sources within the 80"  $\times$  80" region shown in Fig. 2.6: a bright compact component (labeled A) and a weak component, labeled B, located about 13" southeast of component A. Component A, which corresponds to the jet candidate, is unresolved at all frequencies, whereas component B is resolved out at 4.8 and 8.6 GHz. Methanol maser activity has been detected associated to component A by Walsh et al. (1998), but no water maser was detected by Urquhart et al. (2009).

In order to better determine the nature of the radio sources we present in Figure 2.7, a three-color image of the MIR emission made using the 3.6, 4.5, and 8.0  $\mu$ m data obtained from the *Spitzer*-GLIMPSE survey, and in red contours the 2.4 GHz data. This Figure shows that component A is associated with the central, bright, greenish-like object seen in the *Spitzer* image and with a strong (saturated) source in the MIPS image. Assuming that this star forming region is at a distance of 3.2 kpc (Faúndez et al. 2004), then from the bolometric flux reported by Mottram et al. (2011a,their component "B"), we obtain a bolometric luminosity of  $2.7 \times 10^4 L_{\odot}$ , equivalent to that of B0 ZAMS star.

The radio continuum spectrum of component A (see Figure 2.18) shows that the flux density steadily increases with frequency. A power law fit gives an spectral index of  $0.9 \pm 0.15$ , consistent with a pressure confined jet (Reynolds 1986). Moreover, from Equation (19) of Reynolds (1986), and assuming values similar to that of G345.4938+01.4677 (see Chaps. 4 and 5) of 45° for the inclination, 0.2 rad for the jet aperture, a turnover frequency of 20 GHz, and a wind velocity of 300 km s<sup>-1</sup>, we obtain a mass loss rate of  $\dot{M} \approx 2 \times 10^{-5} M_{\odot}$  yr<sup>-1</sup>. This value is more than an order of magnitude larger than the mass loss rate deduced for G345.4938+01.4677 using a similar model (Chapter 4), but is consistent with G337.4032–00.4037 A having approximately 100 times more radio emission.

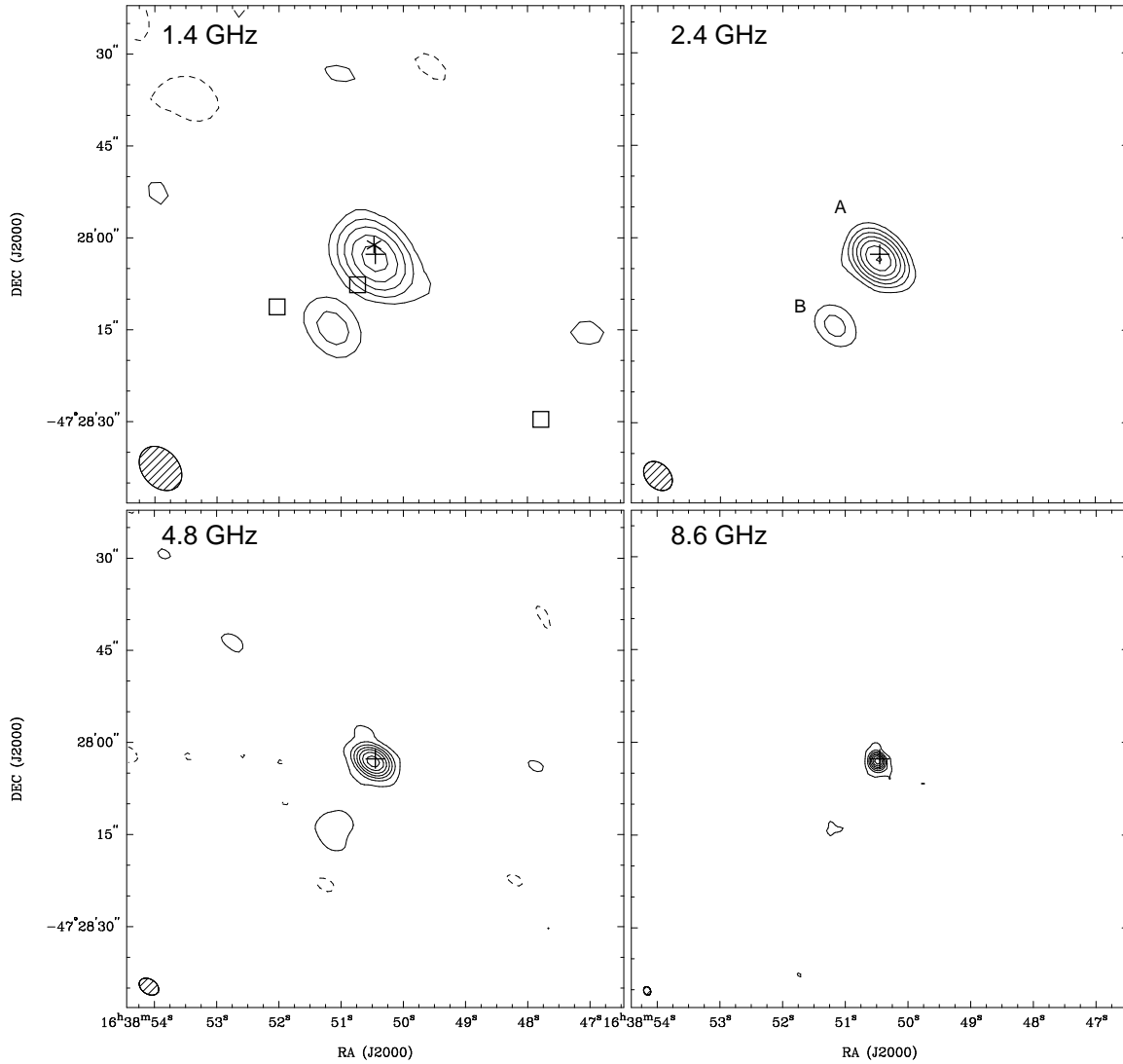


Figure 2.6 ATCA maps of the radio continuum emission from G337.4032–00.4037. The cross marks the position of the radio source reported by Urquhart et al. (2007a). Beams are shown in the lower left corner of each panel. Top left: 1.4 GHz map. The squares show the peak position of the two MSX  $21\ \mu\text{m}$  sources in the field. The star marks the position of the methanol masers detected by Walsh et al. (1998). Top right: 2.4 GHz map, the two main radio components are marked with letters A and B. Bottom left: 4.8 GHz map. Bottom right: 8.6 GHz map. Contour levels are  $-5, 5, 14, 28, 50, 81, 129,$  and  $200$  times  $0.25\ \text{mJy beam}^{-1}$  for the 1.4 and 2.4 GHz images, and  $-5, 5, 29, 65, 118, 199, 319,$  and  $500$  times  $0.15\ \text{mJy beam}^{-1}$  for the 4.8 and 8.6 GHz images.

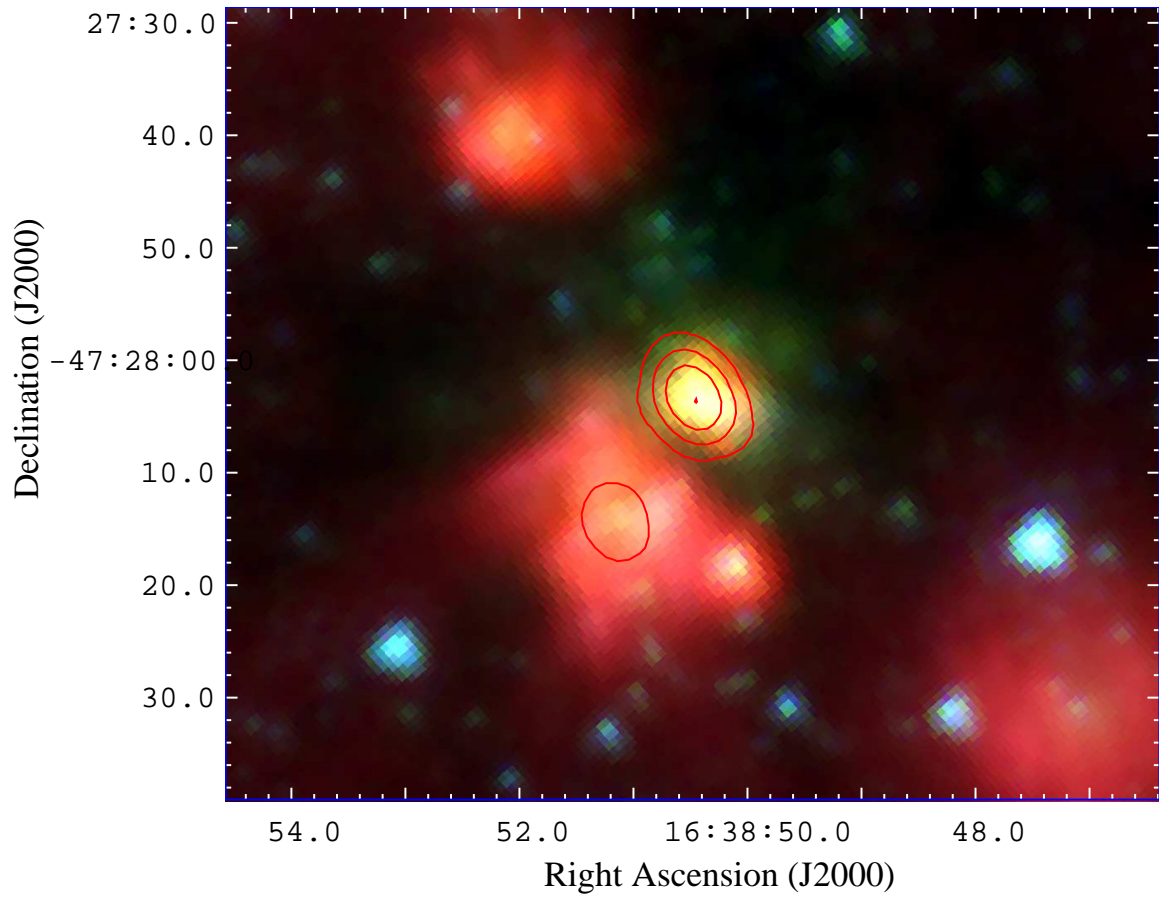


Figure 2.7 Three color MIR image toward G337.4032–00.4037 made using IRAC-GLIMPSE 8.0, 4.5, and 3.6  $\mu\text{m}$  data as red, green, and blue. Red contours correspond to the 2.4 GHz radio emission.

While we argue that this source is a jet, which is supported by the presence of a very high velocity ( $\sim 80 \text{ km s}^{-1}$ ) molecular outflow (see Chapter 3), these type of sources have usually been interpreted as hypercompact H II regions (HCH IIRs) (Franco et al. 2000) with power-law dependence of the density with radius (see Panagia & Felli 1975, Avalos et al. 2006, and also Appendix A). For such an spherical H II region, in which the density follows  $n_e \propto r^{-\beta}$ , the flux density should exhibit a power-law dependence with frequency,  $S_\nu \propto \nu^{-\alpha}$ , with  $\alpha = (2\beta - 3.2)/(\beta - 0.5)$ . There is no hint of the power-law spectrum turning over at high frequencies, indicating that the emission does not reach optically thin conditions in the whole observed frequency range. Assuming ionization equilibrium, with  $N_\star \sim 2.6 \times 10^{47}$  (appropriate for a ZAMS star with  $2.7 \times 10^4 L_\odot$ ), and that the power-law index of the density law is 2.41 (to be consistent with the above equation), the observed spectrum and source size can be well reproduced if the region has an inner radius of 0.0032 pc, an outer radius of 0.044 pc and an electron density of  $3.6 \times 10^5 \text{ cm}^{-3}$  at the inner radius. We note, however, that the jet and the HCH IIR models have many free parameters, and that the solutions are not unique.

Figure 2.7 shows that component B is associated with the bright, central part of an extended, diffuse MIR object, most prominent at  $8.0 \mu\text{m}$ , likely to correspond to a PDR around an H II region. From the bolometric flux reported by Mottram et al. (2011a) we derive a bolometric luminosity for component B of  $8.4 \times 10^4 L_\odot$ . The flux density expected at 1.4 GHz from of an optically thin H II region excited by a star with that luminosity is  $\sim 0.5 \text{ Jy}$ , considerably larger than the measured 5 mJy. This implies, as our observations indicate, that the flux density is resolved out by the interferometer even at 1.4 GHz.

**G345.0061+01.7944.** – This RMS source is a jet candidate associated with IRAS 16533–4009. There are two radio objects within the  $80'' \times 80''$  region shown in Fig. 2.8: a compact component (labeled B) and an extended source, labeled A, located about  $22''$  southwest of component B. Component B, which corresponds to the jet candidate, is unresolved at all frequencies whereas component A is partially resolved out at 4.8 GHz and highly resolved out at 8.6 GHz.

Figure 2.9 presents a three-color image of the MIR emission made using the 3.6, 4.5, and  $8.0 \mu\text{m}$  data obtained from the *Spitzer*-GLIMPSE survey, together with red contours displaying the 2.4 GHz data. This Figure shows that component B is associated with a bright, compact MIR source prominent in the  $4.5 \mu\text{m}$  band (green color) whereas component A is associated an extended source of diffuse emission most prominent at  $8.0 \mu\text{m}$ . Methanol maser activity has been detected by Walsh et al. (1998) toward two positions: one associated to radio component B, and another located approximately  $20''$  to the northwest. These positions correspond to the position of the “green” sources seen in Fig. 2.9. Water maser activity has been detected in the field Forster & Caswell (1999), but not directly associated to any radio or IR source.

The radio continuum spectrum of component B (see Figure 2.18) suggests it corresponds to an optically thick H II region. A fit with a theoretical spectra of an homogeneous constant density H II region, gives an emission measure of  $4.6 \times 10^8 \text{ pc cm}^{-6}$  and an angular size of  $0.73''$ . The rate of ionizing photons required to excite the H II region is  $1.7 \times 10^{47} \text{ s}^{-1}$ , which can be provided by a B0 ZAMS star. Component B is associated with one of the three IR sources reported by Mottram et al. (2011a) within the region (their component “C”). From its bolometric flux, of  $1.19 \times 10^{-10} \text{ W m}^{-2}$ , and assuming it is at the near distance of 1.7 kpc, we derive that this IR source has a luminosity of  $L_{bol} = 1.1 \times 10^4 L_\odot$ , equivalent to that of a

B0.5 ZAMS star. The ionizing photon flux provided by such a star ( $N_{\star} \approx 1.7 \times 10^{46}$ ) is about an order of magnitude smaller than that implied from the modeling of the radio spectra, being this source *overluminous* in radio rather than underluminous. We note however that there is considerable uncertainty in the determination of the bolometric flux: taking a value closer to the given upper limit ( $19.4 \times 10^{-11} \text{ W m}^{-2}$ ) makes both quantities consistent within a factor of less than 2.

The radio continuum spectrum of component A indicates that it corresponds to an optically thin region of ionized gas. A fit with a theoretical spectra of an homogeneous constant density H II region, gives an emission measure of  $5.0 \times 10^5 \text{ pc cm}^{-6}$  and an angular size of  $8.0''$ . The rate of ionizing photons required to excite this H II region is  $2.2 \times 10^{46} \text{ s}^{-1}$ , which can be provided by a B0.5 ZAMS star. Two of the three MIR sources identified by Mottram et al. (2011a) (their components A and B) are associated with this radio component, but none is located at the peak of the radio emission.

**G345.4938+01.4677.** – This jet candidate, taken from Urquhart et al. is associated with IRAS 16532–3959. A detailed analysis of the characteristics of these sources and of their physical nature is presented later in Chapters 4 and 5. Figure 2.10 shows that there is a string of radio sources consisting of a compact, bright central component flanked by two inner and two outer lobes symmetrically offset from the central source, and aligned approximately in the E-W direction. Table 2.3 displays the fluxes of the central object. The spectrum correspond to a power law with a spectral index between 1.4 and 8.6 GHz of  $0.85 \pm 0.15$  (see Fig. 2.18) consistent with free-free emission from a thermal jet. The radio emission from the lobes have spectral indices in the range characteristic of thermal emission.

In summary, the central object corresponds to a ionized jet and the emission from the lobes arises in shocks resulting from the interaction of the collimated wind with the surrounding medium. This source, which is currently one of the most massive and luminous ( $7.0 \times 10^4 L_{\odot}$ ) HMYSO known to be associated with an ionized jet, was discovered as part of this search.

**G352.5173–00.1549.** – This jet candidate, taken from the Walsh et al. survey, is associated with IRAS 17238–3516, and to water maser activity (Forster & Caswell 1999). There are two radio sources within the  $80'' \times 80''$  region shown in Fig. 2.11: a bright compact component (labeled A) detected at the four frequencies, and a weaker, presumably extended component (labeled B) only seen at 1.4 and 2.4 GHz and resolved out at the higher frequencies.

Component A, which corresponds to the jet candidate, can be well modeled by a homogeneous H II region with  $T_e \sim 15000 \text{ K}$ ,  $EM \sim 2.8 \times 10^8 \text{ pc cm}^{-6}$  and an angular size of  $0.42''$  (Figure 2.18). The rate of ionizing photons required to excite this H II region is  $3.2 \times 10^{47} \text{ s}^{-1}$ , which can be provided by a O9.5-B0 ZAMS star. Figure 2.12 shows that component A is associated with a deeply embedded object seen conspicuously in MIPS at  $24 \mu\text{m}$  but undetected in the GLIMPSE images, indicating a very high absorption. We note that the object located  $3''$  to the west of component A, seen at  $4.5$  and  $3.6 \mu\text{m}$  (GLIMPSE 352.5170–00.1540), and in 2MASS bands (Skrutskie et al. 2006, source 2MASS17271105–3519310), is a foreground object. Assuming that the emission detected in the IRAS bands (IRAS 17238–3516) corresponds to reprocessed emission from the exciting source of component A and that it is located at its kinematical distance of  $5.2 \text{ kpc}$ , we derive a total luminosity of  $\sim 10^5 L_{\odot}$ , equivalent to that of an O7 ZAMS star. The ionizing photon rate expected from a star of that luminosity ( $N_{\star} \sim 4.2 \times 10^{48} \text{ s}^{-1}$ ) is about 13 times greater than that derived from the fit to the radio

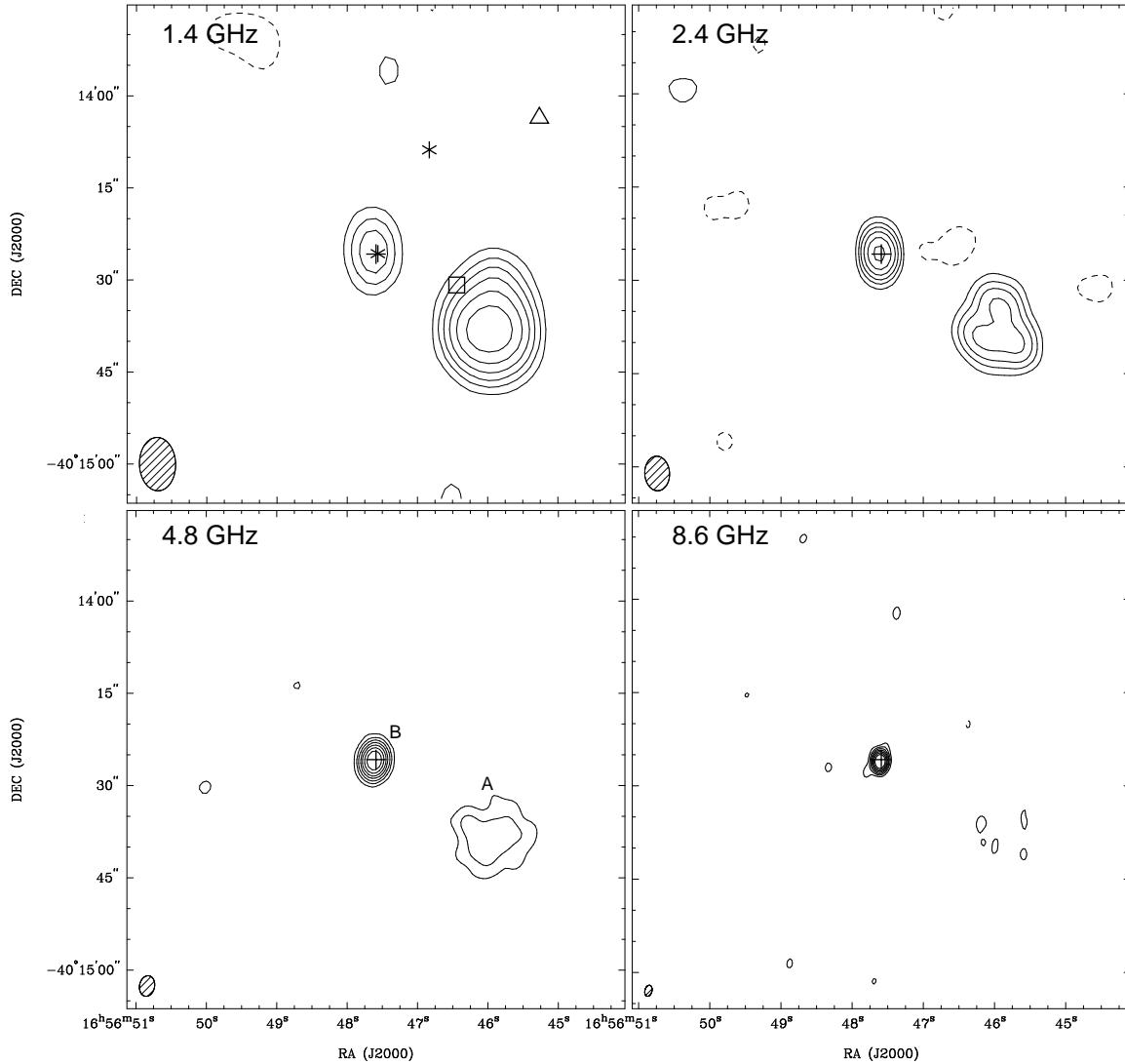


Figure 2.8 ATCA maps of the radio continuum emission towards G345.0061+01.7944. The cross marks the position of the radio source reported by Urquhart et al. (2007a). Beams are shown in the lower left corner of each panel. Top left: 1.4 GHz map. The square marks the peak position of the MSX source detected at  $21 \mu\text{m}$ , the triangle the position of the  $\text{H}_2\text{O}$  maser reported by Forster & Caswell (1999), and the stars the position of methanol masers detected by Walsh et al. (1998). Top right: 2.4 GHz map. Bottom left: 4.8 GHz map. Labeled are the two radio components detected in the field. Bottom right: 8.6 GHz map. Contour levels are  $-5, 5, 11, 19, 31, 50, 78, 120$  times  $0.4 \text{ mJy beam}^{-1}$  for the 1.4 and 2.4 GHz images and  $-5, 5, 14, 28, 50, 81, 129, 200$  times  $0.4 \text{ mJy beam}^{-1}$  for the 2.4 and 8.6 GHz images.

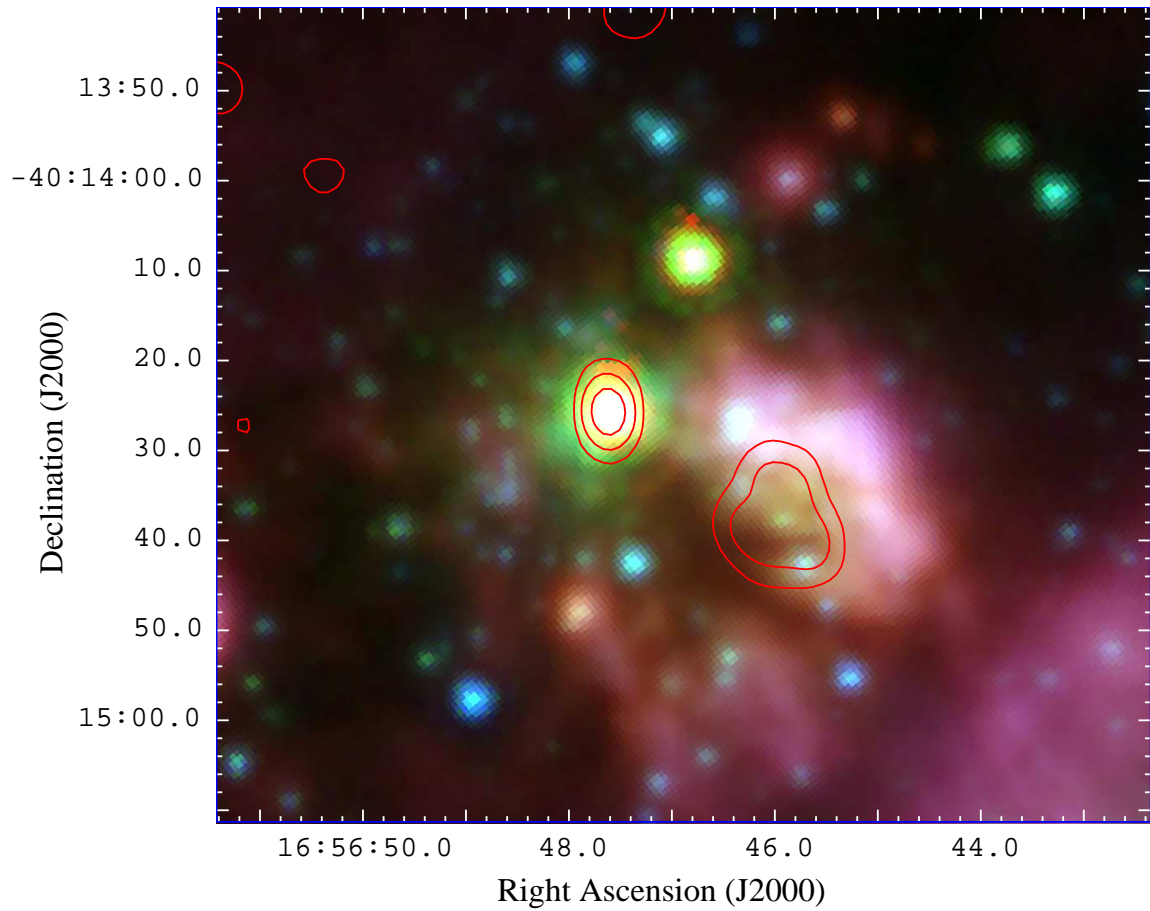


Figure 2.9 Three color *Spitzer* MIR image of G345.0061+01.7944, made using 8.0, 4.5, and 3.6  $\mu\text{m}$  data from GLIMPSE, and superimposed red contours showing the 2.4 GHz radio emission.

spectra, indicating that this source is intrinsically underluminous in radio. Water maser has been observed towards the central radio source (Forster & Caswell 1999). There has also been methanol maser activity detected toward this field (Pestalozzi et al. 2005), but its position is not well constrained by the observations.

We note also that there is a discrepancy in a factor  $\sim 6$  between the flux we measure at 8.6 GHz and the flux reported by Walsh et al. (1998) at 8.64 GHz. Moderate flux variations in hypercompact H II regions have been detected (e.g. Galván-Madrid et al. 2008), but according to recent models, it is very unlikely to observe a flux increment so large as implied by our observations in a  $\sim 10$  year basis (Galván-Madrid et al. 2011). Either the reason of the difference being observational or physical, we do not discuss it further in the present work.

Component B corresponds probably to a more developed H II region, which is consistent with the radio emission at the lower frequencies (Fig. 2.25). Figure 2.12 also shows that this source is associated with a faint  $24 \mu\text{m}$  counterpart.

**G009.9937–00.0299.** – This jet candidate, taken from Walsh et al., is associated with the MSX source G009.9983–00.0334 and with IRAS 18048–2019. It is the only radio source within the  $80'' \times 80''$  region shown in Fig. 2.13. Its radio continuum spectrum (see Fig. 2.18) can be well modeled with the theoretical spectra of an homogeneous constant density H II region. Assuming an electron temperature of 8000 K, we derive an emission measure of  $5.9 \times 10^5 \text{ pc cm}^{-6}$  and an angular size of  $1.5''$ . The rate of ionizing photons required to excite the H II region is  $7.9 \times 10^{45} \text{ s}^{-1}$ . Assuming that this object is located at 5 kpc — the *near* distance derived from the observed  $v_{LSR} = 49 \text{ km s}^{-1}$  (Bronfman et al. 1996) — its total luminosity is  $1.7 \times 10^4 L_{\odot}$  (Lackington 2011), in between those of B0 and a B0.5 ZAMS stars, and for which  $N_{\star} = 7.9 \times 10^{46} \text{ s}^{-1}$  (interpolated from Panagia 1973). The G009.9937–00.0299 object is then underluminous in radio by a factor of  $\sim 10$ . However, we do not see neither the spectral nor morphological features to characterize this radio source as a jet and conclude it corresponds to an UC H II region. Walsh et al. (1998) reported methanol maser emission located approximately  $45''$  toward the southwest of the radio source and probably not directly related to it. Water maser activity has also been detected toward this source (Valdettaro et al. 2001).

The mid-infrared images, specially the  $24 \mu\text{m}$  MIPS image shown in Figure 2.14, clearly establish that the field contains at least two embedded stars, possibly B-type. Both are GLIMPSE sources with counterpart at  $24 \mu\text{m}$ : one is the central source, associated to the radio emission and probably to most of the FIR flux (GLIMPSE G009.9978-00.0332) and the other is a compact “red” source (as seen red in the IRAC three-color image) located  $13''$  northeast from the first, catalogued as GLIMPSE G010.0014-00.0344.

**G025.6469+01.0534.** – This jet candidate was taken from the catalog of Walsh et al., and is associated with IRAS 18316–0602 and MSX G025.6498+01.0491. It is the only radio source located within the  $80'' \times 80''$  region shown in Figure 2.15. Assuming this source is located at 3.1 kpc (Faúndez et al. 2004), the total luminosity derived for this object is  $2.05 \times 10^4 L_{\odot}$  (Lackington 2011), consistent with a B0 ZAMS star for which  $N_{\star} = 1.25 \times 10^{47} \text{ s}^{-1}$  (interpolated from Panagia 1973).

The radio emission consist of a small single source at all frequencies, except in the K band where the emission is resolved in two peaks. The spectrum of the source shown in Figure 2.16

is well fitted by an uniform H II region of temperature 8000 K,  $EM = 1.17 \times 10^7 \text{ pc cm}^{-6}$ , and  $0.40''$  of size. The ionizing photon rate required to excite this ionized region is  $N_i = 3.07 \times 10^{45} \text{ s}^{-1}$ , about 50 times below  $N_*$ . The source G025.6469+01.0534 is underluminous in radio, but it has no spectral nor morphological features that indicates it is a jet. It is, however, associated to a strong molecular outflow (see Chapter 3 and also Shepherd & Churchwell 1996) and to  $\text{H}_2$  emission detected at  $2.12 \mu\text{m}$  (Varricatt et al. 2010). This source was also observed with the VLA by Kurtz et al. (1994) in the X band, obtaining 3.8 mJy, consistent with our flux. Figure 2.17 shows a three color IRAC image of G025.6469+01.0534, a compact source with some enhancement of the green  $4.5 \mu\text{m}$  emission. Methanol masers activity has been detected toward this source by Walsh et al. (1998). Its position is indicated in Fig. 2.15). Water maser activity has also been observed (Valdettaro et al. 2001), but with no accurate determination of its position.

### 2.3.2 Other sources of interest

In this section we report the results of the observations five radio sources, chosen from the Urquhart et al. (2007a) or Walsh et al. (1998) catalogs, but that do not fulfilled all the requirements to be considered jet candidates. These sources were selected in an early phase of our study. Emission was detected toward four of the five objects: three of them correspond to ionized regions associated to a HMYSO, and one to an extragalactic source. Maps of the radio continuum emission at the frequencies of 1.4, 2.4, 4.8, and 8.6 GHz, in regions of  $80'' \times 80''$  in size, are shown in Figures 2.19 through 2.22. The position of the target radio object, as reported in either catalog of is indicated in the maps with a cross. Spectra of the four detected sources are shown in Fig. 2.24.

**G263.7759–00.4281.** – This RMS radio source is associated with IRAS 08448–4343, and is known to be associated with an  $\text{H}_2\text{O}$  maser (Urquhart et al. 2009), and a  $\text{H}_2$  bipolar flow (Giannini et al. 2005). The luminosity derived from the IRAS bands and assuming this source is located at a distance of 1.6 kpc (Urquhart et al. 2007b), is  $\sim 3 \times 10^3 L_\odot$ , therefore failing our luminosity selection criterion. It is the only radio source within the  $80'' \times 80''$  region shown in Fig. 2.19. Its radio continuum spectrum (see Figure 2.24) can be well modeled with the theoretical spectra of an homogeneous constant density H II region. Assuming an electron temperature of 8000 K, we derive an emission measure of  $4.1 \times 10^6 \text{ pc cm}^{-6}$  and an angular size of  $0.53''$ . The rate of ionizing photons required to excite the H II region is  $7.0 \times 10^{44} \text{ s}^{-1}$ .

Using MSX, IRAS and TIMMI2 data, (Mottram et al. 2011a) derived a bolometric flux of  $F_{\text{bol}} \approx 5.77 \times 10^{-8} \text{ erg cm}^{-2} \text{ s}^{-1}$ . Assuming that this object is at the distance of 1.6 kpc (Urquhart et al. 2007b), then the bolometric luminosity is  $L \sim 4.6 \times 10^3 L_\odot$ , equivalent to that of B1-B2 zero-age main sequence (ZAMS) star. The ionizing flux from such a star is  $1.4 \times 10^{45} \text{ s}^{-1}$  (interpolated from Panagia 1973), similar to that required to excite the region of ionized gas. We conclude that this radio object corresponds to a small ( $0.004 \text{ pc}$  in diameter), optically thin H II region excited by a single B1-B2 ZAMS star.

**G268.6162–00.7389.** – This RMS radio source is associated with IRAS 09014–4736. It is the only radio source within the  $80'' \times 80''$  region shown in Fig. 2.20. No water masers were detected toward this source by Urquhart et al. (2009) at the 0.25 Jy sigma level. The luminosity derived from the IRAS bands and assuming this source is located at a distance of 1.7 kpc (Beck et al. 1991), is  $\sim 5 \times 10^3 L_\odot$ , therefore failing our luminosity selection criterion.

The radio source is unresolved and its radio continuum spectrum (see Figure 2.24) is well fitted by that of a uniform density H II region with an emission measure of  $7.0 \times 10^6 \text{ pc cm}^{-6}$ , temperature of 15000 K and an angular size of  $0.84''$ . The ionizing photon flux needed to excite the H II region is  $3.4 \times 10^{45} \text{ photons s}^{-1}$ .

Mottram et al. (2011a) reported for this object a bolometric flux of  $7.1 \times 10^{-11} \text{ W m}^{-2}$ . Assuming it is located at a distance of 1.7 kpc (Beck et al. 1991), then the implied bolometric luminosity is  $6.4 \times 10^3 L_{\odot}$ , equivalent to that of a ZAMS star with a spectral type between B0.5 and B1. The ionizing flux from such a star is  $3.4 \times 10^{45} \text{ s}^{-1}$  (interpolated from Panagia 1973), equal to that required to excite the region of ionized gas. We conclude that this radio object corresponds to a small (0.007 pc in diameter), optically thin H II region excited by a single B0.5-B1 ZAMS star.

**G327.1307+00.5259**— This radio source is in the field of the RMS source MSX-G327.1192+00.5103, although it is located at an angular distance of  $\sim 1'$  to the north of the peak MSX emission. No infrared counterpart has been detected at MIR wavelengths, neither in *Spitzer* (GLIMPSE or MIPS GAL) nor MSX, which makes it unlikely that this object corresponds to an embedded HMYSO.

It is the only radio source detected within the  $80'' \times 80''$  region shown in Fig. 2.21. Its radio continuum spectrum (see Figure 2.24) shows a decrease in the flux density at the higher frequencies. Being unresolved at all wavebands, the drop is not produced by the resolving power of the interferometer. We suggest that the radio emission from this source has a non-thermal origin. From the available evidence, we further suggest that this is an extragalactic source, possibly a radio-loud galaxy. The spectrum can be well fitted with a simple model of a gigahertz peaked galaxy (Snellen et al. 1998) (see Fig. 2.24), the spectral indices in the optically thick and thin regimes being 0.91 and  $-0.69$ , respectively. The lack of infrared emission could be explained by the source being intrinsically faint at these wavelengths compared to the radio emission, and/or due to absorption in the Galactic plane. Similar objects without MIR counterpart had already been detected in extragalactic surveys (Norris et al. 2006, Huynh et al. 2010).

**G333.1306–00.4275**. – This radio object was selected from the Urquhart et al. catalog due to its steep spectral index ( $\gtrsim 1$ ) between 4.8 and 8.6 GHz. It is located  $\sim 25''$  east of the RMS/MSX source G333.1306–00.4275 (also IRAS 16172–5028), therefore failing our selection criteria. There are two radio sources within the  $80'' \times 80''$  region shown in Fig. 2.22: a compact central component (the target object; labeled B) and a complex, extended component, labeled A, associated with the RMS source.

The radio continuum spectrum of component B (see Figure 2.24) is well fitted with a power-law spectrum with a spectral index of  $\sim 1$ , similar to those of HC H II region (Franco et al. 2000). The bolometric flux is  $15.4 \times 10^{-11} \text{ W m}^{-2}$  (Mottram et al. 2011a), which at a distance of 3.5 kpc (Faúndez et al. 2004) implies that its total bolometric luminosity is  $5.9 \times 10^4 L_{\odot}$ .

Figure 2.23 shows a three-color image of the MIR emission towards G333.1306–00.4275 made using the 3.6, 4.5, and 8.0  $\mu\text{m}$  data obtained from the *Spitzer*/GLIMPSE survey, and superimposed in red contours the radio emission detected in 4.8 GHz. This Figure clearly shows that component B is associated with a green extended object probing regions of shocked

Table 2.4. Physical parameters of the ionized regions

Source	Dist. (kpc)	$T_e$ ( $10^4\text{K}$ )	EM ( $\text{pc cm}^{-6}$ )	$\theta$ ( $''$ )	$N_i$ ( $10^{45}\text{s}^{-1}$ )	L (pc)	$\langle n_e \rangle$ ( $\text{cm}^{-3}$ )	Type
<b>Jet candidates</b>								
G305.7984–00.2416 A	3.0	0.8	$2.30 \times 10^6$	1.40	9.56	0.020	$1.1 \times 10^4$	UC H II
G317.4298–00.5612 A	15.	0.8	$1.90 \times 10^8$	0.27	718	0.020	$9.8 \times 10^4$	HC H II
G337.4032–00.4037 A	3.2	0.8	$> 2 \times 10^8$	$< 0.64$	...	$< 0.01$	$> 1.5 \times 10^5$	jet
G345.0061+01.7944 B	1.7	1.5	$4.60 \times 10^8$	0.73	170	0.006	$2.8 \times 10^5$	HC H II
G345.4938+01.4677	1.7	0.8	$> 2 \times 10^8$	$< 0.19$	...	$< 0.002$	$> 3.6 \times 10^5$	jet
G352.5173–00.1549 A	5.2	1.5	$2.80 \times 10^8$	0.42	318	0.011	$1.0 \times 10^5$	HC H II
G009.9937–00.0299	5.0	0.8	$5.94 \times 10^5$	1.49	7.89	0.036	$4.1 \times 10^3$	UC H II
G025.6469+01.0534	3.1	0.8	$1.17 \times 10^7$	0.40	125	0.006	$4.4 \times 10^5$	UC H II
<b>Other sources of interest</b>								
G263.7759–00.4281	1.6	0.8	$4.05 \times 10^6$	0.53	0.697	0.004	$3.2 \times 10^4$	UC H II
G268.6162–00.7389	1.7	1.5	$7.00 \times 10^6$	0.84	3.40	0.007	$1.9 \times 10^4$	UC H II
G333.1306–00.4275 B	3.5	1.5	$> 2 \times 10^8$	$< 2.5$	...	$< 0.042$	$> 7.1 \times 10^4$	HC H II
<b>Additional sources detected in the field</b>								
G305.7984–00.2416 B	3.0	1.0	$1.3 \times 10^8$	0.066	1.23	0.001	$3.67 \times 10^5$	HC H II
G305.7984–00.2416 C	3.0	0.8	$1.0 \times 10^6$	0.901	1.74	0.013	$8.74 \times 10^3$	UC H II
G305.7984–00.2416 D	3.0	0.8	$2.0 \times 10^5$	8.027	27.6	0.117	$1.31 \times 10^3$	C H II
G317.4298–00.5612 B	15.0	0.8	$3.5 \times 10^5$	7.030	926.	0.511	$8.30 \times 10^2$	C H II
G333.1306–00.4275 A	3.5	0.8	$1.0 \times 10^6$	24.998	1820	0.424	$1.54 \times 10^3$	C H II
G337.4032–00.4037 B	3.2	0.8	$3.0 \times 10^5$	2.657	5.16	0.041	$2.70 \times 10^3$	UC H II
G345.0061+01.7944 A	1.7	0.8	$5.0 \times 10^5$	8.027	22.2	0.066	$2.75 \times 10^3$	UC H II
G352.5173–00.1549 B	5.2	0.8	$5.0 \times 10^5$	1.329	5.68	0.033	$3.86 \times 10^3$	UC H II

gas. Component A is associated with a bright, extended MIR source, specially bright at  $8.0 \mu\text{m}$ , associated with PAH emission in a PDR. The radio spectrum is flat (Fig. 2.25) and probably correspond to a more evolved H II region.

**G345.3768+01.3926.** – This source was chosen from the catalog of Walsh et al. (1998). It is located more than  $1'$  away from the IRAS 16561–4006 source. Walsh et al. (1998) reported a peak flux of  $5 \text{ mJy beam}^{-1}$  at  $8.64 \text{ GHz}$  and a flux density<sup>2</sup> of  $12.3 \text{ mJy}$ . No sources were detected towards the radio position in GLIMPSE or MSX, which makes this object an unlikely YSO candidate. We do not detect emission towards this radio object in any of the four frequencies at the  $\sim 0.1 \text{ mJy beam}^{-1}$  level, indicating that this is a highly variable radio source. We propose an extragalactic origin. Such extreme variability in radio-loud galaxies is rare, but has been observed (e.g., Barvainis et al. 2005).

<sup>2</sup>The integrated fluxes were published online in VizieR (Ochsenbein et al. 2000)

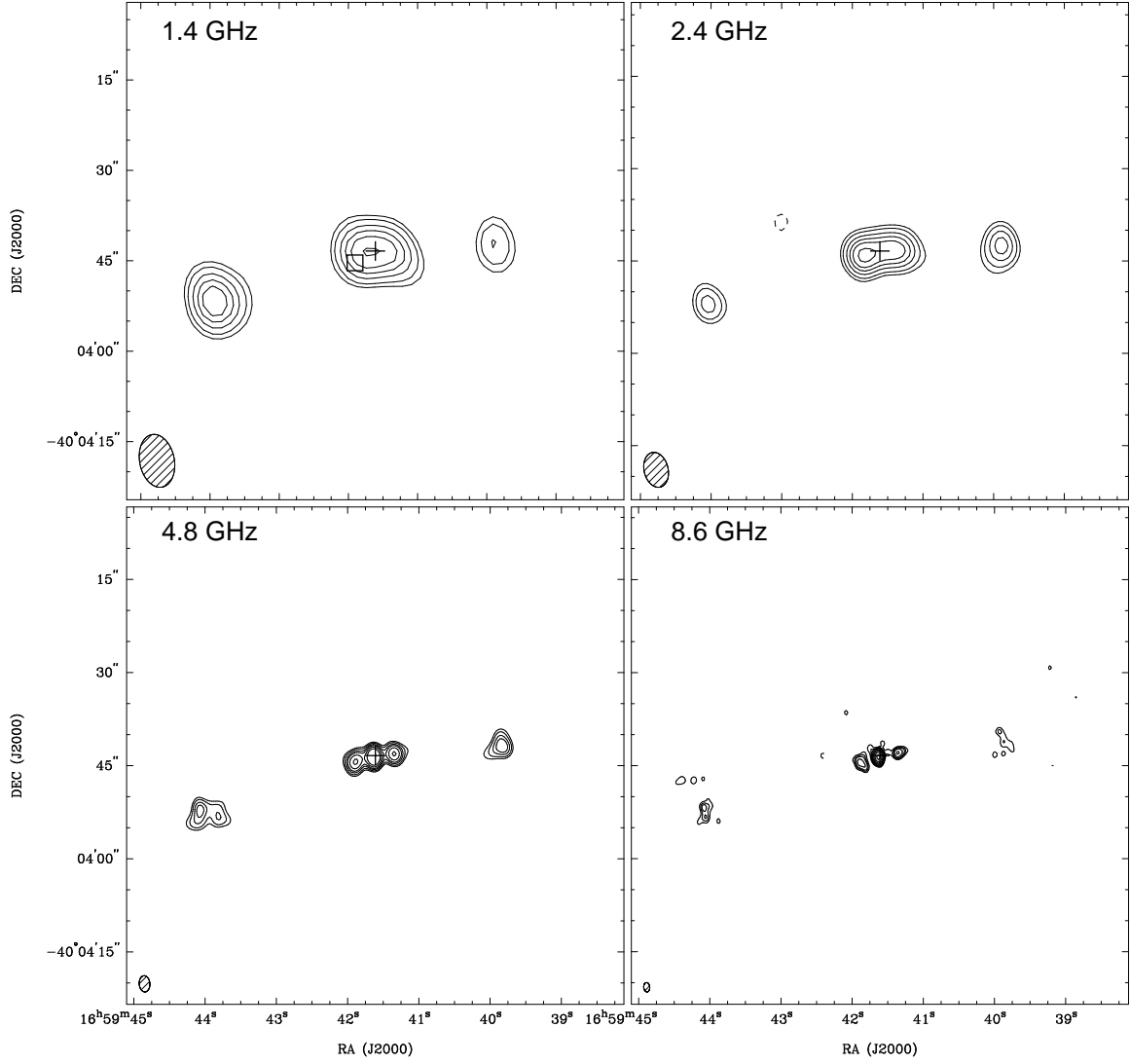


Figure 2.10 ATCA maps of the radio continuum emission from G345.4938+01.4677. Beams are shown in the lower left corner of each panel. A cross marks the position of the radio source reported by Urquhart et al. (2007a). Top left: 1.4 GHz map. A square marks the position of the MSX source. Contour levels are  $-4, 4, 6, 8, 10, 13, 16, 18,$  and  $20$  times  $\sigma$  ( $1\sigma = 0.35$  mJy beam $^{-1}$ ). Top right: 2.4 GHz map. Contour levels are  $-7, 7, 12, 17, 25, 32, 38, 45, 54,$  and  $60$  times  $\sigma$  ( $1\sigma = 0.12$  mJy beam $^{-1}$ ). Bottom left: 4.8 GHz map. Contour levels are  $-4, 3, 6, 9, 13, 19, 28, 40, 60,$  and  $80$  times  $\sigma$  ( $1\sigma = 0.086$  mJy beam $^{-1}$ ). Bottom right: 8.6 GHz map. Contour levels are  $-4, 3, 6, 9, 13, 16, 19, 24, 50,$  and  $100$  times  $\sigma$  ( $1\sigma = 0.081$  mJy beam $^{-1}$ ).

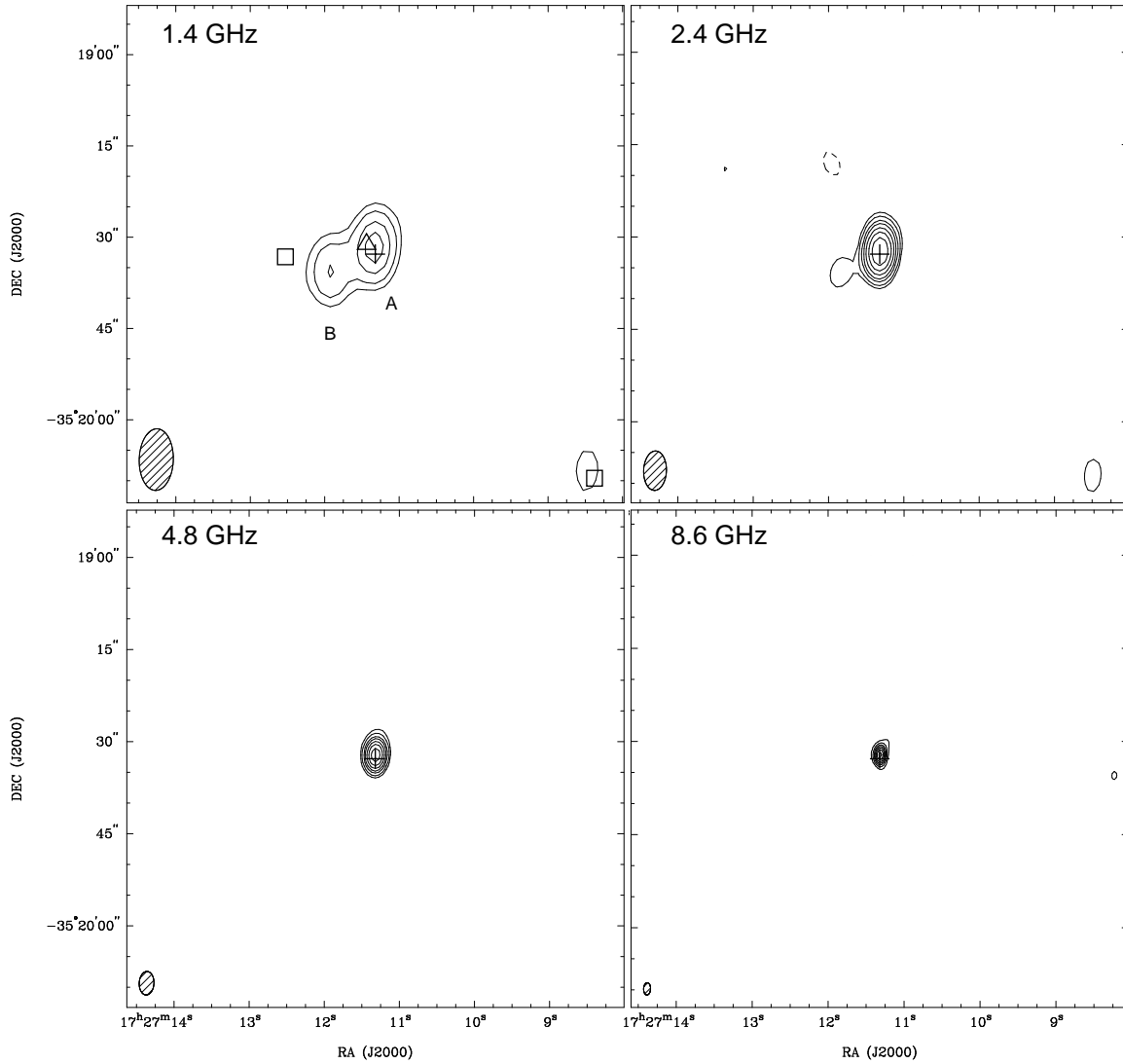


Figure 2.11 ATCA maps of the radio continuum emission towards G352.5173–00.1549. Beams are shown in the lower left corner of each panel. A cross marks the position of the radio source reported by Walsh et al. (1998). Top left: 1.4 GHz map. Labeled are the two radio components detected in the field. Contour levels are  $-5, 5, 8, 13,$  and  $18 \times 0.20 \text{ mJy beam}^{-1}$ . Squares mark the position of MSX sources. The triangle marks the position of the  $\text{H}_2\text{O}$  maser detected by Forster & Caswell (1999). Top right: 2.4 GHz map. Contour levels are  $-5, 5, 8, 13, 18, 26, 36,$  and  $50 \times 0.20 \text{ mJy beam}^{-1}$ . Bottom left: 4.8 GHz map. Contour levels are  $-5, 5, 8, 13, 18, 26, 36,$  and  $50 \times 0.60 \text{ mJy beam}^{-1}$ . Bottom right: 8.6 GHz map. Contour levels are  $-3, 3, 9, 18, 29, 44, 64,$  and  $90 \times 0.60 \text{ mJy beam}^{-1}$ .

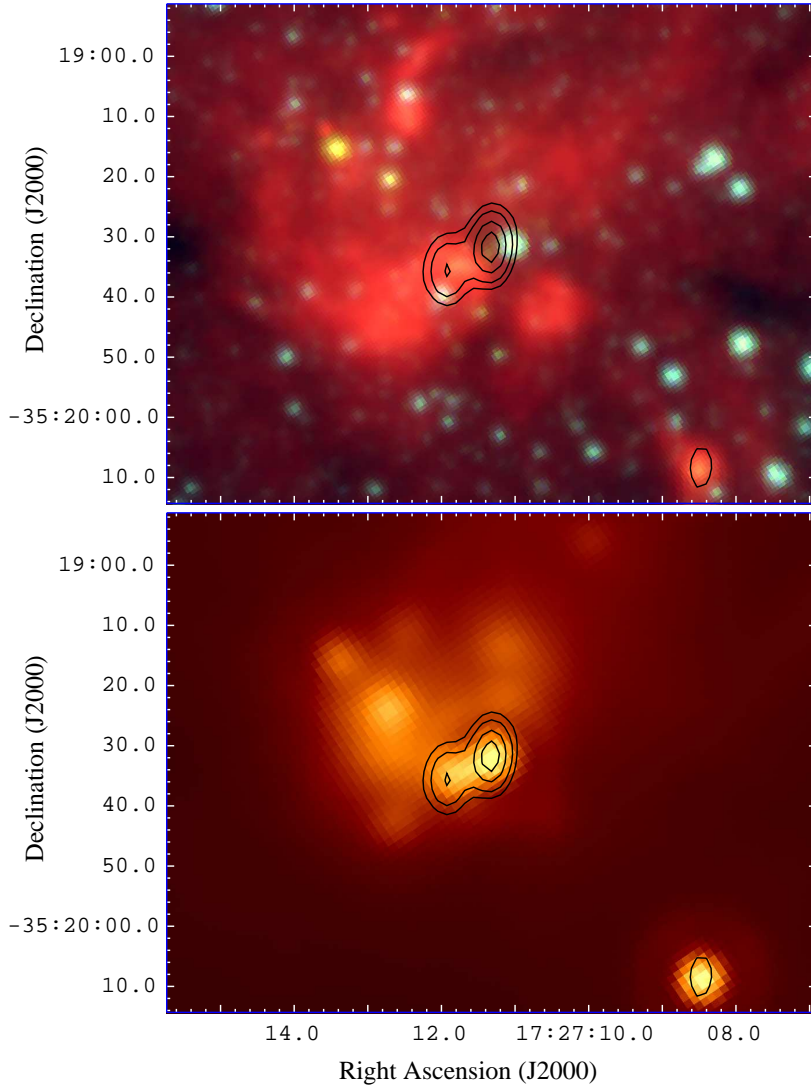


Figure 2.12 Mid-infrared images toward G352.5173–00.1549, with black contours corresponding to 1.4 GHz emission (Fig. 2.11). Top Panel: 3 color IRAC image using 8.0, 4.5, and 3.6  $\mu\text{m}$  data from GLIMPSE. The peak of the 1.4 GHz emission is consistent with the peak detected at higher frequencies, and to radio component A. The source seen  $\sim 3''$  to the west is not embedded, and is unrelated with the radio emission. Radio component B appears to be related with the 8.0  $\mu\text{m}$  emission seen at south-east from the peak. Bottom Panel: MIPS 24  $\mu\text{m}$  emission. Component A is consistent with the peak at MIR wavelengths, and component B also shows MIR counterpart.

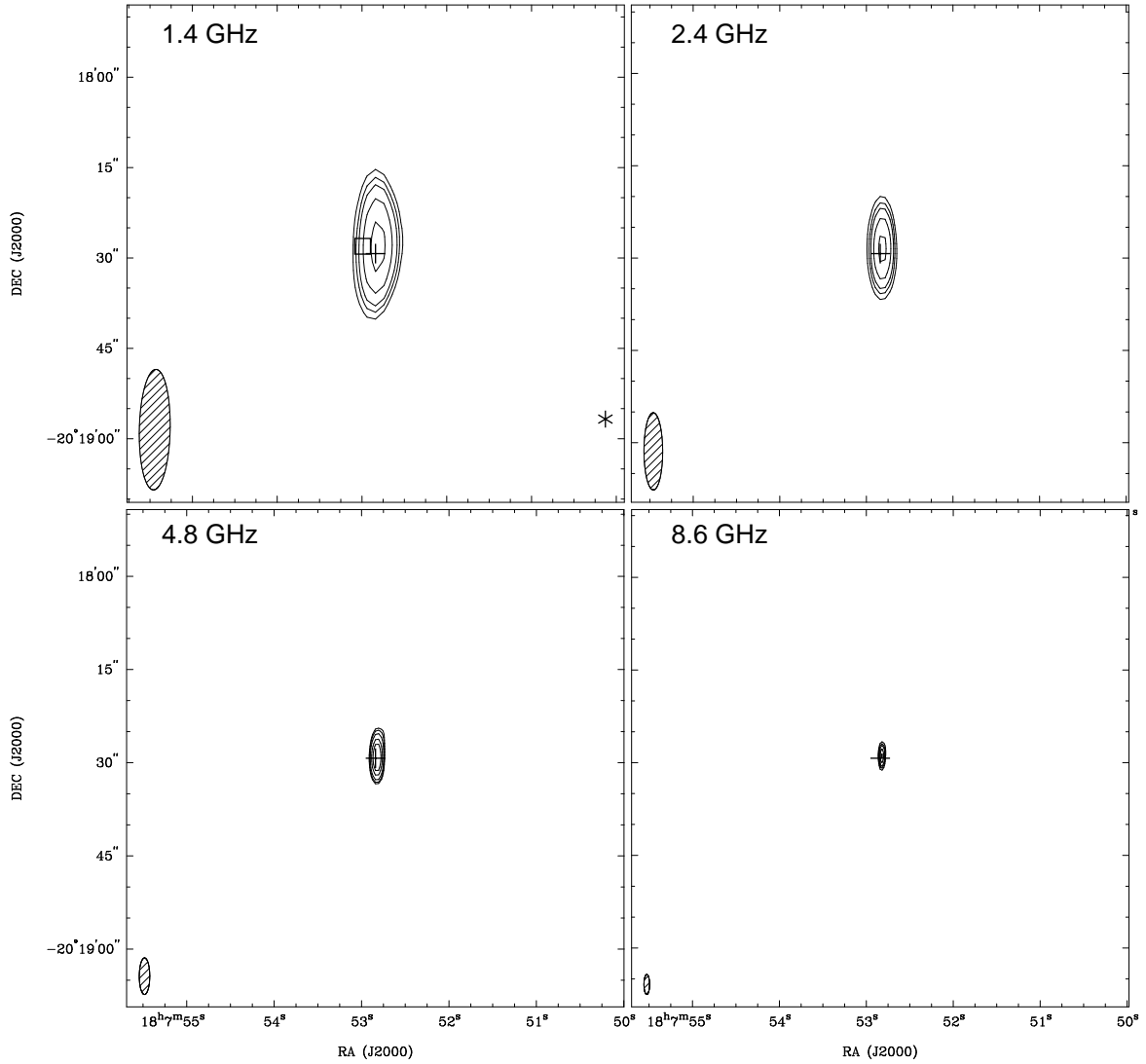


Figure 2.13 ATCA maps of the radio continuum emission toward G009.9937–00.0299. The cross marks the position of the radio source reported by Walsh et al. (1998). Beams are shown in the lower left corner of each panel. Top left: 1.4 GHz map. The square marks the peak position at  $21 \mu\text{m}$  of the associated MSX source G009.9983–00.0334 and the star the position of the methanol masers detected by Walsh et al. (1998). Top right: 2.4 GHz map. Bottom left: 4.8 GHz map. Bottom right: 8.6 GHz map. Contour levels are  $-3, 3, 4, 5, 7,$  and  $10$  times  $0.30 \text{ mJy beam}^{-1}$  for the 1.4 and 2.4 GHz maps, and  $0.23 \text{ mJy beam}^{-1}$  for the 4.8 and 8.6 GHz maps.

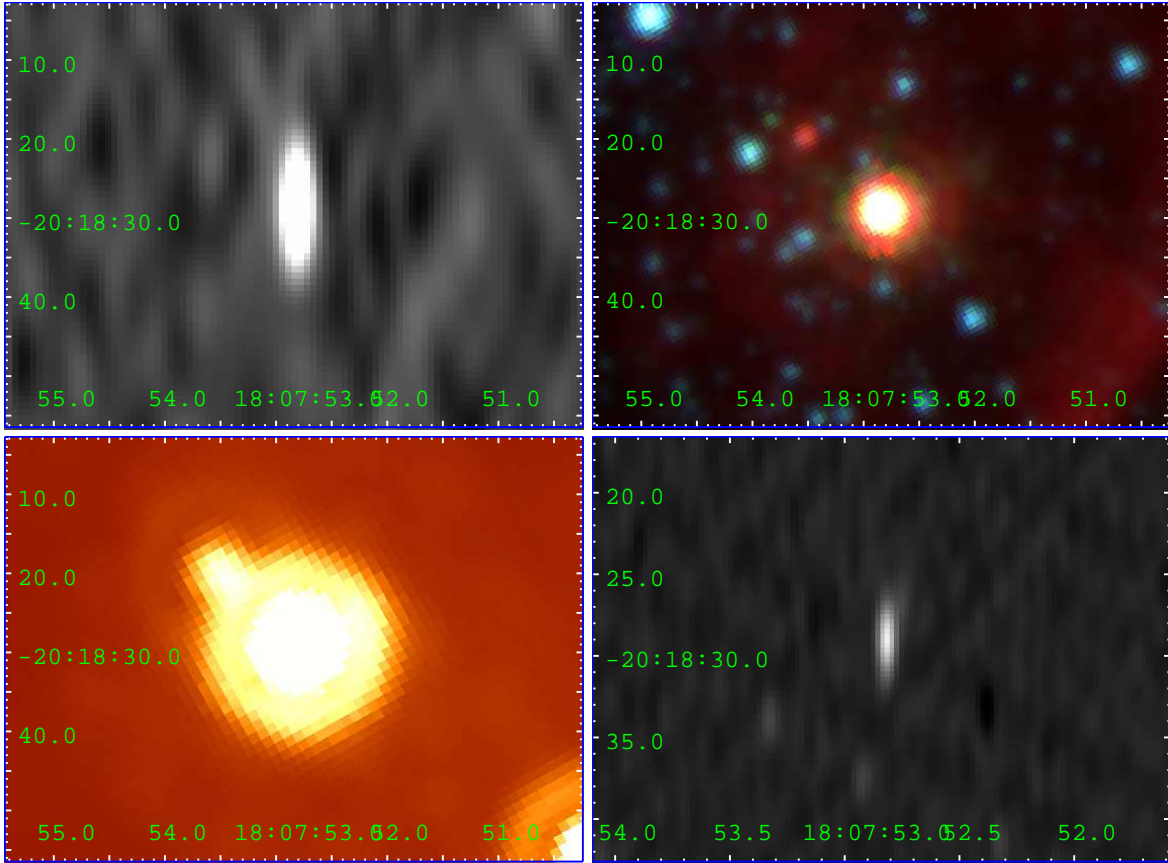


Figure 2.14 Comparison between the radio and IR images for G009.9937-00.0299. Top left panel: 2.4 GHz image. Top right: 3 color IRAC image using 8.0, 4.5, and 3.6  $\mu\text{m}$  data from GLIMPSE. Bottom left: 24  $\mu\text{m}$  MIPS image from MIPS GAL. Bottom right: 8.6 GHz image.

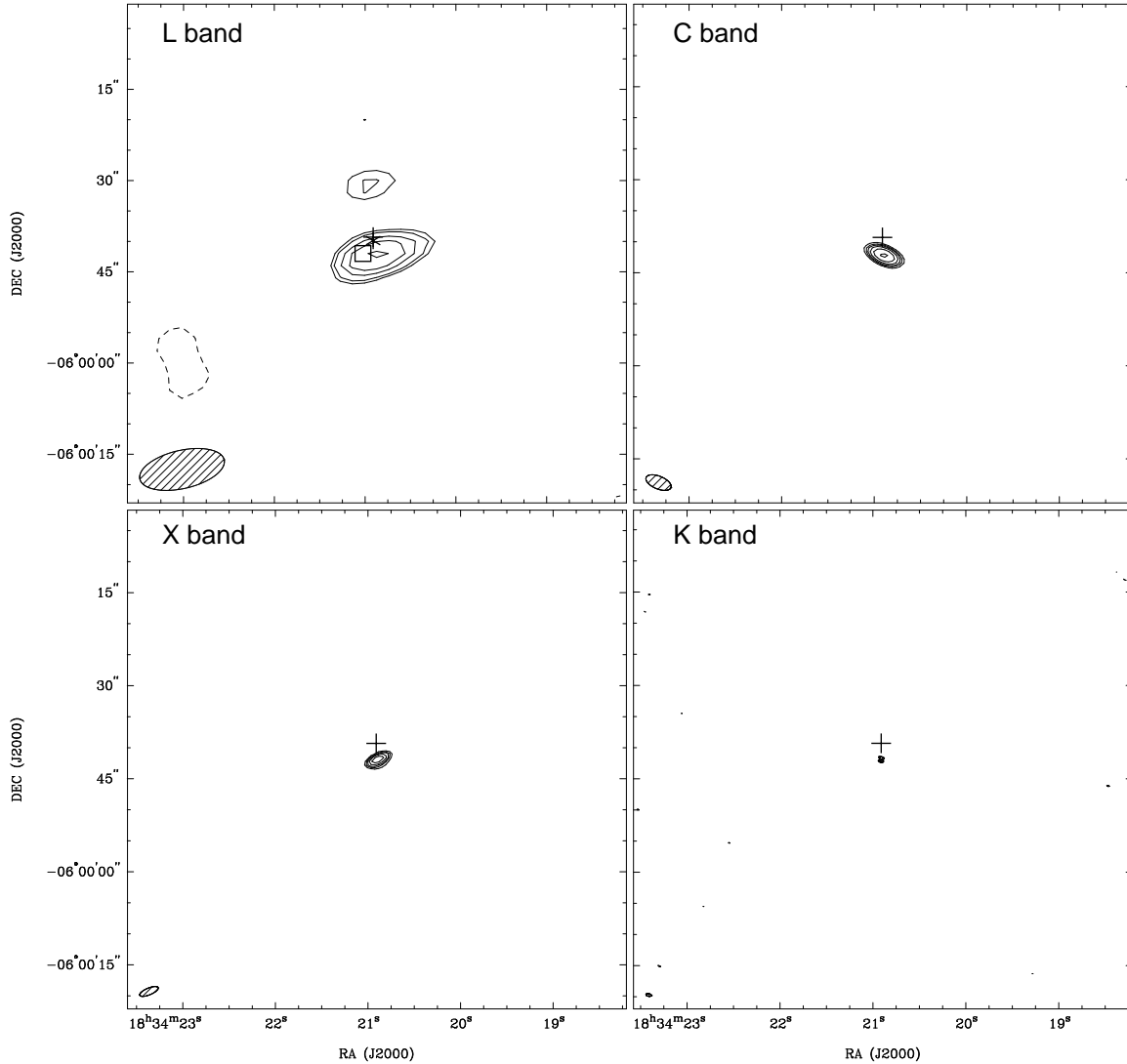


Figure 2.15 VLA maps of the radio continuum emission toward G025.6469+01.0534. The cross marks the position of the radio source reported by Walsh et al. (1998). Beams are shown in the lower left corner of each panel. Top left: L band map. The square marks MSX G025.6498+01.0491 and the cross the position of the methanol masers detected by Walsh et al. (1998). Top right: C band map. Bottom left: X band map. Bottom right: K band map. Contour levels are  $-5, 5, 6, 8, 10,$  and  $13$  times  $0.9 \text{ mJy beam}^{-1}$  for the L band map, and  $-5, 5, 7, 9, 12, 17,$  and  $25$  times  $0.1 \text{ mJy beam}^{-1}$  for the C, X, and K band.

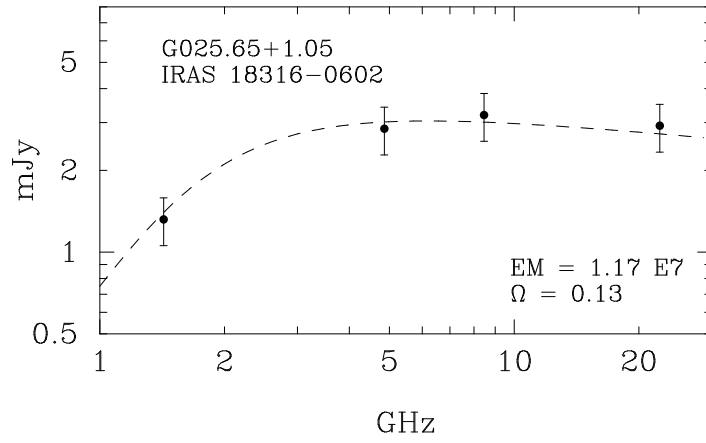


Figure 2.16 Spectrum of the G025.6469+01.0534 jet candidate. The dashed line represents an uniform H II region free-free emission model, whose parameters are indicated in the lower right corner.

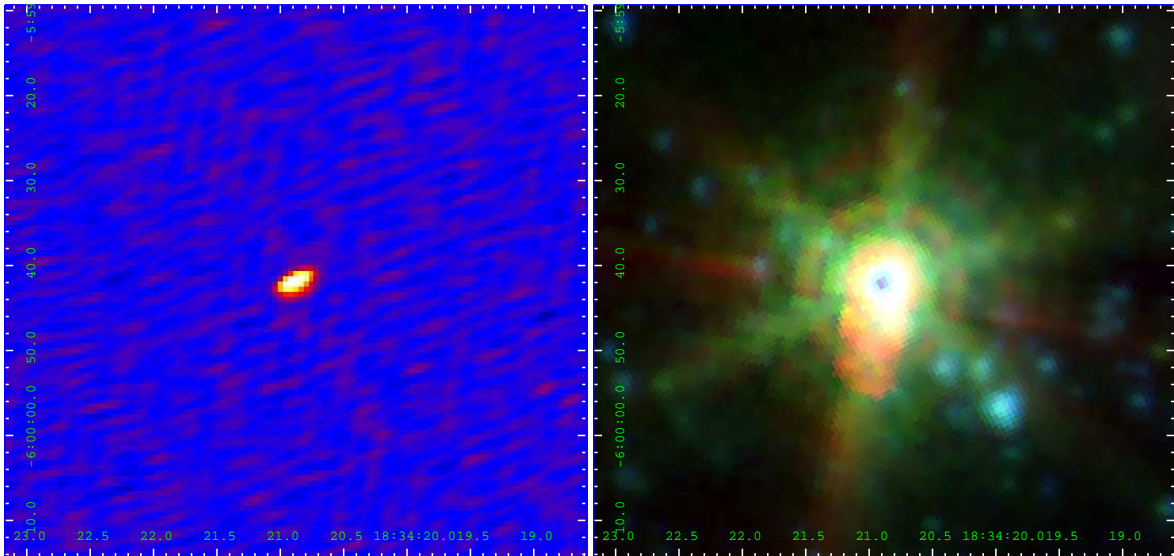


Figure 2.17 *Left*: Radio image of G025.6469+01.0534 in the X band. *Right*: Blue, green and red color image of this source using IRAC data at 3.6, 4.5, and 8.0  $\mu\text{m}$ .

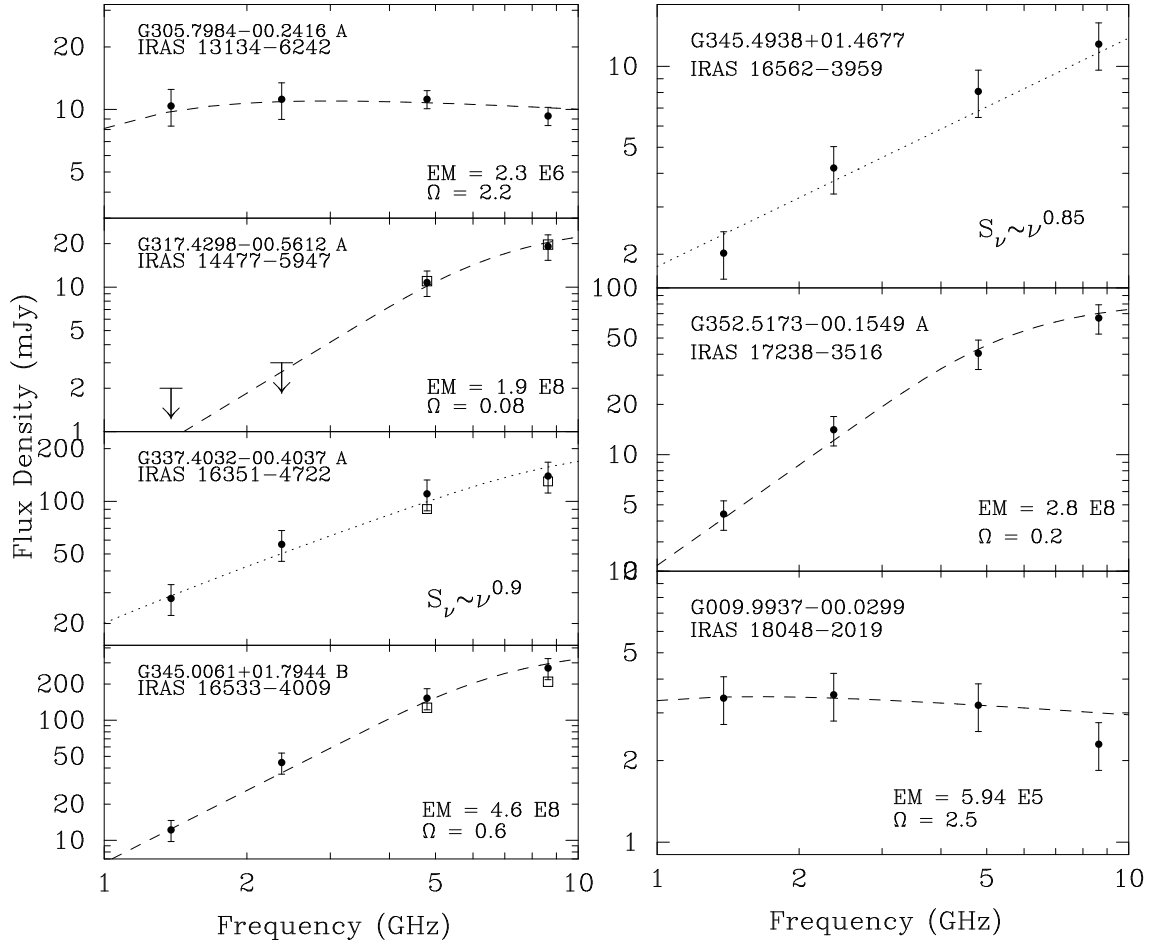


Figure 2.18 Radio continuum spectra of the jet candidates. The source name is given in the upper left of each panel. The dashed line corresponds to the best-fit obtained with an homogeneous HII region model. The derived emission measure (in pc cm<sup>-6</sup>) and solid angle (in arcsec<sup>2</sup>) are indicated in the lower right corner of each panel. Dotted lines in the G337.4032-00.4037 A and G345.4938+01.4677 panels show best fits obtained with ionized jet models.

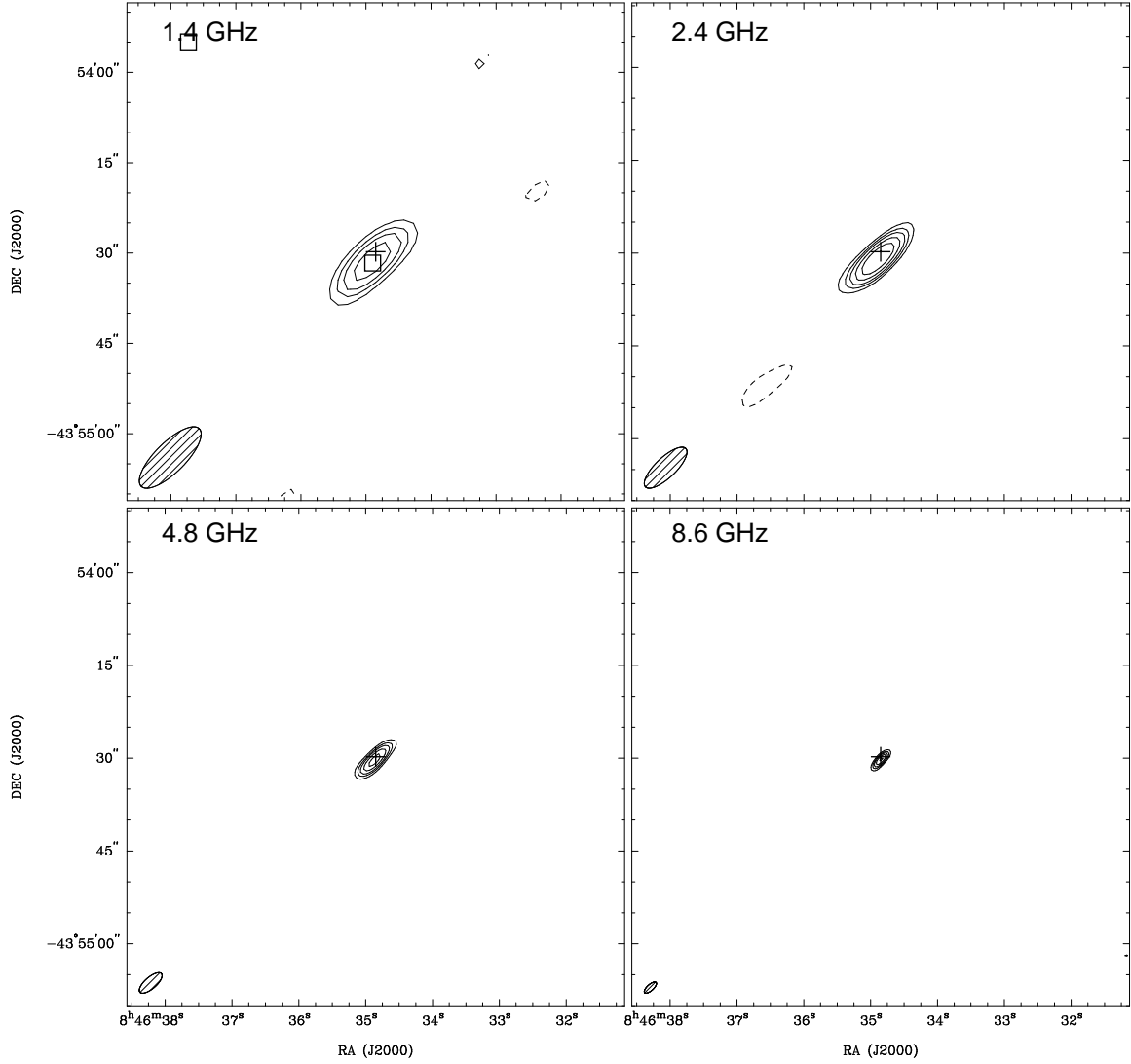


Figure 2.19 ATCA maps of the radio continuum emission from G263.7759–00.42813. A cross marks the position of the radio source reported by Urquhart et al. (2007a). Beams are shown in the lower left corner of each panel. Top left: 1.4 GHz map. Squares mark the position of MSX sources. Top right: 2.4 GHz map. Bottom left: 4.8 GHz map. Bottom right: 8.6 GHz map. Contour levels are  $-3, 3, 5, 7,$  and  $10$  times  $0.15 \text{ mJy beam}^{-1}$  for the 1.4 GHz image and  $-3, 3, 5, 7, 10,$  and  $14$  times  $0.15 \text{ mJy beam}^{-1}$  for the 2.4, 4.8, and 8.6 GHz images.

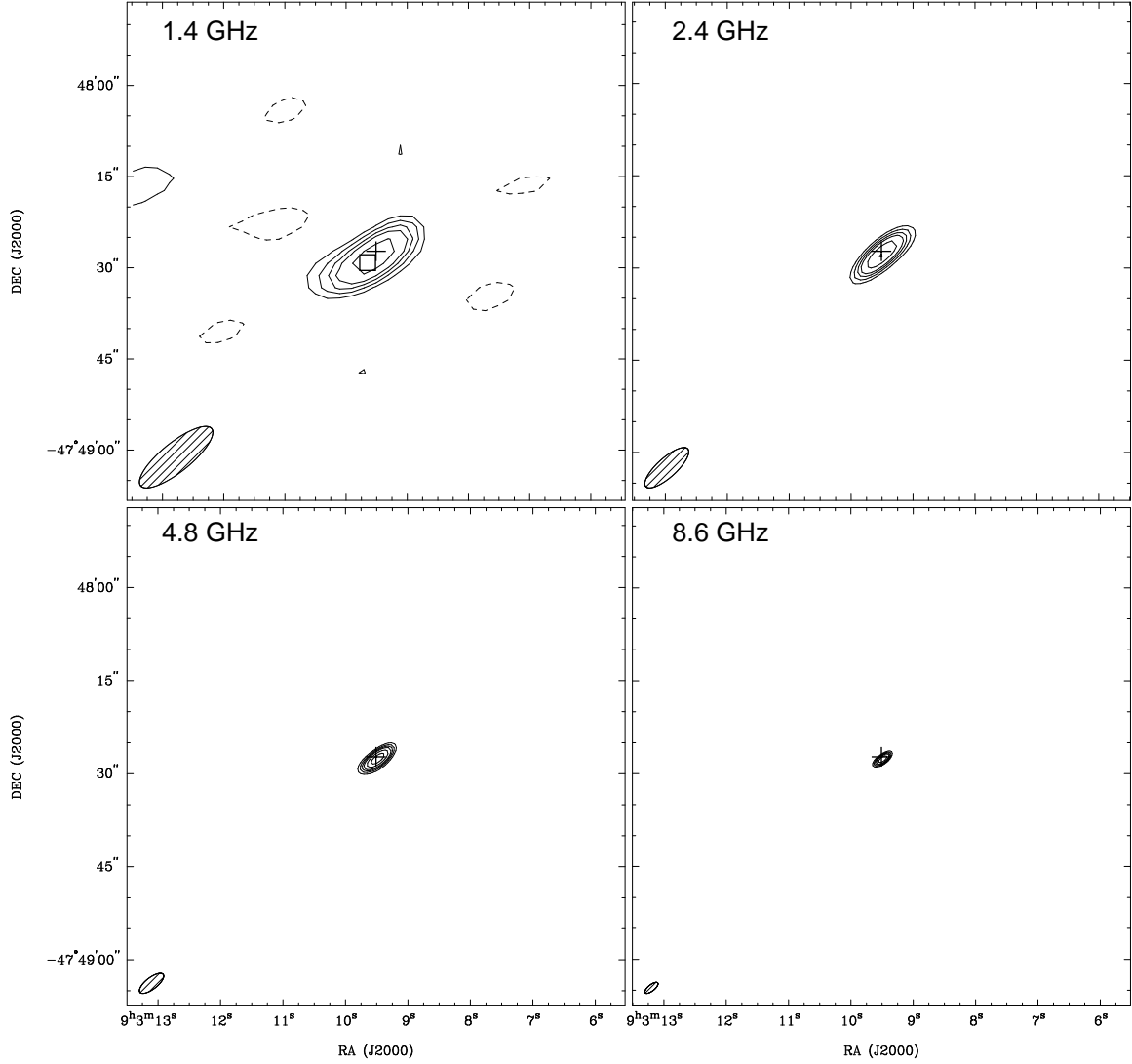


Figure 2.20 ATCA maps of the radio continuum emission from G268.6162–00.7389. A cross marks the position of the radio source reported by Urquhart et al. (2007a). Beams are shown in the lower left corner of each panel. Top left: 1.4 GHz map. A square marks the position of the MSX source. Top right: 2.4 GHz map. Bottom left: 4.8 GHz map. Bottom right: 8.6 GHz map. Contour levels are  $-5, 5, 7, 9, 11,$  and  $15$  times  $0.40 \text{ mJy beam}^{-1}$  for the 1.4, 4.8, and 8.6 GHz images, and  $-5, 5, 7, 9, 11, 15$  and  $20$  times  $0.40 \text{ mJy beam}^{-1}$  for the 2.4 GHz image.

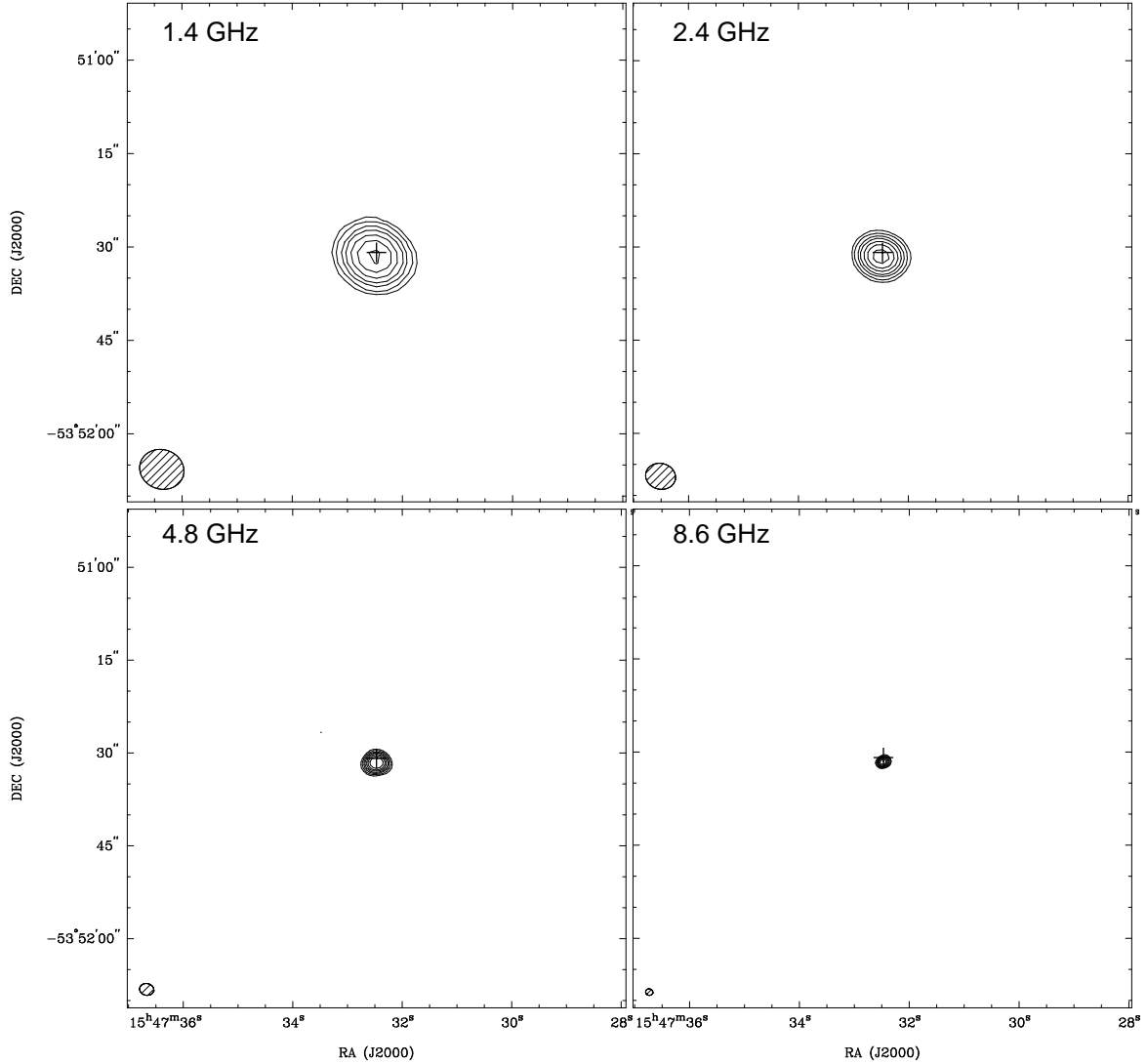


Figure 2.21 ATCA maps of the radio continuum emission from G327.1307+00.5259. A cross marks the position of the radio source reported by Urquhart et al. (2007a). Beams are shown in the lower left corner of each panel. Top left: 1.4 GHz map. Top right: 2.4 GHz map. Bottom left: 4.8 GHz map. Bottom right: 8.6 GHz map. Contour levels are  $-5, 5, 8, 13, 18, 26, 36, 50$  times  $0.35 \text{ mJy beam}^{-1}$  for the 1.4 and 2.4 GHz images, and  $0.2 \text{ mJy beam}^{-1}$  for the 4.8 and 8.6 GHz images.

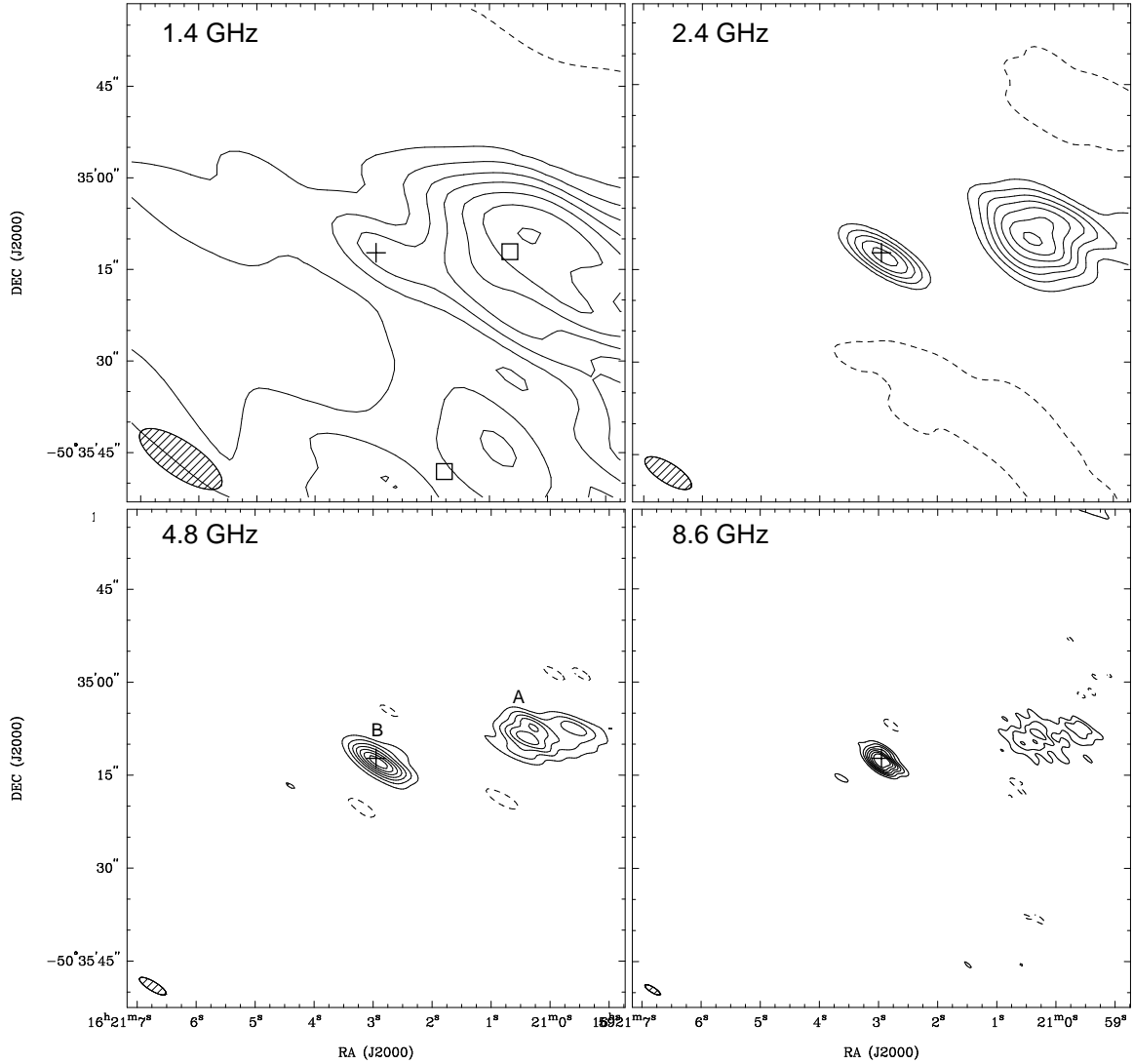


Figure 2.22 ATCA maps of the radio continuum emission from G333.1306–00.4275. Beams are shown in the lower left corner of each panel. A cross marks the position of the radio source reported by Urquhart et al. (2007a). Beams are shown in the lower left corner of each panel. Top left: 1.4 GHz map. Squares mark the positions of MSX sources. Top right: 2.4 GHz map. Bottom left: 4.8 GHz map. The two main radio components are marked with letters A and B. Bottom right: 8.6 GHz map. Contour levels are  $-7, 7, 17, 31, 49, 74, 107,$  and  $150$  times  $3 \text{ mJy beam}^{-1}$ .

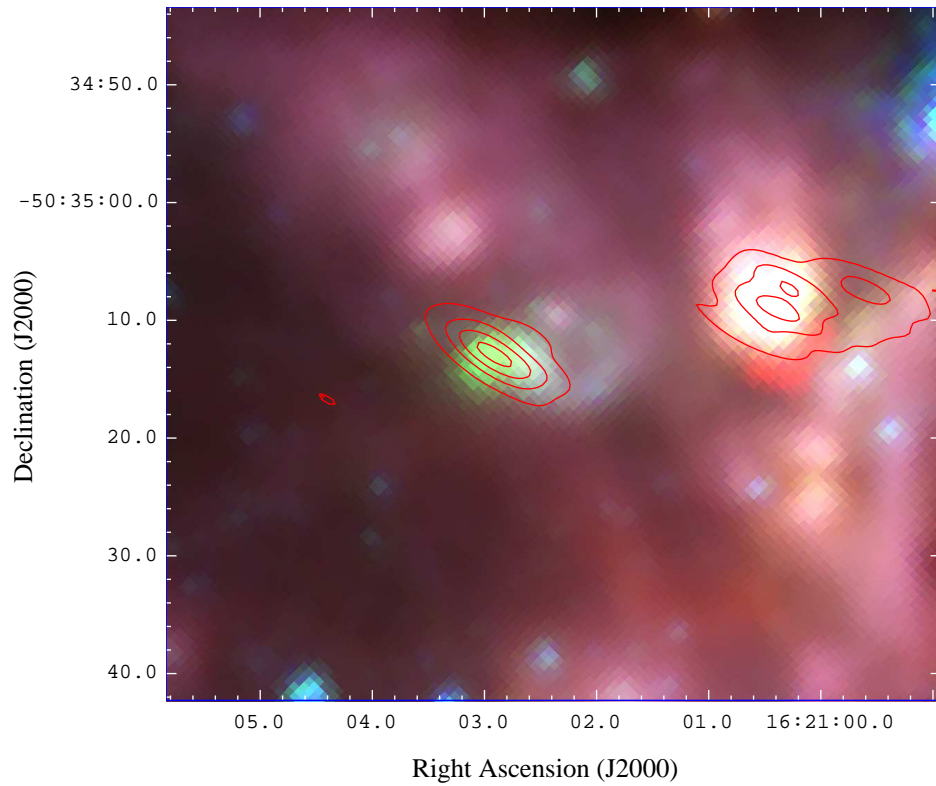


Figure 2.23 Three color IRAC image of G333.1306–00.4275 made using 8.0, 4.5, and 3.6  $\mu\text{m}$  data from GLIMPSE. Intercalated contours of the 4.8 GHz data (Fig. 2.22) are shown in red.

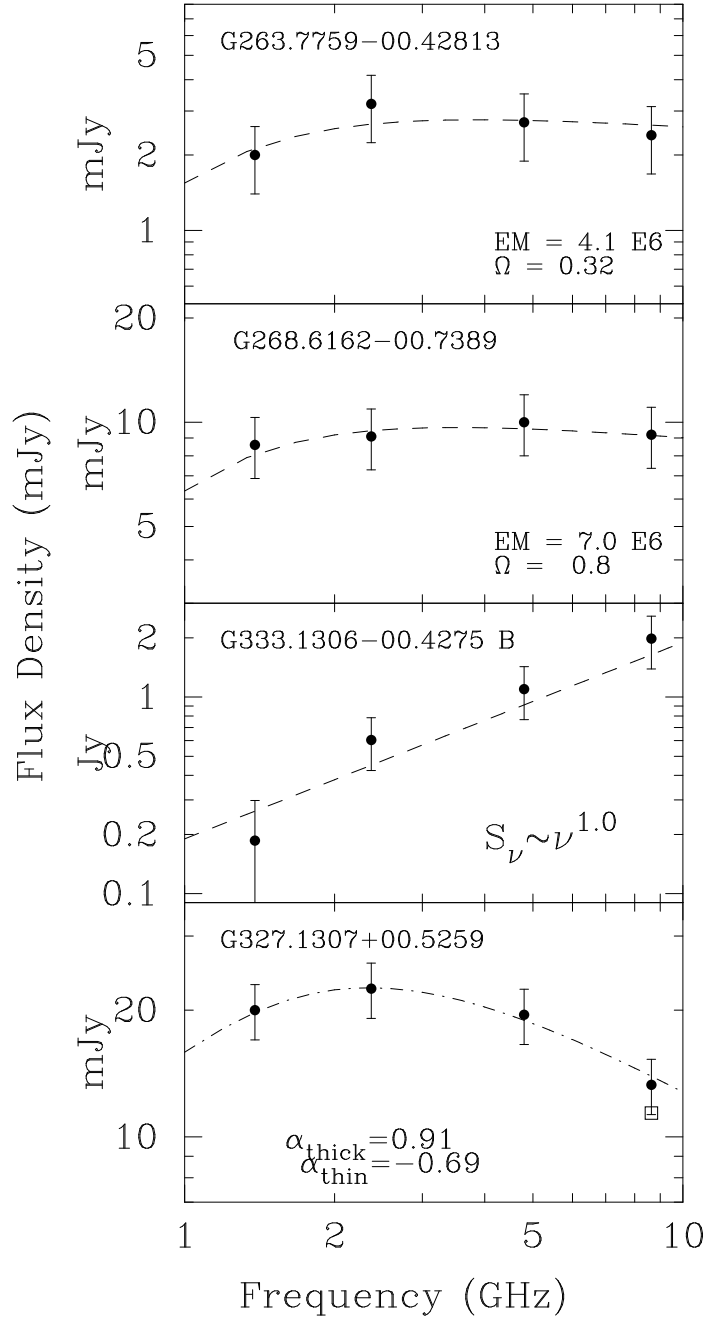


Figure 2.24 From top to bottom: spectral energy distributions of G263.7759-00.4281, G268.6162-00.7389, G333.1306-00.4275 B, and G327.1192+00.5103. *First and second panel:* The dashed line shows the best-fit obtained with an homogeneous H II region, with the solid angle and emission measure indicated in each panel, in units of  $\text{pc cm}^{-6}$  and  $\text{arcsec}^2$ , respectively. *Third panel:* The dashed line shows the best fit obtained with a rising power-law. *Fourth panel:* Dot-dashed line is the best fit obtained with a gigahertz peaked source model (Snellen et al. 1998).

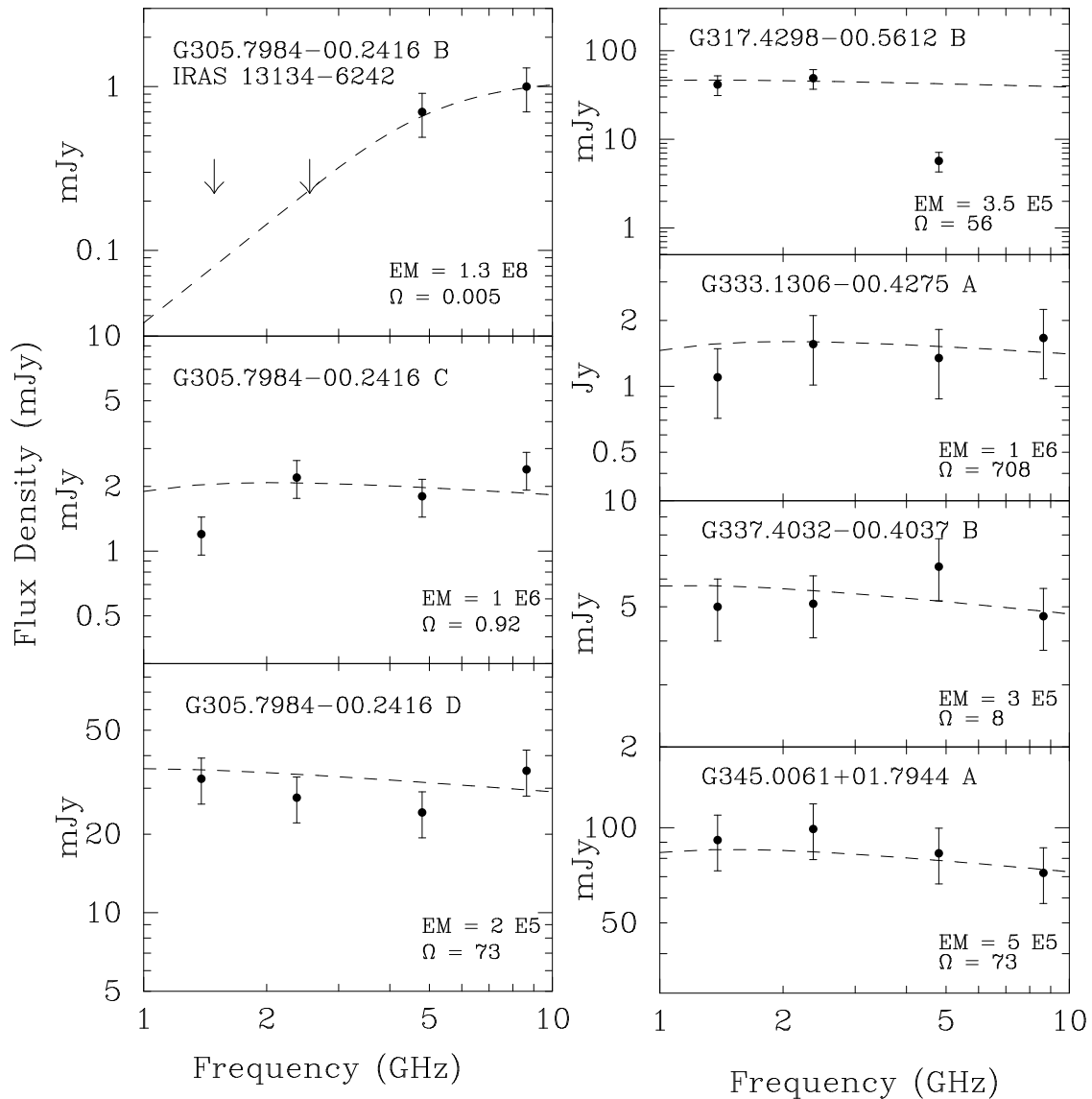


Figure 2.25 *Left column:* Spectral energy distributions of G305.7984-00.2416 B, C and D. *Right column:* Spectral energy distributions of G317.4298-00.5612 B, G333.1306-00.4275 A, G337.4032-00.4037 B, and G345.0061+01.7944 A. The dashed line shows the best-fit obtained with an homogeneous H II region, with the solid angle and emission measure indicated in each panel in units of pc cm<sup>-6</sup> and arcsec<sup>2</sup>, respectively.

## 2.4 Summary

In this section we summarize the nature of 8 of the 33 jet candidates listed in Table 2.1, and observed in this work (Chapter 2). We find that two candidates — G337.4032–00.4037 A and G345.4938+01.4677 — can be identified, from their radio continuum spectral characteristics, as ionized jets. Even though the angular resolution of the observations was insufficient to resolve the jet morphology, there is good evidence, such as the presence of collimated lobes of radio emission and energetic bipolar molecular outflows, to consider these two objects as collimated ionized stellar winds.

Three candidates, G317.4298–00.5612 A, G345.0061+01.7944 B, and G352.5173–00.1549 A, correspond to small (diameter of less than 0.03 pc) regions of ionized gas with large emission measures ( $EM > 10^8 \text{ pc cm}^{-6}$ ), and thus can be classified as hypercompact H II regions, according to the definition of Sewilo et al. (2011). HCH II regions are thought to trace the earliest stages of formation of a single massive star or a binary system. To date, about a dozen of these regions are known (Hoare et al. 2007). Finally, the remaining two candidates observed, G009.9937–00.0299 and G305.7984–00.2416 A, correspond to UCH II regions ( $EM > 10^6 \text{ pc cm}^{-6}$ , size  $< 0.1 \text{ pc}$ ). An important issue regarding the consistency of the jet list candidate is the determination to which radio source corresponds the emission seen at FIR wavelengths. At least in one case, G305.7984–00.2416 A, we determine that the cataloged RMS radio source was not related with the luminosity seen in the IRAS bands, and that the much fainter component B is likely to be the youngest and more embedded source of this high-mass star maternity.

Considering the the 8 jet candidates observed in this work, plus G343.1262–00.0620 (also IRAS 16547–4247), which Garay et al. (2003) have shown that corresponds to a collimated ionized jet, then there are 9 of the 33 jet candidates for which their nature have been determined. Of these, 33.3% corresponds to collimated ionized winds, 33.3% corresponds to HC H II regions and the other third corresponds to UCH II regions. Due to the homogeneity of the selection criteria used in building the jet candidate list (Table 2.1) we expect the same proportion of objects in the whole list. Thus, we expect to find about 8-9 new ionized jets among the 25 candidates not yet observed.

## Chapter 3

# Molecular outflows toward ionized jet candidates

High-mass stars are formed inside cold (35 K) molecular and dusty cores of diameters of  $\sim 1$  pc, masses of typically  $1500 M_{\odot}$ , column densities of  $N(\text{H}_2) \approx 10^{22}..10^{24} \text{ cm}^{-2}$ , and average volume densities of  $\sim 2 \times 10^5 \text{ cm}^{-3}$  (Faúndez et al. 2004, Motte et al. 2007, Lackington 2011). The observation of these cores in molecular emission lines allows us to determine their physical and chemical conditions. Here, we focus mostly on phenomena seen in molecular lines — and related to the presence of jets in high-mass star formation — which are massive bipolar outflows and shocks. The theoretical unified scenario, which is still under debate, proposes that the ionized collimated jet is the source of momentum, kinetic energy and thermal energy of the outflow. The collimated ionized jet rams into the high density dusty core, entrains and sweeps-up material and produces the supersonic shocks that heat the gas. It is from these zones that the outflow molecular emission is produced.

This chapter presents the results of molecular line observations made toward eight HMYSOs candidates of harboring jets and five other HMYSOs. There is not yet a systematic study of the molecular gas content and kinematics of all the sources in the jet candidate list (Table 2.1). We observed line emission in three molecular species: CO, SiO, and  $\text{HCO}^+$ . The main tracers of the outflows are the CO lines, due to its large optical depths, and the SiO lines. Usually, the  $^{12}\text{C}^{16}\text{O}$  emission from the outflowing gas is moderately optically thick ( $\tau \lesssim 1$ ) in the low velocity range and optically thin in the high velocity range. Silicon monoxide (SiO) is thought to be generated in dust disruption zones within shocks, and thus is a good shock tracer (Hartquist et al. 1980, Caselli et al. 1997).

The  $^{12}\text{C}^{16}\text{O}$  emission from the core ambient gas is usually optically thick, typically  $\tau > 10$ , and exhibit complex self-absorption features. We refer as self-absorption of the line to the absorption produced by material that is part of the molecular core but at a lower excitation temperature than the bulk of the gas. The opacity of the lines in the  $^{13}\text{CO}$  and  $\text{C}^{18}\text{O}$  isotopic species are, due to their relative abundances, approximately one and two orders of magnitude smaller than that of CO, respectively. Hence these lines are better probes of the physical and kinematical properties of the core gas. The  $\text{HCO}^+$  lines have been used to probe the kinematics of the bulk of star forming cores (e.g. Masunaga & Inutsuka 2000, Chen et al. 2010). For some, but key, of the molecular cores observed in this work, we detected

the characteristic blue-asymmetry profile related with infall motions. Although not directly related with the outflows, the presence of this spectral feature is a strong argument in favor of these cores being in a very young state of collapse.

In this chapter we present molecular line observations toward 13 HMYSOs in total. As remarked, eight of them are in the list of jet candidates presented in Table 2.1. Seven of these have been observed with ATCA and VLA (previous Chapter). Of the five other sources, not in the list of jet candidates, two were selected from the literature due to the presence of extended and collimated H<sub>2</sub> 2.12  $\mu$ m line emission (IRAS 18151–1208 and 18264–1152, Varricatt et al. 2010), tracing outflow and shock activity. The remaining three sources (G333.1306–00.4275, G319.3993–00.0135 and G332.8256–00.5498) are HMYSOs candidates selected during an early phase of this work, one of them was also observed in radio centimeter (Ch. 2).

## 3.1 Observations

In this section we describe the observations of molecular outflows performed with the telescopes APEX and ASTE located in northern Chile.

### 3.1.1 Observational strategy and calibration

The general features and observational radioastronomical concepts are described in Wilson et al. (2009) and Kraus (1986). Issues related directly with millimeter wave line observations and calibration are described in Ulich & Haas (1976) and Kutner & Ulich (1981).

The main observational challenges that affect molecular outflow observations in millimeter and submillimeter wavelengths using ground-based telescopes are directly or indirectly caused by the atmosphere, and specially by the amount of water vapor in it. The atmosphere forms an absorbing, emitting, and unstable “screen” whose effects needs to be corrected. Different calibration procedures have for objective the correction of the flux, or the pointing of the telescope, but they share a common approach: correct the data according to the response of the instrument when measuring known radiation sources, that could be astronomical sources or known temperature loads. Usually, the calibration details also depends on a model of the atmospheric absorption.

The principal calibration mechanism that allows us to correct for the sky opacity is the “chopper-wheel” method, described in Penzias & Burrus (1973) and in Ulich & Haas (1976). In its simplest idealized form, this method considers the atmosphere as an homogeneous absorbing screen at ambient temperature.

In addition to the opacity correction, the observation of molecular millimeter lines require to cancel the sky contribution across the waveband. To accomplish this, we observe using a technique called the position-switching mode (P-S mode) or “on-off” method, which consist of observing toward the source (the *on*-position), and subtracting the antenna response obtained from a previous — or posterior — observation of blank sky (the *off*-position). In order to cancel out the variable sky contribution, the “off” observation needs to be taken as close to the line of sight of the “on” position as possible, and approximately at the same time. We constructed maps, observing each position of a rectangular grids with its axes parallel to the

RA-Dec directions, separated by 1 or 1/2 beam, depending on the transition. These maps have typically between 9 and 50 spectra. A single off-position is used for the entire grid, but a different off is needed for each source. When observing extended sources (such as outflows) with this technique, the off-position has to be taken far enough so it does not include emission from the source. Typically, off-positions were taken between 20' and 1.5° from the source. Also, in order to minimize the noise in each spectrum, equal amounts of time needs to be spent on the “on” and “off” positions.

The observations were made using the 12-m Atacama Pathfinder Experiment (APEX) Telescope and the 10-m Atacama Submillimeter Telescope Experiment (ASTE). The APEX observations took place during April 2008, June, July, and August 2009; and the ASTE observations were performed during July 2010.

A detailed description of APEX and its performance are given by Güsten et al. (2006). All the APEX observations were made using a front-end consisting on a single pixel heterodyne SiS receiver operating in the 275-370 GHz band (Risacher et al. 2006). For the back-end we used the APEX Fast Fourier Transform Spectrometer (Klein et al. 2006) with a bandwidth of 1 GHz and 2048 frequency channels. The main characteristics of the ASTE telescope are described in Ezawa et al. (2004). The front-end consisted of a heterodyne single pixel SiS receiver operating between 324 and 372 GHz. As back-end we use the MAC XF-type digital spectro-correlator with 1024 channels (Iguchi & Okuda 2008). We used the 512 MHz bandwidth for the CO lines, its isotopologues, and for the SiO line transitions. For the HCO<sup>+</sup>(4→3) observations we used 128 MHz bandwidth. In the APEX and ASTE observations we used line pointing on IRAS 15194–5115, W-Aql, RT-Sco, and X-TrA, depending on which was nearer to the target source. Continuum sources were used to calibrate the pointing of the CO(6→5) and CO(7→6) observations toward G345.4938+01.4677 (see Chapter 5). Standard reduction procedures were performed using the software CLASS<sup>1</sup> for APEX data, and Newstar (Ikeda et al. 2001) for ASTE data.

Table 3.1 summarizes the main observational and instrumental parameters of the of the molecular line observations made towards HMYSOs. Column (1) gives the source name, cols. (2-3) the coordinates, col. (4) the observed line, col. (5) the frequency of the transition, col. (6) the telescope used (APEX or ASTE), col. (7) the main-beam at the line frequency, cols. (8-9) the size of the mapped region and spacing, respectively, col. (10) the spectral resolution in km s<sup>-1</sup>, and the last two columns give the average noise per channel and the main beam efficiency of the observations, respectively. The main-beam temperatures given in the next section are obtained simply dividing the antenna temperature by the main-beam efficiency ( $\eta_{mb}$ ).

---

<sup>1</sup><http://www.iram.fr/IRAMFR/GILDAS>

Table 3.1. Molecular line observational parameters

Source	R.A. (J2000)	Dec (J2000)	Line	Freq. (GHz)	Telesc.	$\theta_{mb}$ (")	Map	Spacing (")	$\Delta v$ (km s <sup>-1</sup> )	Noise <sup>1</sup> (K)	$\eta_{mb}$
(1)	(2)	(3)	(4)	(5)	(6)	(7)	(8)	(9)	(10)	(11)	(12)
<b>Jet candidates</b>											
G305.7984-00.2416	13 <sup>h</sup> 16 <sup>m</sup> 42 <sup>s</sup> .62	-62°58'21".2	CO(3→2)	345.796	APEX	17.6	7 × 7 <sup>2</sup>	20	0.423	0.08	0.73
G317.4298-00.5612	14 51 37.60	-60 00 19.4	CO(3→2)	345.796	APEX	17.6	5 × 3	20	0.423	0.09	0.73
			SiO(8→7)	347.331	ASTE	22.2	Point	-	0.432	0.04	0.70
G337.4032-00.4037	16 38 50.45	-47 28 02.7	CO(3→2)	345.796	APEX	17.6	5 × 5	20	0.423	0.10	0.73
			SiO(8→7)	347.331	APEX	17.5	5 × 5	20	0.432	0.07	0.73
			HCO <sup>+</sup> (4→3)	356.734	ASTE	21.6	5 × 5	20	0.105	0.34	0.70
			<sup>13</sup> CO(3→2)	330.588	ASTE	23.3	5 × 5	20	0.453	0.13	0.70
			C <sup>18</sup> O(3→2)	329.331	ASTE	23.4	5 × 5	20	0.455	0.15	0.70
G337.8442-00.3748	16 40 26.67	-47 07 13.1	CO(3→2)	345.796	APEX	17.6	3 × 3	20	0.423	0.14	0.73
G345.0061+01.7944	16 56 47.59	-40 14 25.8	CO(3→2)	345.796	APEX	17.6	5 × 5	20	0.423	0.12	0.73
			<sup>13</sup> CO(3→2)	330.588	ASTE	23.3	Point	-	0.453	0.07	0.73
			C <sup>18</sup> O(3→2)	329.331	ASTE	23.4	Point	-	0.455	0.09	0.73
			SiO(8→7)	347.331	ASTE	22.2	Point	-	0.432	0.02	0.73
G345.4938+01.4677	16 59 41.61	-40 03 43.4	CO(3→2)	345.796	APEX	17.6	5 × 5	20	0.423	0.07	0.73
			CO(6→5)	691.627	APEX	8.8	29 × 21	4	0.318	0.24	0.47
			CO(7→6)	806.898	APEX	7.7	27 × 19	4	0.272	0.43	0.43
			SiO(8→7)	347.331	APEX	17.5	3 × 3	20	0.432	0.04	0.73
			HCO <sup>+</sup> (4→3)	356.734	ASTE	21.6	5 × 5	10	0.105	0.34	0.70
			<sup>13</sup> CO(3→2)	330.588	ASTE	23.3	5 × 5	20	0.453	0.07	0.73
			C <sup>18</sup> O(3→2)	329.331	ASTE	23.4	5 × 5	20	0.455	0.08	0.73
			CO(3→2)	345.796	APEX	17.6	6 × 6 <sup>2</sup>	20	0.423	0.07	0.73
G352.5173-00.1549	17 27 11.32	-35 19 32.8	CO(3→2)	345.796	ASTE	22.3	6 × 6 <sup>2</sup>	20	0.433	0.07	0.70
			CO(3→2)	345.796	ASTE	22.3	6 × 6 <sup>2</sup>	20	0.433	0.07	0.70
			HCO <sup>+</sup> (4→3)	356.734	ASTE	21.6	5 × 5	10	0.105	0.17	0.70

Table 3.1 (cont'd)

Source	R.A.	Dec	Line	Freq.	Telesc.	$\theta_{mb}$	Map	Spacing	$\Delta v$	Noise <sup>1</sup>	$\eta_{mb}$
(1)	(J2000)	(J2000)	(4)	(GHz)	(6)	( $''$ )	(8)	( $''$ )	(km s <sup>-1</sup> )	(K)	(12)
(1)	(2)	(3)	(4)	(5)	(6)	(7)	(8)	(9)	(10)	(11)	(12)
G025.6469+01.0534	18 34 19.80	-05 59 44.0	CO(3→2)	345.796	APEX	17.6	6 × 6 <sup>2</sup>	20	0.423	0.08	0.73
			CO(3→2)	345.796	ASTE	22.3	6 × 6 <sup>2</sup>	20	0.433	0.05	0.70
<b>Other outflow and HMYSOs candidates</b>											
IRAS 18151-1208	18 <sup>h</sup> 17 <sup>m</sup> 57 <sup>s</sup> .10	-12°07'22".0	CO(3→2)	345.796	APEX	17.6	5 × 5	20	0.423	0.13	0.73
			SiO(8→7)	347.331	ASTE	22.2	Point	-	0.432	0.08	0.70
IRAS 18264-1152	18 29 14.29	-11 50 26.0	CO(3→2)	345.796	APEX	17.6	5 × 5	20	0.423	0.08	0.73
			SiO(8→7)	347.331	APEX	17.5	5 × 5	20	0.423	0.10	0.73
G319.3993-00.0135	15 03 17.52	-58 36 12.7	CO(3→2)	345.796	APEX	17.6	4 × 4	20	0.423	0.10	0.73
G332.8256-00.5498	16 20 11.07	-50 53 15.3	CO(3→2)	345.796	APEX	17.6	3 × 3	20	0.423	0.10	0.73
G333.1306-00.4275	16 21 02.95	-50 35 12.3	CO(3→2)	345.796	APEX	17.6	3 × 3	20	0.423	0.09	0.73

<sup>1</sup>Average noise of the map in main beam temperature.<sup>2</sup>APEX and ASTE data were combined to obtain this coverage.

## 3.2 Results

In this section we present the results of the molecular line observations for each source individually. In most cases we first present a map of the  $^{12}\text{C}^{16}\text{O}(3\rightarrow 2)$  spectra observed toward the source and then a contour map of the integrated high-velocity emission. This line is the best probe of the optically thin emission from the high-velocity wings arising from the outflows. As a first step, we determined the ranges in which emission from high-velocity gas was detected. Table 3.2 show these ranges for all the sources that display significant wing emission (all objects except G319.3993–00.0135, G337.8442–00.3748 and G332.8256–00.5498). Columns (2) and (3) give, respectively, the distance (kpc) and the  $v_{LSR}$  ( $\text{km s}^{-1}$ ) of the ambient gas. Column (4) shows a “B” or an “R” depending on whether the parameters refer to the blueshifted or redshifted flow, respectively. Column (5) gives the high-velocity range where emission is detected, col. (6) display the peak value of the high-velocity integrated emission, and cols. (7) and (8) give the right ascension and declination of this peak, respectively. The ambient gas velocity was assumed to be that of the peak of the  $\text{C}^{18}\text{O}(3\rightarrow 2)$  line, which is usually an optically thin transition. If this line was not observed, we choose as ambient gas velocity the peak of the  $\text{CO}(3\rightarrow 2)$  line in a position where it does not show optically thick nor self-absorption features, usually toward the outskirts of the core. In one case, we select the  $v_{LSR}$  velocity from the  $\text{CS}(2\rightarrow 1)$  line (Bronfman et al. 1996). The velocity ranges do not vary throughout the location in the map. The outer limit of the blue and red-shifted intervals correspond to the lowest and highest velocities, respectively, where emission is detected above the 3 sigma level. The inner limit of the intervals are more difficult to estimate: the form of the line in the high opacity regions always exhibits complex self-absorption features that vary from source to source. The procedure we adopted in this work consist of fitting a gaussian component to the line with its mean fixed at the ambient cloud velocity. We select the inner limit of the velocity intervals at the velocity where the emission expected from the gaussian accounts for approximately half of the measured intensity. In order to be more consistent and to avoid biases, we decided to select this inner limits symmetrically respect to the ambient cloud velocity. As an example, Figure 3.1 shows three profiles detected toward G305.7984–00.2416: the blue and red displaying respectively intense blue-shifted and red-shifted wings, and the green represents the ambient cloud. The velocity ranges that define the high-velocity features of the outflow are also displayed.

Table 3.2. High Velocity (HV) gas parameters

Source	Dist. (kpc)	$v_{LSR}$ ( $\text{km s}^{-1}$ )	Flow (B or R)	HV range ( $\text{km s}^{-1}$ )	Peak ( $\text{K km s}^{-1}$ )	Peak R.A. (J2000)	Peak Dec. (J2000)
(1)	(2)	(3)	(4)	(5)	(6)	(7)	(8)
<b>Jet candidates</b>							
G025.6469+01.0534	3.1	+41.4	B	[−00.8, +26.4]	24.84	18 <sup>h</sup> 34 <sup>m</sup> 21 <sup>s</sup> .2	−06°00′05″
			R	[+56.4, +86.0]	35.59	18 34 20.0	−05 59 44
G305.7984−00.2416	3.0	−31.6	B	[−57.9, −40.6]	28.35	13 16 42.6	−62 58 51
			R	[−22.6, −09.1]	17.62	13 16 45.6	−62 58 41
G317.4298−00.5612	15.	+27.6	B	[+04.7, +23.0]	55.27	14 51 37.7	−60.00.20
			R	[+28.0, +41.0]	21.80	14 51 37.7	−60.00.20
G337.4032−00.4037	3.2	−40.7	B	[−85.0, −55.7]	32.56	16 38 50.5	−47 28 03
			R	[−25.7, +30.9]	68.14	16 38 50.5	−47 28 03
G337.8442−00.3748 <sup>a</sup>	3.1	−42.5			...		
G345.0061+01.7944	1.7	−12.7	B	[−51.7, −22.7]	65.18	16 56 47.4	−40 14 25
			R	[−02.7, +20.6]	32.15	16 56 47.5	−40 14 07
G345.4938+01.4677 <sup>b</sup>	1.6	−12.5	B	[−46.0, −22.0]	49.00	16 59 41.6	−40 03 43
			R	[−03.0, +14.0]	26.40	16 59 41.6	−40 03 43
G352.5173−00.1549	5.6	−49.2 <sup>b</sup>	B	[−75.0, −55.2]	27.77	17 27 11.4	−35 19 33
			R	[−43.2, −20.0]	35.91	17 27 11.4	−35 19 33
<b>Other outflow and HMYSO candidates</b>							
IRAS 18151−1208	3.0	+33.0	B	[+22.0, +26.0]	4.42	18 <sup>h</sup> 17 <sup>m</sup> 57 <sup>s</sup> .8	−12°07′33″
			R	[+40.0, +52.1]	31.60	18 17 56.4	−12 07 34
IRAS 18264−1152	3.5	+44.4	B	[+07.7, +34.0]	37.61	18 29 14.2	−11 50 28
			R	[+54.0, +73.7]	38.96	18 29 13.4	−12 07 34
G333.1306−00.4275	3.5	−51.2 <sup>c</sup>	B	[−85.0, −66.2]	164.99	16 21 03.0	−50 35 13
			R	[−36.2, −28.0]	9.29	16 21 03.0	−50 34 49
G332.8256−00.5498 <sup>a</sup>	3.7	−55.7 <sup>b</sup>			...		
G319.3993−00.0135 <sup>a</sup>	0.9	−12.0			...		

<sup>a</sup>No significant outflow emission was detected toward this source.

<sup>b</sup>These parameters correspond to the CO(3→2) transition.

<sup>c</sup>For these sources the ambient  $v_{LSR}$  was taken from the CS line (Bronfman et al. 1996).

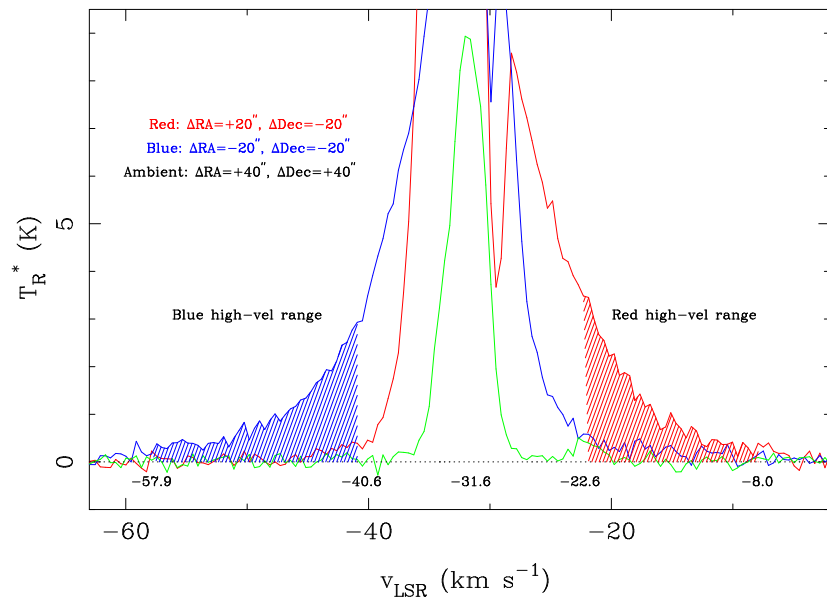


Figure 3.1 CO(3→2) emission detected toward G305.7984–00.2416. Blue and red profiles are taken as representative of spectra with dominant blue and red-shifted features, respectively. The green spectrum represents the ambient cloud. Also shown are the high-velocity range limits and the ambient cloud velocity (see Table 3.2).

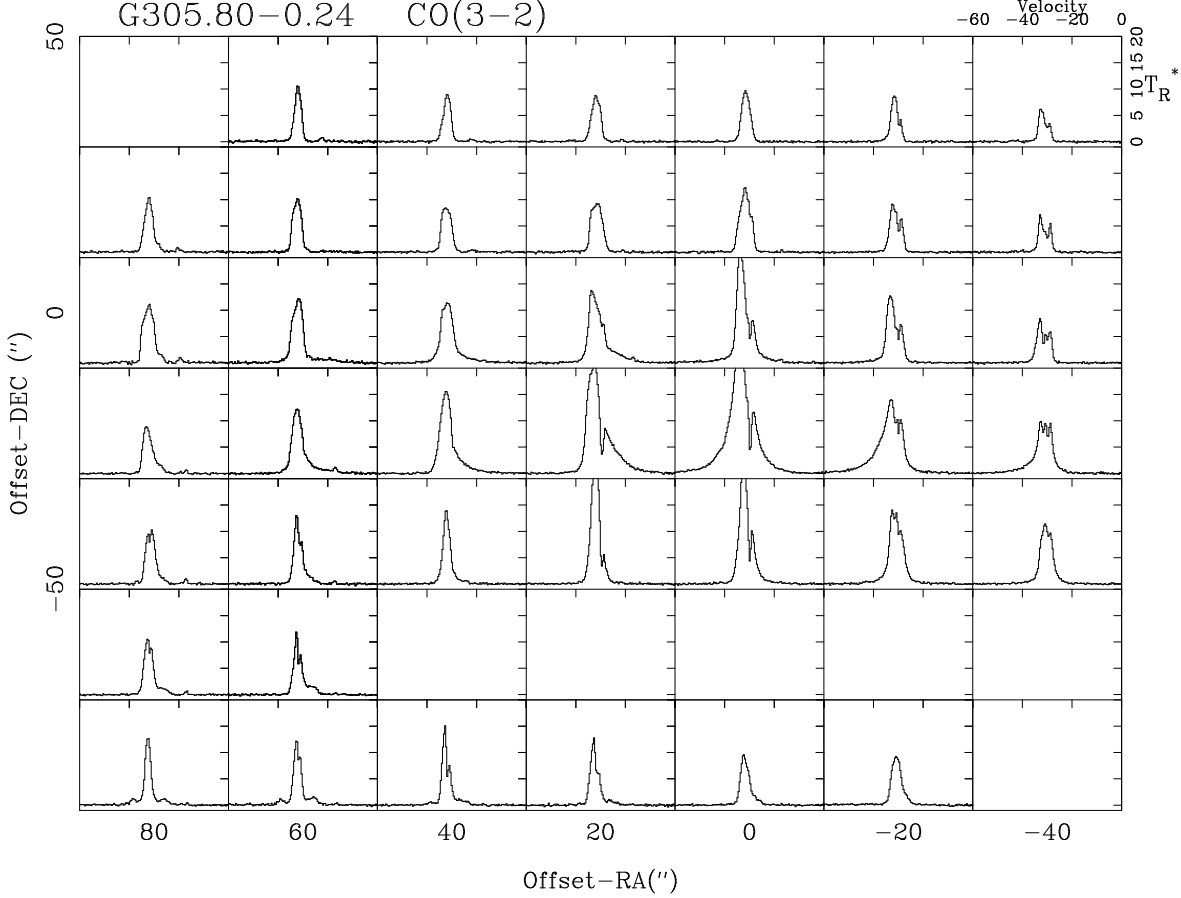


Figure 3.2 APEX and ASTE data observed toward G305.7984–00.2416 in the CO(3→2) transition.

### 3.2.1 Jet candidates

#### *G305.7984–00.2416.*

Toward this jet candidate we mapped the CO(3→2) emission within a region of  $120'' \times 120''$ , although not fully mapped (see Figure 3.2). Strong emission from high velocity gas is detected near the ( $\Delta\alpha = 0$ ,  $\Delta\text{Dec} = -20''$ ) offset position. Redshifted and blueshifted wing emission are clearly seen toward the east and west, respectively. The wing emission span a velocity range of  $-57.9 \text{ km s}^{-1} < v_{LSR} < -10.1 \text{ km s}^{-1}$ . We assume that the ambient cloud velocity is  $v_{LSR} = -32.6 \text{ km s}^{-1}$ , corresponding to the velocity of the peak emission detected toward  $\Delta\text{R.A.} = +40''$  and  $\Delta\text{Dec.} = +40''$ . This line shows a single component with no signs of high-velocity gas or self-absorption. Singly self-absorbed profiles are mainly seen toward the peak of the core, with predominance of the blueshifted peak.

Figure 3.3 shows a contour map of the velocity integrated redshifted and blueshifted CO(3→2) emission. We can clearly see a bipolar outflow, with a redshifted lobe located toward the east and a blueshifted lobe located toward the west and whose peaks are separated by  $22.7''$ . The axis of symmetry of the bipolar outflow is located  $\sim 15''$  south of the central position of the map (Table 3.1).

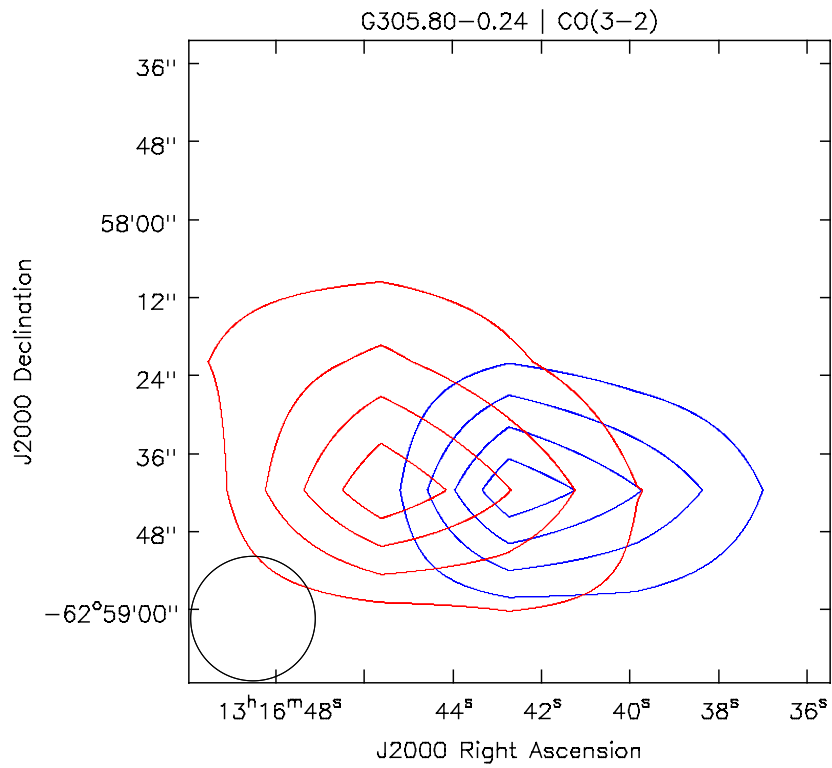


Figure 3.3 Contour map of the velocity integrated CO(3→2) emission detected toward G305.7984-00.2416. Blue contours represent emission integrated over the blueshifted high-velocity range indicated in Table 3.2, and red contours represent the emission integrated over the redshifted high-velocity range. Contour levels are 20, 40, 60, and 80% of the peak emission. Peak blueshifted emission:  $28.4 \text{ K km s}^{-1}$ . Peak redshifted emission:  $17.6 \text{ K km s}^{-1}$ .

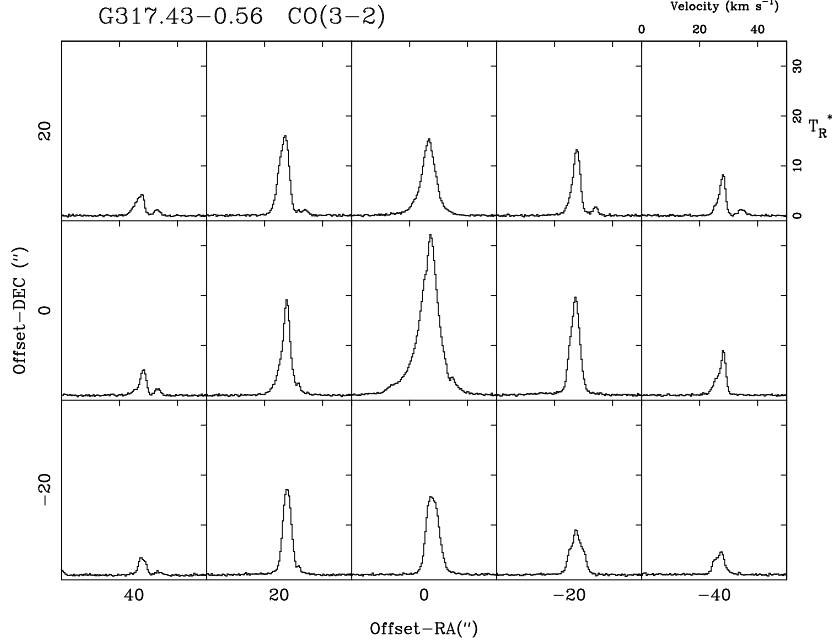


Figure 3.4 CO(3→2) spectra observed toward G317.4298–00.5612.

***G317.4298–00.5612.***

Toward this jet candidate we mapped the CO(3→2) emission within a region of  $100'' \times 60''$  (see Figure 3.4). Wing emission is mainly seen toward the central position, spanning the velocity range  $10.9 \text{ km s}^{-1} < v_{LSR} < 39.0 \text{ km s}^{-1}$ . The spectra do not show evidence of self-absorption features. We determined that the ambient cloud velocity is  $v_{LSR} = 27.6 \text{ km s}^{-1}$ . We did not detect SiO(8→7) emission at the 0.04 K level (see Figure 3.5).

***G337.4032–00.4037.***

Toward this jet candidate we mapped the CO(3→2) emission within a region of a  $100'' \times 100''$  (see Fig. 3.7). Strikingly seen toward the central spectra is strong wing emission spanning a

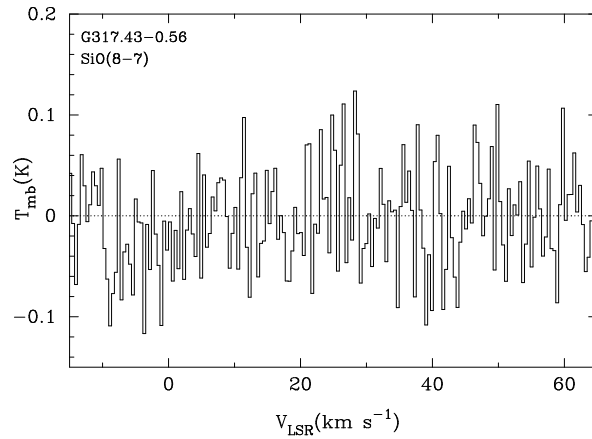


Figure 3.5 SiO(8→7) spectra observed toward the central position of G317.4298–00.5612. No emission is detected at the 0.04 K level.

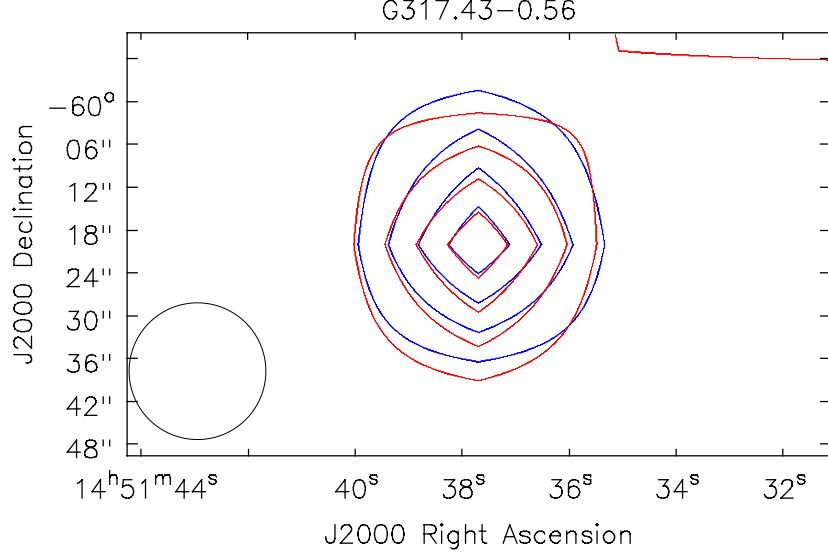


Figure 3.6 Velocity integrated CO(3→2) wing emission. Red and blue lines indicate redshifted and blueshifted emission, respectively. Contour levels are 20, 40, 60, and 80% of the peak value. *Blue contours*: Velocity range (km s<sup>-1</sup>): [4.7, 23.0], Peak: 55.3 K km s<sup>-1</sup>. *Red contours*: Velocity range (km s<sup>-1</sup>): [32.0, 41.0], Peak: 21.8 K km s<sup>-1</sup>.

wide velocity range, of about 115 km s<sup>-1</sup>, from -85 km s<sup>-1</sup> to 30 km s<sup>-1</sup>. Figure 3.12 shows a contour map of the blueshifted and redshifted wing emission, showing that the outflowing gas is confined to the central position. For the ambient cloud velocity we assumed a value of  $v_{LSR} = -40.7$  km s<sup>-1</sup>, corresponding to the velocity of the peak emission in the C<sup>18</sup>O(3→2) line.

Also mapped toward this source, within the same 100'' × 100'' region, is the emission in the SiO(8→7), HCO<sup>+</sup>(4→3), <sup>13</sup>CO(3→2) and C<sup>18</sup>O(3→2) lines. In SiO(8→7), strong and broad emission was detected only toward the central position (see Fig. 3.8, consistent with strong outflow activity at this position. In the HCO<sup>+</sup>(4→3) and <sup>13</sup>CO(3→2) lines (Figures 3.9 and 3.10) the profiles show a blueshifted peak and a red shoulder, characteristic of infall. In the HCO<sup>+</sup> line the blue asymmetry is restricted to the central position, whereas in the <sup>13</sup>CO(3→2) line this spectral feature appears more spatially extended. The C<sup>18</sup>O(3→2) profiles, on the other hand, are a single Gaussian optically thin component.

***G337.8442-00.3748.***

Toward this jet candidate we mapped the CO(3→2) emission within a region of a 60'' × 60'' (see Fig. 3.13). The spectra are complex, exhibiting two or three components, but there is no indication of broad wing emission. The total velocity range spanned by this line is  $-31.5$  km s<sup>-1</sup> <  $v_{LSR}$  <  $-6.2$  km s<sup>-1</sup>.

***G345.0061+01.7944.***

Toward this jet candidate we mapped the CO(3→2) emission within a region of 100'' × 100'' (see Figure 3.14). Clearly seen toward the central position is strong blueshifted wing emission, whereas weaker redshifted wing emission is seen toward the north. The emission ranges be-

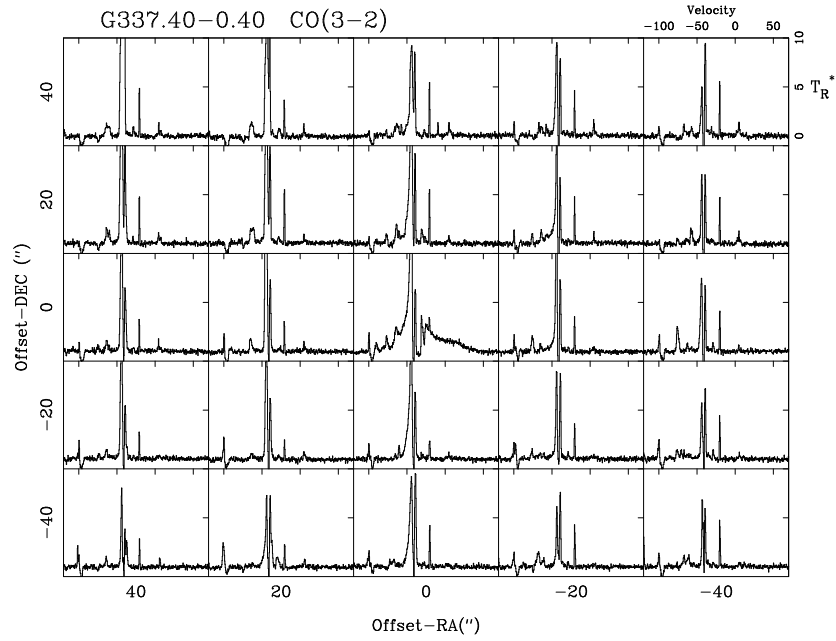


Figure 3.7 CO(3 $\rightarrow$ 2) spectra observed toward G337.4032–00.4037. High velocity emission is clearly seen toward the central position.

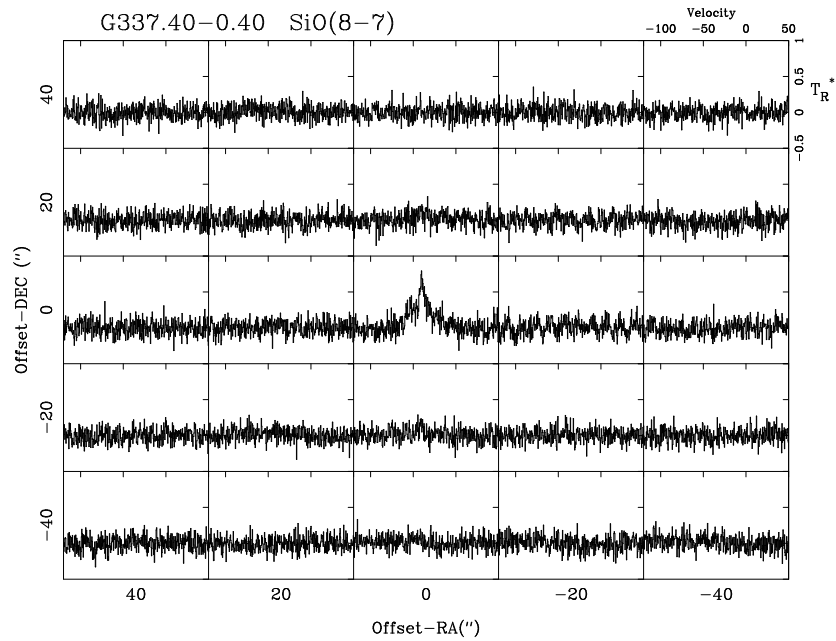


Figure 3.8 Emission detected toward G337.4032–00.4037 in the SiO(8 $\rightarrow$ 7) transition.

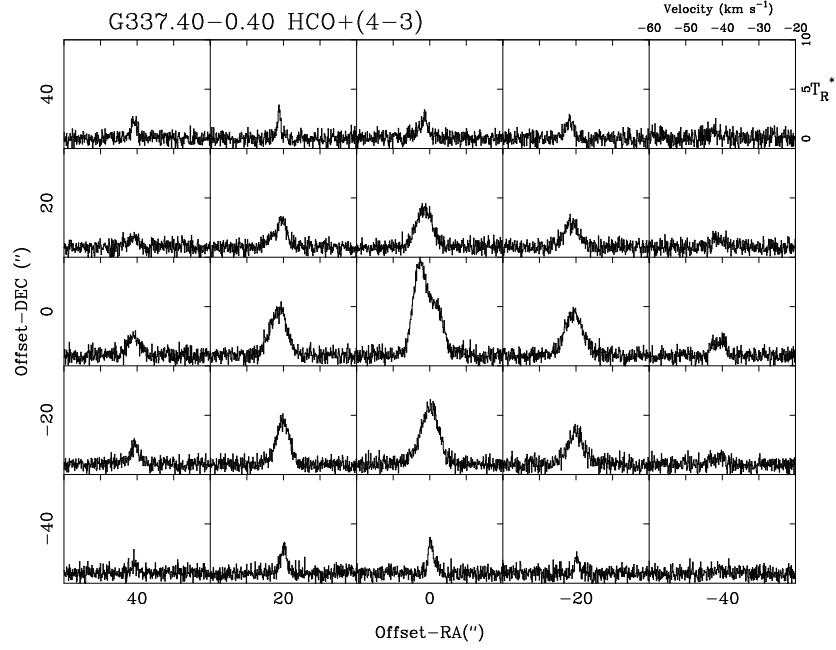


Figure 3.9 Emission detected toward G337.4032-00.4037 in the  $\text{HCO}^+(4\rightarrow 3)$  transition.

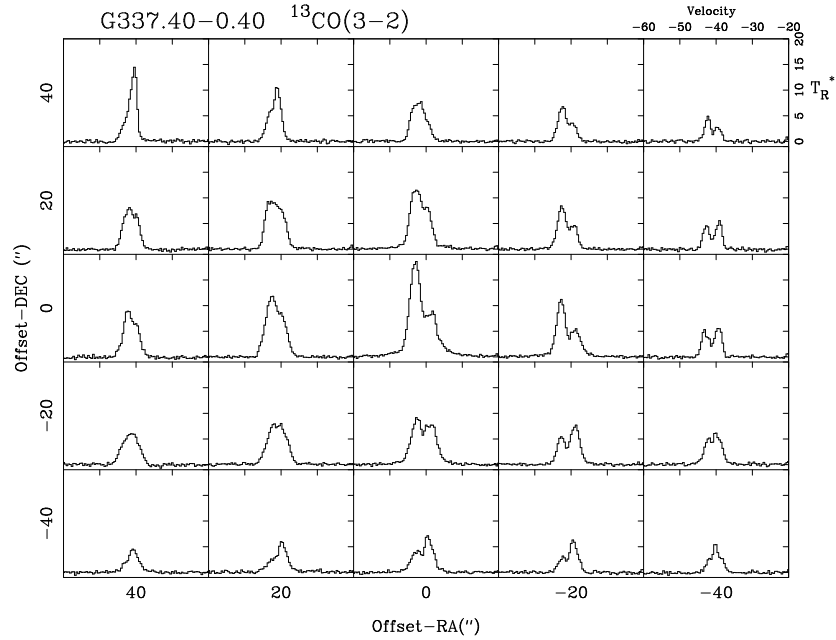


Figure 3.10 Emission detected toward G337.4032-00.4037 in the  $^{13}\text{CO}(3\rightarrow 2)$  transition. The central position shows a clear blue-shoulder infall profile.

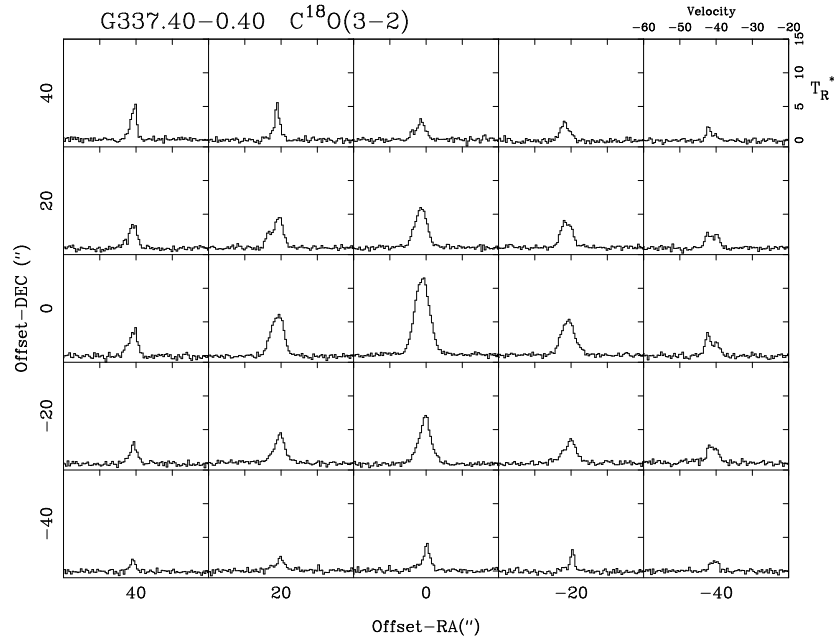


Figure 3.11 Emission detected toward G337.4032–00.4037 in the  $C^{18}O(3\rightarrow 2)$  transition.

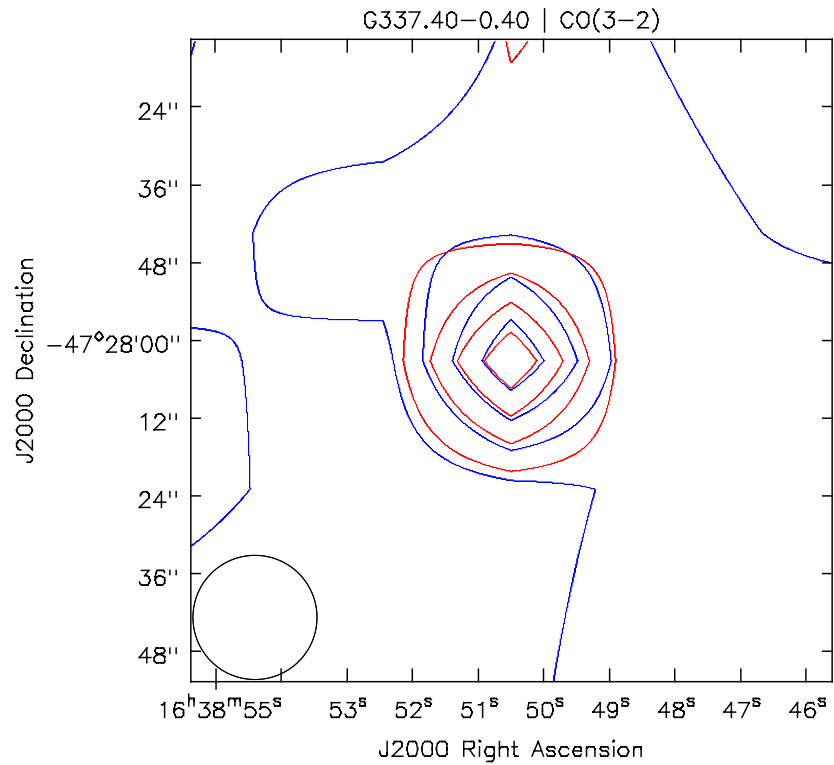


Figure 3.12 High-velocity  $CO(3\rightarrow 2)$  emission. Red and blue contours show the redshifted and blueshifted integrated temperature, and they correspond to the 20, 40, 60, and 80% of the peak. The emission is mostly confined toward the central position. *Blue contours*: Velocity range ( $\text{km s}^{-1}$ ):  $[-85.0, -55.7]$ , Peak:  $32.6 \text{ K km s}^{-1}$ . *Red contours*: Velocity range ( $\text{km s}^{-1}$ ):  $[-25.7, +30.9]$ , Peak:  $68.1 \text{ K km s}^{-1}$ .

tween  $-75.0 \text{ km s}^{-1} < v_{LSR} < 20.0 \text{ km s}^{-1}$ , spanning  $55 \text{ km s}^{-1}$ . The ambient cloud velocity is  $-12.7 \text{ km s}^{-1}$ , taken as the peak of the  $\text{C}^{18}\text{O}(3\rightarrow 2)$  emission. Figure 3.15 shows a contour map of the blueshifted and redshifted velocity integrated emission. It shows a bipolar outflow aligned in the north-south direction, with peaks separated by  $18.1''$ . The driving source of the flow, however, does not appear to be associated to the center of the map. Perhaps the most striking characteristic of the CO lines of Fig. 3.14 are the red-asymmetric profiles detected toward all the 9 central spectra, indicative of large scale expansion. This feature could hardly be attributed to a bipolar outflow excited by a jet.

Figure 3.16 shows three complementary transitions, from top to bottom panels:  $^{13}\text{CO}(3\rightarrow 2)$ ,  $\text{C}^{18}\text{O}(3\rightarrow 2)$ , and  $\text{SiO}(8\rightarrow 7)$ . Both CO isotopes display similar characteristics, exhibiting a single peak and a small blueshifted wing. Consistent with the  $\text{CO}(3\rightarrow 2)$  profiles, the  $^{13}\text{CO}(3\rightarrow 2)$  line shows a red-shifted asymmetry characteristic of expansion. As expected, the profile of  $\text{C}^{18}\text{O}$  is more symmetric than that of  $\text{C}^{13}\text{O}$ . According with the stronger blueshifted outflow activity, the SiO line, although rather faint, shows blueshifted wing.

### ***G345.4938+01.4677.***

Towards this jet candidate (also IRAS 16562–3959) we observed the emission in the  $\text{CO}(3\rightarrow 2)$  within a region of  $100'' \times 100''$ , and  $\text{CO}(6\rightarrow 5)$  and  $\text{CO}(7\rightarrow 6)$ , within  $110'' \times 90''$ . A complete analysis of this data, which indicates the presence of a quadrupolar outflow, is presented in Chapter 5. In this section we discuss the observations made in the  $^{13}\text{CO}(3\rightarrow 2)$ ,  $\text{C}^{18}\text{O}(3\rightarrow 2)$ ,  $\text{HCO}^+(4\rightarrow 3)$ , and  $\text{SiO}(8\rightarrow 7)$  lines.

Figure 3.17 shows The emission in the  $^{13}\text{CO}(3\rightarrow 2)$  and  $\text{C}^{18}\text{O}(3\rightarrow 2)$  lines was mapped within a region of  $100'' \times 100''$  (see Fig. 3.17). The profiles in both lines show little evidence for self-absorption features, hence, we can use them to estimate the total molecular mass of the core (Section 3.3.3.1).

The  $\text{HCO}^+(4\rightarrow 3)$  (Figure 3.18) transition was mapped within a region of  $50'' \times 50''$ , with  $10''$  spacing (roughly half-beam). The profiles show signatures of infalling motions, namely blueshifted profiles, in several positions across the mapped region. The profiles also show prominent high-velocity wings, their extent being closely matched by that seen in the  $\text{SiO}(8\rightarrow 7)$  line. This analysis is further developed in Chapter 5. Figure 3.19 shows all the  $\text{SiO}(8\rightarrow 7)$  data, mapped in a  $40'' \times 40''$  grid. Most of the emission comes from the central spectrum, but there are positive detection toward all positions.

***G352.5173–00.1549.*** We mapped the  $\text{CO}(3\rightarrow 2)$  transition toward this jet candidate in a  $120'' \times 120''$  region (see Fig. 3.20) using APEX and ASTE. Strong wing emission is seen toward the central position, spanning a velocity range between  $-63.6 \text{ km s}^{-1}$  and  $-30.4 \text{ km s}^{-1}$  ( $v_{LSR}$ ). We find that the ambient cloud velocity, which we take as the peak of the spectrum detected toward  $\Delta\text{R.A.} = -20''$  and  $\Delta\text{Dec} = -40''$ , is  $v_{LSR} = -48.2 \text{ km s}^{-1}$ .

We also mapped the emission in  $\text{HCO}^+(4\rightarrow 3)$  line within a  $50'' \times 50''$  region (Figure 3.22), detecting only weak, possibly optically thin emission.

### ***G025.6469+01.0534.***

We mapped the  $\text{CO}(3\rightarrow 2)$  emission towards this jet candidate, within a region of  $120'' \times 120''$  (see Figure 3.23). High velocity gas is evident in several positions, specially toward spectra in

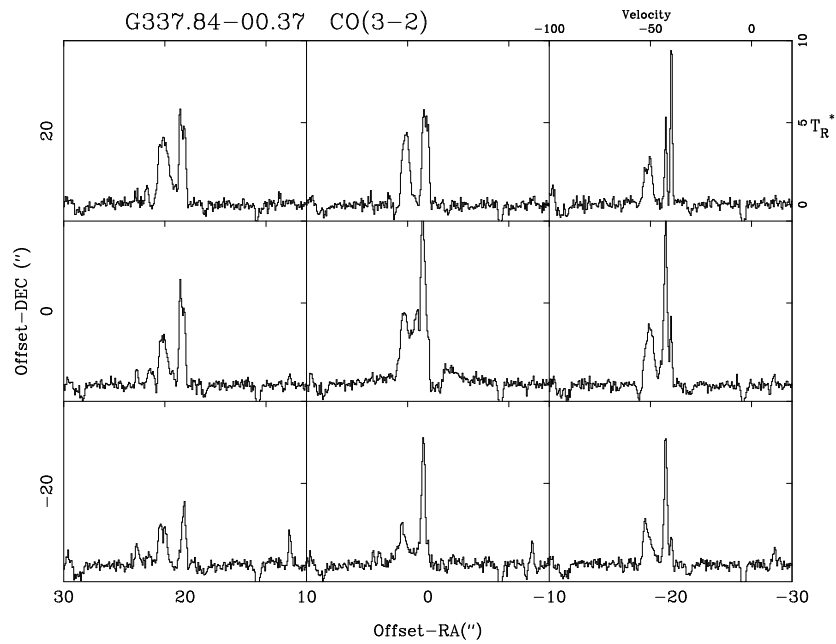


Figure 3.13 Emission detected toward G337.84–00.37 in the CO(3→2) transition. There is some high-velocity gas confined to the central position.

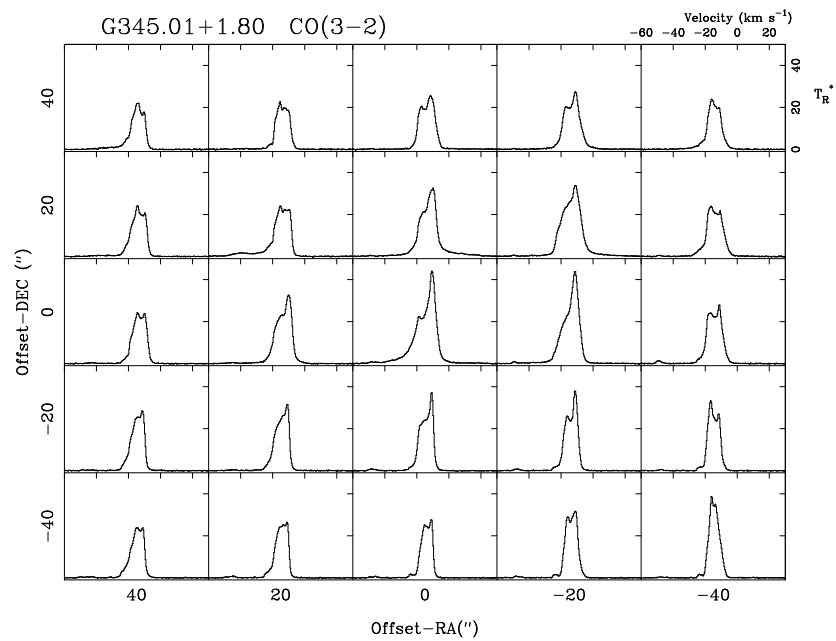


Figure 3.14 Spectra of the CO(3→2) transition detected toward the source G345.0061+01.7944.

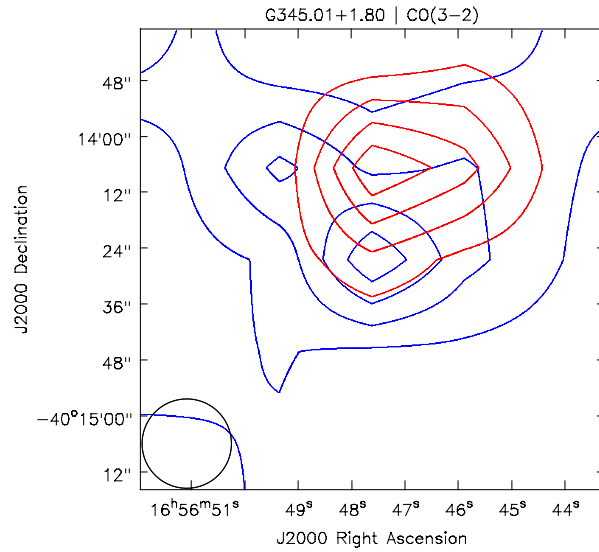


Figure 3.15 High-velocity CO(3→2) emission. Red and blue contours show the redshifted and blueshifted integrated temperature, and they correspond to the 20, 40, 60, and 80% of the peak. A bipolar outflow is detected aligned in the north-south direction *Blue contours*: Velocity range ( $\text{km s}^{-1}$ ):  $[-51.7, -22.7]$ , Peak:  $65.2 \text{ K km s}^{-1}$ . *Red contours*: Velocity range ( $\text{km s}^{-1}$ ):  $[-2.7, 20.6]$ , Peak:  $32.2 \text{ K km s}^{-1}$ .

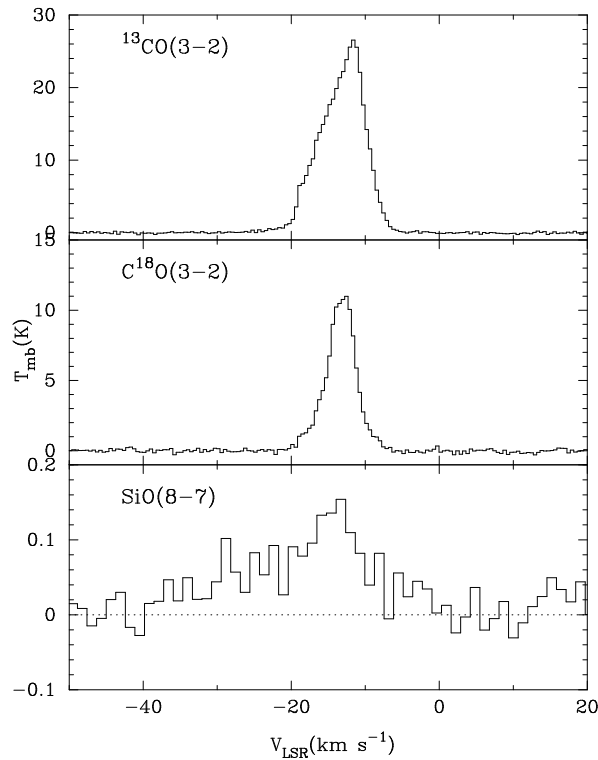


Figure 3.16 Three molecular profiles detected toward G345.0061+01.7944. Upper:  $^{13}\text{CO}(3\rightarrow 2)$ . Middle:  $\text{C}^{18}\text{O}(3\rightarrow 2)$ . Bottom:  $\text{SiO}(8\rightarrow 7)$ .

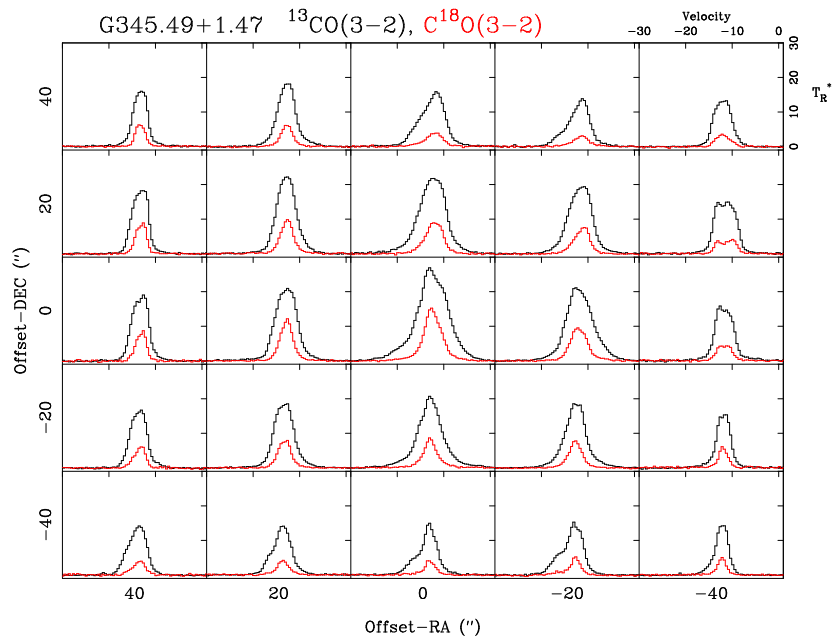


Figure 3.17 Spectra of the  $^{13}\text{CO}(3\rightarrow 2)$  and  $\text{C}^{18}\text{O}(3\rightarrow 2)$  transitions detected toward the source G345.4938+01.4677.

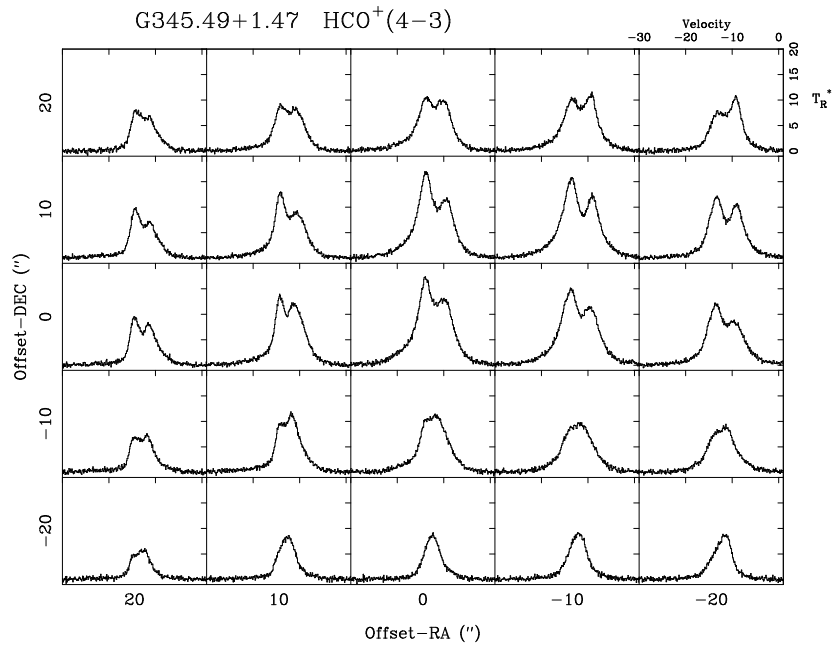


Figure 3.18 Spectra of the  $\text{HCO}^+(3\rightarrow 2)$  transition detected toward the source G345.4938+01.4677 .

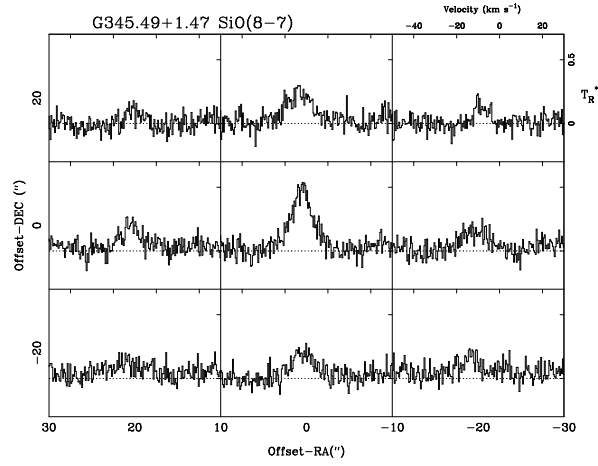


Figure 3.19 Spectra of the SiO(8→7) transition detected toward the source G345.4938+01.4677 .

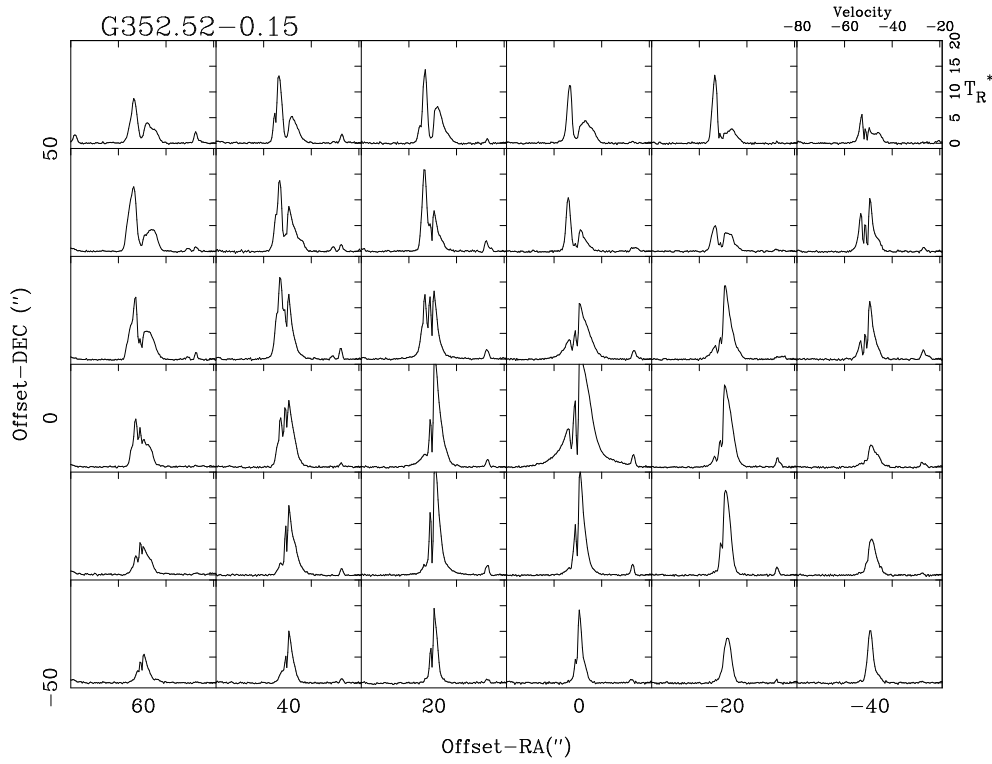


Figure 3.20 Map of the CO(3→2) line detected toward G352.5173-00.1549.

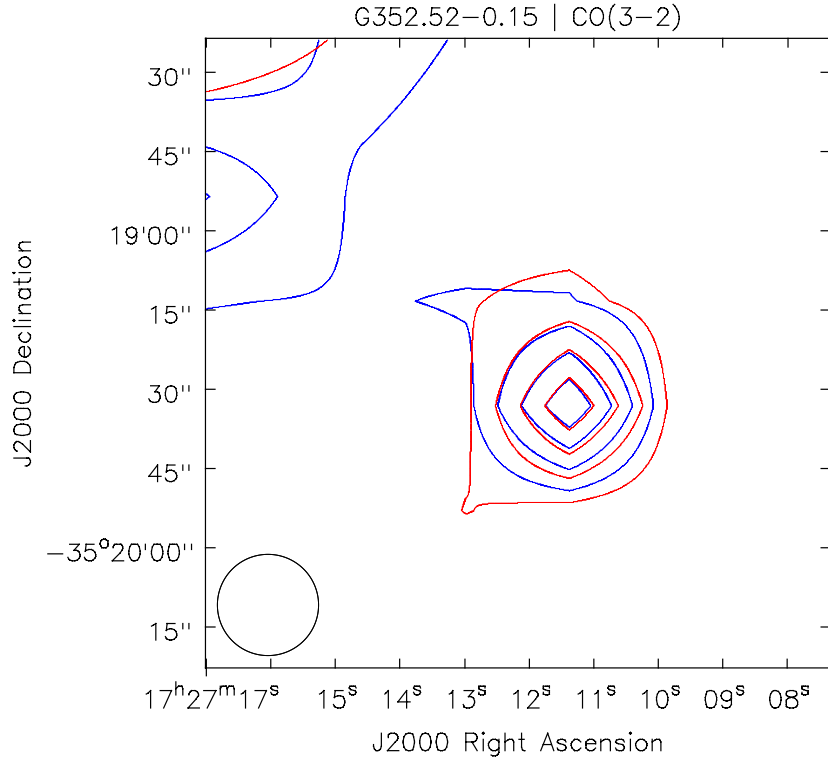


Figure 3.21 High-velocity CO(3→2) emission toward G352.5173–00.1549. Red and blue contours show the redshifted and blueshifted integrated temperature, and they correspond to the 20, 40, 60, and 80% of the peak. *Blue contours:* Velocity range ( $\text{km s}^{-1}$ ):  $[-80.0, -55.2]$ , Peak:  $27.7 \text{ K km s}^{-1}$ . *Red contours:* Velocity range ( $\text{km s}^{-1}$ ):  $[-43.2, -20.0]$ , Peak:  $35.9 \text{ K km s}^{-1}$ .

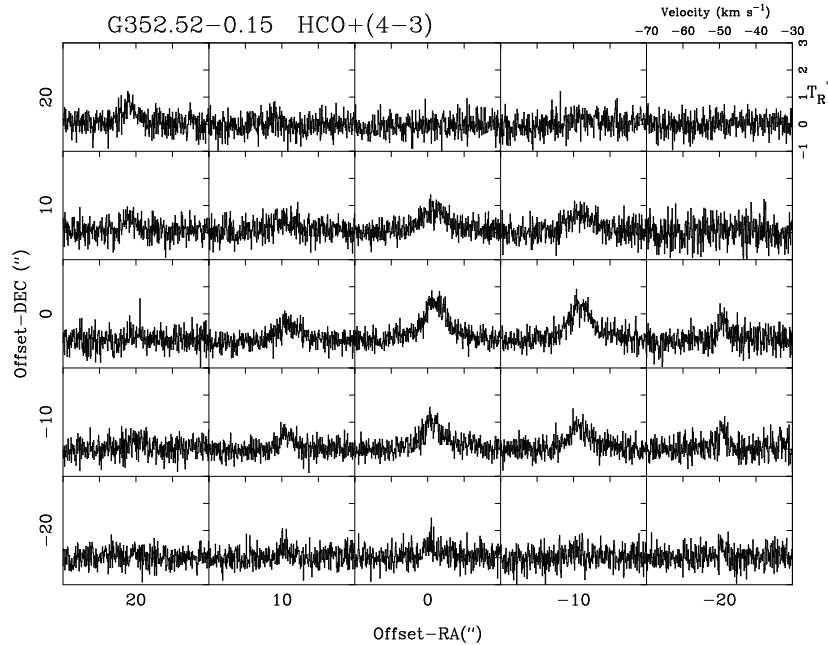


Figure 3.22 Map of the HCO<sup>+</sup>(4→3) line detected toward G352.5173–00.1549.

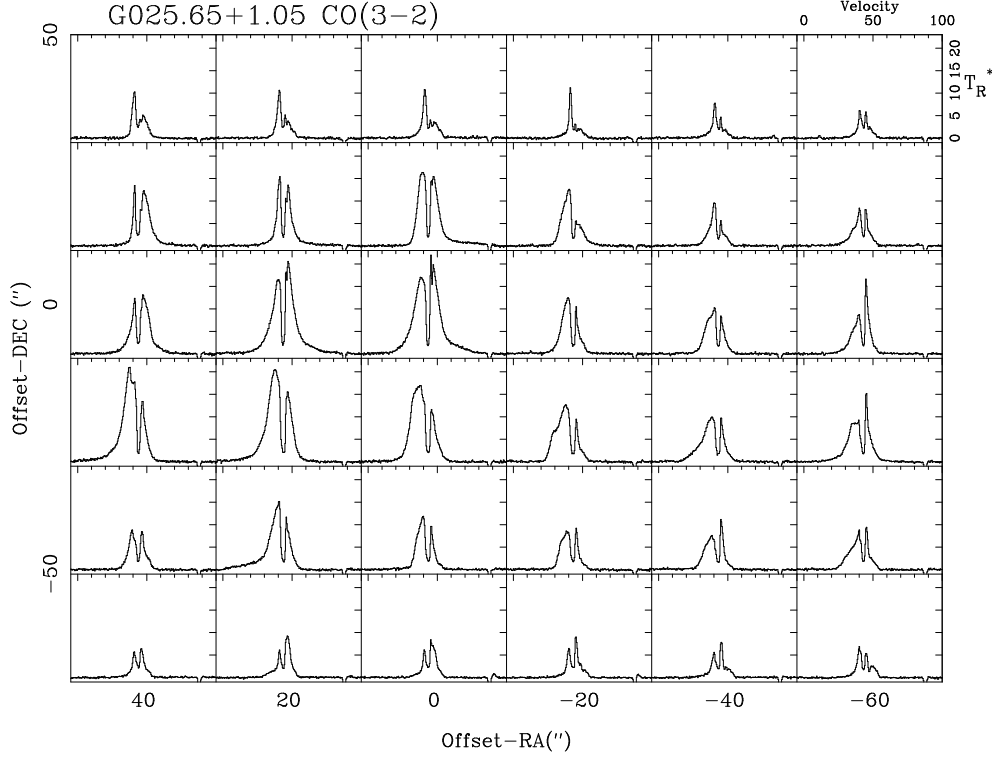


Figure 3.23 Map of the CO(3 $\rightarrow$ 2) line detected toward G025.6469+01.0534.

the center of the field. High-velocity gas emission is detected between  $86 \text{ km s}^{-1}$  toward the redshifted, and  $0 \text{ km s}^{-1}$  ( $v_{LSR}$ ) toward the blueshifted sides of the spectra. The absorption feature near  $v_{lsr} \approx 90 \text{ km s}^{-1}$  correspond to emission detected toward the off-position. We did not observe an optically thin line, thus it is difficult to determine an ambient cloud velocity. We take it at  $v_{LSR} = 42 \text{ km s}^{-1}$ , and select the inner limits of the velocity ranges symmetrically respect to this velocity.

A characteristic feature seen in all line profiles is an absorption line observed at  $\sim 43 \text{ km s}^{-1}$ . We suggest that this feature, common to all spectra, is due to absorption from a cooler and extended component, most likely associated with the larger molecular structure in which this core resides. The depth of the absorption is similar in all positions, reaching a value of  $\sim 3\text{-}4 \text{ K}$ . This is illustrated in Figure 3.25 which shows the maxima and minima envelope-curves among all spectra, in magenta and cyan, respectively. This Figure clearly shows that there is a cold absorbing and optically thick screen, at  $v_{LSR} \approx 43.5 \text{ km s}^{-1}$ , which varies very little across the CO map position, and has an excitation temperature of  $\sim 7\text{-}8 \text{ K}$ , consistent with the coldest parts of a molecular cloud.

Figure 3.24 shows the integrated CO(3 $\rightarrow$ 2) emission in the high-velocity ranges defined in Table 3.2, that also gives the peak values and positions of the blue and redshifted flows. The flow presents bipolar characteristics, with the peaks of the blue and red-shifted integrated emission separated by  $27.6''$  and aligned in the direction with position angle (P.A.)  $\sim 330^\circ$ . We also detected a faint blueshifted high velocity component extending toward the west.

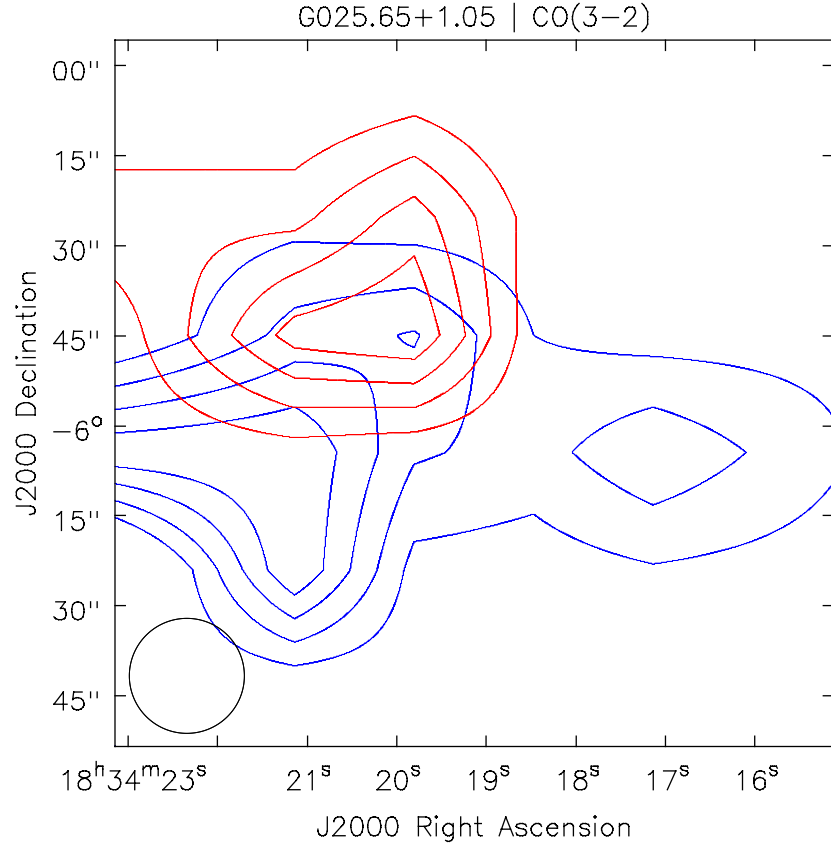


Figure 3.24 Contour map of the velocity integrated CO(3→2) line detected toward G025.6469+01.0534. Blue contours represent emission integrated over the blueshifted high-velocity range indicated in Table 3.2, and red contours represent the emission integrated over the redshifted high-velocity range. Contour levels are 20, 40, 60, and 80% of the peak emission. Peak blueshifted emission:  $24.8 \text{ K km s}^{-1}$ . Peak redshifted emission:  $35.6 \text{ K km s}^{-1}$ .

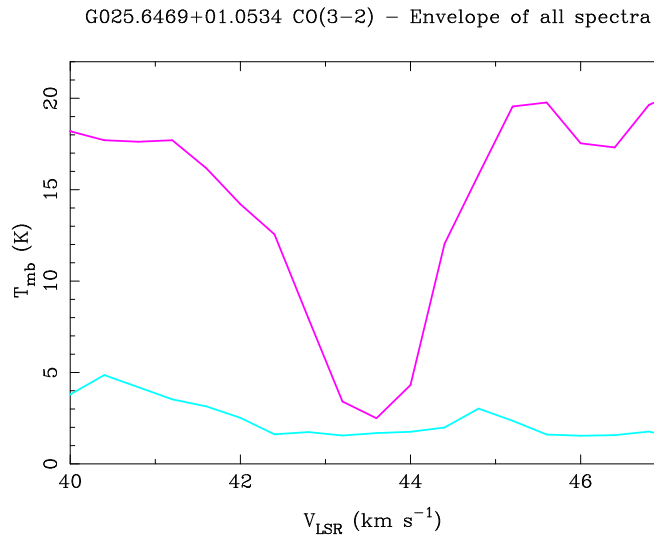


Figure 3.25 Maxima and minima-curves of all the spectra shown in Fig. 3.23, in magenta and cyan, respectively.

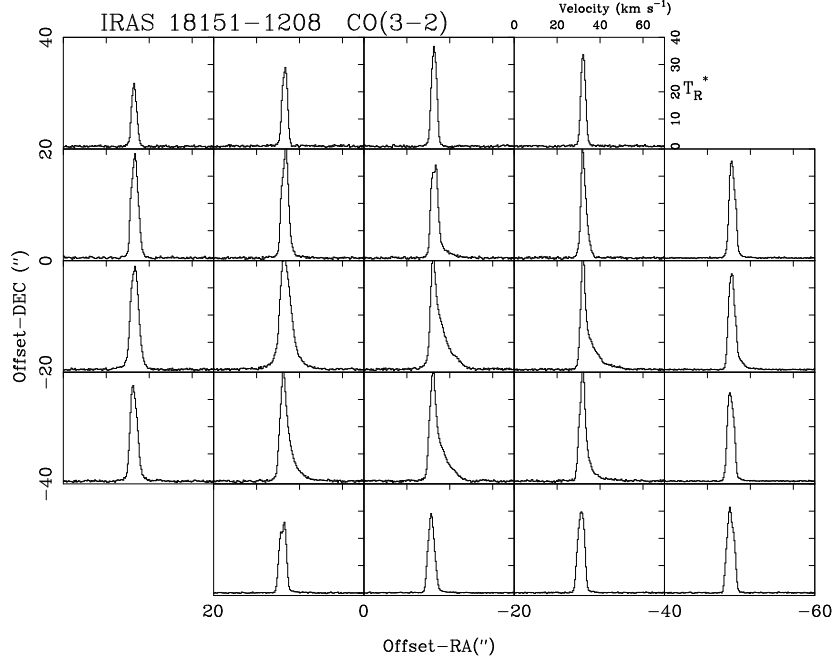


Figure 3.26 CO(3 $\rightarrow$ 2) emission detected toward IRAS 18151–1208.

### 3.2.2 Other HMYSO candidates

#### *IRAS 18151–1208.*

This source was selected due to its association with extended and collimated H<sub>2</sub> emission (Varricatt et al. 2010). The CO(3–2) emission was mapped within a region of  $100'' \times 100''$  (see Figure 3.26). Clearly seen towards the western part of the region is strong redshifted emission. The total velocity range of the emission detected is  $22.0 \text{ km s}^{-1} < v_{LSR} < 52.1 \text{ km s}^{-1}$ . Despite the presence of this high-velocity gas, emission in the SiO(8 $\rightarrow$ 7) line was not detected at the 0.08 K sigma level (see Fig. 3.27).

Figure 3.28 shows a contour map of the blueshifted and redshifted velocity integrated emission. The peak positions of the red and blue lobes are displaced by about  $20''$ . The map shown in Fig. 3.28 is consistent with the map shown in Beuther et al. (2002b), who observed this source in the CO(2 $\rightarrow$ 1) transition. They show an irregular outflow also aligned in the east-west direction. However, an important difference respect to the present work are the different velocity ranges adopted — the inner limits being specially relevant for mass estimations. Our estimation of the outflow mass is  $0.75 M_{\odot}$  and  $2.1 M_{\odot}$  for the blue and red lobes, respectively (see section 3.3.2). On the other hand, Beuther et al. (2002b) obtained 8 and  $4 M_{\odot}$  (blue and red). In order to check for data consistency, we calculate the masses using our data and their velocity intervals. They also corrected by an average line opacity, but not for low-velocity flow gas. By contrast, we correct for low-velocity gas, but not for opacity. Even though all these differences, we obtain masses of  $7.8$  and  $4.0 M_{\odot}$  for the blue and red flows, showing good data consistency between Beuther et al. and our work. Nevertheless, we think that our selection of the velocity intervals corresponds more closely to the outflow gas, and the velocity ranges selected by Beuther et al. (2002b) include too much “core” emission. Note that by inspection of the line profiles shown in Fig. 3.26, we expect the redshifted flow

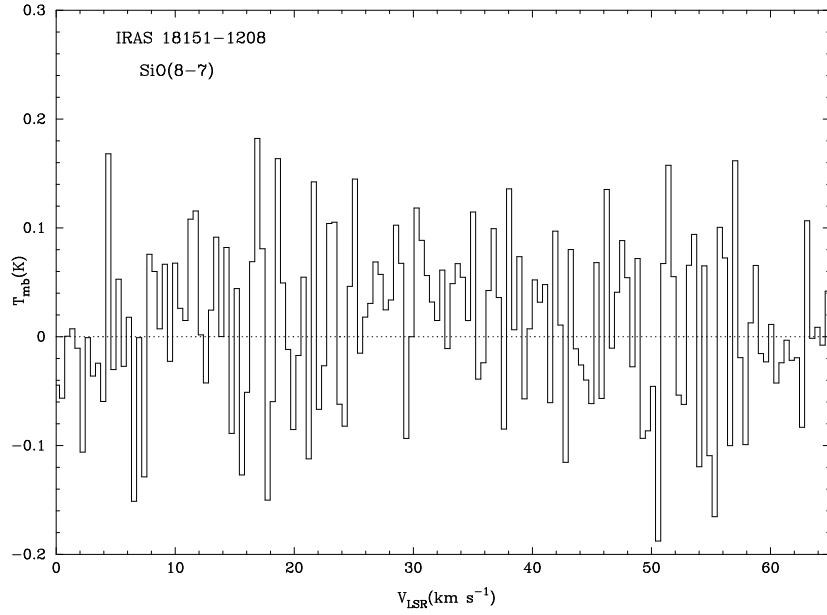


Figure 3.27 SiO(8→7) spectra observed toward IRAS 18151–1208.

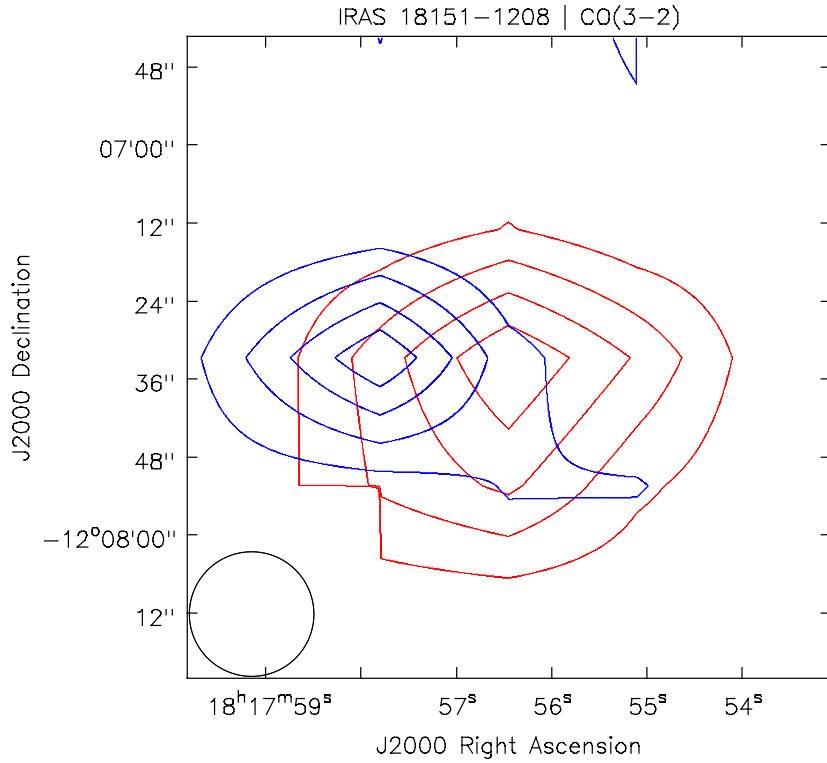


Figure 3.28 High-velocity CO(3→2) emission. Red and blue contours show the redshifted and blueshifted integrated temperature, and they correspond to the 20, 40, 60, and 80% of the peak. *Blue contours*: Velocity range ( $\text{km s}^{-1}$ ): [22.0, 26.0], Peak:  $4.4 \text{ K km s}^{-1}$ . *Red contours*: Velocity range ( $\text{km s}^{-1}$ ): [40.0, 52.1], Peak:  $31.6 \text{ K km s}^{-1}$ .

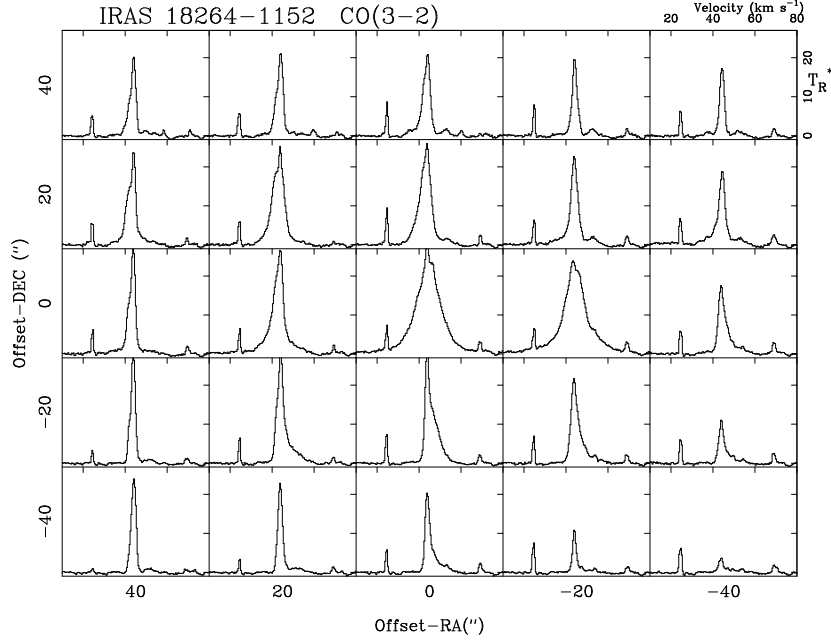


Figure 3.29 CO(3→2) spectra observed toward IRAS 18264–1152.

mass to be more than the blueshifted, which is an important qualitative feature that our results reproduce, but not the ones of Beuther et al. (2002b).

### ***IRAS 18264–1152.***

This source was selected due to its association with extended and collimated H<sub>2</sub> emission (Varricatt et al. 2010). We mapped the emission in the CO(3→2) line within a 100'' × 100'' region (see Fig. 3.29). Blueshifted and redshifted high velocity gas is detected toward the central position, and mostly redshifted gas toward south positions. The velocity adopted for the ambient cloud of  $v_{LSR} \approx 44.4 \text{ km s}^{-1}$  was taken as the peak of the spectrum detected at the  $\Delta\text{R.A.} = 40''$ ,  $\Delta\text{Dec} = -40''$  position, since here there is no more evidence of high-velocity wings. The total velocity range the line spans is  $17.0 \text{ km s}^{-1} < v_{LSR} < 73.7 \text{ km s}^{-1}$ , reaching radial velocities of  $\sim 28 \text{ km s}^{-1}$  respect to the ambient cloud. Despite the presence of this high-velocity molecular outflow, we do not detect any SiO(8→7) emission at the 0.11 K level (Figure 3.30).

As Figure 3.31 shows, the high velocity gas displays a symmetric distribution, with no spatial separation between the peaks of the blueshifted and redshifted emission, and no significant difference between the peak magnitudes either.

### ***G319.3993–00.0135.***

We mapped the CO(3→2) transition toward this HMYSO candidate within a region of 80'' × 80'' (Figure 3.32). The line profiles are Gaussian and do not show emission from high velocity wings. We conclude that there is no outflow activity in this region. The ambient cloud velocity is  $v_{LSR} = -11.8 \text{ km s}^{-1}$ .

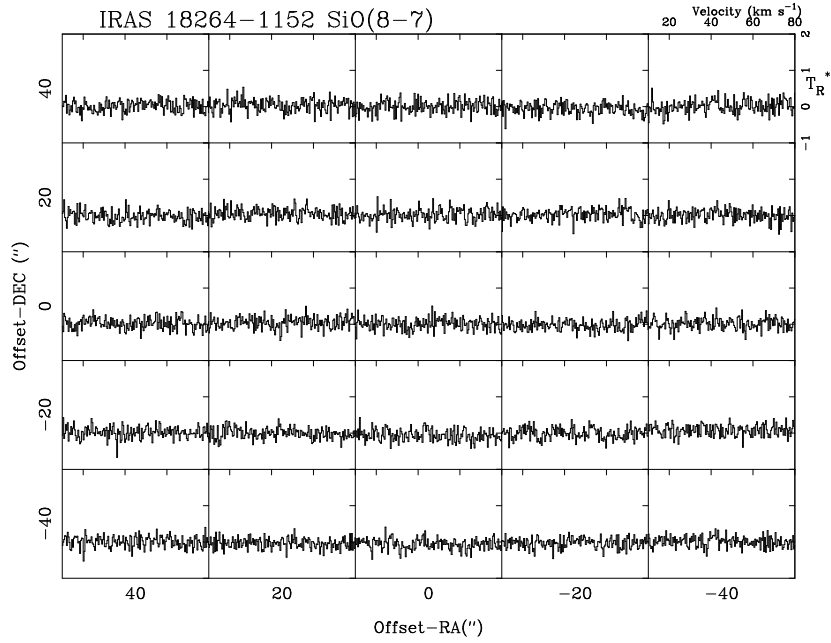


Figure 3.30 SiO(8→7) spectra observed toward IRAS 18264–1152.

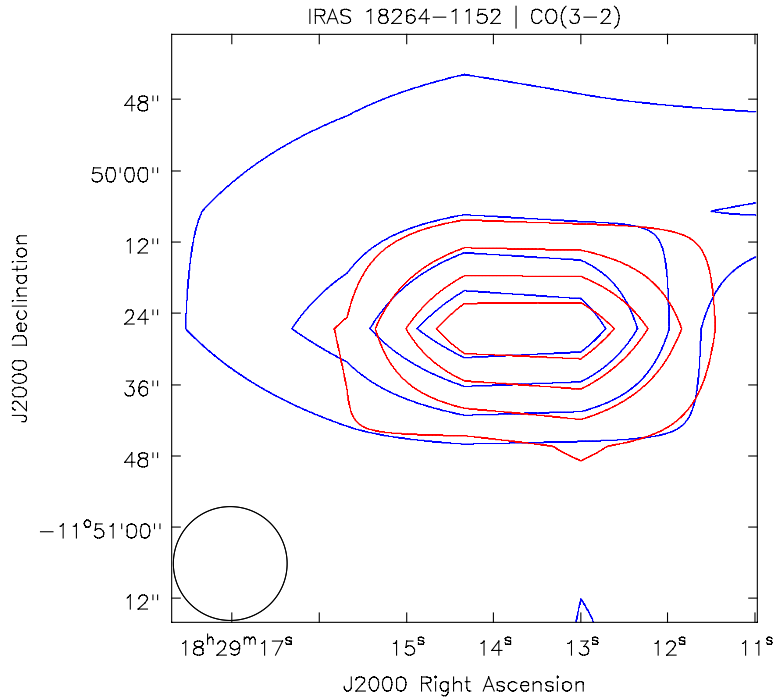


Figure 3.31 High-velocity CO(3→2) emission. Red and blue contours show the redshifted and blueshifted integrated temperature, and they correspond to the 20, 40, 60, and 80% of the peak. *Blue contours*: Velocity range ( $\text{km s}^{-1}$ ): [17.0, 34.0], Peak:  $37.6 \text{ K km s}^{-1}$ . *Red contours*: Velocity range ( $\text{km s}^{-1}$ ): [54.0, 73.7], Peak:  $39 \text{ K km s}^{-1}$ .

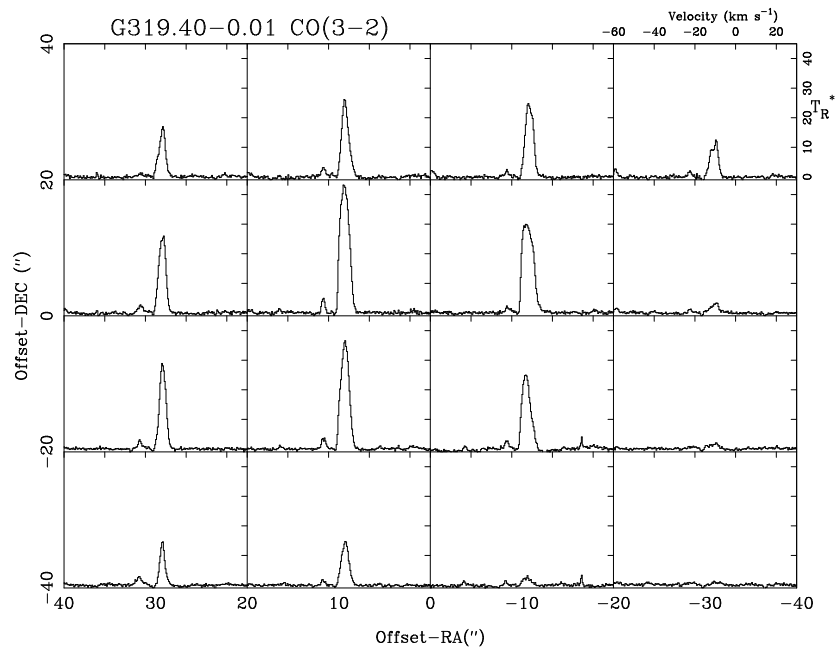


Figure 3.32 CO(3→2) emission detected toward G319.3993-00.0135. No high velocity gas is detected in these spectra.

***G332.8256–00.5498.***

Toward this HMYSO candidate, the CO(3→2) emission was mapped within a region of  $60'' \times 60''$  (see Figure 3.33). All spectra show complex self-absorbed profiles from several velocity components. The velocity range of the emission, including high-velocity wings detected toward the central spectrum, is  $-86.2 \text{ km s}^{-1} < v_{LSR} < -35.5 \text{ km s}^{-1}$ .

***G333.1306–00.4275.***

We mapped the CO(3→2) transition toward this HMYSO, which corresponds to one of the control sources observed with ATCA, within a region of  $60'' \times 60''$  (see Figure 3.34). The most striking features in the spectra are the strong and extended blueshifted emission and the sudden drop of the line emission at the velocity of  $\sim 50 \text{ km s}^{-1}$ . The line spans a total velocity range of  $-85.6 \text{ km s}^{-1} < v_{LSR} < -28.6 \text{ km s}^{-1}$ .

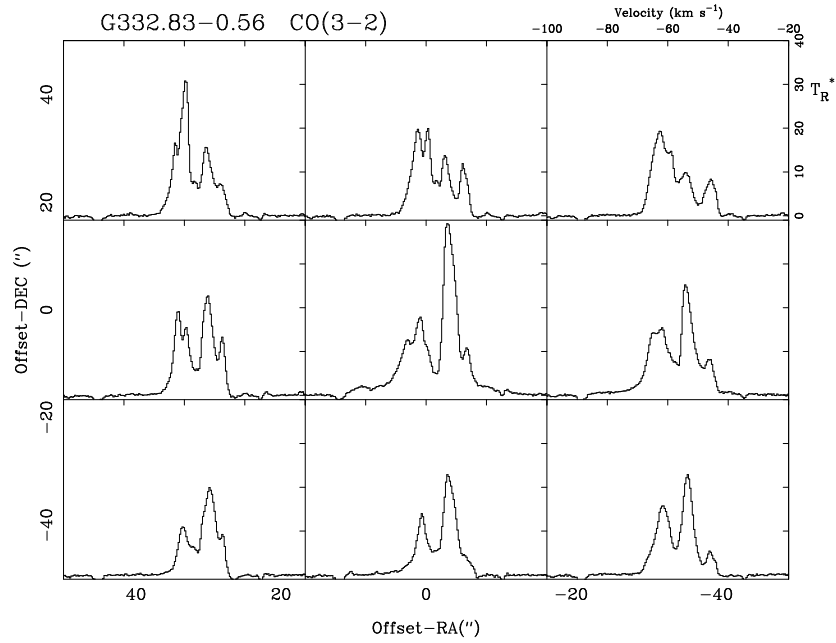


Figure 3.33 Spectra of the CO(3→2) transitions detected toward the source G332.8256–00.5498.

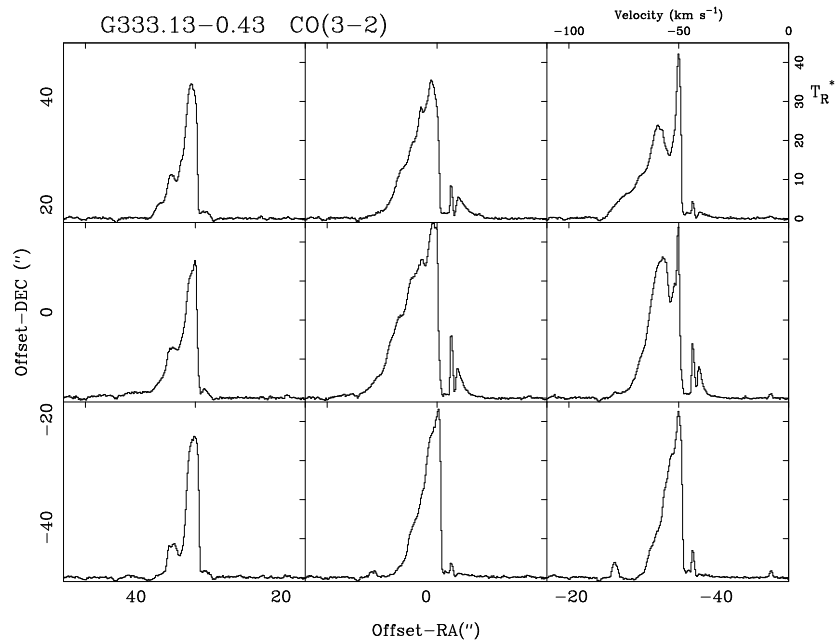


Figure 3.34 Spectra of the CO(3→2) transitions detected toward the source G333.1306–00.4275.

### 3.3 Derived parameters

In this section we present the derivation of physical parameters of the outflows (masses, momentum, momentum rates, energy), focusing on the properties of the outflows associated to the jet candidates. In §3.3.1 we describe the basic equations and in §3.3.2 we give the physical parameters of the flows. In §3.3.3 we give parameters of the cores harboring the HMYSOs, in particular of the opacities and masses computed using the emission in the CO isotopologues, the dynamical state of the large scale ambient material estimated using the  $\text{HCO}^+(4\rightarrow3)$  transition, and the presence and abundance of SiO.

#### 3.3.1 Basic relations

Extensive literature exists about the fundamentals of molecular line emission (Rank et al. 1971, Garden et al. 1991, Goldsmith & Langer 1999, Wilson et al. 2009). We present here the main formulae, stressing on the hypotheses used, their pertinence, and caveats. The standard formalism for our case is described in Bourke et al. (1997).

The first parameter to be determined is the mass of the outflow. Here, the principal hypothesis is that the high-velocity gas emission detected in the CO(3→2) line is optically thin. A general discussion of the sources of errors have been given by Margulis & Lada (1985), Cabrit & Bertout (1986) and Cabrit & Bertout (1990). The main source of error comes from the estimate of the contribution of gas which is moving at velocities between the inner limits of the high-velocity ranges defined in Table 3.2. To estimate this mass, we follow the prescription of Margulis & Lada (1985), which consist of replacing the spectrum by linear interpolation between the values in the inner limits of the velocity ranges.

The column density of CO molecules in the velocity range  $[v1, v2]$  is given by

$$N_{\text{CO}} = 2.31 \times 10^{14} \frac{(T_{\text{ex}} + hB/3k)}{1 - \exp(-h\nu/kT_{\text{ex}})} \frac{\exp(E_J/kT_{\text{ex}})}{(J+1)} \int_{v1}^{v2} \tau_v dv \quad \text{cm}^{-2}, \quad (3.1)$$

where  $T_{\text{ex}}$  is the rotational excitation temperature in K,  $J$  is the rotational quantum number of the lower state,  $E_J = hBJ(J+1)$  is the energy of level  $J$ ,  $B$  is the rotational constant of the CO molecule. The frequency of the CO( $J+1\rightarrow J$ ) transition is  $\nu \approx 2B(J+1)$ , and  $\tau_v$  is the opacity of the material moving at velocity  $v$ , the latter measured in  $\text{km s}^{-1}$ . Besides the assumptions implied in the quantum mechanics modeling of the CO molecule as a rigid linear rotor, the main assumptions of Equation (3.1) are:

- All the CO-column share a common excitation-rotational temperature. That is, the amount of CO molecules in a certain rotational energy level is given by the Maxwell-Boltzmann statistic with a unique excitational temperature. We call our assumption “single excitation temperature” (SET). Usually, this temperature is found to be higher in the outflow gas than in the bulk of the cloud, but unfortunately, G345.4938+01.4677 is the only source for which we probe the emission at several  $J$ , allowing us to constrain the excitational temperature. This analysis is made in Chapter 5. For most of the sources, we will use the value  $T_{\text{ex}} = 35$  K. Of course, SET need not to be strictly fulfilled to apply Equation 3.1, as long as the temperature chosen is representative or close to some opacity-averaged temperature of the flow.
- An implicit assumption is that  $N_{\text{CO}}$  represents molecules moving at systematic velocities

between  $v_1$  and  $v_2$ . This supposition is valid while this velocity interval is relatively large compared to the typical width of the emission line. The width is dominated by turbulent motions, and typically reaches  $\sigma \sim 1.2 \text{ km s}^{-1}$ . In our case, this is a safe assumption, since the velocity intervals are large ( $> 10 \text{ km s}^{-1}$ ).

The observed main-beam brightness temperature is related to the opacity by

$$T_{\text{mb}}^*(v) = \eta_{\text{ff}} [J_r(\nu, T_{\text{ex}}) - J_r(\nu, T_{\text{bg}})] (1 - e^{-\tau_v}) \quad , \quad (3.2)$$

where  $\eta_{\text{ff}}$  is the beam filling factor (or beam dilution factor) and  $J_r(\nu, T)$  is defined as

$$J_r(\nu, T) = \frac{h\nu/k}{\exp(h\nu/kT) - 1} \quad .$$

In the optically thin limit ( $\tau_v \ll 1$ ),

$$T_{\text{mb}}^*(v) = [J_r(\nu, T_{\text{ex}}) - J_r(\nu, T_{\text{bg}})] \eta_{\text{ff}} \tau_v \quad . \quad (3.3)$$

Some of the assumptions of equations (3.2) and (3.3) are: there is a single excitation temperature (SET) for all the CO and the emission is distributed in a fraction  $\eta_{\text{ff}}$  of the area of the molecular core covered by the instrument beam.

As evident from Equation (3.3), in the optically thin case it is not possible to disentangle the opacity from the filling factor. However, we can estimate the opacity of the line independently using another tracer molecule. A simple choice is to use a pair of isotopologue molecules, and the assumption that both molecules are distributed similarly is more justified. The molecules  $^{13}\text{CO}$  and  $\text{C}^{18}\text{O}$  have been widely used to this effect (e.g. Myers et al. 1983). In this work we use the  $^{13}\text{CO}(3 \rightarrow 2)$  and  $\text{C}^{18}\text{O}(3 \rightarrow 2)$  transitions. Equations (A2) and (A3) from Bourke et al. (1997) gives for the ratio of the temperatures

$$\frac{T_{\text{mb}}(^{13}\text{CO})}{T_{\text{mb}}(\text{C}^{18}\text{O})} = Q_1(T_{\text{ex}}) \frac{1 - \exp(-\tau_{13})}{1 - \exp(-\tau_{13}/r)} \quad , \quad (3.4)$$

$$r = \frac{\tau_{13}}{\tau_{18}} = Q_2(T_{\text{ex}}) \left[ \frac{^{13}\text{CO}}{\text{C}^{18}\text{O}} \right] \quad . \quad (3.5)$$

where  $T_{\text{mb}}$  are the main beam temperatures,  $T_{\text{ex}}$  is the excitation temperature,  $\tau_{13}$  and  $\tau_{18}$  are the line opacities of the  $^{13}\text{CO}(3 \rightarrow 2)$  and  $\text{C}^{18}\text{O}(3 \rightarrow 2)$  transitions, respectively.  $Q_1$  and  $Q_2$  are two factors that depends on the excitation temperatures, the background temperature (taken to be 2.73 K), the molecular dipoles and the frequencies of the transitions. However, under the case of two isotopologue molecules and the same ( $J+1 \rightarrow J$ ) transitions, they can be considered constant and equal to 1. Thus, Equation (3.5) implies that the ratio of the opacities ( $r$ ) is equal to the ratio of isotopic abundances. From the quotient of brightness temperatures and using Eq. (3.4), we can obtain the opacities, and then from Eq. (3.2) we can determine the filling factor ( $\eta_{\text{ff}}$ ). Under SET conditions, the ratio of the measured temperatures goes asymptotically to 1 when  $\tau \gg 1$ , and approaches the ratio of the opacities — the abundance ratio in our case — in the optically thin case. This behavior of the quotient exposes a problem with the method: if the opacities are too low or too high, it is very difficult to determine its actual value. We will avoid using the line quotient method in those cases.

In order to obtain an estimate of the total mass from of a particular molecular line, it is necessary to know their abundance ratio respect to  $\text{H}_2$ . For the molecules observed in this work, we adopt the following values:

$$\begin{aligned}
[\text{H}_2 : \text{CO} : {}^{13}\text{CO} : \text{C}^{18}\text{O}] &= 10^4 : 1 : \frac{1}{80} : \frac{1}{480} \quad , \\
[\text{HCO}^+/\text{H}_2] &\sim 10^{-9} \quad , \\
[\text{SiO}/\text{H}_2] &\approx 10^{-8} \quad (\text{strong shocks}) \\
&\sim 10^{-10} \quad (\text{High-mass hot cores}) \\
&\leq 10^{-12} \quad (\text{PDRs, quiescent dark clouds}) \quad .
\end{aligned}
\tag{3.6}$$

The  $[\text{H}_2/\text{CO}] = 10^4$  abundance ratio (Frerking et al. 1982) is widely used in the literature. The isotopic abundance of  $[{}^{12}\text{C}/{}^{13}\text{C}] = 80$  is taken according to the values found in the local ISM and in the Solar System (Wilson & Rood 1994, Langer 1997, Allen & Cox 2000). The isotopic molecular ratio  $[{}^{13}\text{CO}/\text{C}^{18}\text{O}] = 6$  is given only as an average since we estimate it from our data for each source. The values we found in this work are similar to the terrestrial ratio of 5.5 (Taylor & Dickman 1989). For estimating masses, we will use the CO molecules as tracers. The abundance ratio of  $\text{HCO}^+$  to  $\text{H}_2$  seems to be much more variable and uncertain than that of CO. We find in the literature variations over 2 orders of magnitude, ranging from  $10^{-10}$  to  $10^{-8}$  (see e.g. Lucas & Liszt 1994, Di Francesco et al. 2002). The value we take is close to the value assumed by De Vries & Myers (2005). We expect the relative abundance of SiO to vary according to the the presence of shocks. The values given in Eqs. (3.6) are taken from Miettinen et al. (2006).

An important process that diminishes the amount of carbonated molecules in dense environments is depletion onto dust grains. Within dense and cold star-forming cores, we expect that in the inner region the amount of CO (and its isotopologues) to decrease by a factor of 10 or more (Bacmann et al. 2002). While this effect is very important in infrared-dark clouds and quiescent cores, in our case a protostellar object is already formed and heats the environment. When the dust reaches the evaporation temperature ( $\sim 30$  K), the abundance ratio returns to its non-depleted value (Alonso-Albi et al. 2010).

### 3.3.2 Outflow parameters

Table 3.3 displays physical parameters derived for the sources that display high-velocity emission. Two rows per source display the parameters of the blue and redshifted gas, and are marked with a “B” and “R”, respectively. The “high-velocity” (HV) mass (Column 2 of Table 3.3) is calculated using equations (3.1), with the optically thin approximation (Eq. 3.3), assuming an excitation temperature of  $T_{ex} = 35$  K. This temperature is close to the values used in other studies of outflows (Beuther et al. 2002b). The third column gives the momentum associated to the high-velocity part of the spectrum, that was calculated using the first moment of the line emission (Calvet et al. 1983), and the fourth column shows the  $Mv^2$  parameter, associated to the high-velocity second moment. The n-th moment is defined by

$$\int T v^n dv$$

None of these last two quantities are corrected for any inclination effect. For a  $45^\circ$  inclination, the correction on the first and second moment are  $\sqrt{2}$  and 2, respectively. The “low-velocity” (LV) parameters (Columns 7 to 9) are calculated using the prescription of Margulis & Lada (1985) described in the previous section, using the same hypothesis that for the HV case. Finally, columns (10-12) list the sum of the HV and LV parameters. A more detailed analysis of the outflow detected toward G345.4938+01.4677 is presented in Chapter 5.

In the case of IRAS 18264–1152, G337.4032–00.4037, and G352.5173–00.1549, we find that there is non-negligible contamination within the outflow emission, probably due to gas intervening in the line of sight. We employ a procedure similar to that applied to the low-velocity gas correction, that is, we select velocity intervals where we think contamination exists and replace the spectrum with a linear interpolation. The following table lists the “contaminated” velocity ranges, and Table 3.3 lists the contamination-corrected parameters for these three sources:

Source	“Contaminated” intervals
IRAS 18264–1152	[+23.0, +26.0], [+67.0, +72.0]
G337.4032–00.4037	[−66.5, −59.1], [−78.4, −71.5], [−21.9, −18.8]
G352.5173–00.1549	[−28.6, −25.0]

We can see from Table 3.3 that most of the mass of the outflows comes from the low-velocity correction, but most of the momentum and second moment are due to the high-velocity gas. The momentum estimated in Table 3.3 is a lower limit due to the inclination correction, that amounts to a multiplication by a factor of  $\cos(i)^{-1}$ . We consider the inclination angle as the angle between the axis of the flow and the line of sight. The second moment inclination correction factor is evidently  $\cos(i)^{-2}$ .

We detect bipolarity, that is, we could spatially disentangle the red from the blueshifted emission, in the cases of G025.6469+01.0534, G305.7984–00.2416, G345.4938+01.4677, and IRAS 18151–1208. For these sources, Table 3.4 displays in col. (2) the angular separation in arcsecs between the peaks of the blue and redshifted integrated high-velocity emission (cols. (7) and (8) from Table 3.2). Column (3) displays the position angle considering the blue-to-red direction. Column (4) shows the characteristic size of the flow, which is simply half of the transverse distance subtended by the angular size. Column (5) displays the momentum rate calculated according to (Calvet et al. 1983)

$$\dot{P} = Mv^2/r_{\text{char}} \quad (3.7)$$

where  $Mv^2$  is the second moment of the spectrum (see Table 3.3) and  $r_{\text{char}}$  its characteristic radius. The inclination correction factor of the momentum rate is  $\sin(i)\cos(i)^{-2}$ .

### 3.3.3 Core parameters

In this section we discuss the derivation of some of the physical parameters of the cores from our molecular data.

#### 3.3.3.1 Total mass

Due to the uncertainties in the molecular parameters (excitation, abundance, depletion,

Table 3.3. Physical Parameters of the outflows

Source (1)	$T_{ex}$ (2)	Flow (3)	High-velocity			Low-velocity			Total		
			$M$ (4)	$P$ (5)	$Mv^2$ (6)	$M$ (7)	$P$ (8)	$Mv^2$ (9)	$M$ (10)	$P$ (11)	$Mv^2$ (12)
<b>Jet candidates</b>											
G305.7984–00.2416	35	B	0.52	7.21	109.	0.862	3.85	23.0	1.37	11.0	132.
	35	R	0.49	6.49	91.9	0.9	4.09	24.5	1.38	10.5	116.
G317.4298–00.5612	35	B	16.4	143.	1529.	20.4	46.5	139.	37.	190.	1669.
	35	R	10.1	69.	505.	19.	42.2	125.	29.1	110.	632.
G337.4032–00.4037	35	B	0.198	4.7	122.	0.293	2.18	21.6	0.491	6.88	144.
	35	R	0.509	18.3	782.	0.311	2.36	23.7	0.82	20.7	806.
G345.0061+01.7944	35	B	0.901	16.6	377.	1.62	8.90	61.7	2.53	25.5	441.
	35	R	0.219	3.9	78.4	0.750	3.01	17.6	0.970	6.91	96.1
G345.4938+01.4677 <sup>a</sup>	145	B	0.39	5.8	96.8	0.61	2.9	27.0	1.00	8.7	124
	120	R	0.27	3.5	49.5	0.65	3.1	29.3	0.92	6.6	78.8
G352.5173–00.1549	35	B	1.06	9.17	80.4	2.32	6.92	27.5	3.4	16.0	107.
	35	R	1.90	15.3	211.	2.41	7.31	29.3	4.32	22.6	240.
G025.6469+01.0534	35	B	1.38	31.1	769.	3.09	23.8	241.	4.48	55.0	1009.
	35	R	1.16	27.4	710.	2.61	18.9	186.	3.77	46.4	897.
<b>Other outflow and HMYSO candidates</b>											
IRAS 18151–1208	35	B	0.088	0.757	6.63	0.66	1.97	8.41	0.75	2.7	15.0
	35	R	0.884	9.23	103.	1.25	4.71	22.8	2.13	13.9	126.
IRAS 18264–1152	35	B	1.01	18.8	405.	2.26	10.5	68.5	3.28	29.4	474.
	35	R	0.924	13.6	232.	3.0	16.1	109.	4.01	29.8	342.
G333.1306–00.4275	35	B	4.17	85.5	1840.	7.57	62.1	648.	11.7	147.	2480.
	35	R	0.262	4.77	88.2	3.24	19.	162.	3.50	23.7	250.

Note. — Units of excitation temperature ( $T_{ex}$ ), mass ( $M$ ), momentum ( $P$ ), and mass times radial velocity squared ( $Mv^2$ ) are: K,  $M_{\odot}$ ,  $M_{\odot}\text{km s}^{-1}$ , and  $M_{\odot}(\text{km s}^{-1})^2$ , respectively.

<sup>a</sup>These parameters correspond to the SE-NW flow.

Table 3.4. Momentum rates and characteristic size of bipolar flows

Source (1)	Ang. Size ( $''$ ) (2)	P.A. ( $^{\circ}$ ) (3)	$r_{\text{char}}$ (pc) (4)	$\dot{P}$ $10^{-3} M_{\odot}\text{km s}^{-1}\text{yr}^{-1}$ (5)
G305.7984–00.2416	22.7	93	0.17	1.5
G345.0061+01.7944	18.1	5	0.08	7.4
G345.4938+01.4677	60	253	0.25	0.90
IRAS 18151–1208	20.5	270	0.15	0.97
G025.6469+01.0534	27.6	330	0.21	9.4

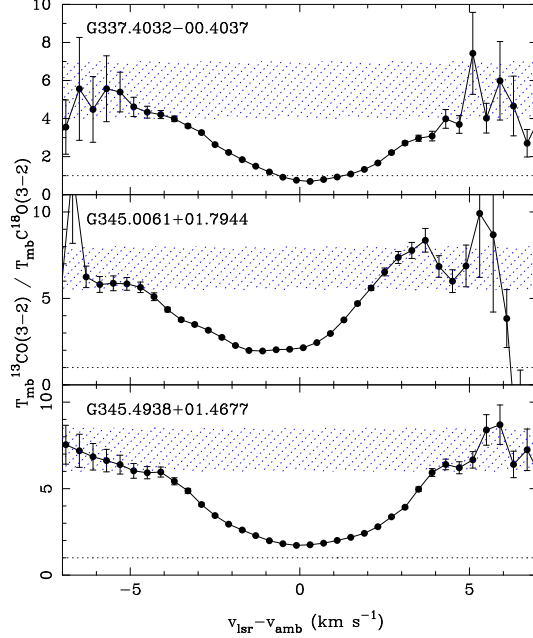


Figure 3.35 Quotient of the  $^{13}\text{CO}(3\rightarrow 2)$  and  $\text{C}^{18}\text{O}(3\rightarrow 2)$  lines detected toward the central position for G337.4032–00.4037 (top panel), G345.0061+01.7944 (middle panel), and G345.4938+01.4677 (bottom panel). The value of the molecular isotopic ratio lies within the blue hatched zones, which also marks the zone where we assume the  $^{13}\text{CO}(3\rightarrow 2)$  emission is optically thin.

etc...) and the difficulty to find an adequate optically thin tracer, millimetric continuum observations of cold dust seem to be better suited to determine the total mass rather than molecular line observations. Lackington (2011) made a study toward several of the jet candidates presented in this work, using  $870\ \mu\text{m}$  continuum data from the ATLASGAL survey (Schuller et al. 2009), made using the bolometer LABOCA in APEX.

There are three sources, G337.4032–00.4037, G345.0061+01.7944, and G345.4938+01.4677, toward which we observed CO molecular isotopologues. We find that the  $\text{C}^{18}\text{O}(3\rightarrow 2)$  transition was optically thin, and therefore the most adequate to trace the bulk of the mass. Using Equation (3.4) we were also able to determine the source filling factor of the emission, as well as the opacities. A first step to determine the masses is to determine the characteristic isotopic ratio of each core. We will use the quotient of the emission toward the high-velocity wings of the  $^{13}\text{CO}(3\rightarrow 2)$  and  $\text{C}^{18}\text{O}(3\rightarrow 2)$  lines, which are expected to be optically thin. Figure 3.35 displays this quotient. In accordance with Eq. (3.4), toward the high velocity ends the ratio tends to the optically thin limit value, that is, the *abundance ratio* [ $^{13}\text{CO}/\text{C}^{18}\text{O}$ ]. Therefore, from Fig. 3.35, we will take [ $^{13}\text{CO}/\text{C}^{18}\text{O}$ ] equal to 5 for G337.4032–00.4037, and 7 for G345.0061+01.7944 and G345.4938+01.4677. These values are consistent with the terrestrial ratio of 5.5. The hatched zones in Fig. 3.35 also mark the zones where we will assume that the  $^{13}\text{CO}(3\rightarrow 2)$  emission is optically thin. We also note that in the case of G337.4032–00.4037, the quotient reaches values below 1 near the line center, a result inconsistent with equation (3.4). This inconsistency is a consequence of the self-absorption of the  $^{13}\text{CO}(3\rightarrow 2)$  line (see Figure 3.10), and of the non-SET conditions. In consequence, we can not apply Eq. (3.4) near the line center on this source. It is also very difficult to apply this method when the opacities are low, because for one hand the uncertainty

in the ratio between both lines increases (Fig 3.35) and also the ratio stabilizes around a constant value. Therefore, for G337.4032–00.4037 we apply this method only when the ratio of both lines is between 1.5 and 4 (just below the hatched zone in Fig. 3.35), that is, between  $-44.6 \text{ km s}^{-1} \leq v_{LSR} \leq -42.3 \text{ km s}^{-1}$  and between  $-38.6 \text{ km s}^{-1} \leq v_{LSR} \leq -36.8 \text{ km s}^{-1}$ . The masses obtained in these two intervals is 81 and 24  $M_{\odot}$ , with filling factors of 0.2 and 0.1, respectively. Most of the mass of the core comes, however, from the central parts of the lines. Assuming that the  $\text{C}^{18}\text{O}(3\rightarrow 2)$  transition is optically thin, we can estimate the total mass using Eqs. (3.1), (3.3), and (3.3) adapted to  $\text{C}^{18}\text{O}(3\rightarrow 2)$ . This amounts to simply multiplying the right hand side of Eq. (3.1) by the abundance ratio  $[\text{CO}/\text{C}^{18}\text{O}] = 400$  and replacing the rotational constant  $B$  by the rotational constant of the isotope. The mass obtained is ( $T_{ex} = 30 \text{ K}$ ) is 1600  $M_{\odot}$ , in good agreement with the mass obtained from dust observations of 1350  $M_{\odot}$  by Lackington (2011).

For G345.4938+01.4677 the total mass obtained using Eq. (3.4) is 650  $M_{\odot}$  ( $\eta_{ff} \approx 0.3$ ). Using only the  $\text{C}^{18}\text{O}(3\rightarrow 2)$  lines, assuming optically thin conditions we obtain 830  $M_{\odot}$ . The dust mass determined by Lackington (2011) on the other hand is 727  $M_{\odot}$ .

For G345.0061+01.7944, the Eq. (3.4) method gives 35  $M_{\odot}$  ( $\eta_{ff} = 0.37$ ), and using only  $\text{C}^{18}\text{O}(3\rightarrow 2)$  it gives 38  $M_{\odot}$ .

### 3.3.3.2 Kinematical state

In this section we will analyze the evidence of large-scale core collapse based on the profile of moderately optically thick lines like  $\text{HCO}^+(4\rightarrow 3)$  and  $^{13}\text{CO}(3\rightarrow 2)$ .

We observed the  $\text{HCO}^+(4\rightarrow 3)$  line toward four sources (see Table 3.1), detecting the blue-asymmetry profile toward all of them except one (G352.5173–00.1549). This same spectral feature also appears in the  $^{13}\text{CO}(3\rightarrow 2)$  spectrum of G337.4032–00.4037. We also found red-asymmetry profiles associated to the  $\text{CO}(3\rightarrow 2)$  and  $^{13}\text{CO}(3\rightarrow 2)$  lines detected toward G345.0061+01.7944. A blue (red) peaked profile has long been interpreted in the literature as an indication of a infalling or contracting (expanding) motions (Hummer & Rybicki 1968, Leung & Brown 1977). The crucial characteristics of the model that explains this feature are two: moderately optically thick and non-SET conditions. To confirm that the first condition is met, that is, that the blue-asymmetry is caused in part by opacity, we observe an optically thin line that should display a single, symmetrical peak (e.g. Mardones et al. 1997). The non-STE condition is necessary to produce self-absorption at the frequencies of highest opacity. Since it is commonly assumed that the kinetic temperature is constant throughout the cloud, these effects are usually described as non-LTE effects. However, the crucial assumption would be more accurately described as non-SET. In principle, it would be possible that in a sufficiently dense medium (densities over the critical values) the populations are distributed according to LTE, but the cloud having a non-zero thermal gradient. In this case, there is no single excitation temperature, but the thermodynamic equilibrium is locally satisfied.

The blue-asymmetric lines can be reproduced satisfactorily if we consider the simple models presented in Myers et al. (1996) and De Vries & Myers (2005). Note that Equation (9) from De Vries & Myers (2005), should read:

$$\Delta T_B(v) = [J(T_P) - J(T_0)] \left[ \frac{1 - e^{-\tau_f(v)}}{\tau_f(v)} - e^{-\tau_f(v)} \frac{(1 - e^{-\tau_r(v)})}{\tau_r(v)} \right] + [J(T_0) - J(T_b)] [1 - e^{-\tau_r(v) - \tau_f(v)}] .$$

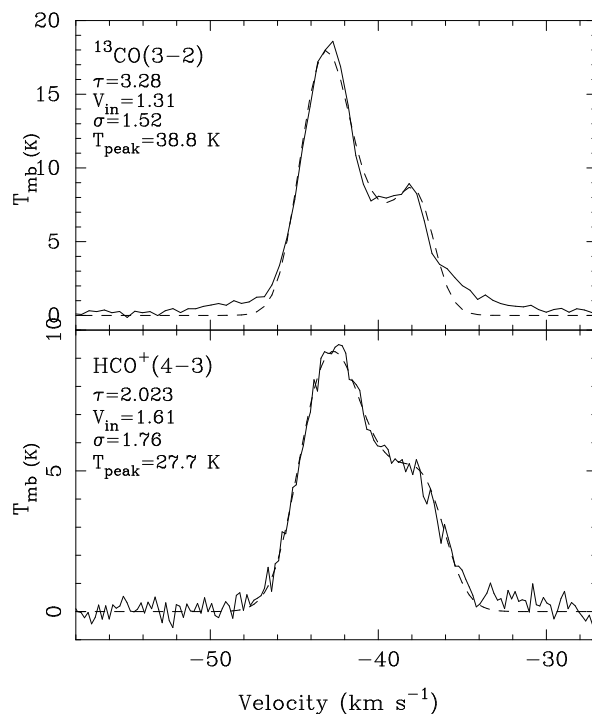


Figure 3.36 The first and second panel display in continuous line the central ( $\Delta R.A. = 0''$  and  $\Delta Dec. = 0''$ ) profiles of CO(3→2) and HCO<sup>+</sup>(4→3), respectively, and in dashed lines the best-fit infall models of De Vries & Myers (2005). Both fittings are reasonable, with good concordance between the kinematical parameters ( $V_{in}$  and  $\sigma$ ).

This equation gives the on-off difference brightness temperature measured between an homogeneous contracting cloud (on-position) and the background (off-position). In this equation, the excitation temperature in the cloud increases from a value  $T_0$  in the outer-edges to reach  $T_P$ , the peak excitation temperature, in the center. We take  $T_0 = T_b$ , the background temperature (2.73 K). The opacity  $\tau_f(v)$  correspond to that of the front (receding in the case of collapse) part of the cloud, and  $\tau_r(v)$  is the opacity of the rear (advancing in the case of collapse) part.

We apply the model of De Vries & Myers (2005) to the HCO<sup>+</sup>(4→3) and <sup>13</sup>CO(3→2) lines detected toward G337.4032–00.4037. Figure 3.36 shows the results of the fitting toward the spectra detected toward the position  $\Delta R.A. = 0''$ ,  $\Delta Dec. = 0''$ . The kinematic parameters are consistent for both fittings, giving mean turbulent linewidth of  $\sigma \approx 1.6$  km s<sup>-1</sup> and infall velocities of  $V_{in} \approx 1.5$  km s<sup>-1</sup>. We note that the HCO<sup>+</sup>(4→3) line has kinematical parameters somewhat larger than that associated to the <sup>13</sup>CO(3→2) line fitting, perhaps because it traces emission from deeper into the core, where we expect higher infall and turbulent velocities. Note also that the model in the <sup>13</sup>CO(3→2) line does not reproduce the wings of high velocity emission, related to the outflow. Considering that the core has a radius of 0.2 pc and a mass of 1350  $M_\odot$  (Lackington 2011), and that the infall velocity is 1.4 km s<sup>-1</sup>, we obtain a envelope mass infall rate of  $9.66 \times 10^{-3} M_\odot \text{ yr}^{-1}$ .

The source G345.0061+01.7944 is qualitatively different to the rest of the sample: its

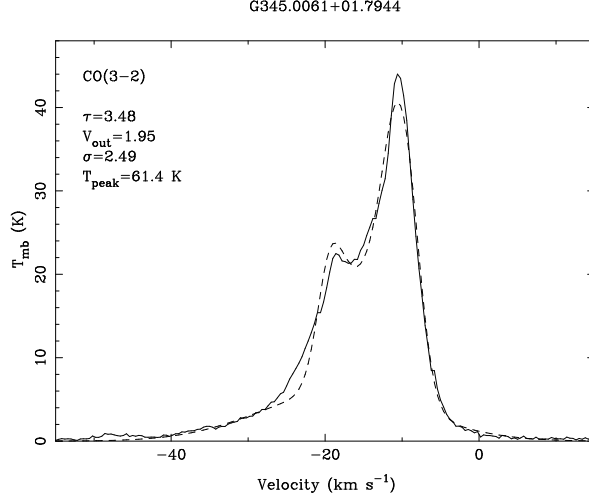


Figure 3.37 The continuous line show the central ( $\Delta$ R.A. =  $0''$  and  $\Delta$ Dec. =  $0''$ ) profile of CO(3 $\rightarrow$ 2). The dashed lines is best-fit of infall models of De Vries & Myers (2005) plus a gaussian component to take into account the high-velocity wings (FWHM $\approx$  24 km s $^{-1}$ ). Decent fit.

CO(3 $\rightarrow$ 2) line profiles (Fig. 3.14) have a very clear two-peaked red-asymmetric shape, indicative of core expansion. The shape of the  $^{13}\text{CO}(3\rightarrow 2)$  also displays red-asymmetry, while the  $\text{C}^{18}\text{O}(3\rightarrow 2)$  transition is much more symmetric, typical of optically thin emission (Fig. 3.16). We use the model of De Vries & Myers (2005) to fit the CO(3 $\rightarrow$ 2) line toward the central position, but we have to add a wide (FWHM $\approx$  24 km s $^{-1}$ ) gaussian component to take into account the high-velocity outflow gas. Figure 3.37 shows the result of this fit, which is acceptable, the largest differences are produced by the blueshifted outflowing gas. The kinematical parameters derived from the fit are  $V_{out} \approx 2$  km s $^{-1}$ ,  $\sigma = 2.5$  km s $^{-1}$ . This expansion feature is not confined to the central spectrum, but is seen toward most spectra in the central  $40'' \times 40''$ , evidencing a bulk expansion. Despite the fitting being acceptable, the parameters derived are not very reliable, specially the opacity which is likely to be underestimated. The reason are two: if the CO(3 $\rightarrow$ 2) opacity were  $\sim 3.5$ , i) it would imply a mass for the central position of only  $5.6 M_{\odot}$ , seven times less than the estimation made in §3.3.3.1; ii) we would expect that the opacity of the  $^{13}\text{CO}(3\rightarrow 2)$  line being at least 50 times less than the  $^{13}\text{CO}(3\rightarrow 2)$  (due to the abundance ratio), that is, about 0.07. In consequence, the  $^{13}\text{CO}(3\rightarrow 2)$  would be optically thin and would not show the red-asymmetric spectral feature. Nevertheless, the core is expanding. Approximately 10% of the low-mass star forming cores are observed to be in expansion (Lee & Myers 2011), but the causes are not clear .

The analysis of G345.4938+01.4677 is presented in Chapter 5.

### 3.3.3.3 SiO abundance ratios

We calculate the abundance ratio of SiO using SiO(8 $\rightarrow$ 7) observations toward 6 sources, 4 of them jet candidates. The hydrogen column densities were taken from Lackington (2011) for all jet sources, except G345.0061+01.7944. For this source, we used the  $\text{C}^{18}\text{O}(3\rightarrow 2)$  transition and the mass estimation of §3.3.3.1. For IRAS 18151–1208 and IRAS 18264–1152 we use the column densities from Beuther et al. (2002a). In all cases we assume that the SiO(8 $\rightarrow$ 7) line is

Table 3.5. SiO abundances

Source	N(SiO) ( $10^{12}$ cm $^{-2}$ )	N(H $_2$ ) ( $10^{22}$ cm $^{-2}$ )	[SiO/H $_2$ ]
(1)	(2)	(3)	(4)
G317.4298–00.5612	< 1.97	2.8	$< 7 \times 10^{-11}$
G337.4032–00.4037	13.6	22.	$6.7 \times 10^{-11}$
G345.0061+01.7944	2.70	7.6	$3.6 \times 10^{-11}$
G345.4938+01.4677	35.0	19.	$1.8 \times 10^{-10}$
IRAS 18151–1208 <sup>a</sup>	< 3.30	22.	$< 1.5 \times 10^{-11}$
IRAS 18264–1152 <sup>a</sup>	< 9.00	80	$< 1.2 \times 10^{-11}$

<sup>a</sup>The H $_2$  column density was taken from Beuther et al. (2002a), but corrected by a factor of 1/2 according to Beuther et al. (2005).

optically thin, and their rotational energy distribution population is described by a Maxwell-Boltzmann relation with  $T_{ex} = 50$  K. Considering  $T_{ex} = 100$  K changes the estimations in  $\sim 7\%$ .

Table 3.5 shows the results. The abundance ratios are low compared to the shocked emission zones, but this is somewhat expected since we are comparing the SiO column with the total column density of the core. In case of no detection, we calculate an upper bound by multiplying the noise level by the entire velocity range of the CO(3 $\rightarrow$ 2) line.

### 3.4 Conclusions

We mapped the CO(3 $\rightarrow$ 2) transition toward 8 jet candidates from the list presented in Table 2.1, with  $\sim 17''$  resolution. We detect high velocity wings indicative of outflow activity toward 7 of them. For these sources, the mean, standard deviations, maximum, and minimum of the velocity ranges, masses, radial momentum and energy ( $E = Mv^2/2$ ) of the flows are displayed in Table 3.6. When comparing these parameters with the outflows studied by Beuther et al. (2002b) and Zhang et al. (2005), we note:

- The outflow gas detected in jet candidates spans larger velocity ranges by  $\sim 20$  km s $^{-1}$  on average.
- The mean mass of the outflows of this sample is  $2.6 M_{\odot}$ . The mean mass of the outflows presented in Beuther et al. (2002b) and Zhang et al. (2005) are  $10 M_{\odot}$  and  $20 M_{\odot}$ , respectively. However, these values are not statistically representative due to the large dispersions of the samples, reaching  $100 M_{\odot}$  for Beuther et al. and  $25 M_{\odot}$  for Zhang et al. samples. Anyway, the mean outflow mass detected by Beuther et al. (2002b) and Zhang et al. (2005) are larger than that of our sample by an order of magnitude.
- The momenta measured by us are also about an order of magnitude smaller than that of Beuther et al. (2002b), but note that they use the maximum velocity to estimate

Table 3.6. Jet candidates outflow statistics

Parameter (1)	Mean (2)	Deviation (3)	Min (4)	Max (5)
Velocity Range (km s <sup>-1</sup> )	63.7	27	36.3	116
Mass ( $M_{\odot}$ )	2.6	11	0.5	37
Momentum ( $M_{\odot}\text{km s}^{-1}$ )*	19.6	53	6.6	191
Energy ( $M_{\odot}\text{km}^2\text{s}^{-2}$ )*	118	239	37.4	840

\*These parameters are calculated without inclination correction.

them, while we use the first moment of the optically thin part of the line. Considering this correction, our sample has a smaller average momentum only by a factor of  $\sim 2$ .

- The mean kinetic energy of the jet candidate sample and that of Beuther et al. (2002b) and Zhang et al. (2005) samples are consistent, being the ones associated to our jet candidates slightly larger by a factor of  $\sim 2$ .

The samples are similar in kinematic parameters, but they are quite different in other respects: while the Beuther et al. (2002b) and Zhang et al. (2005) sample are very massive outflows, our sample consist of less massive flows, but with higher velocities. We also could detect bipolarity only in 4 candidates.

The latter considerations, namely larger velocities and smaller sizes, are evidences that the sample of outflows presented in this study are somewhat younger than the ones in the reference works of Beuther et al. (2002b) and Zhang et al. (2005). We will analyze the link of the present study to ionized collimated jets in Chapters 5 and 6.

## Chapter 4

# A collimated jet toward G345.4938+01.4677

We report the discovery made using the Australia Telescope Compact Array of a remarkable aligned radio emission towards G345.4938+01.4677 (IRAS 16562–3959), a luminous infrared source with a bolometric luminosity of  $7.0 \times 10^4 L_{\odot}$ . The radio emission arises from a compact, bright central component, two inner lobes, which are separated by about  $7''$  and symmetrically offset from the central source, and two outer lobes which are separated by about  $45''$ . The emission from the central object has a spectral index between 1.4 and 8.6 GHz of  $0.85 \pm 0.15$ , consistent with free-free emission from a thermal jet. The radio emission from the lobes have spectral indices in the range characteristic of thermal emission. We suggest that the emission from the lobes arises in shocks resulting from the interaction of a collimated wind with the surrounding medium. The radio string is located within a massive dense molecular core, and is associated with extended green emission (Spitzer 3-color), Herbig-Haro type emission (2MASS  $K_s$ -band) and OH maser sites – all phenomena readily observed towards sites of high-mass star formation. We conclude that the massive core hosts a high-mass star in an early stage of evolution in which it is undergoing the ejection of a powerful collimated stellar wind, showing that jets found in the formation of low-mass stars are also produced in high-mass stars.

---

Based on the work published in Guzmán et al. (2010) and reproduced by permission of the AAS.

## 4.1 Introduction

The determination whether high-mass stars are formed via accretion or via merging processes is one of the main observational challenges in the field of star formation. If high-mass O-type stars are formed by an accretion process similar to that inferred for low-mass stars, then we expect that circumstellar disks and jets will be present in their earliest stages of evolution.

To date there are only a handful of high-mass young stellar objects (YSO) known to be associated with highly collimated jets and/or Herbig-Haro (HH) objects. All except one have luminosities smaller than  $2 \times 10^4 L_{\odot}$  corresponding to that of a B0 ZAMS star. They include IRAS 18162–2048 ( $L \sim 1.7 \times 10^4 L_{\odot}$ ; Martí et al. 1993); Cepheus A HW2 ( $L \sim 1 \times 10^4 L_{\odot}$ ; Rodríguez et al. 1994); IRAS 20126+4104 ( $L \sim 1.3 \times 10^4 L_{\odot}$ ; Cesaroni et al. 1997); G192.16–3.82 ( $L \sim 3 \times 10^3 L_{\odot}$ ; Shepherd et al. 1998; Devine et al. 1999; Shepherd et al. 2001); and W75N, which contains several molecular and HH outflows powered by at least four late to early-B protostars (Shepherd et al. 2003). There is only one YSO with  $L > 2 \times 10^4 L_{\odot}$  that is associated with a highly collimated jet (IRAS 16547–4247,  $L \sim 6.2 \times 10^4 L_{\odot}$ ; Garay et al. 2003; Rodríguez et al. 2005; Brooks et al. 2007; Rodríguez et al. 2008). Two other luminous YSOs, IRAS 18089–1732 ( $L \sim 3.2 \times 10^4 L_{\odot}$ ; Beuther & Walsh 2008) and G331.51–0.10 ( $L \sim 1 \times 10^5 L_{\odot}$ ; Bronfman et al. 2008), are associated with radio continuum sources with spectral indices characteristic of collimated stellar winds, but the angular resolution of the observations is insufficient to resolve the jet/flow morphology. It is not clear whether the lack of young high-mass stars with spectral types earlier than B0 ZAMS associated with jets and/or disks is an intrinsic property of the most massive stars or due to observational disadvantages – high-mass stars are rarer and their evolutionary time scales are much shorter than those of low mass stars.

We report the discovery, made using the Australia Telescope Compact Array (ATCA), of a string of radio continuum emission associated with G345.4938+01.4677 (also IRAS 16562–3959). Assuming that this source is located at the distance of 1.6 kpc ( $V_{\text{LSR}} = -12.6 \text{ km s}^{-1}$ , Urquhart et al. 2008b)<sup>1</sup>, the total far-infrared luminosity, computed using the observed IRAS fluxes (see Casoli et al. 1986), is  $\sim 7.0 \times 10^4 L_{\odot}$ . The target was selected from a list of sources compiled by us with IRAS luminosities in excess of  $2 \times 10^4 L_{\odot}$  and radio emission much weaker than that expected from the total FIR luminosity. The expectation is that objects with these characteristics are high-mass objects in the pre-UC H II region phase, in which the weak radio emission is most likely arising from stellar wind phenomena (see Fig. 6 from Hoare et al. 2007). G345.4938+01.4677 was observed as part of the RMS Survey (Urquhart et al. 2008a). The emission detected at 4.8 and 8.6 GHz with ATCA (Urquhart et al. 2007a) was weaker than expected. Moreover, the positive radio spectral index between these two frequencies and the hint of a string of multiple sources gave us strong indications that this source could be an ionized jet associated with a high-mass young stellar object (HMYSO).

We present in this Chapter ATCA data taken at 4 frequencies (1.4, 2.4, 4.8 and 8.6 GHz). Based on these data, we propose that the string of five radio sources detected towards G345.4938+01.4677 is composed of a central thermal jet, plus inner and outer lobes of shock ionized gas resulting from the interaction of the highly collimated stellar wind with the surrounding medium.

---

<sup>1</sup>The two-fold distance ambiguity was resolved in Faúndez et al. (2004)

## 4.2 Observations

The radio continuum observations were made using the Australia Telescope Compact Array (ATCA)<sup>2</sup> during 2008 June, October and 2009 February. We used the 1.5B, 1.5C and 6.0A configurations, utilizing all six antennas and covering east-west baselines from 30 m to 5.9 km. Observations were made at four frequencies: 1.384, 2.368, 4.800 and 8.640 GHz, each with a bandwidth of 128 MHz, full Stokes. Throughout this work we will refer to these frequencies as 1.4, 2.4, 4.8, and 8.6 GHz, respectively. The phase center of the array was RA = 16<sup>h</sup>59<sup>m</sup>41<sup>s</sup>.61, DEC = -40°03'43".4 (J2000). The total integration time at each frequency was about 180 minutes, obtained from 10-minute scans taken over a wide range of hour angles to provide good (u,v) coverage. The calibrator PKS 1740-517 was observed for 3 min. before and after every on-source scan in order to correct the amplitude and phase of the interferometer data for atmospheric and instrumental effects as well as to calibrate the bandpass.

The flux density was calibrated by observing PKS 1934-638 (3C84) for which values of 14.95, 11.59, 5.83, and 2.84 Jy were adopted at 1.4, 2.4, 4.8, and 8.6 GHz, respectively. Standard calibration and data reduction were performed using MIRIAD (Sault et al. 1995). Maps were made by Fourier transformation of the uniformly weighted interferometer data. The noise level achieved in the images are 0.38, 0.21, 0.096, and 0.070 mJy beam<sup>-1</sup> and the synthesized (FWHM) beams obtained were 10.23"×5.71", 5.97"×3.27", 2.81"×1.83", and 1.62"×1.01", at the frequencies of 1.4, 2.4, 4.8, and 8.6 GHz, respectively. We estimate the flux uncertainty to be approximately 20%.

## 4.3 Results

Figure 4.1 shows maps of the radio continuum emission from G345.4938+01.4677 at the four frequencies observed with ATCA. The maps at the lower frequencies (1.4 and 2.4 GHz) show three sources roughly lying in a linear structure along a direction with P.A. of 99.1°. The outermost sources which we will call Outer-East and Outer-West, labeled O-E and O-W in Fig. 4.1, respectively, are separated by an angular distance of  $\sim 45''$  (corresponding to 0.35 pc at 1.6 kpc). The maps at the higher frequencies (4.8 and 8.6 GHz) show that the central object seen at low frequencies is resolved into three components aligned along a direction with P.A. 98.9°. The external components of this triplet, which we will call Inner-East and Inner-West components (labeled I-E and I-W) are symmetrically located in opposite directions from the bright central source (labeled C), and separated by  $\approx 7''$ . Throughout this work, we will use the abbreviations C, I-E, I-W, O-E, and O-W for the Central, Inner-East, Inner-West, Outer-East, and Outer-West components, respectively.

We note that the five radio components are not exactly aligned, exhibiting a small bending. The lines joining the east components and the central source and the west components and the central source form an angle of 168°. We also note that in the 8.6 GHz image there are three small knots located about 4" north from the Outer-East lobe, with peak fluxes of 0.6 mJy. The knots are well aligned with the Inner and Central components suggesting that they could be part of a string of emission, but more sensitive observations are needed to confirm

---

<sup>2</sup>The Australia Telescope Compact Array is funded by the Commonwealth of Australia for operation as a National Facility managed by CSIRO

Table 4.1. Observed Parameters of Radio Sources

Source	8.6 GHz peak position		Flux density (mJy)			
	$\alpha(2000)$	$\delta(2000)$	1.4 GHz	2.4 GHz	4.8 GHz	8.6 GHz
Central (C)	16 <sup>h</sup> 59 <sup>m</sup> 41 <sup>s</sup> .63	−40° 03′ 43″.61	2.0 ± 1.0	4.2 ± 0.8	8.1 ± 0.2	12.1 ± 0.2
Inner-East (I-E)	16 59 41.87	−40 03 44.55	5.4 ± 0.9	7.0 ± 0.7	6.3 ± 0.2	5.7 ± 0.1
Inner-West (I-W)	16 59 41.35	−40 03 42.94	5.3 ± 0.9	6.7 ± 0.7	5.8 ± 0.2	3.3 ± 0.2
Outer-East (O-E)	16 59 44.07	−40 03 52.21	9.7 ± 0.3	5.2 ± 0.2	9.0 ± 0.3	7.6 ± 0.4
Outer-West (O-W)	16 59 39.83	−40 03 41.90	4.0 ± 0.7	8.0 ± 0.5	6.2 ± 0.2	3.9 ± 0.3

this or disprove as artifacts of the data reduction. We will not discuss these components further in this work.

The position and flux densities of all radio components detected towards G345.4938+01.4677 are given in Table 4.1. For all sources the flux densities were determined from Gaussian fittings using the MIRIAD task IMFIT, with the exception of the outer components at 4.8 and 8.6 GHz. For these, the flux density was measured over the  $3\sigma$  contour level. To estimate the flux densities of the C, Inner-East and Inner-West components at 1.4 and 2.4 GHz we fitted the observed morphology with three unresolved Gaussians centered at the positions determined from the 8.6 GHz observations.

Figure 4.2 shows the SED of the integrated radio continuum emission from the five components. Also plotted in the spectra of the central component are the values reported by Urquhart et al. (2007a) at 4.8 and 8.6 GHz of 4.8 and 12.5 mJy, respectively. We find that the radio continuum spectra of component C is well fitted by a power law spectrum ( $S_\nu \propto \nu^\alpha$ , where  $S_\nu$  is the flux density at the frequency  $\nu$ ), with an spectral index  $\alpha$  of  $0.85 \pm 0.15$ . For the other components the data were fitted using a model of thermal emission from a homogeneous region of ionized gas. The parameters EM and  $\Omega$ , emission measure and solid angle, are given in each panel.

## 4.4 Discussion

### 4.4.1 The nature of the radio sources

The spectral index of the radio continuum emission from component C, of  $0.85 \pm 0.15$ , indicates free-free emission arising from a thermal jet. Theoretical calculations show that collimated stellar winds can have spectral indices in the range 0.25 to 1.1 depending on the radial dependence of the physical quantities of the jet (Reynolds 1986). They also predict that the angular size depends with frequency. However, the angular resolution of our observations does not allow us to investigate this dependence and observations with higher angular resolution are needed to resolve the jet.

Assuming that the Central source is a bipolar, pressure confined jet, which has an spectral index of 0.84, Eqs. (13) and (19) of Reynolds (1986) yield, for a distance of 1.6 kpc and an observed flux density at 8.6 GHz of 12.1 mJy, the following constraints on the jet physical

parameters:

$$\left( \frac{n_{\text{jet}}(r)}{10^6 \text{ cm}^{-3}} \right) = 1.32 \left( \frac{r}{10^{-3} \text{ pc}} \right)^{-0.9} \left( \frac{\nu_m}{10 \text{ GHz}} \right)^{0.818} \left( \frac{\theta}{0.2} \right)^{-0.7} \left( \frac{\sin i}{\sin 45^\circ} \right)^{0.3} \quad (4.1)$$

$$\left( \frac{\dot{M}_w}{10^{-6} M_\odot \text{ yr}^{-1}} \right) = 2.8 \left( \frac{v_w}{10^3 \text{ km s}^{-1}} \right) \left( \frac{\nu_m}{10 \text{ GHz}} \right)^{0.18} \left( \frac{\theta}{0.2} \right)^{3/4} \left( \frac{\sin i}{\sin 45^\circ} \right)^{-1/4}, \quad (4.2)$$

where  $n_{\text{jet}}(r)$  is the number density of the jet at a distance  $r$  from the HMYSO,  $\nu_m$  is the turnover frequency,  $\theta$  the opening angle at the base of the jet,  $i$  the inclination angle with respect to the line of sight,  $v_w$  the wind velocity and  $\dot{M}_w$  is the mass loss rate. Most of these parameters are unknown. In deriving these expressions, in addition to the observational constraint, we assumed an ionization fraction of 1 and a temperature of 8000 K at the base of the jet; and a mean particle mass of  $1.3 m_H$  per hydrogen atom.

The degree of collimation of the jet source can be estimated from the size of the lobes and their distance to the central component. Using the data obtained for the East and West outer lobes we derive that  $\theta \sim 0.2$  radians. Assuming that  $v_w$  is  $500 \text{ km s}^{-1}$ , a value typical of jets associated with luminous objects (Anglada 1996, Martí et al. 1998, Curiel et al. 2006, Rodríguez et al. 2008), then the constraint equation (4.2) implies that the mass loss rate is  $\sim 1.4 \times 10^{-6} M_\odot \text{ yr}^{-1}$ .

If the total luminosity of G345.4938+01.4677 is produced by a ZAMS star it would correspond to an O8 star, which emits a rate of ionizing photons of  $2.2 \times 10^{48} \text{ s}^{-1}$  (Panagia 1973). Embedded in a constant density medium, this star would generate an H II region with a flux density of  $\sim 8.4 \text{ Jy}$  at optically thin radio frequencies, far in excess of the observed value of  $\sim 10 \text{ mJy}$ . We suggest that the weak radio emission from the central source is a consequence of G345.4938+01.4677 undergoing an intense accretion phase, with the central object still being in the pre-UCH II region sequence phase. The high-mass accretion rate of the infalling material forbids the development of a sizeable H II region (Yorke 1979, Walmsley 1995), and the free-free emission from the ionized material is considerably lowered at centimeter wavelengths.

The spectra of the radio emission from the lobes are rather flat, indicative of optically thin free-free emission. We suggest that the radio emission from the lobes arises in shocks resulting from the interaction of a collimated stellar wind with the surrounding medium. The dotted lines in Fig. 4.2 correspond to fits of the observed spectra using a model of thermal emission from a homogeneous region of ionized gas. From these fits we derive emission measures of  $\sim 1 \times 10^6 \text{ pc cm}^{-6}$  towards the inner lobes and  $\sim 1 \times 10^5 \text{ pc cm}^{-6}$  towards the outer lobes. For all lobes the emission is optically thin within the range of observed frequencies. The solid angles were derived from the radio images giving  $3.7$ ,  $0.8$ ,  $25$ , and  $15 \text{ arcsec}^2$  for the Inner-East, Inner-West, Outer-East and Outer-West lobes, respectively. The derived electron densities within the lobes are about  $\sim 10^3 \text{ cm}^{-3}$  for the outer lobes and  $\sim 10^4 \text{ cm}^{-3}$  for the inner lobes.

#### 4.4.2 Characteristics of the exciting source and its environment

The string of sources is associated with a massive ( $\sim 1.0 \times 10^3 M_\odot$ ) and dense ( $1.2 \times 10^6 \text{ cm}^{-3}$ ) core detected at 250 GHz (1.2 mm) by Faúndez et al. (2004), with the Central component

offset from the millimeter continuum peak by  $\sim 13''$ , equivalent to 0.1 pc at 1.6 kpc.

Figure 4.3 shows that associated with the dust core there is strong diffuse  $K_s$  band emission, centered near the Central source and aligned along the jet axis. This emission extends  $\sim 1.5'$  in the East and West directions. There is also diffuse  $K_s$  band emission arising from two regions located  $\sim 3'$  towards the North and South of the Central source. They are roughly symmetrically displaced from the Central source but aligned in a perpendicular direction to the jet axis. The strong  $K_s$  band emission is likely to be produced by excited  $H_2$   $2.12 \mu\text{m}$  emission arising from shocked gas. Moreover, the arc-like morphology of the northern  $K_s$  band emission feature located approximately at RA =  $16^{\text{h}}59^{\text{m}}42^{\text{s}}$ , DEC =  $-40^{\circ}00'13''$  (J2000) is also consistent with HH phenomena. We note that the North-South structure is also seen as diffuse mid-infrared emission in the four MSX bands (8.28, 12.13, 14.65, and  $21.34 \mu\text{m}$ ), indicating also a strong contribution from warm (and perhaps reflected) dust emission.

Figure 4.4 shows a zoom in of the  $8 \mu\text{m}$  emission from Spitzer and  $K_s$  band emission from 2MASS towards the central part of the core. There is an extended “V” shape feature extending along the East jet axis seen in both  $K_s$  band and  $8 \mu\text{m}$ . In addition, there are three OH masers (Caswell 1998, 2004): one is associated with the central source, a second is associated with a  $8 \mu\text{m}$  source, unseen in 2MASS, located  $\sim 15''$  northeast of the central source and the third is located close to the East jet axis at about  $2''$  from the Outer-East lobe. Their velocities are close to the radial velocity of the ambient cloud ( $V_{\text{LSR}} = -12.6 \text{ km s}^{-1}$ , Urquhart et al. 2008b), except for the eastern OH maser, which has a radial velocity of  $-24.5 \text{ km s}^{-1}$ . Infrared continuum emission at  $10.4 \mu\text{m}$  is shown in Fig. 4.5, which displays an image<sup>3</sup> obtained by Mottram et al. (2007). It shows intense emission associated with the Central source and more diffuse emission associated with the Inner-East radio lobe. There is also an extended  $4.5 \mu\text{m}$  emission enhancement associated to the central source (see Fig. 4.6). These “green fuzzies”, as seen green in a three color IRAC images, have been related to shocked gas in protostellar environments (Chambers et al. 2009). All of the phenomena described above is readily associated with high-mass star formation and therefore support the notion that G345.4938+01.4677 is a high-mass young stellar object with energetic outflow activity.

While the East-West  $K_s$  band structure can be related directly to the radio jet, the identification of the energy source of the North-South  $K_s$  band feature is less clear. One possibility is that the North-South feature is driven by the Central jet source, which will imply a re-orientation of the jet in almost  $90^\circ$ . Models of close stellar encounters do not, however, predict such large precession of the outflow axis (e.g. Moeckel & Bally 2006), and thus this possibility appears unlikely. Since high-mass YSOs are known to be formed in clusters, the most plausible explanation is that a yet unidentified nearby source is the exciting source of the North-South  $K_s$ -band emission. A possible candidate is the YSO, located  $16''$  north-east of the Central component, identified from the Spitzer data. As pointed out previously, this object is associated to an OH maser with a radial velocity similar to that of the ambient cloud. This and the Central source belong thus to the same star forming region, as suggested by Caswell (1998).

Figure 4.7 shows the spectral energy distribution (SED) of G345.4938+01.4677 from  $3.6 \mu\text{m}$  to  $1200 \mu\text{m}$ , including flux densities at 1.2 millimeter (Faúndez et al. 2004); at 12, 25, 60,

---

<sup>3</sup>Downloaded from <http://www.ast.leeds.ac.uk/RMS/>

Table 4.2. SED FITTING

Parameter	Value
Inclination	41°
Stellar Age	$4.5 \times 10^4$ yr
Stellar Mass	$14.7 M_{\odot}$
Envelope accretion rate	$3.4 \times 10^{-3} M_{\odot} \text{ yr}^{-1}$
Disk Mass	$0.26 M_{\odot}$
Disk accretion rate	$5.5 \times 10^{-4} M_{\odot} \text{ yr}^{-1}$
Total Luminosity	$5.8 \times 10^4 L_{\odot}$
Envelope Mass	$1.7 \times 10^3 M_{\odot}$

and  $100 \mu\text{m}$  obtained from the IRAS database; at  $8.3$ ,  $12.1$ ,  $14.7$ , and  $21.3 \mu\text{m}$  obtained from the *Midcourse Space Experiment (MSX)* Survey of the Galactic Plane database (Price et al. 2001, MSX source G345.4938+01.4677), and at  $3.6$  and  $4.5 \mu\text{m}$  obtained from Spitzer-IRAC images using an aperture of  $\sim 1'$ . The IRAC images at  $5.8$  and  $8.0 \mu\text{m}$  data were saturated and an adequate flux estimation was not possible. In the frequency range covered by the SED the emission is mainly due to thermal dust emission. The spectral energy distribution was analyzed by fitting model SEDs using a large grid of precomputed models (Robitaille et al. 2007). The continuous line in Fig. 4.7 presents the result of the best fit. The derived parameters from the fit are given in Table 4.2. The SED fitting indicates that the energy source corresponds to a deeply embedded YSO, and rules out the possibility of being a heavily extincted star.

The mass of the host envelope derived from the fitting is  $\sim 1700 M_{\odot}$ . However, the model of Robitaille et al. (2007) does not consider the increase of absorption at mm frequencies due to ice coatings in the dust grains (Ossenkopf & Henning 1994) and in consequence is probably overestimating the mass of the envelope by a factor of 2 or 3. Therefore, the mass of the core derived from the  $1.2 \text{ mm}$  observations of  $910 M_{\odot}$  is in fair agreement with the SED fitting. We note that Faúndez et al. (2004) reported a mass of  $1500 M_{\odot}$ , but a new analysis of the data shows that for this particular source an erroneous calibration factor was applied, which produced an overestimation of the flux density by a factor of 1.76 (López et al. 2011).

The fitting also indicates that the central YSO has a mass of  $\sim 15 M_{\odot}$  and a luminosity of  $5.8 \times 10^4 L_{\odot}$ , that the envelope is undergoing an intense accretion phase with a rate of  $3.4 \times 10^{-3} M_{\odot} \text{ yr}^{-1}$  and that the accretion rate onto the central object is  $5.5 \times 10^{-4} M_{\odot} \text{ yr}^{-1}$ . The derived stellar parameters are similar to those of a B0~O9.5 main sequence star (Sternberg et al. 2003) and a O8.5 ZAMS star (Panagia 1973). We also note that the derived infall accretion rate is greater than  $\sim 1.0 \times 10^{-5} M_{\odot} \text{ yr}^{-1}$ , the infall rate needed to quench the development of a sizeable H II region (Walmsley 1995).

The linear morphology and spectral characteristics of the radio sources suggest that the string is physically associated with a highly collimated wind arising from a young, high-mass YSO with the lobes tracing the interaction between the jet and the ambient cloud. We postulate that the lobes radio emission corresponds to thermal emission coming from shocked

ionized gas situated in the working surfaces of the Central jet source. Particularly, we rule out the possibility that the radio emission has an extragalactic origin – the probability of finding an extragalactic source at 5 GHz with a flux density above 5 mJy within  $20''$  from the peak of the 1.2 mm dust emission is  $3.5 \times 10^{-4}$  (Fomalont et al. 1991).

### 4.4.3 Jet and Shock parameters

In this section we make use of the observed quantities of the lobe emission to derive parameters of the jet-ambient medium interaction. Considering that the free-free emission from the lobes arises from a shock wave formed at the head of the jet, then the emission measure, EM, is given in terms of shock parameters by (Curiel et al. 1993)

$$\left( \frac{\text{EM}}{10^6 \text{ pc cm}^{-6}} \right) = 1.39 \left( \frac{n_a}{10^5 \text{ cm}^{-3}} \right) \left( \frac{V_s}{100 \text{ km s}^{-1}} \right)^{1.68} \left( \frac{T_e}{10^4 \text{ K}} \right)^{0.8}, \quad (4.3)$$

where  $n_a$ ,  $V_s$  and  $T_e$  are the particle ambient density, the shock velocity and the temperature of the shock-ionized gas. If the ambient density is known, this expression can be used to estimate the shock velocity.

To estimate the ambient density at the position of the lobes we re-analyzed the 1.2-mm data taken by Faúndez et al. toward G345.4938+01.4677 and fitted the observed radial intensity profiles from the core region using a model in which the density and temperature follow power-law radial distributions (Adams 1991). The best fit to the image was obtained with the following molecular gas density and temperature profiles:  $n_a(r) = n_0(0.1 \text{ pc}/r)^{1.9}$  and  $T(r) = T_0(0.1 \text{ pc}/r)^{0.4}$ , where  $n_0 = 1.4 \times 10^5 \text{ cm}^{-3}$  and  $T_0 = 50 \text{ K}$ . We assumed a gas to dust mass ratio of 100 and a mean molecular mass of  $2.3 m_H$ . The derived density profile implies that the mass of the core, within a radius of  $\sim 90''$ , is  $790 M_\odot$ , and that the ambient density at the position of the East and West inner lobes – displaced from the core center by  $10''$  and  $18''$  – are  $2.3 \times 10^5$  and  $7.6 \times 10^4 \text{ cm}^{-3}$ , respectively. Using these densities and the emission measures computed in §4.3, we derive from Eq. (4.3) that the shock velocities at the East and West inner lobes are 119 and 91  $\text{km s}^{-1}$ , respectively. The same analysis applied to the East and West outer lobes gives shock velocities of  $\sim 24$  and  $\sim 66 \text{ km s}^{-1}$ , respectively, consistent with the expectation that shock velocity should decrease away from the jet source.

Assuming a simple one dimensional isothermal shock model (e.g. Masson & Chernin 1993) and that the momentum flux imparted to the shock ionized material by the jet equals the ram pressure of the ambient material, then

$$(V_j - V_s)^2 \rho_j = V_s^2 \rho_a, \quad (4.4)$$

where  $\rho_j$  and  $V_j$  are the mass density and velocity of the jet, respectively, and  $\rho_a$  is the ambient gas mass density. If the shock velocity, ambient density and jet density are known this expression can be used to estimate the jet velocity. The density of the jet at the positions of the inner lobes can be estimated from Eq. (4.1). The lobes are displaced from the jet by  $3''$ , which translates into a physical distance of 0.033 pc, assuming an inclination of  $45^\circ$ . Using  $\theta=0.2$  and assuming  $\nu_m=10 \text{ GHz}$ , then the density of the jet at 0.033 pc is  $1.2 \times 10^{-19} \text{ gr cm}^{-3}$ , about  $\sim 4$  times lower than the ambient density. Using the values derived for the East and West inner lobes of the shock velocity, ambient density and jet density we determine from Eq. (4.4) jet velocities of 360 and 280  $\text{km s}^{-1}$ , respectively.

We further estimate that the most recent ejection, giving rise to the inner lobes, took place between 90 and 120 years ago. Moreover, from Eq. (4.2) and taking again 10 GHz as the turnover frequency, we derive mass loss rates of 1.0 and  $0.79 \times 10^{-6} M_{\odot} \text{ yr}^{-1}$ , which in combination with the ejecta velocities give momentum rates of  $3.7 \times 10^{-4}$  and  $2.2 \times 10^{-4} M_{\odot} \text{ km s}^{-1} \text{ yr}^{-1}$  for the East and West halves of the bipolar jet, respectively.

## 4.5 Summary

We made radio continuum observations at 1.4, 2.4, 4.8 and 8.6 GHz, using ATCA, toward G345.4938+01.4677, a luminous object ( $L \sim 7 \times 10^4 L_{\odot}$ ) thought to be a high-mass star forming region in an early stage of evolution. The main results and conclusions are summarized as follows:

1. The radio continuum observations show the presence of a remarkable string of radio emission, consisting of a compact, bright central component, two inner lobes, separated by about  $7''$  and symmetrically located from the central source, and two outer lobes, separated by about  $45''$ .
2. The emission from the central object has a spectral index between 1.4 and 8.6 GHz of  $0.85 \pm 0.15$ , consistent with free-free emission from a thermal jet. Assuming that the jet corresponds to a bipolar pressure confined wind with an aperture angle  $\theta = 0.2$ , we estimate that the jet has a total mass loss rate of  $\sim 1 \times 10^{-6} M_{\odot} \text{ yr}^{-1}$ . Guzmán et al. (2010) gives  $\sim 2 \times 10^{-6} M_{\odot} \text{ yr}^{-1}$  instead of this last number, adding together the estimations (made at the end of §4.4.3) from the east and west halves of the *bipolar* jet. However, the same radio flux density was used for each estimation, and the consistent procedure should have been to separate the flux density from the unresolved central source. Nevertheless, considering the systematic errors of the data only —not to mention the model assumptions— the uncertainty in the mass loss rate could reach a factor of 4.
3. The radio emission from the lobes have spectral indices of typically  $-0.1$ , characteristic of thermal emission. We suggest that the emission from the lobes arises in shocks resulting from the interaction of a collimated wind with the surrounding medium.
4. The string is found projected towards a massive and dense core and associated with several indicators of high-mass star formation and shock gas tracers. The jet is located near the peak position of the dust emission. We conclude that the massive core hosts a high-mass star in an early stage of evolution in which it is undergoing the ejection of a powerful collimated stellar wind, showing that jets found in the formation of low-mass stars are also produced in high-mass stars.

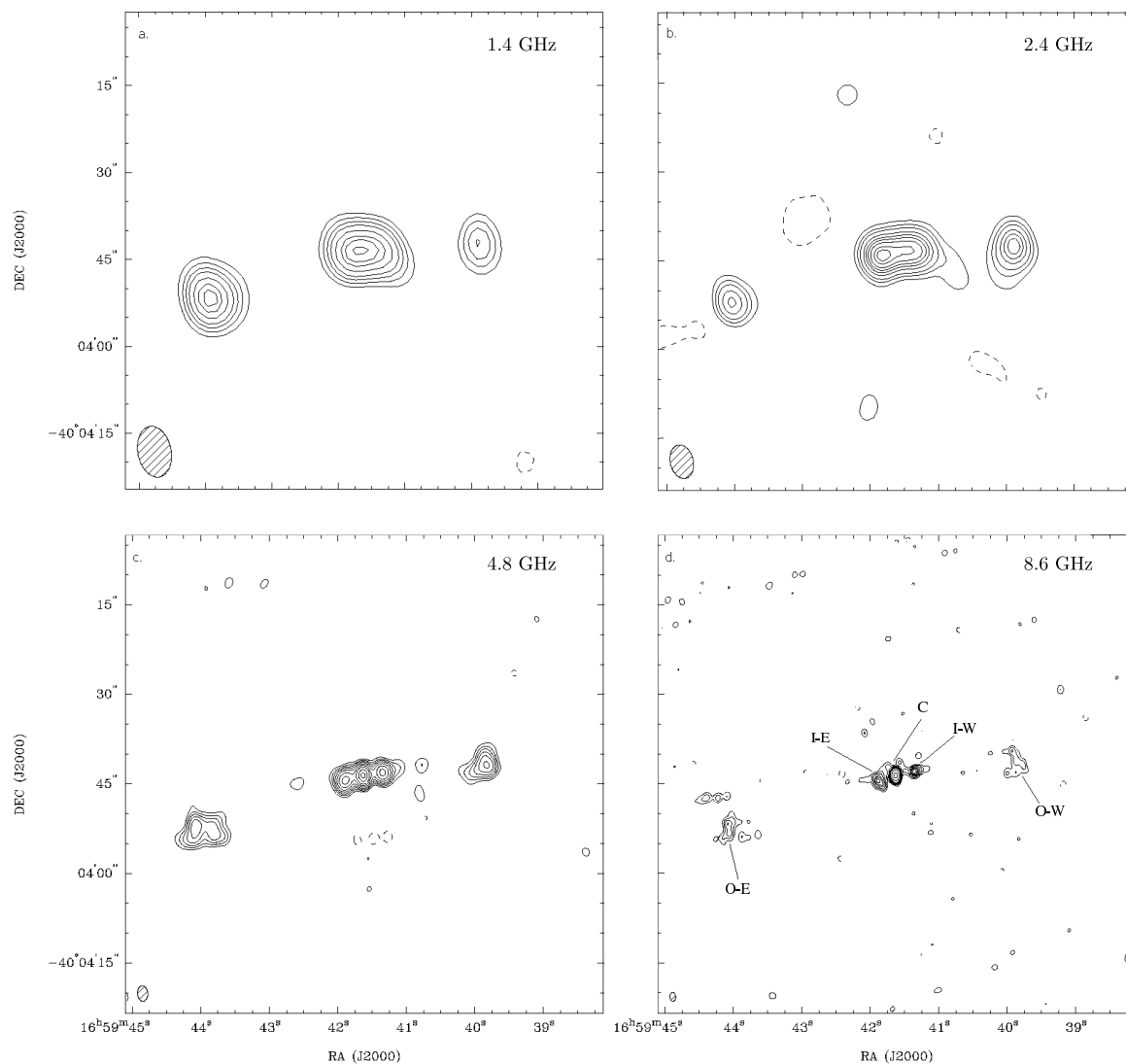


Figure 4.1 ATCA maps of the radio continuum emission from G345.4938+01.4677. Beams are shown in the lower left corner of each panel. Top left: 1.4 GHz map. Contour levels are  $-4, 4, 6, 8, 10, 13, 16, 18,$  and  $20$  times  $\sigma$  ( $1\sigma = 0.35$  mJy beam $^{-1}$ ). Top right: 2.4 GHz map. Contour levels are  $-7, 7, 12, 17, 25, 32, 38, 45, 54,$  and  $60$  times  $\sigma$  ( $1\sigma = 0.12$  mJy beam $^{-1}$ ). Bottom left: 4.8 GHz map. Contour levels are  $-4, 3, 6, 9, 13, 19, 28, 40, 60,$  and  $80$  times  $\sigma$  ( $1\sigma = 0.086$  mJy beam $^{-1}$ ). Bottom right: 8.6 GHz map. Contour levels are  $-4, 3, 6, 9, 13, 16, 19, 24, 50,$  and  $100$  times  $\sigma$  ( $1\sigma = 0.081$  mJy beam $^{-1}$ ). The synthesized (FWHM) beams obtained were  $10.23'' \times 5.71'', 5.97'' \times 3.27'', 2.81'' \times 1.83'',$  and  $1.62'' \times 1.01'',$  at the frequencies of 1.4, 2.4, 4.8, and 8.6 GHz, respectively.

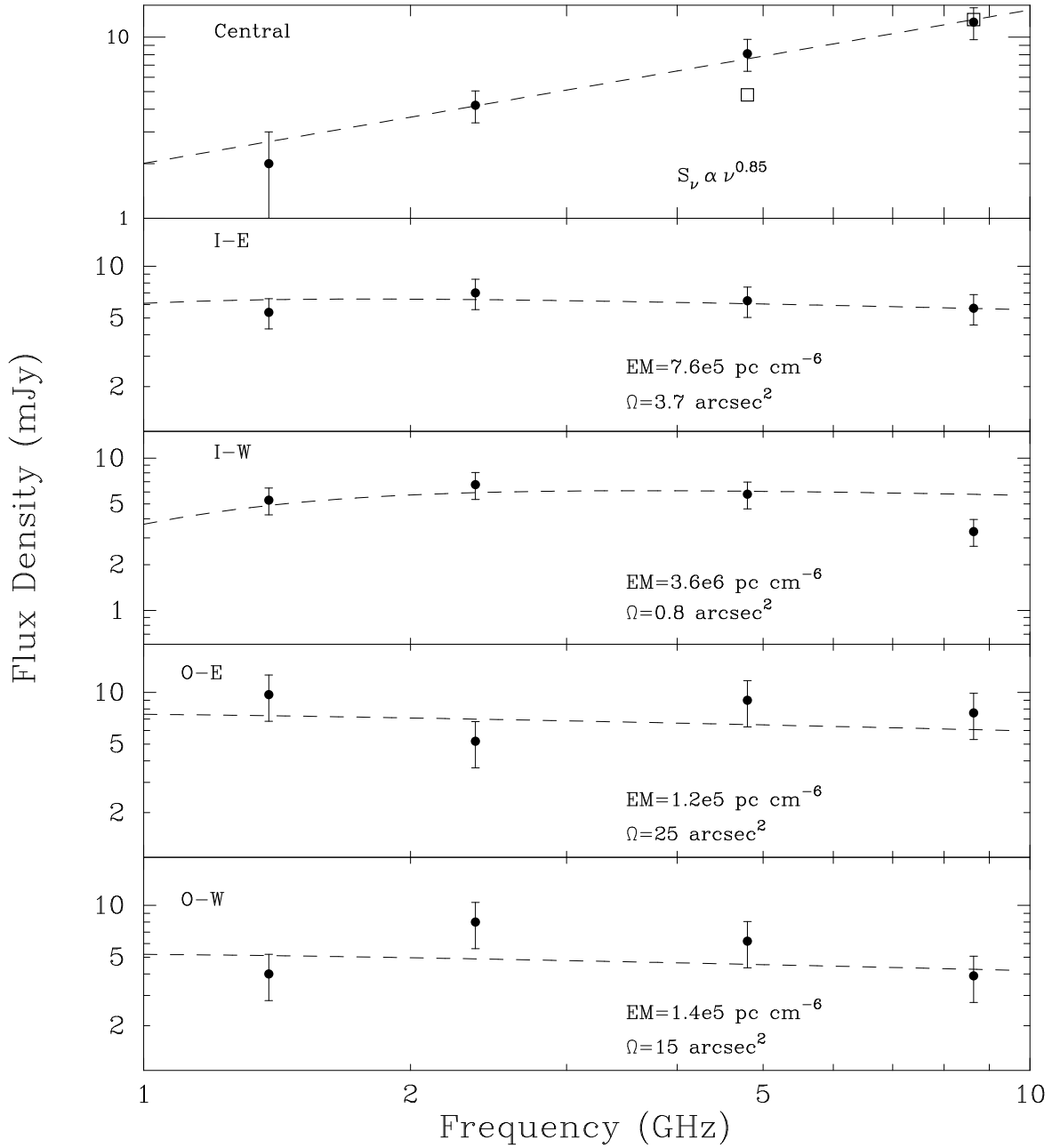


Figure 4.2 Radio continuum flux density versus frequency for the five principal radio components detected toward G345.4938+01.4677. From top to bottom, spectra of the Central, Inner-East, Inner-West, Outer-East and Outer-West components. In the top panel the dashed line indicates a least squares power law fit to the data. Empty squares represent the data reported by Urquhart et al. (2007a). In the other panels the dashed line indicates a least square fits to the observed spectra with a model of homogeneous region of ionized gas. The emission measure (EM) was fitted, and the solid angle ( $\Omega$ ) was obtained from the deconvolved size of the radio images at 8.6 GHz. Both parameters are given in each of the panels. Error bars are the maximum of either the error values in Table 4.1 or 20%.

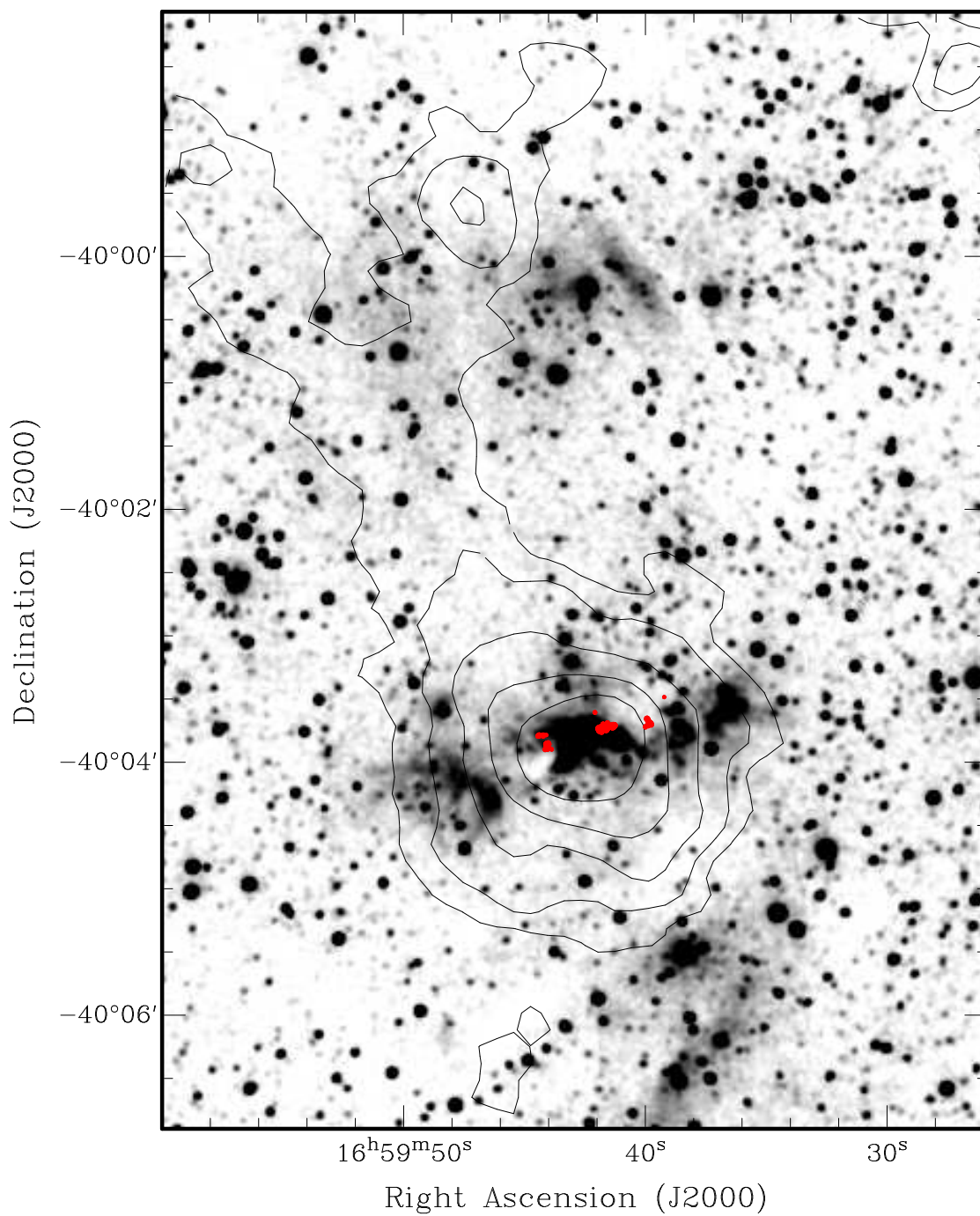


Figure 4.3 Gray scale image of the  $K_s$  band emission towards G345.4938+01.4677. Black contours: 1.2 mm dust continuum emission (SIMBA/SEST). Red contours: 8.6 GHz radio continuum emission (ATCA).

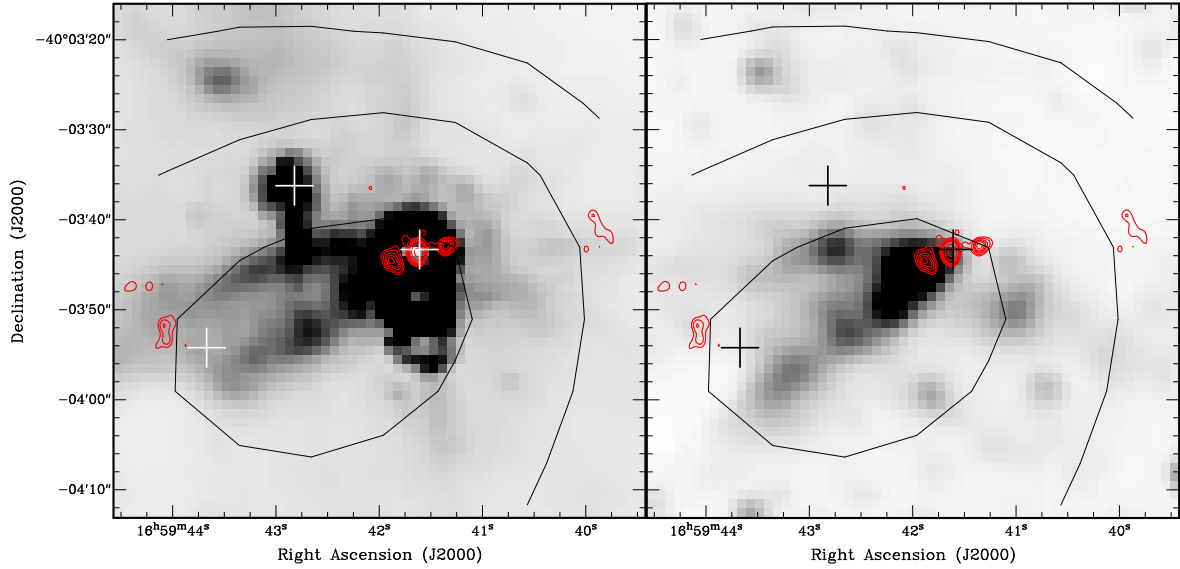


Figure 4.4 *Left*: Gray image:  $8\ \mu\text{m}$  IRAC-Spitzer emission. Black contours: 250 GHz dust emission detected with SIMBA. Red contours: 8.6 GHz emission. Crosses mark the position of the OH masers. Note that the  $8\ \mu\text{m}$  data is saturated near the central source, which produces an spurious extension running towards the south. *Right*: Gray image:  $K_s$  band emission. Contours and symbols same as in the left panel.

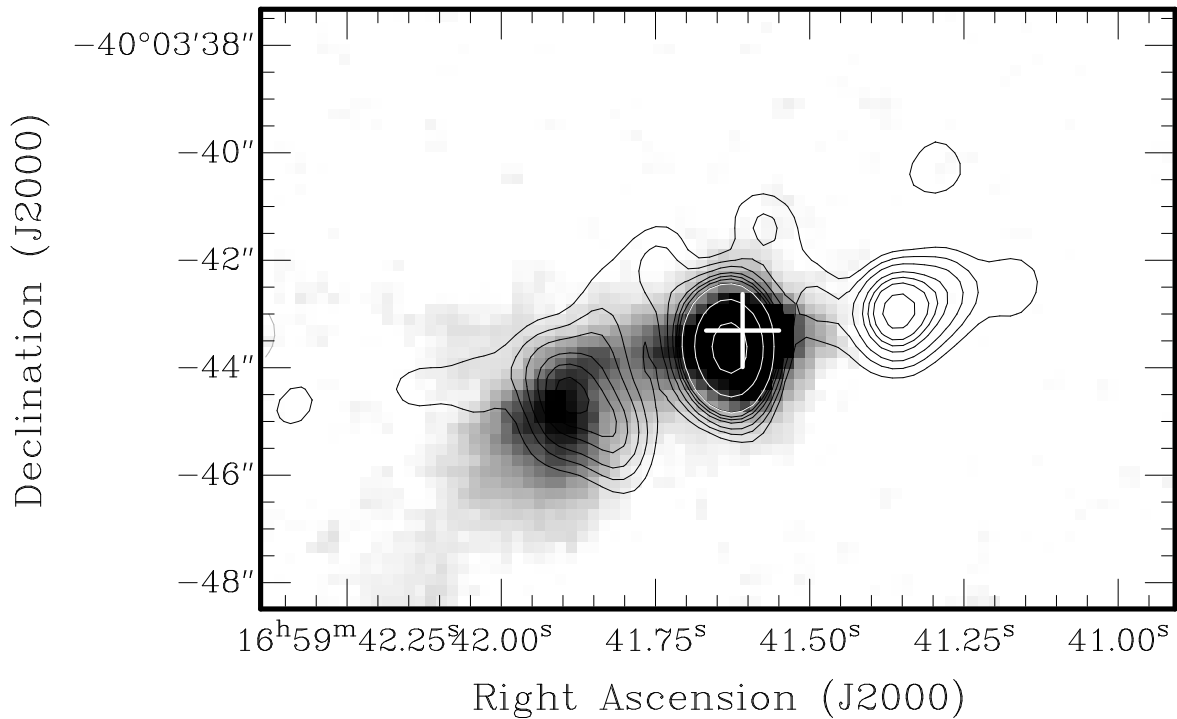


Figure 4.5 *Grey scale*:  $10.4\ \mu\text{m}$  emission observed by Mottram et al. (2007). *Contours*: 8.6 GHz radio emission. The cross marks the position of the OH maser associated with the central source. There is strong  $10.4\ \mu\text{m}$  emission associated with the central source and more diffuse emission associated with the Inner-East lobe.

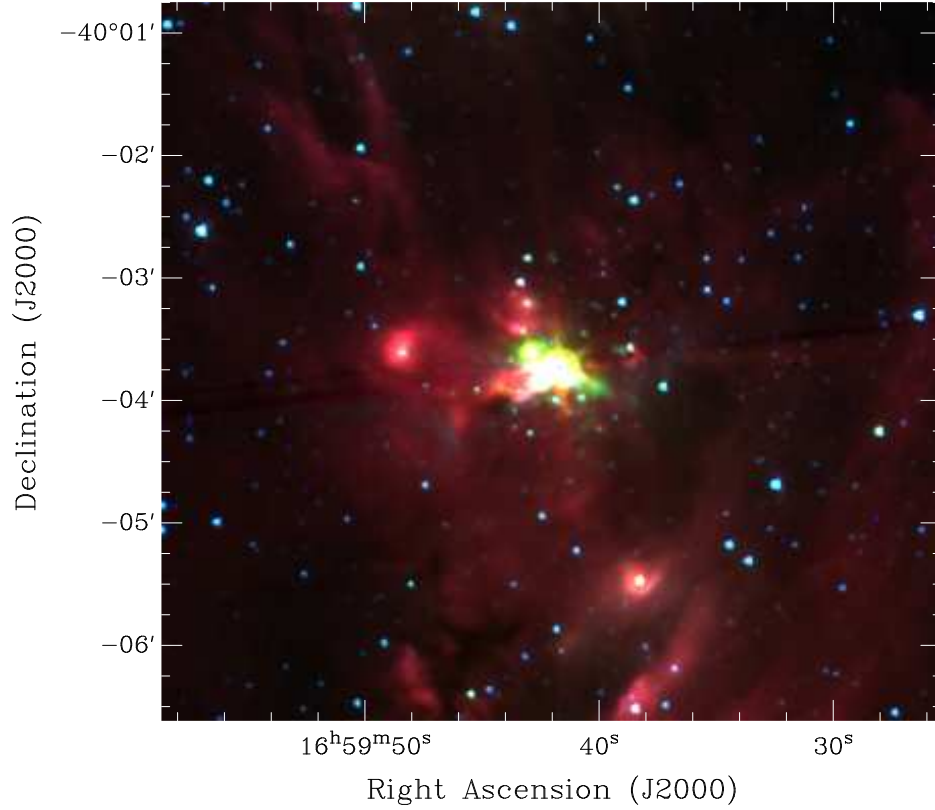


Figure 4.6 Spitzer three color image using the 8.0  $\mu\text{m}$ , 4.5  $\mu\text{m}$  and 3.6  $\mu\text{m}$  IRAC images for red, green and blue, respectively. The jet is located at the center of the image associated with an extended diffuse "green fuzzy" or enhancement of the 4.5  $\mu\text{m}$  band.

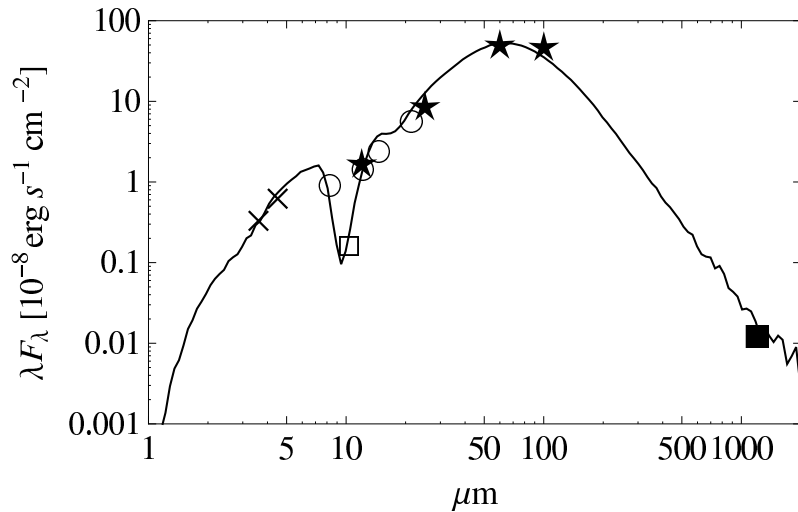


Figure 4.7 Spectral energy distribution of the Central source. *Crosses*: Spitzer/IRAC data at 3.6 and 4.5  $\mu\text{m}$ . *Empty square*: TIMMI2 data at 10.4  $\mu\text{m}$ . *Empty circles*: MSX data at 8.3, 12.1, 14.7 and 21.3  $\mu\text{m}$ . *Stars*: IRAS data at 12, 25, 60 and 100  $\mu\text{m}$ . *Filled Square*: SIMBA data at 1200  $\mu\text{m}$ . The line indicates the best fit using the models described in Robitaille et al. (2007).

## Chapter 5

# A hot molecular outflow driven by the ionized jet associated with G345.4938+01.4677

We report molecular line observations in the CO J=3→2, 6→5 and 7→6 transitions, made using the Atacama Pathfinder Experiment Telescope (APEX), toward the massive and dense core G345.4938+01.4677 (IRAS 16562–3959). This core harbors a string of radio sources thought to be powered by a central collimated jet of ionized gas. The molecular observations show the presence of high velocity gas exhibiting a quadrupolar morphology, most likely produced by the presence of two collimated outflows. The southeast-northwest molecular outflow is aligned with the string of radio continuum sources, suggesting it is driven by the jet. We find that the excitation temperature of the gas in the SE-NW outflow is high, with values of 145 and 120 K for the blueshifted and redshifted lobes, respectively. This outflow has a total mass of  $1.92 M_{\odot}$ , a total momentum of  $\sim 89 M_{\odot} \text{ km s}^{-1}$  and an averaged momentum rate of  $\sim 3.0 \times 10^{-2} M_{\odot} \text{ km s}^{-1} \text{ yr}^{-1}$ , values characteristics of flows driven by young massive stellar objects with high luminosities ( $L_{\text{bol}} \sim 2 \times 10^4 L_{\odot}$ ). Complementary data taken with the Atacama Submillimeter Telescope Experiment (ASTE) in high density and shock tracers support the picture that G345.4938+01.4677 is an accreting young massive star associated with an ionized jet, which is the energy source of a molecular outflow.

---

Based on the work published in Guzmán et al. (2011) and reproduced by permission of the AAS.

## 5.1 Introduction

G345.4938+01.4677 (also IRAS 16562–3959) is a mid-infrared (MIR) source, with *MSX* (*Midcourse Space Experiment*) colors characteristics of high-mass young stellar objects (Lumsden et al. 2002). Observations of dust continuum emission at 1.2 mm, made with SIMBA at the SEST telescope, show that G345.4938+01.4677 is associated with a massive ( $1.3 \times 10^3 M_{\odot}$ ) and dense ( $9 \times 10^5 \text{ cm}^{-3}$ ) molecular core (López et al. 2011). Maser emission has been detected in transitions of OH (Caswell 1998, 2004), giving further support to the hypothesis that G345.4938+01.4677 is a young high-mass star forming region.

We reported the detection toward G345.4938+01.4677 of a string of radio continuum emission consisting of a bright compact central object and four outer lobes. We argue in Chapter 4 that the continuum emission from the central object corresponds to free-free emission from a thermal jet whereas the radio emission from the lobes correspond to thermal emission arising in shocks generated from the interaction of the collimated wind with the surrounding medium. Assuming that G345.4938+01.4677 is located at a distance of  $1.6 \pm 0.1$  kpc ( $V_{\text{LSR}} = -12.6 \text{ km s}^{-1}$ , Urquhart et al. 2008b)<sup>1</sup>, the total far-infrared luminosity, computed using the observed IRAS fluxes (see Casoli et al. 1986), is  $\sim 7.0 \times 10^4 L_{\odot}$ . This implies that G345.4938+01.4677 harbors the most luminous HMYSO known to date associated with an ionized jet.

Mid-infrared images taken from the *Spitzer Space Telescope*-GLIMPSE survey data (Benjamin et al. 2003) show bright emission associated with the jet in all IRAC bands. In particular, at  $8.0 \mu\text{m}$  there is extended emission roughly aligned with the jet axis. Further, there appears to be an excess of emission at  $4.5 \mu\text{m}$ , which is thought to be indicative of shock activity (Cyganowski et al. 2008, Chambers et al. 2009). The GLIMPSE data also show that there is at least one more young stellar object (YSO) within the core, located about  $15''$  northeast of the jet, that is not detected at  $2 \mu\text{m}$  and hence likely to be deeply embedded.

We present molecular line observations toward G345.4938+01.4677 in the CO( $3 \rightarrow 2$ ), CO( $6 \rightarrow 5$ ), and CO( $7 \rightarrow 6$ ) transitions, made using APEX, which have revealed the presence of two high velocity bipolar molecular outflows. Their observed and derived characteristics suggest that the driving sources are young, luminous protostellar objects. One of the outflows is aligned in the same direction as the string of radio sources strongly suggesting that it is being driven by the thermal radio jet.

## 5.2 Observations

The observations were made using the 12-m Atacama Pathfinder Experiment Telescope (APEX) located at Llano de Chajnantor, Chile. A detailed description of APEX and its performance are given by Güsten et al. (2006). The observed transitions and basic observational parameters are summarized in Table 5.1. Columns (1) and (2) give, respectively, the observed transition and line frequency. Columns (3), (4) and (5) give the telescope used, the half-power beam width and main beam efficiency at the observed frequency. Columns (6) to (9) give, respectively, the number of positions observed, the angular spacing, the chan-

---

<sup>1</sup>The near/far kinematic distance ambiguity was resolved in Faúndez et al. (2004)

Table 5.1. Observational Parameters

Line	Frequency [GHz]	Tel.	Beam [ $''$ ]	$\eta_{mb}$	Map	Spacing [ $''$ ]	$\Delta v$ [km s $^{-1}$ ]	Noise [K]
(1)	(2)	(3)	(4)	(5)	(6)	(7)	(8)	(9)
CO(3 $\rightarrow$ 2)	345.796	APEX	17.3	0.73	5 $\times$ 5	20 $''$	0.423	0.1
CO(6 $\rightarrow$ 5)	691.627	APEX	8.8	0.47	29 $\times$ 21	4 $''$	0.318	0.5
CO(7 $\rightarrow$ 6)	806.898	APEX	7.7	0.43	27 $\times$ 19	4 $''$	0.272	1.0
SiO(8 $\rightarrow$ 7)	347.331	APEX	17.	0.73	3 $\times$ 3	20 $''$	0.423	0.05
HCO $^+$ (4 $\rightarrow$ 3)	356.734	ASTE	22	0.7	Central Pos.	—	0.11	0.1
C $^{18}$ O(3 $\rightarrow$ 2)	329.331	ASTE	23	0.7	Central Pos.	—	0.43	0.05

nel width, and the resulting rms noise in antenna temperature, for each of the observed transitions.

The CO(3  $\rightarrow$  2) observations were made during June, 2008 and July, 2009. The front-end consisted of a single pixel heterodyne SiS receiver operating in the 275-370 GHz band (Risacher et al. 2006). For the back-end we used the APEX Fast Fourier Transform Spectrometer (Klein et al. 2006) with a bandwidth of 1 GHz and 2048 frequency channels. The velocity coverage was  $\sim 870$  km s $^{-1}$  centered at  $-13.6$  km s $^{-1}$   $V_{\text{LSR}}$  with a channel width of  $0.42$  km s $^{-1}$ . In this transition the emission was mapped within a region of  $100'' \times 100''$  in size, with  $20''$  angular spacing (roughly full beam spacing), centered on the position of the radio source. System temperatures were typically 270 K. The pointing accuracy is  $2 - 3''$  calibrated towards the source RT-Sco (R.A. =  $17^{\text{h}}03^{\text{m}}32^{\text{s}}.6$ , Dec =  $-36^{\circ}55'14''$ ) and the uncertainty in the absolute flux scale is  $\sim 10\%$ . The observations were performed in position-switching mode under good atmospheric conditions ( $\tau \sim 0.07$ ) using R.A. =  $16^{\text{h}}58^{\text{m}}15^{\text{s}}$  and Dec =  $-39^{\circ}00'00''$  as off-position. The integration time on-source in each position was  $\sim 30$  seconds, resulting in an rms noise of typically 0.1 K in antenna temperature per channel.

The CO(6  $\rightarrow$  5) and CO(7  $\rightarrow$  6) observations were made during August, 2009, under good weather conditions (0.35-0.45 mm of water vapor, corresponding to  $0.5 < \tau < 0.8$ ) using an off-position located at  $\Delta$ R.A. =  $+6^{\text{m}}$ . The pointing calibration source was NGC6334, attaining an accuracy of  $\sim 2''$ . The front-end consisted of a dual heterodyne SIS receiver array of 7 pixels operating in the 600-720 GHz and 750-950 GHz atmospheric windows, known as the CHAMP $^+$  receiver (Güsten et al. 2008). In these two transitions we mapped the emission within a region of  $110'' \times 90''$  in size, with  $4''$  angular spacing. The back-ends were operated with 2.4 GHz total bandwidth with 2048 channels each.

We complement the above data with additional spectra taken toward the radio source position in the SiO(8 $\rightarrow$ 7), HCO $^+$ (4 $\rightarrow$ 3) and C $^{18}$ O(3 $\rightarrow$ 2) lines. The SiO(8 $\rightarrow$ 7) observations were performed using APEX with the same APEX FFT spectrometer. The integration time was  $\sim 450$  seconds giving an rms noise of 0.05 K.

The HCO $^+$ (4 $\rightarrow$ 3) and C $^{18}$ O(3 $\rightarrow$ 2) spectra were taken as part of a larger mapping of the core using the ASTE 10 m submillimeter telescope (Ezawa et al. 2004) during June-July, 2010, under good atmospheric conditions ( $\tau \sim 0.08$ ). The front-end consisted in a heterodyne

single pixel SiS receiver operating between 324 and 372 GHz. As back-end we used the MAC FX-type digital spectro-correlator with 1024 channels (Iguchi & Okuda 2008). For the  $\text{C}^{18}\text{O}(3\rightarrow 2)$  line we used a total bandwidth of 512 MHz, giving a velocity resolution of about  $0.43 \text{ km s}^{-1}$ , whereas for the  $\text{HCO}^+(4\rightarrow 3)$  transition we used a 125 MHz bandwidth, giving a velocity resolution of  $\sim 0.11 \text{ km s}^{-1}$ .

### 5.3 Results

Figure 5.1 shows a grid of the CO spectra in the three observed transitions within a region of  $100'' \times 100''$  in size, with  $20''$  spacing. The spectra of the  $\text{CO}(6\rightarrow 5)$  and  $\text{CO}(7\rightarrow 6)$  transitions were convolved to match the angular resolution of the  $\text{CO}(3\rightarrow 2)$  spectra. Clearly seen in this figure is the presence of broad and strong wing emission across the molecular core.

Figure 5.2 shows the  $\text{HCO}^+(4\rightarrow 3)$ ,  $\text{C}^{18}\text{O}(3\rightarrow 2)$  and  $\text{SiO}(8\rightarrow 7)$  spectra observed toward the peak position of G345.4938+01.4677. The  $\text{HCO}^+(4\rightarrow 3)$  spectrum shows a double-peaked line profile, with a bright blue-shifted peak at  $-14.0 \pm 0.2 \text{ km s}^{-1}$  and a weaker red-shifted peak at  $-10.1 \pm 0.2 \text{ km s}^{-1}$ . On the other hand, the  $\text{C}^{18}\text{O}(3\rightarrow 2)$  line profile shows a symmetric single component with a peak line center velocity of  $-12.5 \text{ km s}^{-1}$ . We also note that the  $\text{HCO}^+(4\rightarrow 3)$  and the  $\text{SiO}(8\rightarrow 7)$  spectra show prominent high velocity wings.

The  $^{12}\text{CO}$  profiles exhibit redshifted wing emission mainly towards the west and south, up to an LSR velocity of  $14 \text{ km s}^{-1}$ , whereas blueshifted wing emission is seen mainly towards the east and north, up to an LSR velocity of  $-46 \text{ km s}^{-1}$ . The full velocity range of the wing emission observed is then  $\sim 60 \text{ km s}^{-1}$ . The radial flow velocity is defined as  $|v_{LSR} - v_{\text{amb}}|$ , where  $v_{\text{amb}}$  is the systemic velocity of the ambient gas. For the later we adopt a value of  $-12.5 \text{ km s}^{-1}$ , corresponding to the peak velocity of the  $\text{C}^{18}\text{O}(3\rightarrow 2)$  line profile observed toward the central position of the core. The maximum outflow velocity is then  $\sim 33.5 \text{ km s}^{-1}$  towards the blue and  $\sim 26.5 \text{ km s}^{-1}$  towards the red. Figure 5.3 shows contour maps of the wing emission in the three CO lines integrated over the velocity range  $-46 < v_{LSR} < -22.0 \text{ km s}^{-1}$  (blue contours) and  $-3 < v_{LSR} < 14 \text{ km s}^{-1}$  (red contours). The star marks the position of the radio jet (the central source, see Chap. 4). These velocity limits define the ranges in which emission from the high-velocity outflow gas is seen. We note that the blueshifted flow emission is slightly stronger and reaches higher radial flow velocities compared to the redshifted emission, hence the wider blueshifted velocity range. The inner limits of the ranges were selected as to leave out the contribution of the ambient cloud and chosen symmetrically respect to the ambient cloud velocity.

The spatial distribution of the blueshifted and redshifted emissions shows a quadrupole morphology, with blueshifted emission seen mainly toward the east and north and redshifted emission seen toward the west and south. We propose that the quadrupolar morphology is produced by the superposition of two bipolar outflows, one along a southeast-northwest direction (hereafter the SE-NW flow) with a position angle of  $\sim 107^\circ$ , and a second outflow aligned roughly in a north-south (N-S) direction. The collimation factors — length divided by width — of the molecular outflows are not high: for the blueshifted and redshifted lobes of the SE-NW outflow are  $\gtrsim 2$  and  $\sim 1$ , respectively, whereas for the lobes of the N-S outflow we found values close to 1. These values are similar to those derived for massive outflows (Beuther et al. 2002b). We note, however, that the highest velocity gas emission of the

SE-NW outflow appears to be associated with more collimated structures.

Figure 5.4 presents a contour map of the outflow emission in the CO(6→5) line overlaid with the 8.6 GHz radio continuum emission observed toward G345.4938+01.4677. It appears that the SE-NW outflow is associated with the string of radio sources, the peak position of the blue-shifted and red-shifted lobes being symmetrically displaced from the bright central radio source. The SE blueshifted and NW redshifted lobes extend up to  $\sim 27''$  and  $\sim 32''$  from the central radio source, respectively. The symmetry axis of the SE-NW outflow is along a direction with a position angle of  $\sim 107^\circ$ , roughly the same as the P.A. of the symmetry axis of the jet of  $110^\circ$ . As noted in Chapter 4, the radio lobes and the jet are not completely aligned, showing a small bending, which is also seen in the SE-NW outflow. Possible bending mechanisms of protostellar jets are discussed in Fendt & Zinnecker (1998), but with the available data we can not discern between the various alternatives.

The spectroscopic signatures of the HCO<sup>+</sup>(4→3) and C<sup>18</sup>O(3→2) transitions suggest that the bulk of the molecular gas toward G345.4938+01.4677 is undergoing large-scale inward motions (e.g. Sanhueza et al. 2010). Infalling motions traced by optically thick molecular lines are expected to produce line profiles showing blue asymmetry, whereas optically thin lines are expected to exhibit symmetrical profiles (Mardones et al. 1997).

## 5.4 Analysis and discussion

### 5.4.1 $K_s$ -band evidence of shocked H<sub>2</sub>

Figure 5.5 presents an image of the Two Micron All Sky Survey (2MASS, Skrutskie et al. 2006)  $K_s$ -band emission across an  $8' \times 8'$  region of the sky, centered near G345.4938+01.4677. Clearly seen toward the center is diffuse emission along the SE-NW direction extending by more than  $1.5'$  on each side of the bright radio source. The position angle of this diffuse  $K_s$ -band emission is  $\sim 104^\circ$ , a value similar to that of the SE-NW molecular outflow. We suggest that the outer parts of this diffuse emission, which are at greater distances from the central jet than the molecular lobes, are tracing shocked H<sub>2</sub>- $2.12 \mu\text{m}$  gas produced by an older episode of mass ejection from the jet.

We note that the infrared emission detected close to the central jet comes mainly from a region associated with the SE blueshifted lobe. Much less emission is seen associated with the NW redshifted lobe (see also Fig. 4.4). A similar situation has been observed in other bipolar outflows, for example in BHR 71 (Bourke 2002). Most likely, the strong infrared emission from the eastern, closer to the jet, feature correspond to scattered light from the inner walls of the outflow cavity.

The second outflow detected toward G345.4938+01.4677 is roughly aligned in the north-south direction, having a symmetry axis with a position angle of  $7^\circ$ . The blueshifted lobe extends up to  $\sim 21''$  to the north of the jet and the redshifted lobe up to  $\sim 17''$  to the south. Interestingly, Fig. 5.5 also shows the presence of diffuse  $K_s$ -band emission roughly along the N-S direction but located about  $3.4'$  north and  $2'$  south from the NS molecular outflow. This emission exhibits a bow shock morphology, characteristic of HH objects, most likely produced by the interaction of a collimated flow with the ambient medium. However, we remarked in Chapter 4 that this diffuse emission is bright in all mid-infrared *MSX* bands.

In consequence, it is likely that this  $K_s$ -band emission has an important NIR continuum component, in addition to the  $\text{H}_2$ -2.12  $\mu\text{m}$  line.

We suggest that there is an independent source of energy driving the NS outflow, although from the available data we are not able to pinpoint its location. We have already argued (Chap. 4), on the basis that a re-orientation of the central jet in  $\sim 90^\circ$  seems physically unfeasible, for the presence of two high-mass YSOs driving the outflows.

## 5.4.2 Parameters of the outflows

To compute physical parameters of the molecular outflows we followed the standard formalism described in Bourke et al. (1997), Garden et al. (1991) and Goldsmith & Langer (1999), assuming that the high velocity gas is optically thin and its excitational state can be described by a single excitation temperature. If the transitions are sub-thermally excited, then the derived excitation temperature would correspond to a lower limit of the kinetic temperature of the outflowing gas.

A general discussion of the sources of errors have been given by Margulis & Lada (1985) and Cabrit & Bertout (1990). The main sources of error arise from the difficulty in determining the contribution to the outflow in the velocity range of the ambient cloud, and not knowing the flow inclination. To be conservative we adopt as velocity boundary between the blue and red wing emission and the ambient emission the values of  $-22.0$  and  $-3.0 \text{ km s}^{-1}$ , respectively.

### 5.4.2.1 Column densities and excitation temperatures

The column density of CO molecules in the velocity range  $[v1, v2]$  is given by

$$N_{\text{CO}} = 2.31 \times 10^{14} \frac{(T_{\text{ex}} + hB/3k)}{1 - \exp(-h\nu/kT_{\text{ex}})} \frac{\exp(E_J/kT_{\text{ex}})}{(J+1)} \int_{v1}^{v2} \tau_v dv \quad \text{cm}^{-2} \quad , \quad (5.1)$$

where  $T_{\text{ex}}$  is the rotational excitation temperature in K,  $J$  is the rotational quantum number of the lower state,  $E_J = hBJ(J+1)$  is the energy of level  $J$ , where  $B$  is the rotational constant of the CO molecule. The frequency of the  $\text{CO}(J+1 \rightarrow J)$  transition is  $\nu \approx 2B(J+1)$ , and  $\tau_v$  is the opacity of the material moving at velocity  $v$  (the latter measured in  $\text{km s}^{-1}$ ). Assuming a beam filling factor of 1, the observed main-beam brightness temperature is related to the opacity by

$$T_{\text{mb}}^*(v) = [J_r(\nu, T_{\text{ex}}) - J_r(\nu, T_{\text{bg}})](1 - e^{-\tau_v}) \quad , \quad (5.2)$$

where  $J_r(\nu, T)$  is defined as

$$J_r(\nu, T) = \frac{h\nu/k}{\exp(h\nu/kT) - 1} \quad .$$

In the optically thin limit,

$$T_{\text{mb}}^*(v) = [J_r(\nu, T_{\text{ex}}) - J_r(\nu, T_{\text{bg}})]\tau_v \quad . \quad (5.3)$$

From the observations of the emission in the three transitions of CO it is possible to determine both the excitation temperature and column density of the outflowing gas using

Table 5.2. Parameters of High-Velocity and Ambient Gas

Lobe	V range (km s <sup>-1</sup> )	N <sub>CO</sub> (10 <sup>16</sup> cm <sup>-2</sup> )	T <sub>ex</sub> (K)
(1)	(2)	(3)	(4)
Blue SE	[-46, -22]	8.72	145
Red NW	[-03, +14]	6.06	120
Blue N	[-46, -22]	5.70	76
Red S	[-03, +14]	3.37	88
Ambient	[-22, -03]	11.30	54

Eqs. (3.1) and (3.3), and taking  $T_{\text{bg}} = 2.7$  K. Figure 5.6 presents plots of the velocity integrated emission versus the  $J$  quantum number from the blueshifted and redshifted lobes of both outflows and from the ambient gas. The velocity intervals of integration for the blueshifted and redshifted emission are  $[-46, -22]$  and  $[-3, 14]$  km s<sup>-1</sup>, respectively. The areas over which the emission has been spatially integrated for the different outflow lobes are shown in Fig. 5.4. In the positions in which lobes overlap we assumed equal contributions from each lobe, except at offset position ( $\Delta\text{R.A.} = +20''$   $\Delta\text{Dec} = +20''$ ) where we assumed that the contribution to the blueshifted emission from the NS and SE-NW outflows are in a 2:1 ratio. Dashed lines show the results of the best fit to the observed integrated emission assuming optically thin conditions and filling factors of 1. The derived CO column densities and excitation temperatures are given in Table 5.2. The parameters for the ambient cloud were derived using the spectra observed at offset position ( $\Delta\text{R.A.} = +40''$ ,  $\Delta\text{Dec} = -40''$ ), which does not show evidence of self-absorption nor high velocity gas.

One of the less well known physical parameter of the gas in molecular outflows is its kinetic temperature. Our observations of three lines of CO allowed us to determine the excitation temperature of both outflows, concluding that their kinetic temperatures are high. The derived excitation temperatures of the high-velocity gas are 145 and 120 K for the blueshifted and redshifted lobes of the SE-NW outflow, and 76 and 88 K for the blueshifted and redshifted lobes of the NS outflow. All these temperatures are considerably higher than the ambient cloud temperature, indicating that part of the energy used in accelerating the gas has also heated it.

#### 5.4.2.2 Mass, momentum and momentum rates

The mass in the outflows can be computed from the derived column densities as,

$$M = [\text{H}_2/^{12}\text{CO}] \mu_m \sum N_{\text{CO}} dA \quad , \quad (5.4)$$

where  $N_{\text{CO}}$  is given by Eq. (3.1),  $\mu_m$  is the mean molecular mass per H<sub>2</sub> molecule,  $[\text{H}_2/^{12}\text{CO}]$  the molecular hydrogen to carbon monoxide abundance ratio,  $dA$  the size of the emitting area in an individual position, and the sum is over all the observed positions.

The derived masses of the SE-NW and NS flows are given in Columns (2-4) of Table 5.3. Column (2) gives the mass of the outflows in the high-velocity (HV) ranges, computed using

Table 5.3. Outflow Parameters <sup>a</sup>

Outflow (1)	Mass ( $M_{\odot}$ )			Momentum <sup>b</sup> ( $M_{\odot} \text{ km s}^{-1}$ )			Momentum rate <sup>b</sup> ( $10^{-4} M_{\odot} \text{ km s}^{-1} \text{ yr}^{-1}$ )		
	HV (2)	LV (3)	Total (4)	HV (5)	LV (6)	Total (7)	HV (8)	LV (9)	Total (10)
<b>SE-NW outflow</b>									
Blue SE	0.39	0.61	1.00	5.8	2.9	8.7	4.3	1.2	5.5
Red NW	0.27	0.65	0.92	3.5	3.1	6.6	2.2	1.3	3.5
Total	0.66	1.26	1.92	9.3	6.0	15.3	6.5	2.5	9.0
<b>NS outflow</b>									
Blue N	0.25	0.49	0.74	3.4	2.4	5.8	3.3	1.0	4.3
Red S	0.15	0.43	0.58	1.9	2.0	3.9	1.7	0.8	2.5
Total	0.40	0.92	1.32	5.3	4.4	9.7	5.0	1.8	6.8

<sup>a</sup>HV and LV denotes parameters of the high-velocity and low-velocity flows, derived as described in §5.4.2.2.

<sup>b</sup>Not corrected for inclination.

the column densities given in Table 5.2,  $\mu_m = 2.3 m_H$ , and  $[\text{H}_2/^{12}\text{CO}] = 10^4$ . To estimate the contribution to the mass from the outflowing gas emitting in the same velocity range as the ambient cloud gas, referred as the low-velocity (LV) outflow gas, we followed the prescription of Margulis & Lada (1985). Using expression (A16) of Bourke et al. (1997), adopting as velocity boundary between the wing and ambient emissions values of  $-22 \text{ km s}^{-1}$  in the blue side and  $-3 \text{ km s}^{-1}$  in the red side, we estimate that the mass of the low velocity flow is 1.26 and  $0.92 M_{\odot}$  for the SE-NW and NS flow, respectively. The total masses for the SE-NW and NS outflows are then 1.92 and  $1.32 M_{\odot}$ , respectively.

The momentum of the gas can be estimated from the first moment of the line emission. This procedure has the advantage of using the detailed information of the spectra. The derivation of flow kinematic and dynamical parameters by using moments of the spectrum has been described in detail by Calvet et al. (1983). For this purpose we used the CO(3→2) spectra since it has the best signal-to-noise ratio, but note that using any of the three transitions render consistent values within a 10%. In the low velocity range we selected  $-12.5 \text{ km s}^{-1}$ , the ambient cloud velocity, as the limiting value between what we consider blue or red-shifted gas. The derived momenta are given in Columns (5-7) of Table 5.3. They were computed using the observed radial velocities, and thus correspond to strict lower limits. To correct for inclination they should be multiplied by a factor  $(\cos i)^{-1}$  where  $i$  is the angle between the flow and the line of sight.

The average momentum rates can be estimated from the second moment of the CO(3→2) spectra, from the expression

$$\dot{P} = [\text{H}_2/^{12}\text{CO}] \mu_m \sum_{\text{lobe}} F(J, T_{\text{ex}}) \frac{\int \tau_v v^2 dv}{r_{\text{char}}} dA, \quad (5.5)$$

where  $F(J, T_{\text{ex}})$  is the term that multiplies the integral in the right hand side of Eq. (3.1), and we select  $J = 2$  as indicated previously. The opacity  $\tau_\nu$  can be estimated from Eq. (3.3) in the optically thin limit and assuming  $\eta_{ff} = 1$ . The characteristic radius of the flow,  $r_{\text{char}}$ , is a sensitive parameter that regulates the size of the flow and the time scale (after dividing it by the flow velocity) over which the momentum has been deposited in the pre-stellar core. In Eq. (5.5), we consider  $r_{\text{char}}$  as the projected radius, taken as the length subtended by  $30''$  (0.23 pc at 1.6 kpc) for the high-velocity flow; and as the length subtended by  $20''$  for the low-velocity gas. The momentum rates derived for the outflows, with no correction for inclination, are given in cols. (8-10) of Table 5.3. A correction for inclination will require to multiply by the factor  $(\cos i)^{-2} \sin i$ .

Toward each of the lobes of the SE-NW flow we observe wing emission at both blueshifted and redshifted velocities. This allows us to make an estimate of its inclination using the expression (Cabrit & Bertout 1990, 1986)

$$\tan i = \frac{R + 1}{R - 1} \frac{1}{\tan \theta} \quad ,$$

where  $R$  is the ratio between maximum observed blueshifted and redshifted velocities (in absolute value) toward a single lobe, and  $\theta$  is half of the total aperture angle of the outflow. We estimate the later from the 2-MASS  $K_s$ -band image, obtaining a value of  $\sim 23^\circ$ . Using this and the observed values of  $R$ , we derive an inclination angle for the SE-NW outflow of  $80^\circ$ . Correction factors for the momentum and momentum rate are then 5.8 and 33, respectively. The inclination-corrected momentum of the SE-NW flow is  $89 M_\odot \text{ km s}^{-1}$  and the inclination-corrected momentum rate (calculated with Eq. 5.5) is  $3.0 \times 10^{-2} M_\odot \text{ km s}^{-1} \text{ yr}^{-1}$ .

One of the principal problems of the previous estimation is that one assumes that the momentum has been injected into the molecular gas continuously, despite the molecular high velocity gas and the radio images evidence that the emission comes from discrete episodes of mass ejection. Therefore, the momentum rates calculated are time-averaged over the history of mass ejections from the protostar, that probably includes long periods of inactivity.

The momentum flux of the ionized jet —corrected for  $80^\circ$  inclination— is  $\sim 3 \times 10^{-4} M_\odot \text{ km s}^{-1} \text{ yr}^{-1}$ , while that of the associated SE-NW molecular flow ( $3.0 \times 10^{-2} M_\odot \text{ km s}^{-1} \text{ yr}^{-1}$ ) is approximately 100 times greater. Also, the observed momentum of the flow could not have been deposited in the ambient gas by such a jet in less than  $\sim 10^5 \text{ yr}$ , a time larger than the estimated life of the YSO. A possible solution to this inadequacy of the jet as the driving source of the molecular outflow could be that the protostellar jet is only partially ionized, being its mass and momentum loads greater than the estimated ones.

### 5.4.3 Further tracers of shocks

In addition to the high-velocity CO gas and its high excitation temperature, further evidence for the presence of shocks is provided by the detection of SiO emission. SiO is thought to be generated when strong shocks pass through dense molecular gas disrupting dust grains (Hartquist et al. 1980, Caselli et al. 1997). Therefore, we expect that SiO emission should be associated with the outflowing gas. This suggestion is strongly supported by the almost identical shape of the profile of the high velocity outflowing gas emission observed in the  $\text{HCO}^+(4 \rightarrow 3)$  line and the SiO(8 $\rightarrow$ 7) profile (see next section and bottom panel of Fig. 5.2).

The observed velocity integrated SiO emission is  $\sim 4.6 \text{ K km s}^{-1}$ . Assuming the SiO line is emitted in optically thin conditions with an excitation temperature of 75 K, we derive a column density of SiO of  $7.8 \times 10^{12} \text{ cm}^{-2}$ . Assuming  $T_{\text{ex}} = 100 \text{ K}$  only changes this value by 3%. The critical density for the SiO(8 $\rightarrow$ 7) transition is  $\sim 10^8 \text{ cm}^{-3}$ , considerable larger than the ambient density, indicating that thermal collisions with ambient H<sub>2</sub> is not the main mechanism for excitation to this rotational state. The good correlation between the SiO emission and the high velocity component suggests that this mechanism is shock excitation of the gas.

There are three OH masers reported in the literature toward the region (Caswell 1998, 2004). Figure 5.4 shows their positions with green crosses. The closest to the peak of the SE blue-shifted lobe corresponds to a 1720 MHz OH maser, which has an LSR velocity of  $-24.5 \text{ km s}^{-1}$ . The 1720 MHz OH masers are usually associated with shocked gas (Brogan 2007), and the location and velocity of this particular one is consistent with it being pumped by the shock produced by the high velocity blueshifted flow. Caswell (2004) reported Zeeman splitting on this maser implying a  $\sim 10 \text{ mG}$  magnetic field, the latter probably enhanced through shock compression. We also note that the excitation temperature of the outflowing gas—derived in §5.4.2.1—is above the minimum temperature required to pump this maser collisionally ( $T \approx 90 \text{ K}$ , Elitzur 1976, Hoffman et al. 2003). We conclude that this maser is associated with the G345.4938+01.4677 core and to the shocked gas in the SE-NW outflow, and not located farther away at  $\sim 2.5 \text{ kpc}$  as previously suggested by Caswell (2004).

The other two masers correspond to 1665/1667 MHz OH masers: one is coincident with the central jet source ( $V_{\text{OH}} = -12.7 \text{ km s}^{-1}$ ) and the other, located about  $15.6''$  NE from the jet ( $V_{\text{OH}} = -15.5 \text{ km s}^{-1}$ ), is associated with a mid infrared source in the field, unseen in 2MASS but conspicuous in *Spitzer* 8.0  $\mu\text{m}$  band (see Fig. 4.4).

#### 5.4.4 Infall of molecular core

To derive infall parameters we modeled the HCO<sup>+</sup>(4 $\rightarrow$ 3) profile using the simple analytic model of contracting clouds of Myers et al. (1996). We first subtracted a broad Gaussian profile, shown as a dash-dotted line in the upper panel of Fig. 5.2, to take into account the contribution of the high velocity outflow. We note that the shape of the subtracted Gaussian is very similar to the profile of the SiO(8  $\rightarrow$  7) emission which is expected to come mainly from the outflowing gas. This is illustrated in the bottom panel of Fig. 5.2, which shows the SiO(8  $\rightarrow$  7) spectrum and superimposed the broad Gaussian profile fitted to the HCO<sup>+</sup>(4 $\rightarrow$ 3) emission (scaled by a factor of 1/14).

The simple model can very well fit the observed profile (see top panel of Fig. 5.2). The parameters of the best fitting collapse model are: an infall velocity ( $V_{\text{in}}$ ) of  $0.35 \text{ km s}^{-1}$ , a velocity dispersion ( $\sigma$ ) of  $1.54 \text{ km s}^{-1}$ , an optical depth ( $\tau_0$ ) of 3.8, a kinetic temperature of 32 K, and a rest-frame velocity of the collapsing envelope of  $-11.4 \text{ km s}^{-1}$ . This velocity is about  $1 \text{ km s}^{-1}$  greater than the ambient cloud velocity adopted here, but we note that Bronfman et al. (1996) also reported a velocity of  $-11.6 \text{ km s}^{-1}$  in the CS(2 $\rightarrow$ 1) transition detected towards this source.

In order to estimate the envelope accretion rate we consider the mass distribution model for the parent cloud derived from dust emission presented in the previous chapter. Assuming that the extent of the contracting gas along the line of sight is comparable to the size of the

cloud of about 0.7 pc FWHM ( $1.5'$  at 1.6 kpc) and using the derived values of the infall speed, molecular density, and core size, we obtain a mass infall rate  $\dot{M}_{in}$  of  $\sim 3.7 \times 10^{-4} M_{\odot} \text{ yr}^{-1}$ , a value one order of magnitude below the estimation from the SED fitting shown in Chapter 4. The value derived for the infall velocity is also about one order of magnitude below the free-fall velocity expected for the entire cloud, suggesting a retarded collapse.

## 5.5 Summary

We undertook molecular line observations toward the G345.4938+01.4677 massive and dense core in three CO transitions: CO(3→2), CO(6→5), and CO(7→6), using APEX, with angular resolutions ranging from  $\sim 8''$  to  $\sim 17''$ . Additionally, HCO<sup>+</sup>(4→3), C<sup>18</sup>O(3→2) and SiO(8→7) observations were performed towards the center of the core. The main results and conclusions are summarized as follows:

1. High velocity molecular gas was detected in the three CO transitions, spanning a range in radial velocity of  $\sim 60 \text{ km s}^{-1}$ .
2. The morphology of the high velocity emission, best shown in the CO(6→5) and CO(7→6) lines, is quadrupolar. We conclude that this morphology is due to the presence of two collimated bipolar outflows, one lying in the SE-NW direction and another in the N-S direction. The more extended bipolar flow is in the SE-NW direction, consistent with being excited by the ionized jet detected toward this HMYSO. Extended  $K_s$ -band emission probably tracing excited H<sub>2</sub>-2.12  $\mu\text{m}$  is also associated with the SE-NW flow.
3. From an analysis of the emission in the three CO lines we derive that the excitation temperature of the high-velocity gas, assumed optically thin, is high, with values of  $\sim 140$  in the lobes of the SE-NW outflow and  $\sim 90$  in the lobes of the N-S outflow. This suggests that the excitation of the gas is related with the acceleration mechanism, namely, shock-induced acceleration.
4. The total mass in the SE-NW and NS outflows are, respectively, 1.9 and 1.3  $M_{\odot}$ . The momentum and momentum rates derived for the SE-NW outflow, corrected for an inclination angle of  $80^\circ$ , are  $89 M_{\odot} \text{ km s}^{-1} \text{ yr}^{-1}$  and  $3.0 \times 10^{-2} M_{\odot} \text{ km s}^{-1} \text{ yr}^{-1}$ , respectively. These values are characteristics of flows driven by young high-mass stellar objects with high luminosities.
5. The molecular core in which the outflow is embedded presents evidence of being in gravitational contraction as shown by the blue asymmetric peak seen in the HCO<sup>+</sup>(4→3) transition observations. The derived mass infall rate is of the order of a few times  $10^{-4} M_{\odot} \text{ yr}^{-1}$  and the infall velocity is  $\sim 0.35 \text{ km s}^{-1}$ , which is a factor of  $\sim 10$  below the velocity expected from a free-fall collapse. This implies that the collapse has been retarded and not gravitationally dominated.

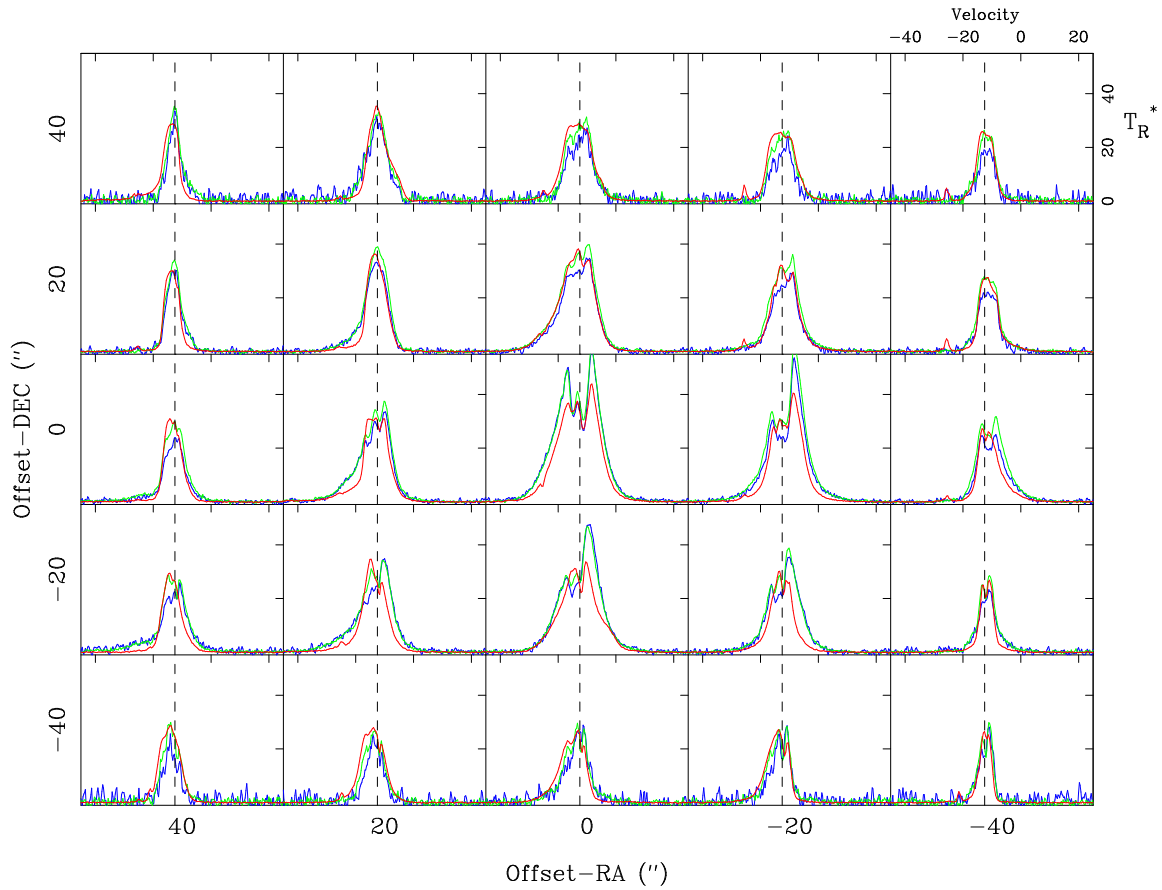


Figure 5.1 Spectral grid of the CO(3 $\rightarrow$ 2) (red), CO(6 $\rightarrow$ 5) (green), and CO(7 $\rightarrow$ 6) (blue) emission observed towards G345.4938+01.4677. The grid spacing is 20". Offsets are from the radio source reference position at  $\alpha_{2000} = 16^{\text{h}}59^{\text{m}}41.61^{\text{s}}0$ ,  $\delta_{2000} = -40^{\circ}03' 43''$ . Velocity scale ranges from  $-45$  to  $25 \text{ km s}^{-1}$ . The dashed line in each spectrum marks the ambient velocity adopted of  $-12.5 \text{ km s}^{-1}$ .

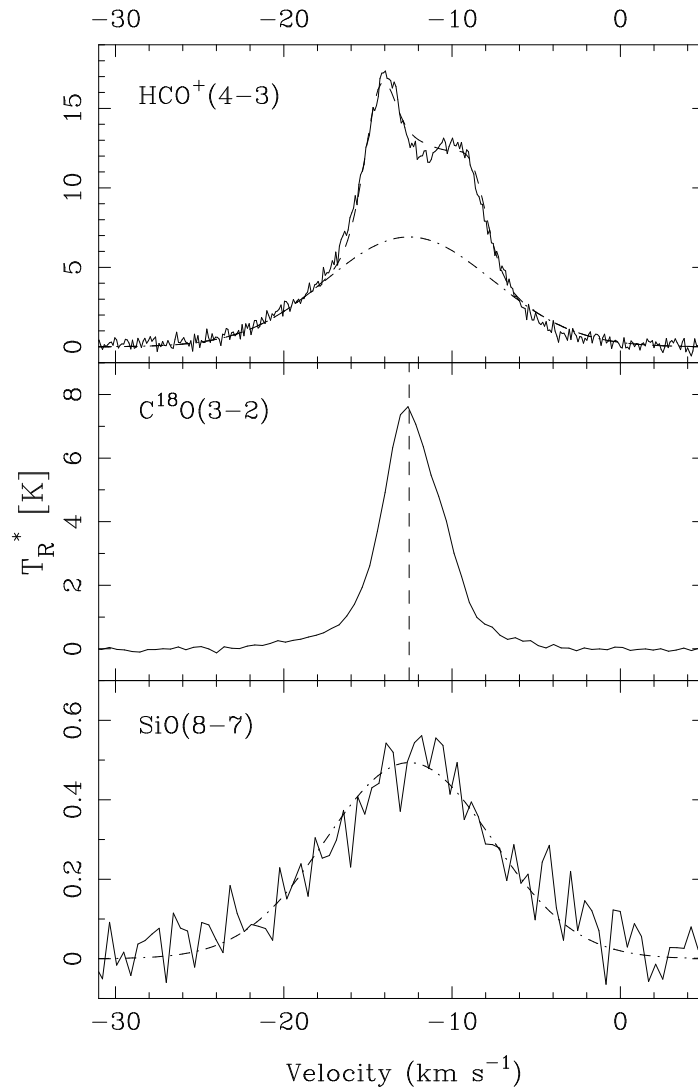


Figure 5.2 Spectra observed toward the peak position of G345.4938+01.4677. *Top:*  $\text{HCO}^+(4\rightarrow3)$  spectrum. The dashed line shows the best-fit using a collapsing envelope model from Myers et al. (1996) plus an outflow component (dot-dashed line). *Middle:*  $\text{C}^{18}\text{O}(3\rightarrow2)$  spectrum. The dashed-line indicates the adopted ambient cloud velocity of  $-12.5 \text{ km s}^{-1}$ . *Bottom:*  $\text{SiO}(8\rightarrow7)$  spectrum. The dot-dashed line is not a fit but shows the outflow profile fitted to the  $\text{HCO}^+(4\rightarrow3)$  spectrum scaled by 1/14.

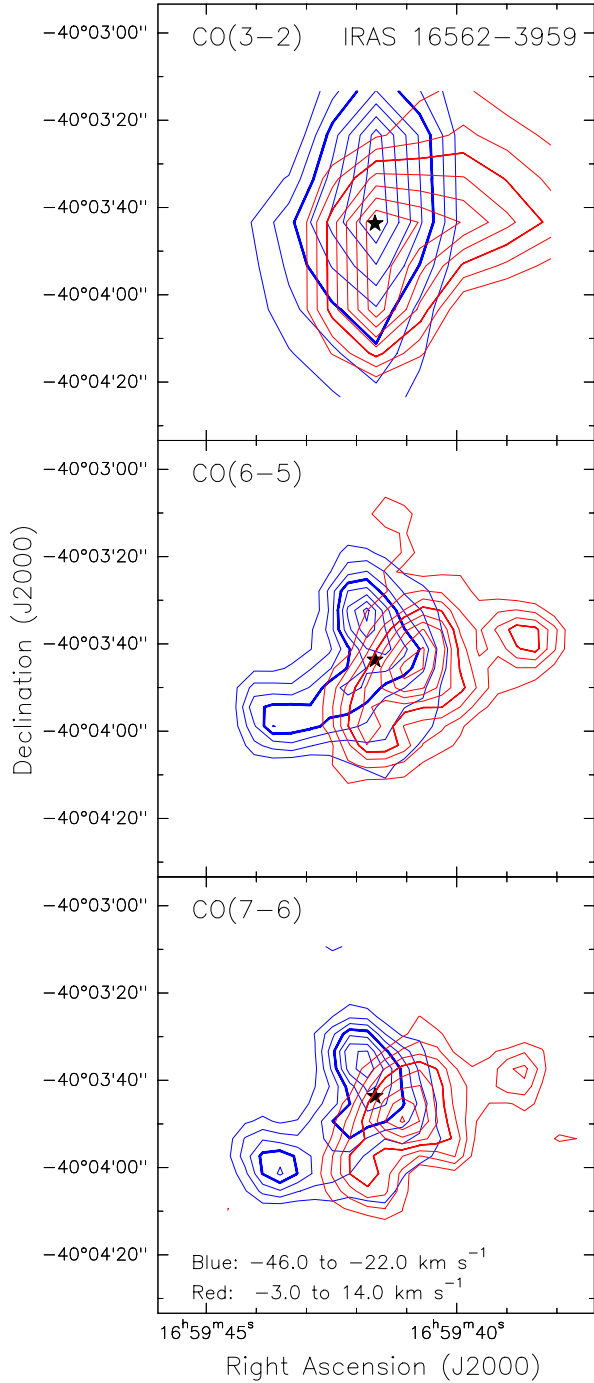


Figure 5.3 Contour maps of the velocity integrated CO line wing emission towards G345.4938+01.4677. Blue lines represent emission integrated over the velocity range  $-46 < v_{LSR} < -22$   $\text{km s}^{-1}$ , which is blueshifted with respect to the ambient velocity of  $-12.5$   $\text{km s}^{-1}$ , and red lines emission integrated over the velocity range  $-3 < v_{LSR} < 14$   $\text{km s}^{-1}$ , which is redshifted with respect to the ambient velocity. The star marks the position of the jet source. Contour levels are 20, 30, 40, 50, 60, 70, 80, and 90% of the peak emission. Top: CO(3 $\rightarrow$ 2) emission. Peak blueshifted emission:  $49.0$   $\text{K km s}^{-1}$ . Peak redshifted emission:  $26.4$   $\text{K km s}^{-1}$ . Middle: CO(6 $\rightarrow$ 5) emission. Peak blueshifted emission:  $85.2$   $\text{K km s}^{-1}$ . Peak redshifted emission:  $49.6$   $\text{K km s}^{-1}$ . Bottom: CO(7 $\rightarrow$ 6) emission. Peak blueshifted emission:  $85.1$   $\text{K km s}^{-1}$ . Peak redshifted emission:  $54.3$   $\text{K km s}^{-1}$ .

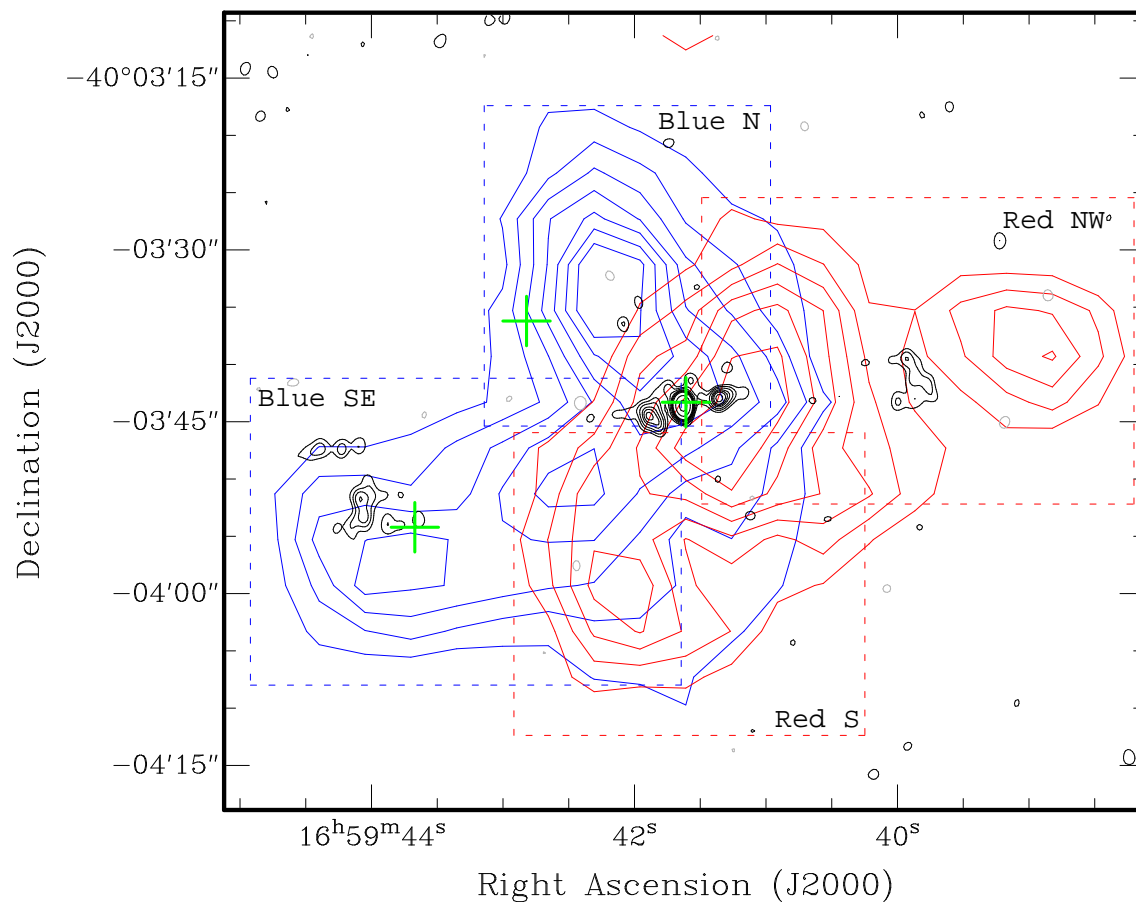


Figure 5.4 Map of the CO(6→5) velocity integrated blueshifted (blue contours) and redshifted (red contours) wing emission, as in Fig. 5.3, overlaid with a map of the 8.6 GHz emission (black contours) showing the string of radio emission described in Chapters 2 and 4. The red and blue dashed-line boxes mark the regions of the sky where the CO emission was integrated to determine the parameters of the red and blue lobes, respectively. The green crosses marks the position of the OH masers.

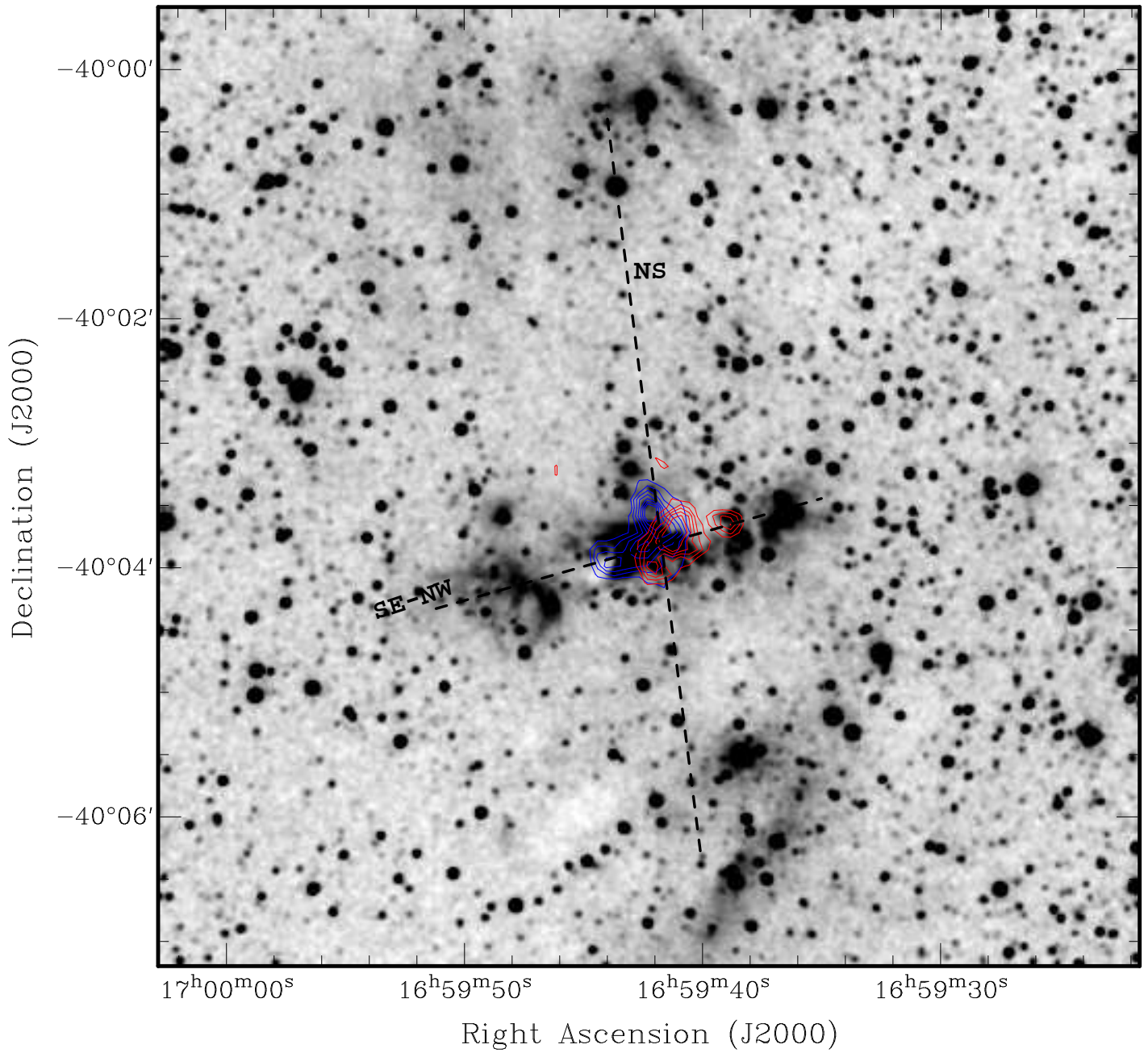


Figure 5.5 *Greyscale*:  $K_s$ -band 2MASS emission. Overlaid are contours of the blueshifted (blue contours) and redshifted (red contours) CO(6→5) emission. The approximate directions of the SE-NW and NS flows are indicated by dashed lines.

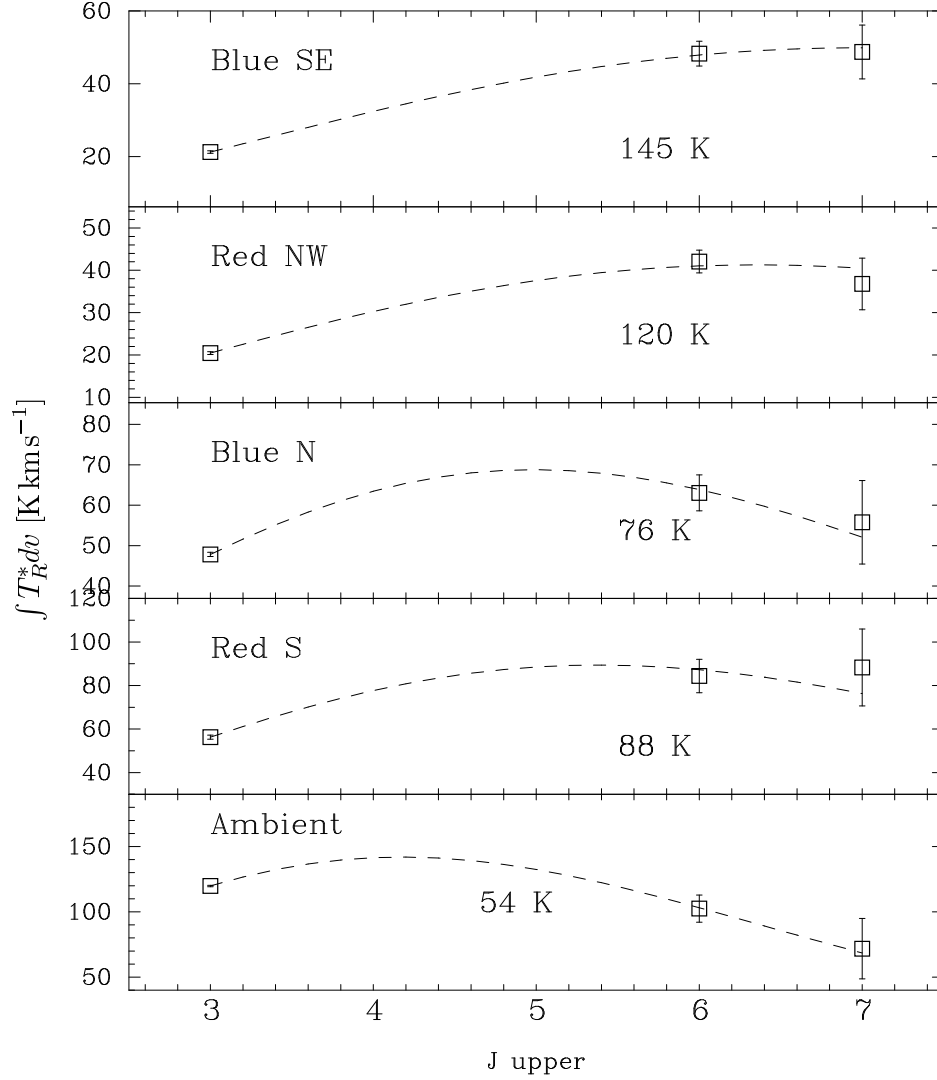


Figure 5.6 Velocity integrated CO emission versus upper rotational quantum level  $J$ . The range of velocity integration for the different features is indicated in Column 2 of Table 5.2. The outflow emission from the lobes has been averaged over the zones indicated in Fig. 5.4. Dashed lines represent fits to the data using Eq. (3.1) and optically thin conditions. The derived column densities and excitation temperatures are shown in Table 5.2, and the latter are also indicated in each panel. *Top*: Wing emission from the blueshifted lobe of the SE-NW outflow. *Middle-top*: Wing emission from the redshifted lobe of the SE-NW outflow. *Middle*: Wing emission from the blueshifted lobe of the NS outflow. *Middle-bottom*: Wing emission from the redshifted lobe of the NS outflow. *Bottom*: Ambient cloud emission, measured from spectrum observed at offsets  $\Delta\text{RA} = +40''$ ,  $\Delta\text{Dec} = -40''$ .

# Chapter 6

## Discussion and analysis

### 6.1 Ionized jets in high-mass star formation

The systematic search of jets presented in Chapter 2, plus a few other investigations, have shown this phenomenon does occur during the formation process of high-mass stars, at least for HMYSOs with luminosities up to  $1 \times 10^5 L_{\odot}$ . This result strongly supports a disk-mediated accretion scenario for the formation of high-mass stars.

#### 6.1.1 Lifetime of jets in HMYSOs

Although the sample observed as part of this work is limited, in this section we analyze the statistical incidence of jets in the sample of candidates and draw some conclusions about the lifetime of ionized HMYSO jets. For the statistical analysis we will only consider the jet candidates chosen from the RMS survey. This allows us to make use of the results of a recently reported study of HMYSOs and CH II regions identified in the RMS survey (Mottram et al. 2011b). In particular, they estimated that the lifetime of the compact H II region phase, for all range of luminosities, is  $\sim 3 \times 10^5$  yr. Of the 239 RMS sources we initially considered reported by Urquhart et al. (2007a), we find that 92 are located at angular distances smaller than  $25''$  from an IRAS point source with a luminosity  $> 2 \times 10^4 L_{\odot}$ . We assume that these 92 sources form an unbiased sample of the CH II region population analyzed in Mottram et al. (2011b).

Of these 92 sources we find that 23 fulfill two additional criteria, namely, positive spectral index and being underluminous in radio wavelengths by a factor of at least 10, required to be considered jet candidate as described in §2.1. These are the objects with entry “(1)” in col. (10) of Table 2.1. Since we can not disentangle the luminosity from the multiple sources G301.1364–00.2249 A and B, and G317.8908–00.0578 A and B, we count them as if they were single objects. At the high luminosity of the objects, completeness corrections of the RMS survey are small: about 0.8 and 0.97 for sources of 20,000 and 30,000  $L_{\odot}$ , respectively, and essentially complete for more luminous HMYSOs (Mottram et al. 2011b).

We observed four jet candidates drawn from the RMS subsample and found that two of

them are bona-fide jets (G337.4032–00.4037 A and G345.4938+01.4677). Using this detection rate, we then expect to find about 11 jets within the 23 candidates. The jet incidence in the population of CH II regions is therefore  $\sim 11/92$ , which in combination with the CH II region average lifetime of  $\sim 3 \times 10^5$  yr (Mottram et al. 2011b), it implies that the lifetime of the jet phase is roughly  $4 \times 10^4$  yr. This lifetime is comparable to the Kelvin-Helmholtz timescale of a HMYSO of  $10^4 L_{\odot}$ . Afterwards, the central protostar rapidly contracts onto the main sequence, starts producing copious amounts of ionizing photons, and the formation of an HCH II region ensues. The short lifespan found could explain why few jets are observed associated with HMYSOs.

Similarly, for the HCH II regions we derive lifetimes of the order of  $4 \times 10^4$  yr. We find multiple radio sources in 3 of the 4 observed fields, but all companion sources correspond to more diffuse and evolved H II regions which does not affect the statistics.

### 6.1.2 Ionized jets as the driving sources of molecular outflows

The driving source of molecular outflows that better fits the observations in the low-mass case are jets with the following characteristics: low-density ( $\rho_{jet}/\rho_{ambient} < 1$ ), highly supersonic ( $V_{jet} > 100$  km s $^{-1}$ ,  $\mathcal{M} > 10$ ), mainly neutral (ionization fractions  $\lesssim 10\%$ ), and well collimated (length/width  $> 30$ ) probably by magnetic fields (Ray 2007, Cabrit 2007, Bachiller 1996, Hartigan 2008).

The physical parameters of ionized jets associated to HMYSOs are much more uncertain. In particular, it is still controversial if these jets are capable of driving the HMYSOs molecular flows, and whether or not every existing flow was excited by such a jet. Alternative mechanisms have also been proposed (e.g. quadrupolar circulation, Fiege & Henriksen 1996).

In the following we will review the evidence that ionized collimated jets are the driving sources of molecular outflows. We will tackle this issue from two approaches, one based on the few examples we have (particularly G343.1262–00.0620 and G345.4938+01.4677), and the other from a statistical point of view. The hypothesis to be tested is that the momentum of the molecular outflow was delivered by an ionized jet.

The first evidence that jets are related to the molecular outflow is morphological. In G343.1262–00.0620 and G345.4938+01.4677 there are molecular outflows and ionized jets that share the direction of alignment, with the ionized-jet source being located between the blue and red-shifted lobes. However, the morphology of massive molecular outflows is only roughly constrained. This is mostly due to the coarse angular resolution of the observations, but also because massive outflows seem to be poorly collimated. In the case of G343.1262–00.0620, there is a very clear bipolar structure (Garay et al. 2007). In contrast, in the case G345.4938+01.4677, the bipolar outflow structure is confused by the presence of another outflow, roughly perpendicular to the jet direction (Chapter 5). Both outflows could only be separated by observing it at the highest available angular resolution.

In the case of G345.4938+01.4677, in Chapter 5 we presented evidence that there is an alignment between the jet and the outflow cavity. Figure 6.1 shows a three color 2MASS image, in green contours the 4.8 GHz emission from the ionized jet and in blue contours the high-velocity blue emission. We already note in Chapter 5 the alignment between the

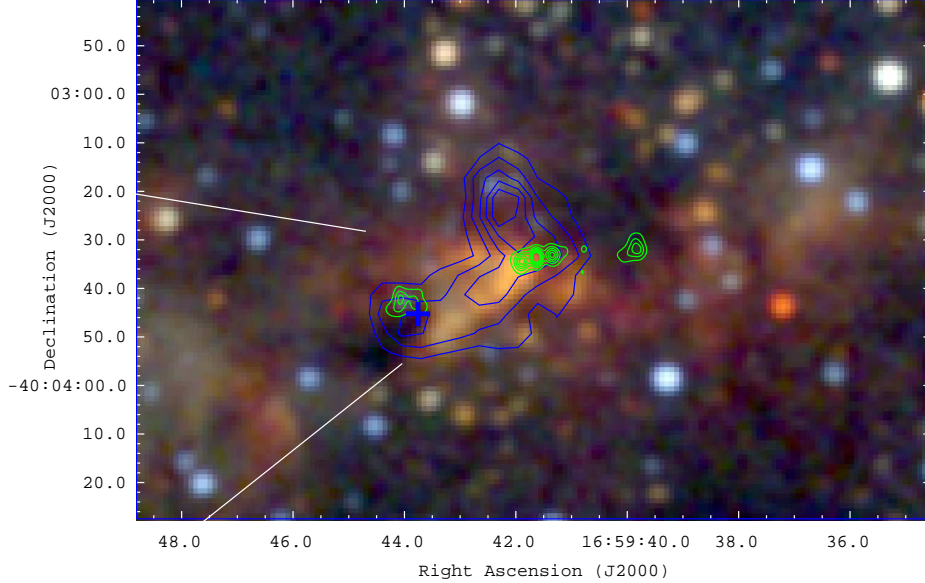


Figure 6.1 Background: Three color 2MASS image. Green contours: 4.8 GHz. Blue contours: Integrated high velocity blueshifted CO(6→5) emission. The blue cross marks the position of the 1720 MHz OH maser. White lines delineates the borders of the cone, and intersect on the central jet source.

blueshifted SE-flow, the SE radio lobe, and the location of the also blue-shifted 1720 OH maser, marked in Fig. 6.1 with a blue cross. We also noted that the  $K_s$ -band emission from the east (blue-shifted) side in the 2MASS data is much more intense respect to that on the west (red-shifted) side. The interpretation of this feature is that we are looking at the heated inner walls of the cavity carved by the outflow in the dust core. An important point to note is that this cone has its apex exactly located in the position of the ionized jet, and as expected, the peak mid-infrared diffuse emission is *not* in the radio central source, but displaced  $\sim 4''$  in the blue-shifted jet direction. This peak corresponds to emission from the point in the inner cone walls that is closest to the protostar that can be seen from our perspective (without being blocked by the outer parts of the cone). In conclusion, whatever carved the cone and excited the blueshifted emission, have its origin in the central radio source.

Another argument in favor of a link between the ionized jets and the molecular outflows would be the existence of a correlation between the kinematics and energy of the flows and the jet parameters. This correlation is a necessary, but not sufficient, condition to establish a causal relation. In other words, no correlation whatsoever would be a strong argument in favor of the *non* existence of a link. For the low-mass objects there is a correlation between the radio luminosity of the jets ( $\propto S_\nu d^2$ ) and the momentum flux of the associated molecular outflows  $\dot{P}_{flow}$  (Anglada et al. 1992). This correlation was extended to the high-mass regime by Rodríguez et al. (2008), and is shown in Figure 6.2, where the dashed line corresponds to the relation  $\dot{P}_{flow} = 10^{-2.6}(S_\nu d^2)^{1.1}$ . We have marked in this diagram with a triangle the position of G345.4938+01.4677, and with a star the position of G025.6469+01.0534.

The correlation presented above has a dispersion of about two orders of magnitude in  $\dot{P}_{flow}$ . Similar relationships have been found between the momentum flux and the total luminosity

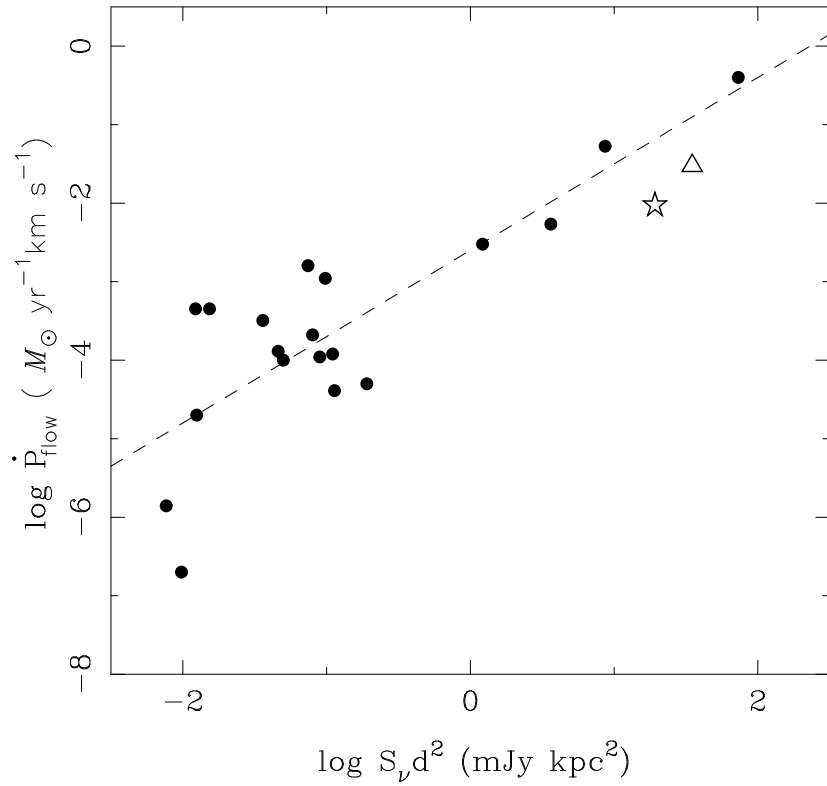


Figure 6.2 Radio luminosity at 8 GHz ( $S_{\nu} d^2$  in  $\text{mJy kpc}^2$ ) versus molecular outflow momentum flux (in  $M_{\odot} \text{ yr}^{-1} \text{ km s}^{-1}$ ) for the high and low-mass YSOs presented in Rodríguez et al. (2008) and Anglada et al. (1992), with ionized jets. The triangle marks the position of G345.4938+01.4677 and the star of G025.6469+01.0534

of the YSO (e.g. Zhang et al. 2005), showing similar dispersions. Does the correlation shown in Fig. 6.2 reflect that jets are the driving sources of outflows? Or does it only show that the radio flux of the ionized jet and  $\dot{P}_{flow}$  scales with YSO mass?

In order to answer these questions, we will compare the momentum that an ionized jet delivers with the momentum of the outflow. Our hypothesis can be summarized as

$$\dot{P}_{jet}t_{jet} = P_{flow}, \quad (6.1)$$

where  $t_{jet}$  is the time the jet has been injecting momentum to the molecular environment. The above equation is equivalent to the requirement of equal momentum fluxes.

Since  $t_{jet}$  is unknown, it is usually estimated as the characteristic age of the outflow. The problem is that the outflow age is one of the most difficult parameters to determine. It relies on estimations of a characteristic dynamical time or characteristic radius, as done in Chapter 5, and assumes a very simple axially symmetric conical model for the flow, while molecular outflows are extended and somewhat irregular. Furthermore, what is the appropriate characteristic size? The one selected in Chapter 5 was based on the CO outflow size, the usual procedure followed in the literature, but from Fig.5.5, the extension of the (purported) shocked-excited H<sub>2</sub> emission indicates that this size could be a low estimation. Hence, the molecular outflow is much older than this dynamical time. In contrast, the molecular outflow momentum is a better determined quantity, or at least its physical meaning is clearer. The momentum flux of the jet is unknown, but probably a simple model would be much more applicable to a collimated jet than to the high-mass molecular flows.

One of the original results presented in this thesis can be stated in terms of the inequality

$$t_{jet} \leq 4 \times 10^4 \text{ yr},$$

which is based on the statistics of the results presented in Chapter 2. To calculate the momentum that the jets G343.1262–00.0620 and G345.4938+01.4677 have delivered, we need to estimate  $t_{jet}$ . Since these jets are still active, we will use half of the estimated jet lifetime, that is,  $t_{jet} = 20,000$  yr. For G343.1262–00.0620 we use  $v_{jet} = 490$  km s<sup>-1</sup> (Rodríguez et al. 2008), implying  $\dot{M}_{jet} = 3.77 \times 10^{-6} M_{\odot} \text{ yr}^{-1}$  (Garay et al. 2003). Therefore, for G343.1262–00.0620 we have  $\dot{P}_{jet} = 1.9 \times 10^{-3} M_{\odot} \text{ km s}^{-1} \text{ yr}^{-1}$ .

For G345.4938+01.4677, the momentum flux derived is  $3.0 \times 10^{-4} M_{\odot} \text{ km s}^{-1} \text{ yr}^{-1}$  (Chapter 5). Summarizing, we have

$$P_{jet} = \dot{P}_{jet}t_{jet} = \begin{cases} 38 M_{\odot} \text{ km s}^{-1} & \text{for G343.1262–00.0620} \\ 6 M_{\odot} \text{ km s}^{-1} & \text{for G345.4938+01.4677.} \end{cases} \quad (6.2)$$

The molecular outflows momenta estimates, on the other hand, are  $2000 M_{\odot} \text{ km s}^{-1}$  for G343.1262–00.0620 (Garay et al. 2007) and  $89 M_{\odot} \text{ km s}^{-1}$  for G345.4938+01.4677. Therefore, the momenta delivered by the jets are below the momenta of the flows by factors of 50 and 15, respectively.

From a statistical point of view (e.g. Beuther et al. 2002b, Zhang et al. 2005), the mean momentum of massive molecular outflows is  $700\text{--}800 M_{\odot} \text{ km s}^{-1}$  (corrected for opacity and mean inclination). The mean mass loss rate estimated from the values of known jets (Garay et al. 2003, see also Chapter 4), is  $\sim 2 \times 10^{-6} M_{\odot} \text{ yr}^{-1}$ . Assuming that the jet velocities are  $\sim 500$  km s<sup>-1</sup> (Anglada 1996, Martí et al. 1998, Curiel et al. 2006, Rodríguez et al.

2008, also Chapter 4), then the momentum delivered by the jets during an average lifetime is  $\sim 40 M_{\odot} \text{km s}^{-1}$ . This is about 20 times less than the momentum of molecular outflows, consistent with the factors found for G343.1262–00.0620 and G345.4938+01.4677.

There are at least two possible explanations for this discrepancy: i) the jet is not entirely ionized, and their ionized fraction is below 10%; ii) as appears in the radio images, the ejection of mass from the jet is episodic and highly discontinuous, most of the momentum being delivered during short bursts, and what we observe now correspond to a more “quiescent” phase of the jet.

### 6.1.2.1 Radio source positions in the bipolar flows

We are arguing in this thesis that all high-mass stars goes through an ionized jet phase during its formation, and that during this phase the jet excites the bipolar molecular flows. This phase ends with the birth of an hypercompact HII region, which evolves and expands into an ultracompact HII region. Therefore, these ionized regions should be located nearby the flow axis. The question arises to: What are the locations of the radio sources we observed relative to the molecular outflows?

There are two cases: unresolved and resolved molecular flows. In the former case, that is, when we could not detect a separation between the blue and red-shifted emission peaks, the radio source was located in the same position as these peaks.

Four of the five resolved outflows observed in this work, listed in Table 3.4, have an associated radio source. The exception is IRAS 18151–1208, for which there is no radio emission detected at 1 mJy level (at X band, Sridharan et al. 2002). The case of the jet G345.4938+01.4677 has already been analyzed. Figures 6.3, 6.4, and 6.5 show for G305.7984–00.2416, G345.0061+01.7944, and G025.6469+01.0534, respectively, the molecular outflow maps and the radio centimetric emission.

The driving source of the outflow detected toward G305.7984–00.2416 (Fig 6.3) is located between the two more evolved HII regions (radio components A and D), near the densest part of the dust core (Lackington 2011), and closer to the younger radio component C. Nevertheless, it appear that neither B nor C can be directly related as the exciting source of the bipolar outflow. The position of the HCHII R G345.0061+01.7944 is in the line of the bipolar outflow (Fig. 6.4), but located over the peak of the blueshifted emission. Finally, Fig. 6.5 shows that the radio source G025.6469+01.0534 is located roughly between both radio lobes. It is also situated in a central position respect to the sites of of  $\text{H}_2$  2.12  $\mu\text{m}$  emission found by Varricatt et al. (2010), marked with dashed circles. Despite G025.6469+01.0534 does not have any of the spectral or morphological radio characteristics of an ionized jet, its position in the diagram of Figure 6.2 — consistent with the locus of jets — could be an indication that this source is a special case of very optically thin jet. We use  $\dot{P}_{flow}$  as given in Table 3.4, with no correction by inclination.

We conclude that, in general, the location of the radio source respect to the outflow is consistent with the location of the purported driving source. However, in most cases, our observations can not disentangle the bipolarity of the molecular outflows. Finally, there is still the possibility that some of the radio-underluminous sources, for example G025.6469+01.0534, are indeed optically thin jets.

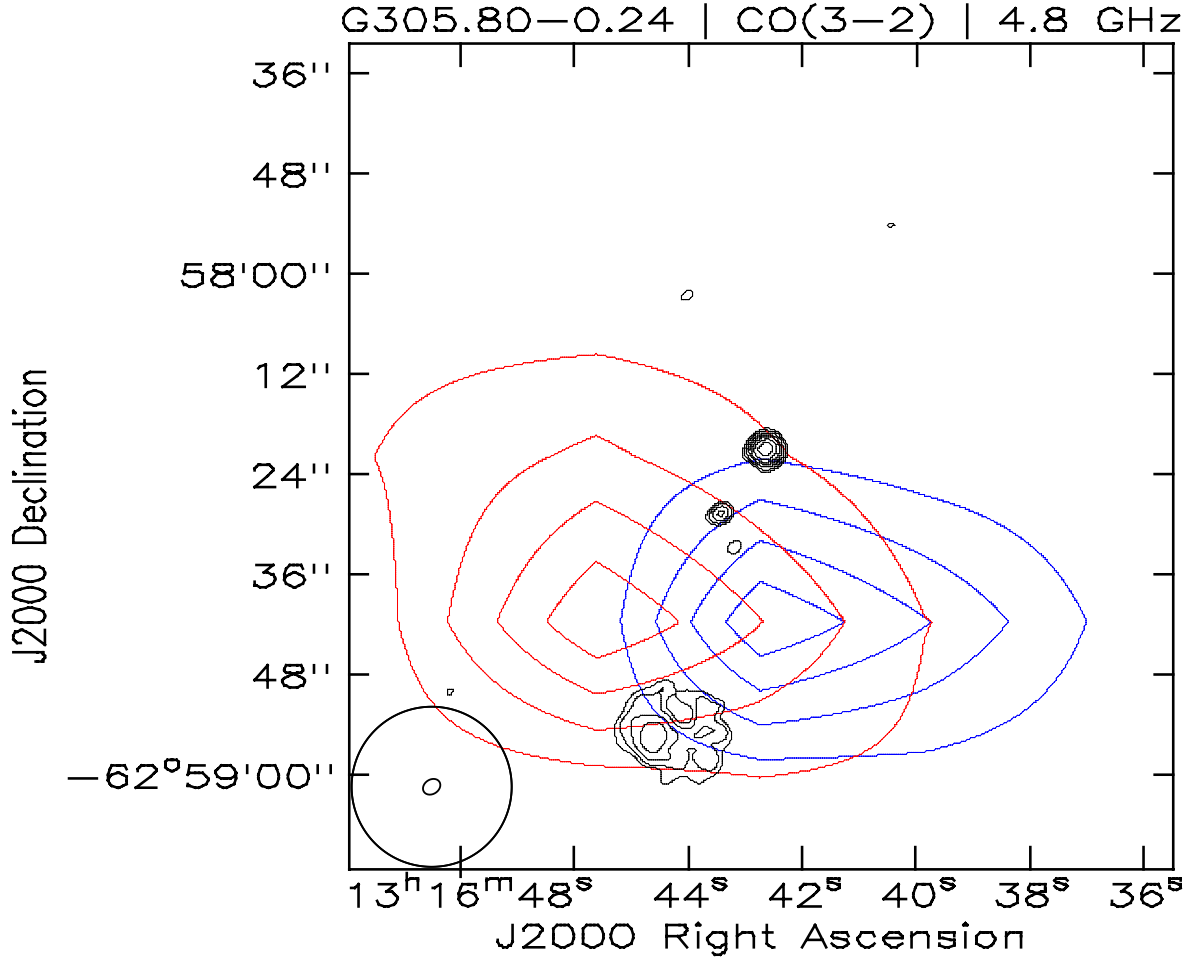


Figure 6.3 Bipolar outflow and radio emission observed toward G305.7984-00.2416 Black contours represent the radio emission detected at 4.8 GHz using ATCA. Blue contours represent CO(3→2) emission integrated over the velocity range  $-57.9 \text{ km s}^{-1} < v_{LSR} < -40.6 \text{ km s}^{-1}$ , which is blueshifted respect to the ambient cloud velocity ( $-31.6 \text{ km s}^{-1}$ ) and red contours represent emission integrated over the velocity range  $-22.6 \text{ km s}^{-1} < v_{LSR} < -9.1 \text{ km s}^{-1}$ , which is redshifted respect to the ambient cloud velocity. Contour levels are 20, 40, 60, and 80% of the respective peaks, which are  $55.3 \text{ K km s}^{-1}$  and  $21.8 \text{ K km s}^{-1}$ , for the blue and redshifted emission, respectively. Beam FWHM is  $17.6''$ .

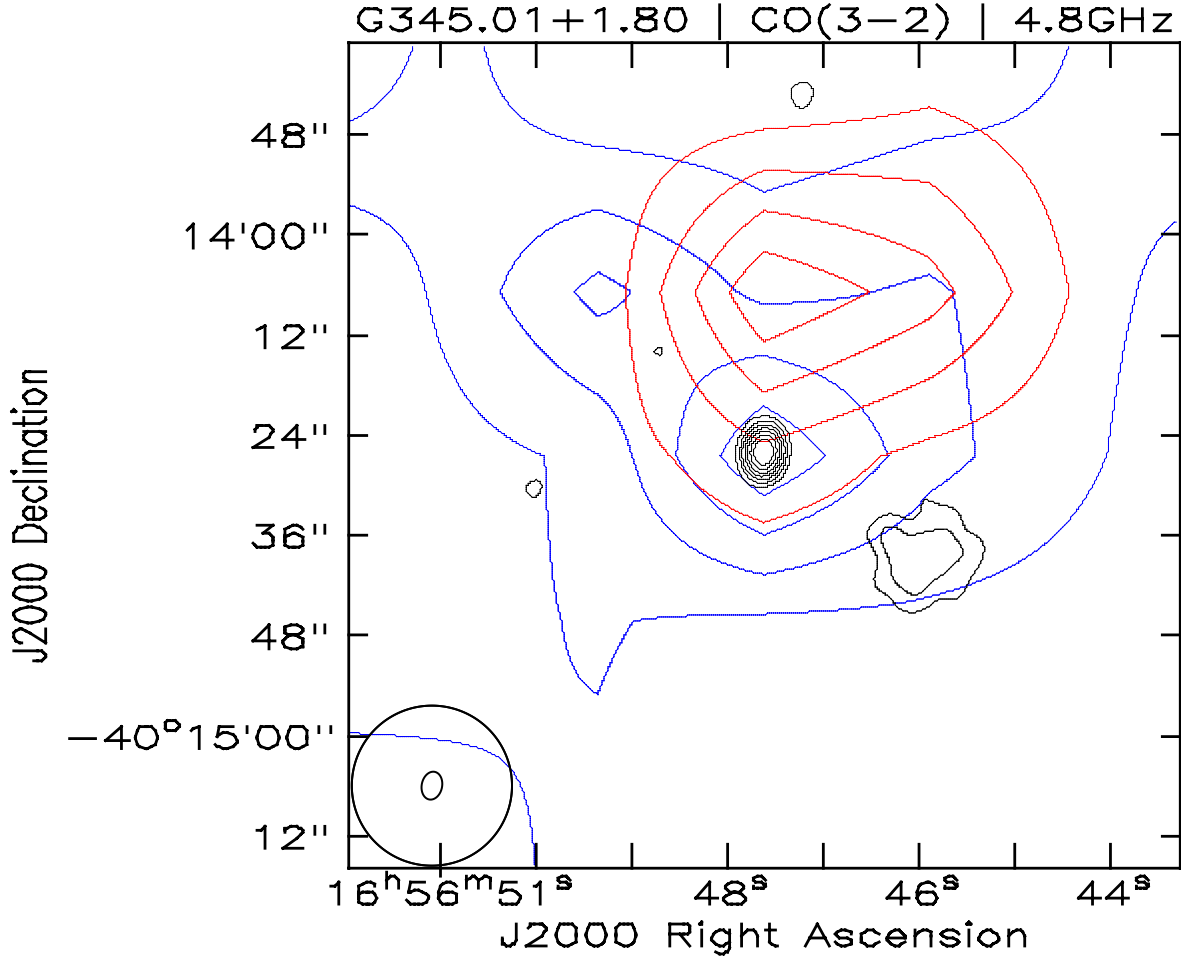


Figure 6.4 Bipolar outflow and radio emission observed toward G345.0061+01.7944. Black contours represent the radio emission detected at 4.8 GHz using ATCA. Blue contours represent CO(3→2) emission integrated over the velocity range  $-51.7 \text{ km s}^{-1} < v_{LSR} < -22.7 \text{ km s}^{-1}$ , which is blueshifted respect to the ambient cloud velocity ( $-12.7 \text{ km s}^{-1}$ ) and red contours represent emission integrated over the velocity range  $-2.7 \text{ km s}^{-1} < v_{LSR} < -20.6 \text{ km s}^{-1}$ , which is redshifted respect to the ambient cloud velocity. Contour levels are 20, 40, 60, and 80% of the respective peaks, which are  $65.2 \text{ K km s}^{-1}$  and  $32.2 \text{ K km s}^{-1}$ , for the blue and redshifted emission, respectively. Beam FWHM is  $17.6''$ .

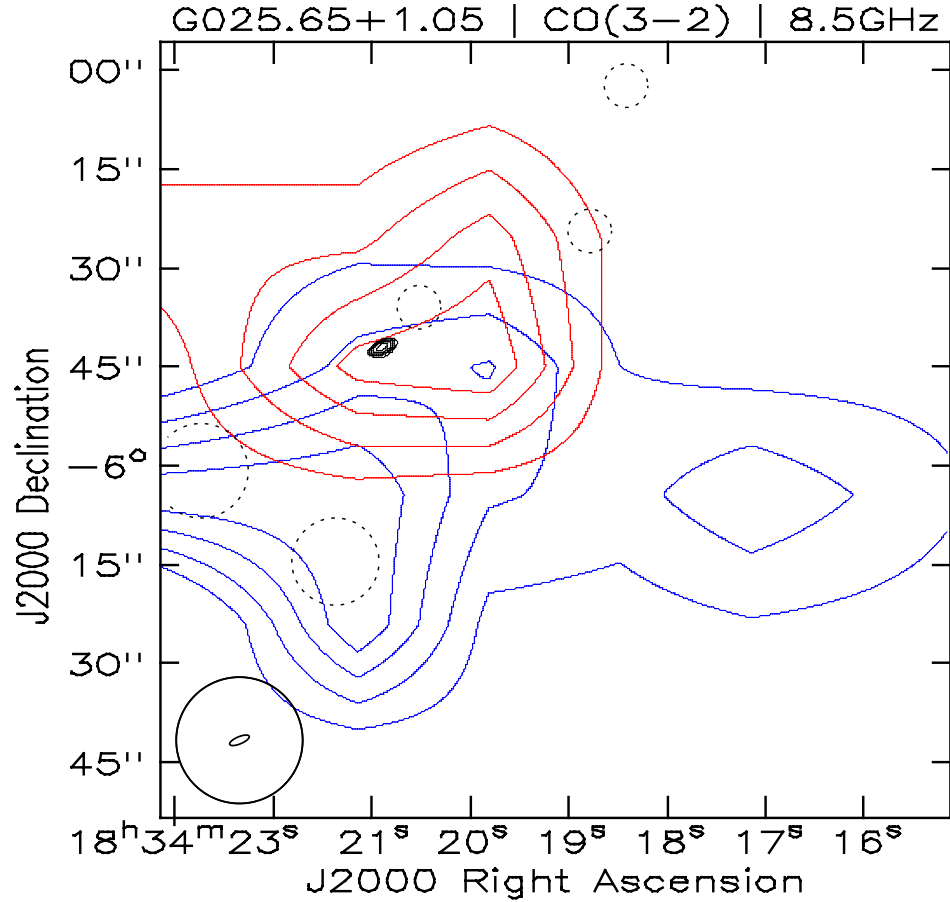


Figure 6.5 Contour maps of the velocity integrated CO line wing emission and from the radio emission detected toward G025.6469+01.0534. Blue lines represent emission integrated over the velocity range  $-0.8 \text{ km s}^{-1} < v_{LSR} < +26.4 \text{ km s}^{-1}$ , which is blueshifted with respect to the ambient velocity of  $+41.4 \text{ km s}^{-1}$ , and red lines emission integrated over the velocity range  $+56.4 \text{ km s}^{-1} < v_{LSR} < +86.0 \text{ km s}^{-1}$ , which is redshifted with respect to the ambient velocity. Contour levels are 20, 40, 60, and 80% of the peak emission. Peak blueshifted emission:  $24.8 \text{ K km s}^{-1}$ . Peak redshifted emission:  $35.6 \text{ K km s}^{-1}$ . Black contours represent the emission detected at 8.46 GHz (X-band). Dashed circles mark the positions of  $\text{H}_2\text{-}2.12 \mu\text{m}$  emission found by Varricatt et al. (2010). Beam FWHM is  $17.6''$ .

### 6.1.3 Collimation mechanism

The determination of the physical parameters of the jet found toward G345.4938+01.4677 was done assuming a pressure confined jet model (Chapter 4). This model reproduces well the observed spectral indexes of G345.4938+01.4677 and G337.4032–00.4037 A. Despite that pressure (thermal, ram and magnetic) has been rejected as the collimation mechanism of jets associated to low-mass stars (Cabrit 2007), we think it is a plausible mechanism in the high-mass case. Jets associated to HMYSOs begin  $\sim 100$ -300 AU away from the protostar (Chapter 4), where the high-mass star forming core have enough density and temperature to confine a jet with the characteristics described above. Furthermore, ram pressure can also be relevant in these cores, since infalling bulk motion has been detected toward all jets. According to Cabrit (2007), the condition imposed by Barral & Canto (1981) for outside pressure to confine the jet is:

$$\dot{P}_{jet} = 4\pi P_0 R_{conf}^2 \quad (6.3)$$

where  $R_{conf}$  is the radius where the wind is confined,  $P_0$  is the external pressure, and  $\dot{P}_{jet}$  is the momentum rate of the jet. This equation intuitively balances the ram “force” of the jet with the outside pressure. For the low-mass Herbig-Haro jets, the collimating pressure at the confinement radius fails by a factor of  $\sim 600$  to equilibrate the momentum flux of the jet.

To analyze the case of G345.4938+01.4677, we use the model of the dust core presented in Section 4.4.3. Considering that the collimation occurs at 200 AU from the protostar, and assuming a 50 K cloud, the right hand side of (6.3) gives a force of  $7 \times 10^{26}$  dyne. The force associated to the ram pressure, considering an infall velocity of  $0.35 \text{ km s}^{-1}$  (Chapter 5), is  $4 \times 10^{26}$  dyne. On the other hand, the momentum flux of the jet derived in Chapter 5 is  $3 \times 10^{-4} M_{\odot} \text{ km s}^{-1} \text{ yr}^{-1}$  equivalent to  $1.8 \times 10^{27}$  dyne. There is a consistency between both quantities within a 60%, but note that from the assumptions it is likely we underestimate the pressure. First, we assume an isotropic 50 K temperature, when it is likely that closer to the center to the core the kinetic temperature gets higher. We also assumed that the infall velocity was constant, when it is also likely that the infall accelerates toward the center. However, as already argued, the momentum flux of the jet could be one order of magnitude higher in order to be consistent with the molecular flow.

We conclude that collimation by external pressure cannot be discarded on the high-mass case using the same arguments as for the low-mass stars. Further detailed observations are needed to determine the physical mechanism behind the collimation of the ionized jets

# Chapter 7

## Summary

### 7.1 Main Conclusions

1. We compiled a list of 33 HMYSOs likely to contain jets using a selection criteria based on their radio and infrared properties. The objects have large bolometric luminosities ( $L > 2 \times 10^4 L_{\odot}$ ) and are underluminous at radio wavelengths compared to what is expected from the total luminosity.
2. The jets discovered here are associated with the two most luminous ( $7 \times 10^4$  and  $1.0 \times 10^5 L_{\odot}$ ) HMYSOs now known to harbor this type of objects. This indicates that the phenomena of collimated ionized jets and disk accretion is a phase of the formation process of stars at least up to masses of  $\sim 20 M_{\odot}$ .
3. From the rate of occurrence of jets in our sample, we estimate that the jet phase in high-mass protostars lasts for  $\sim 4 \times 10^4$  yr.
4. We detected massive and high-velocity ( $> 20 \text{ km s}^{-1}$ ) molecular outflows toward 7 out of 8 observed jet candidates.
5. There is evidence, especially morphological, that supports ionized jets as the driving sources of molecular outflows. In most cases there is a radio source (jet or H IIR) in a position consistent with being the driving source of the flow.
6. The estimated momentum that the observed ionized jets deliver during its main lifetime is about a tenth or less of the momentum of molecular outflows. Whether this is a problem of the models, of jets or flows, or actually ionized jets are not adequate to explain the dynamics of molecular outflows remains to be resolved.
7. An important part of the observed candidates were found to correspond to hypercompact H II regions, thought to be an early phase in the development of the UCH IIR. These hypercompact regions probably form right after the jet phase. We estimated their lifetime in a similar manner as done with the jets obtaining  $\sim 40,000$  yr.
8. The SED of the jets found in this search have spectral indexes characteristics of pressure confined winds ( $\gtrsim 0.85$ ). We believe that this type of collimation mechanism, while

discarded for low-mass jets, is a valid alternative for high-mass ionized jets: the thermal and ram pressure associated to high-mass star forming cores seems to be sufficient to collimate the jet.

## 7.2 Outlook

Besides the very interesting physical problem posed by the jet physics itself, collimated jets are important as the signposts of disk accretion.

We have concluded that the formation of stars until luminosities of around  $50,000L_{\odot}$  have a jet and disk accretion phase (J&DA-phase) characterized by the presence of these two types of objects, phase that lasts for about 40,000 yr. However, there are still many uncertain issues regarding jet phenomenon in high-mass (and low-mass) young stars.

From an extension of the jet search to the rest of the jet candidates presented in Chapter 2, we can address two important issues: first, we can improve the statistics on the incidence of jets in HMYSOs, hence the J&DA-phase lifetime estimation. The second issue is related to the question: What is the most luminous HMYSO associated to a jet? The finding of jets associated with increasingly luminous HMYSOs pushes the limit of the most luminous protostar that we expect it had a J&DA-phase. Is there a limit stellar mass that disk accretion cannot “reach”? From our work, this limit is above  $50,000L_{\odot}$  stars. To go farther, we have to confirm the jet presence in candidates of luminosities above  $10^5L_{\odot}$  (e.g. G337.4032–00.4037 A). Note, however, that if the J&DA-phase is so short, there may be no stars of luminosities much larger than  $10^5L_{\odot}$  in this phase across the Galaxy.

But definitely, the most interesting and important issues are related to the physics of the jets. The first task is to obtain more accurate measurements of the physical parameters associated to the accelerating gas itself. What is the density of the collimated wind? What is its velocity? Answers to these questions are not well established: we only have some idea of the density of their ionized fraction, which could be only a small part of the total mass of the jet. The velocities are also poorly constrained: there are a few examples where proper motions of the lobes had been detected, but these lobes are believed to be the fronts of shocked material, and their velocity may not represent the jet velocity. To tackle these issues, the new sub-millimeter interferometer ALMA will play a crucial role, by allowing us to measure the ionized gas velocity from hydrogen recombination lines. There is still the problem of the non-ionized fraction of the jet: we need to find adequate tracers of the molecular and atomic phases.

Once we have some idea of these basic physical parameters, we will be able to disentangle between the various theoretical models and answer the most important questions: Is jet ejection needed for disk accretion to take place? Is there a link between the jet collimation mechanism and accretion? Is magnetic collimation needed? How much mass is being accreted?

## Appendix A

# Spherical, power-law density ionized regions

In the following, we will describe the spectrum of the free-free emission due to a spherically symmetric ionized H II region for which the density declines as a radial power-law:

$$n(r) = n_0 \left( \frac{r}{r_0} \right)^{-\beta}. \quad (\text{A.1})$$

The free-free absorption coefficient is given by Equation (2) from Reynolds (1986):

$$\kappa_\nu = 0.212 n^2 x^2 \nu^{-2.1} T^{-1.35} \text{ cm}^{-1},$$

an approximation most useful in radio centimetric frequencies, in which  $\nu$  is the frequency,  $T$  is the electronic temperature, and  $nx$  is the density times the ionization fraction of the gas. Throughout this section, we will assume the Rayleigh-Jeans approximation of the blackbody to be valid.

Panagia & Felli (1975) gives formulae for the spectrum of an infinite spherical ionized gas cloud where the density of ionized material decreases as described by Equation (A.1). In this case, the restriction  $\beta > 3/2$  is needed, otherwise the total flux becomes infinite. The infinite emission always comes from the optically thin region of the ionized gas, away from the center. The intensity in any case diverges, because the thermal character of the emission limits the maximum intensity to be below the blackbody. The dominant term of the spectrum is proportional to

$$\nu^{2-2.1/(\beta-1/2)} \quad (\text{A.2})$$

where we have applied also the Rayleigh-Jeans approximation.

A more physical and somewhat more general case is treated by Spergel et al. (1983), who consider an inner and outer radius of the ionized region,  $R_1$  and  $R_2$ , respectively. If  $R_1 \geq 0$  and  $R_2$  is finite, then the integrated emission is always finite, regardless of the exponent of the density in Eq. (A.1).

An unwanted behavior of the model considering  $R_1 = 0$  –besides the singularity in density– would be the infinite mass around the center if  $\beta \geq 3$ . The emission is given ( $T$  constant) in Spergel et al. (1983, Eq. (B7)).

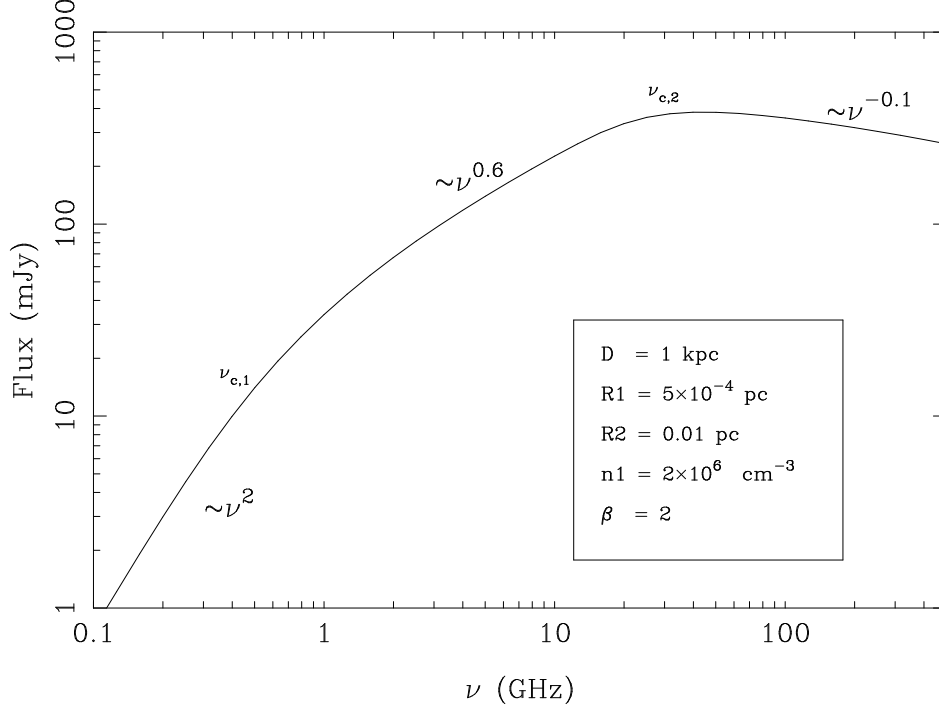


Figure A.1 Typical spectrum of a power law hypercompact H II region (HCH IIR). The three regimes and the critical frequencies are shown.

## A.1 Behavior of the spectrum

Assuming that  $0 < R_1 < R_2 < \infty$ , the spectrum has three principal parts:

1. The high frequency end, where the entire shell is optically thin. In this case, the spectrum is flat with  $S_\nu \propto \nu^{-0.1}$  in the radio regime.
2. A transition part, where there is optically thick emission near the center of the cloud, but still there is considerable emission from the optically thin part. The treatment of Panagia & Felli (1975) and Wright & Barlow (1975) reproduce the behavior of this case.
3. The optically thick emission in the lowest frequencies, which in the Rayleigh-Jeans regime behaves as  $S_\nu \propto \nu^2$ .

There are two critical frequencies which serve as limits of the different regimes. They are given by the condition

$$\tau_\nu = R_i \times \kappa_{\text{ff}}(\nu_{c,i}, n(R_i), T) = 1, \quad \text{where } R_i = R_1, R_2. \quad (\text{A.3})$$

We have that  $\nu_{c,2} < \nu_{c,1}$ , and the transition regime lies between both frequencies. Figure A.1 shows the spectrum of a region with spectral index  $\beta = 2$ , and in where the three regimes are displayed.

In the limit  $R_1 = 0$ , we have that  $\nu_{c,1} = \infty$  and we have only two regimes: the optically thick and the transition. On the other hand, if  $R_2 = \infty$  then  $\nu_{c,2} = 0$  and we have only

the optically thin and the transition regimes. The case  $R_2 = \infty$  and  $R_1 = 0$  only have the transition regime. In the last two cases,  $\beta \leq 3/2$  implies an infinite luminosity of the source. We can probe the transition regime taking the optically thin limit of a cloud with  $R_1 = 0$  for every  $\beta$ . The flux in the  $R_1 = 0$  case is given by

$$S_\nu = \pi \left( \frac{R_2}{D} \right)^2 B_\nu(T) \int_0^1 1 - \exp(-\tau(z)) dz \quad (\text{A.4})$$

$$\tau(z) = 2 \left( \frac{\nu_{c,2}}{\nu} \right)^{2.1} \sqrt{z} {}_2F_1(1, \beta; 3/2; z) \quad (\text{A.5})$$

$$z = 1 - (q/R_2)^2 \quad (\text{A.6})$$

where  $q$  is the impact parameter of a specific line of sight ( $0 < q < R_2$ ),  $D$  is the distance to the source,  $B_\nu(T)$  is the Planck function, and  ${}_2F_1$  is the ordinary gaussian hypergeometric function defined by:

$${}_2F_1(a, b; c; z) = \sum_{k \geq 0} \frac{(a)_k (b)_k}{(c)_k} \frac{z^k}{k!}$$

with  $(x)_0 = 1$  and  $(x)_k = x(x+1)\dots(x+k-1)$  for  $k > 0$ . The mathematical analysis of the transition regime can be reduced to the study of the asymptotic behavior of

$$\mathcal{F}(\epsilon, \beta) = \int_0^1 1 - \exp(-\epsilon \mathcal{T}(\beta, z)) dz, \quad \epsilon \rightarrow 0 \quad (\text{A.7})$$

where  $\epsilon$  corresponds to  $2(\nu_{c,2}/\nu)^{2.1}$  and  $\mathcal{T}(\beta, z) = \sqrt{z} {}_2F_1(1, \beta; 3/2; z)$ . Note that because we are considering  $R_1 = 0$ , the emission is never completely optically thin. The  $\mathcal{T}$  function acquires a simpler form if  $\beta$  is an integer or half-integer. We present such formulae for some cases in Table A.1. General characteristics of the function  $\mathcal{T}$  are the following:

- $\mathcal{T}(\beta, z)$  is an increasing function for  $\beta > 0$  and  $0 \leq z \leq 1$ , in both arguments. This implies that, given a fiducial value for the density, the greater  $\beta$ , greater is the opacity associated to any line of sight.
- $\mathcal{T}(\beta, 0) = 0$  for all  $\beta$ .  $\mathcal{T}(\beta, 1) = (1 - 2\beta)^{-1}$  if  $\beta < 1/2$ , otherwise the function goes to infinity for  $z \rightarrow 1$ .
- $\int_0^1 \mathcal{T}(\beta, z) dz = (\frac{3}{2} - \beta)^{-1}$  if  $\beta < 3/2$ , otherwise the integral diverges.
- $\mathcal{T}$  behaves as  $\sqrt{z}$  near  $z = 0$ .
- The asymptotic behavior of  $\mathcal{T}$  near  $z = 1$  is given by

$$\mathcal{T}(\beta, z) = \begin{cases} -\frac{\pi^{3/2}}{2\Gamma(\beta)} \frac{\sec(\pi\beta)}{\Gamma(3/2-\beta)} (1-z)^{1/2-\beta} - \frac{1}{2\beta-1} + \mathcal{O}_\beta(1-z) & \beta \neq 1/2 \\ \log\left(\frac{2}{\sqrt{1-z}}\right) + \mathcal{O}_{1/2}(1-z) & \beta = 1/2 \end{cases} \quad (\text{A.8})$$

Let us define

$$C[\beta] = -\frac{\pi^{3/2}}{2\Gamma(\beta)} \frac{\sec(\pi\beta)}{\Gamma(3/2-\beta)}.$$

Appropriate limits should be taken in case these formal expressions are not well defined.  $C[\beta]$  diverges at  $\beta = 1/2$  as  $(2\beta - 1)^{-1} + 0.69315$ .

Table A.1 The function that appears in the exponent of Eq. (A.7) can be expressed as the composition of explicit functions for every integer and half-integer value between 0 and 3.

$\beta$	$\sqrt{z} {}_2F_1(1, \beta; 3/2; z)$
0	$\sqrt{z}$
1/2	$\operatorname{arctanh}(\sqrt{z})$
1	$\frac{\arcsin(\sqrt{z})}{\sqrt{1-z}}$
3/2	$\frac{\sqrt{z}}{1-z}$
2	$\frac{\sqrt{z} + \frac{\arcsin(\sqrt{z})}{\sqrt{1-z}}}{2-2z}$
5/2	$\frac{(3-z)\sqrt{z}}{3(z-1)^2}$
3	$\frac{-2\sqrt{(1-z)z^3} + 5\sqrt{(1-z)z} + 3\arcsin(\sqrt{z})}{8(1-z)^{5/2}}$

This asymptotic expansion can be used to deduce the approximate behavior of function  $\mathcal{F}$  in Eq. (A.7): the first term in its asymptotic expansion is:

$$\mathcal{T}(\epsilon, \beta) \sim \begin{cases} \Gamma\left[\frac{2\beta-3}{2\beta-1}\right] (\epsilon C[\beta])^{\frac{1}{\beta-1/2}} & \beta > 3/2 \\ -\epsilon \ln(\epsilon) & \beta = 3/2 \\ \frac{2}{3-2\beta} \epsilon & 0 \leq \beta < 3/2. \end{cases} \quad (\text{A.9})$$

The problem of these first-order asymptotic expansions is that for fixed  $\epsilon$ , they are arbitrarily bad close enough to  $\beta = 3/2$ . For example, given  $\epsilon = 0.01$  (which correspond to  $\nu \approx 12\nu_c$ ), the first-order approximation is reasonably good for  $\beta = 3$  ( $\sim +4\%$  error), for  $\beta = 2$  has  $\sim +23\%$  error, but for  $\beta = 1.6$  reaches  $\sim 200\%$  error.

Equation (A.9) reproduce the spectral behavior determined by Panagia & Felli (1975) for  $\beta > 3/2$ . If we replace  $\epsilon$  by  $2(\nu_c/\nu)^{2.1}$  and we add the Rayleigh-Jeans dependence of the blackbody spectrum ( $\propto \nu^2$ ) we obtain the spectral index of the transition spectrum which is

$$2 - \frac{2.1}{\beta - 0.5}.$$

For  $\beta < 3/2$ , the dominant term in the approximation is linear, which is equivalent to optically thin conditions. In this case, there is no “transition” spectrum and the qualitative behavior is similar to the homogeneous Strömngren sphere.

## A.2 Recombination equilibrium

In order to determine the size of the ionized zone, we will assume that the gas is completely optically thick to Lyman continuum and Ly- $\alpha$  photons. Through the equation that relates the ionizing photon rate produced by star and the total number of recombinations occurring

in the H II nebula per second, we can determine the size of the H II R. This problem is treated in several books, Dyson & Williams (e.g. 1997), Spitzer (e.g. 1998) and Shu (1991).

We will assume  $\beta < 3$  so the amount of mass enclosed by a finite radius remains finite. We have that  $M = \mu \int n(r) dV$ , where  $\mu$  is the mean molecular mass. The equation of radiative recombination equilibrium in the case of a power-law density, radially symmetric cloud (Equation A.1) is:

$$N_{\star} = 4\pi \int_{R_1}^{R_2} n^2(r) r^2 \alpha_2 dr = 4\pi n_0^2 r_0^3 \alpha_2 \begin{cases} \frac{1}{2\beta-3} \left(\frac{r_0}{r}\right)^{2\beta-3} \Big|_{R_2}^{R_1} & \beta \neq 3/2 \\ \log\left(\frac{R_2}{R_1}\right) & \beta = 3/2 \end{cases} \quad (\text{A.10})$$

We can see immediately that in the limit  $R_1 \rightarrow 0$  there are qualitatively two situations: if  $\beta$  is less than  $3/2$ , and if it is equal or greater than this critical value. The  $R_1 = 0$  case is only well defined if  $\beta < 3/2$ , whereas for  $\beta \geq 3/2$ , the recombination integral diverges in the  $R_1 \rightarrow 0$  limit. These relations are important when considering the confinement of an H II region (Franco et al. 2000). For  $\beta < 3/2$ , the recombination equilibrium does not depart qualitatively from an homogeneous Strömgen sphere, in the sense that given a fiducial density, the H II region cannot be confined to an arbitrarily small radius. Different is the case for  $\beta \geq 3/2$ , where given a fiducial density, the size of the H II region can be reduced until even to the radius of the star, given that  $R_1$  reaches small enough values.

# Bibliography

- Adams, F. C. 1991, *ApJ*, 382, 544
- Allen, C., & Cox, A. 2000, *Allen's astrophysical quantities* (AIP Press)
- Alonso-Albi, T., et al. 2010, *A&A*, 518, A52+
- Anglada, G. 1996, in *Astronomical Society of the Pacific Conference Series*, Vol. 93, *Radio Emission from the Stars and the Sun*, ed. A. R. Taylor & J. M. Paredes, 3–7
- Anglada, G., Rodríguez, L. F., Canto, J., Estalella, R., & Torrelles, J. M. 1992, *ApJ*, 395, 494
- Avalos, M., Lizano, S., Rodríguez, L. F., Franco-Hernández, R., & Moran, J. M. 2006, *ApJ*, 641, 406
- Bachiller, R. 1996, *ARA&A*, 34, 111
- Bacmann, A., Lefloch, B., Ceccarelli, C., Castets, A., Steinacker, J., & Loinard, L. 2002, *A&A*, 389, L6
- Bally, J., & Zinnecker, H. 2005, *AJ*, 129, 2281
- Barral, J. F., & Canto, J. 1981, *Rev. Mex. Astronomía & Astrofísica*, 5, 101
- Barvainis, R., Lehár, J., Birkinshaw, M., Falcke, H., & Blundell, K. M. 2005, *ApJ*, 618, 108
- Bate, M. R., & Bonnell, I. A. 2005, *MNRAS*, 356, 1201
- Beck, S. C., Fischer, J., & Smith, H. A. 1991, *ApJ*, 383, 336
- Benjamin, R. A., et al. 2003, *PASP*, 115, 953
- Beuther, H., Schilke, P., Menten, K. M., Motte, F., Sridharan, T. K., & Wyrowski, F. 2002a, *ApJ*, 566, 945
- . 2005, *ApJ*, 633, 535
- Beuther, H., Schilke, P., Sridharan, T. K., Menten, K. M., Walmsley, C. M., & Wyrowski, F. 2002b, *A&A*, 383, 892
- Beuther, H., & Walsh, A. J. 2008, *ApJ*, 673, L55
- Bonnell, I. A., Bate, M. R., Clarke, C. J., & Pringle, J. E. 2001, *MNRAS*, 323, 785

- Bonnell, I. A., Bate, M. R., & Zinnecker, H. 1998, *MNRAS*, 298, 93
- Bourke, T. L. 2002, in *The Origin of Stars and Planets: The VLT View*, ed. J. F. Alves & M. J. McCaughrean, 247
- Bourke, T. L., et al. 1997, *ApJ*, 476, 781
- Briggs, D. S. 1995, PhD thesis, New Mexico Institute of Mining and Technology, USA
- Brogan, C. L. 2007, in *IAU Symposium, Vol. 242, IAU Symposium*, ed. J. M. Chapman & W. A. Baan, 299–306
- Bronfman, L., Garay, G., Merello, M., Mardones, D., May, J., Brooks, K. J., Nyman, L.-Å., & Güsten, R. 2008, *ApJ*, 672, 391
- Bronfman, L., Nyman, L.-A., & May, J. 1996, *A&AS*, 115, 81
- Brooks, K. J., Garay, G., Mardones, D., & Bronfman, L. 2003, *ApJ*, 594, L131
- Brooks, K. J., Garay, G., Voronkov, M., & Rodríguez, L. F. 2007, *ApJ*, 669, 459
- Cabrit, S. 2007, in *Lecture Notes in Physics, Berlin Springer Verlag, Vol. 723, Jets from Young Stars I: Models and Constraints*, ed. J. Ferreira, C. Dougados, & E. Whelan, 21–50
- Cabrit, S., & Bertout, C. 1986, *ApJ*, 307, 313
- . 1990, *ApJ*, 348, 530
- Calvet, N., Canto, J., & Rodríguez, L. F. 1983, *ApJ*, 268, 739
- Caselli, P., Hartquist, T. W., & Havnes, O. 1997, *A&A*, 322, 296
- Casoli, F., Combes, F., Dupraz, C., Gerin, M., & Boulanger, F. 1986, *A&A*, 169, 281
- Caswell, J. L. 1998, *MNRAS*, 297, 215
- . 2004, *MNRAS*, 349, 99
- Cesaroni, R., Felli, M., Testi, L., Walmsley, C. M., & Olmi, L. 1997, *A&A*, 325, 725
- Cesaroni, R., Galli, D., Lodato, G., Walmsley, C. M., & Zhang, Q. 2007, *Protostars and Planets V*, 197
- Chambers, E. T., Jackson, J. M., Rathborne, J. M., & Simon, R. 2009, *ApJS*, 181, 360
- Chen, X., Shen, Z.-Q., Li, J.-J., Xu, Y., & He, J.-H. 2010, *ApJ*, 710, 150
- Chini, R., Hoffmeister, V. H., Nielbock, M., Scheyda, C. M., Steinacker, J., Siebenmorgen, R., & Nürnberger, D. 2006, *ApJ*, 645, L61
- Curiel, S., Rodríguez, L. F., Moran, J. M., & Canto, J. 1993, *ApJ*, 415, 191
- Curiel, S., et al. 2006, *ApJ*, 638, 878
- Cyganowski, C. J., et al. 2008, *AJ*, 136, 2391

- De Vries, C. H., & Myers, P. C. 2005, *ApJ*, 620, 800
- Devine, D., Bally, J., Reipurth, B., Shepherd, D., & Watson, A. 1999, *AJ*, 117, 2919
- Di Francesco, J., Hogerheijde, M. R., Welch, W. J., & Bergin, E. A. 2002, *AJ*, 124, 2749
- Dyson, J. E., & Williams, D. A. 1997, *The physics of the interstellar medium* (Bristol: Institute of Physics Publishing)
- Elitzur, M. 1976, *ApJ*, 203, 124
- Ezawa, H., Kawabe, R., Kohno, K., & Yamamoto, S. 2004, in *Society of Photo-Optical Instrumentation Engineers (SPIE) Conference Series*, Vol. 5489, *Society of Photo-Optical Instrumentation Engineers (SPIE) Conference Series*, ed. J. M. Oschmann Jr., 763–772
- Faúndez, S., Bronfman, L., Garay, G., Chini, R., Nyman, L.-Å., & May, J. 2004, *A&A*, 426, 97
- Fendt, C., & Zinnecker, H. 1998, *A&A*, 334, 750
- Fiege, J. D., & Henriksen, R. N. 1996, *MNRAS*, 281, 1038
- Fomalont, E. B., Windhorst, R. A., Kristian, J. A., & Kellerman, K. I. 1991, *AJ*, 102, 1258
- Forster, J. R., & Caswell, J. L. 1999, *A&AS*, 137, 43
- Franco, J., Kurtz, S., Hofner, P., Testi, L., García-Segura, G., & Martos, M. 2000, *ApJ*, 542, L143
- Frerking, M. A., Langer, W. D., & Wilson, R. W. 1982, *ApJ*, 262, 590
- Galván-Madrid, R., Peters, T., Keto, E. R., Mac Low, M.-M., Banerjee, R., & Klessen, R. S. 2011, *MNRAS*, 416, 1033
- Galván-Madrid, R., Rodríguez, L. F., Ho, P. T. P., & Keto, E. 2008, *ApJ*, 674, L33
- Garay, G., Brooks, K. J., Mardones, D., & Norris, R. P. 2003, *ApJ*, 587, 739
- Garay, G., & Lizano, S. 1999, *PASP*, 111, 1049
- Garay, G., et al. 2007, *A&A*, 463, 217
- Garden, R. P., Hayashi, M., Hasegawa, T., Gatley, I., & Kaifu, N. 1991, *ApJ*, 374, 540
- Giannini, T., et al. 2005, *A&A*, 433, 941
- Goldsmith, P. F., & Langer, W. D. 1999, *ApJ*, 517, 209
- Güsten, R., Nyman, L. Å., Schilke, P., Menten, K., Cesarsky, C., & Booth, R. 2006, *A&A*, 454, L13
- Güsten, R., et al. 2008, in *Society of Photo-Optical Instrumentation Engineers (SPIE) Conference Series*, Vol. 7020
- Guzmán, A. E., Garay, G., & Brooks, K. J. 2010, *ApJ*, 725, 734

- Guzmán, A. E., Garay, G., Brooks, K. J., Rathborne, J., & Güsten, R. 2011, *ApJ*, 736, 150
- Hartigan, P. 2008, in *Lecture Notes in Physics*, Berlin Springer Verlag, Vol. 742, *Jets from Young Stars II: Clues From High Angular Resolution Observations*, ed. F. Bacciotti, E. Whelan, & L. Testi, 15–42
- Hartquist, T. W., Dalgarno, A., & Oppenheimer, M. 1980, *ApJ*, 236, 182
- Hoare, M. G., Kurtz, S. E., Lizano, S., Keto, E., & Hofner, P. 2007, *Protostars and Planets V*, 181
- Hoffman, I. M., Goss, W. M., Brogan, C. L., Claussen, M. J., & Richards, A. M. S. 2003, *ApJ*, 583, 272
- Hosokawa, T., & Omukai, K. 2009, *ApJ*, 691, 823
- Hummer, D. G., & Rybicki, G. B. 1968, *ApJ*, 153, L107+
- Huynh, M. T., Norris, R. P., Siana, B., & Middelberg, E. 2010, *ApJ*, 710, 698
- Iguchi, S., & Okuda, T. 2008, *PASJ*, 60, 857
- Ikeda, M., Nishiyama, K., Ohishi, M., & Tatematsu, K. 2001, in *Astronomical Society of the Pacific Conference Series*, Vol. 238, *Astronomical Data Analysis Software and Systems X*, ed. F. R. Harnden Jr., F. A. Primini, & H. E. Payne, 522–+
- Kim, K.-T., & Kurtz, S. E. 2006, *ApJ*, 643, 978
- Klein, B., Philipp, S. D., Krämer, I., Kasemann, C., Güsten, R., & Menten, K. M. 2006, *A&A*, 454, L29
- Kraus, J. D. 1986, *Radio astronomy* (Powell, Ohio: Cygnus-Quasar Books, 1986)
- Kraus, S., et al. 2010, *Nature*, 466, 339
- Krumholz, M. R., McKee, C. F., & Klein, R. I. 2005, *Nature*, 438, 332
- Kuiper, R., Klahr, H., Beuther, H., & Henning, T. 2010, *ApJ*, 722, 1556
- Kurtz, S., Churchwell, E., & Wood, D. O. S. 1994, *ApJS*, 91, 659
- Kutner, M. L., & Ulich, B. L. 1981, *ApJ*, 250, 341
- Lackington, M. 2011, Master's thesis, Universidad de Chile
- Langer, W. D. 1997, in *IAU Symposium*, Vol. 170, *IAU Symposium*, ed. W. B. Latter, S. J. E. Radford, P. R. Jewell, J. G. Mangum, & J. Bally, 98–100
- Larson, R. B. 2005, *MNRAS*, 359, 211
- Lee, C. W., & Myers, P. C. 2011, *ApJ*, 734, 60
- Leung, C. M., & Brown, R. L. 1977, *ApJ*, 214, L73
- López, C., Bronfman, L., May, J., Nyman, L.-A., & Garay, G. 2011, *A&A*, 534, A131

- Lucas, R., & Liszt, H. 1994, *A&A*, 282, L5
- Lumsden, S. L., Hoare, M. G., Oudmaijer, R. D., & Richards, D. 2002, *MNRAS*, 336, 621
- Mardones, D., Myers, P. C., Tafalla, M., Wilner, D. J., Bachiller, R., & Garay, G. 1997, *ApJ*, 489, 719
- Margulis, M., & Lada, C. J. 1985, *ApJ*, 299, 925
- Martí, J., Rodríguez, L. F., & Reipurth, B. 1993, *ApJ*, 416, 208
- . 1998, *ApJ*, 502, 337
- Masson, C. R., & Chernin, L. M. 1993, *ApJ*, 414, 230
- Masunaga, H., & Inutsuka, S.-i. 2000, *ApJ*, 536, 406
- Miettinen, O., Harju, J., Haikala, L. K., & Pomrén, C. 2006, *A&A*, 460, 721
- Moeckel, N., & Bally, J. 2006, *ApJ*, 653, 437
- Motte, F., Bontemps, S., Schilke, P., Schneider, N., Menten, K. M., & Broguière, D. 2007, *A&A*, 476, 1243
- Mottram, J. C., Hoare, M. G., Lumsden, S. L., Oudmaijer, R. D., Urquhart, J. S., Sheret, T. L., Clarke, A. J., & Allsopp, J. 2007, *A&A*, 476, 1019
- Mottram, J. C., et al. 2011a, *A&A*, 525, A149
- . 2011b, *ApJ*, 730, L33
- Myers, P. C., Linke, R. A., & Benson, P. J. 1983, *ApJ*, 264, 517
- Myers, P. C., Mardones, D., Tafalla, M., Williams, J. P., & Wilner, D. J. 1996, *ApJ*, 465, L133
- Norris, R. P., et al. 2006, *AJ*, 132, 2409
- Ochsenbein, F., Bauer, P., & Marcout, J. 2000, *A&AS*, 143, 23
- Ossenkopf, V., & Henning, T. 1994, *A&A*, 291, 943
- Panagia, N. 1973, *AJ*, 78, 929
- Panagia, N., & Felli, M. 1975, *A&A*, 39, 1
- Patel, N. A., et al. 2005, *Nature*, 437, 109
- Penzias, A. A., & Burrus, C. A. 1973, *ARA&A*, 11, 51
- Pestalozzi, M. R., Minier, V., & Booth, R. S. 2005, *A&A*, 432, 737
- Preibisch, T., Ratzka, T., Gehring, T., Ohlendorf, H., Zinnecker, H., King, R. R., McCaughrean, M. J., & Lewis, J. R. 2011, *A&A*, 530, A40
- Price, S. D., Egan, M. P., Carey, S. J., Mizuno, D. R., & Kuchar, T. A. 2001, *AJ*, 121, 2819

- Qiu, K., Wyrowski, F., Menten, K. M., Güsten, R., Leurini, S., & Leinz, C. 2011, *ApJ*, 743, L25
- Rank, D. M., Townes, C. H., & Welch, W. J. 1971, *Science*, 174, 1083
- Ray, T. 2007, in *Lecture Notes in Physics*, Berlin Springer Verlag, Vol. 723, *Jets from Young Stars I: Models and Constraints*, ed. J. Ferreira, C. Dougados, & E. Whelan, 3–19
- Reid, R. I. 2010, in *Bulletin of the American Astronomical Society*, Vol. 42, *American Astronomical Society Meeting Abstracts #215*, 479
- Reynolds, S. P. 1986, *ApJ*, 304, 713
- Risacher, C., et al. 2006, *A&A*, 454, L17
- Robitaille, T. P., Whitney, B. A., Indebetouw, R., & Wood, K. 2007, *ApJS*, 169, 328
- Rodríguez, L. F., Garay, G., Brooks, K. J., & Mardones, D. 2005, *ApJ*, 626, 953
- Rodríguez, L. F., Garay, G., Curiel, S., Ramírez, S., Torrelles, J. M., Gómez, Y., & Velazquez, A. 1994, *ApJ*, 430, L65
- Rodríguez, L. F., Moran, J. M., Franco-Hernández, R., Garay, G., Brooks, K. J., & Mardones, D. 2008, *AJ*, 135, 2370
- Sanhueza, P., Garay, G., Bronfman, L., Mardones, D., May, J., & Saito, M. 2010, *ApJ*, 715, 18
- Sault, R. J., Teuben, P. J., & Wright, M. C. H. 1995, in *Astronomical Society of the Pacific Conference Series*, Vol. 77, *Astronomical Data Analysis Software and Systems IV*, ed. R. A. Shaw, H. E. Payne, & J. J. E. Hayes, 433
- Schuller, F., et al. 2009, *A&A*, 504, 415
- Sewilo, M., Churchwell, E., Kurtz, S., Goss, W. M., & Hofner, P. 2011, *ApJS*, 194, 44
- Shepherd, D. 2005, in *IAU Symposium*, Vol. 227, *Massive Star Birth: A Crossroads of Astrophysics*, ed. R. Cesaroni, M. Felli, E. Churchwell, & M. Walmsley, 237–246
- Shepherd, D. S., & Churchwell, E. 1996, *ApJ*, 472, 225
- Shepherd, D. S., Claussen, M. J., & Kurtz, S. E. 2001, *Science*, 292, 1513
- Shepherd, D. S., Testi, L., & Stark, D. P. 2003, *ApJ*, 584, 882
- Shepherd, D. S., Watson, A. M., Sargent, A. I., & Churchwell, E. 1998, *ApJ*, 507, 861
- Shu, F. 1991, *Physics of Astrophysics: Volume I Radiation* (Published by University Science Books, 648 Broadway, Suite 902, New York, NY 10012, 1991.)
- Shu, F. H., Adams, F. C., & Lizano, S. 1987, *ARA&A*, 25, 23
- Skrutskie, M. F., et al. 2006, *AJ*, 131, 1163
- Smith, M. D. 2004, *The origin of stars* (Imperial College Press)

- Snellen, I. A. G., Schilizzi, R. T., de Bruyn, A. G., Miley, G. K., Rengelink, R. B., Roettgering, H. J., & Bremer, M. N. 1998, *A&AS*, 131, 435
- Spergel, D. N., Giuliani, Jr., J. L., & Knapp, G. R. 1983, *ApJ*, 275, 330
- Spitzer, L. 1998, *Physical Processes in the Interstellar Medium* (Wiley-Interscience)
- Sridharan, T. K., Beuther, H., Schilke, P., Menten, K. M., & Wyrowski, F. 2002, *ApJ*, 566, 931
- Stahler, S. W., Palla, F., & Ho, P. 1997, *Protostars and Planets IV*, 327
- Sternberg, A., Hoffmann, T. L., & Pauldrach, A. W. A. 2003, *ApJ*, 599, 1333
- Taylor, D. K., & Dickman, R. L. 1989, *ApJ*, 341, 293
- Ulich, B. L., & Haas, R. W. 1976, *ApJS*, 30, 247
- Urquhart, J. S., Busfield, A. L., Hoare, M. G., Lumsden, S. L., Clarke, A. J., Moore, T. J. T., Mottram, J. C., & Oudmaijer, R. D. 2007a, *A&A*, 461, 11
- Urquhart, J. S., Hoare, M. G., Lumsden, S. L., Oudmaijer, R. D., & Moore, T. J. T. 2008a, in *Astronomical Society of the Pacific Conference Series*, Vol. 387, *Massive Star Formation: Observations Confront Theory*, ed. H. Beuther, H. Linz, & T. Henning, 381
- Urquhart, J. S., et al. 2007b, *A&A*, 474, 891
- . 2008b, *A&A*, 487, 253
- . 2009, *A&A*, 507, 795
- Valdettaro, R., et al. 2001, *A&A*, 368, 845
- Varricatt, W. P., Davis, C. J., Ramsay, S., & Todd, S. P. 2010, *MNRAS*, 404, 661
- Walmsley, M. 1995, in *Revista Mexicana de Astronomia y Astrofisica Conference Series*, Vol. 1, *Revista Mexicana de Astronomia y Astrofisica Conference Series*, ed. S. Lizano & J. M. Torrelles, 137
- Walsh, A. J., Burton, M. G., Hyland, A. R., & Robinson, G. 1998, *MNRAS*, 301, 640
- Walsh, A. J., Hyland, A. R., Robinson, G., & Burton, M. G. 1997, *MNRAS*, 291, 261
- Wilson, T. L., Rohlfs, K., & Hüttemeister, S. 2009, *Tools of Radio Astronomy* (Springer-Verlag)
- Wilson, T. L., & Rood, R. 1994, *ARA&A*, 32, 191
- Wolfire, M. G., & Cassinelli, J. P. 1987, *ApJ*, 319, 850
- Wood, D. O. S., & Churchwell, E. 1989, *ApJ*, 340, 265
- Wright, A. E., & Barlow, M. J. 1975, *MNRAS*, 170, 41
- Yorke, H. W. 1979, *A&A*, 80, 308

—. 1986, ARA&A, 24, 49

Zhang, Q., Hunter, T. R., Brand, J., Sridharan, T. K., Cesaroni, R., Molinari, S., Wang, J.,  
& Kramer, M. 2005, ApJ, 625, 864

Zinnecker, H., & Yorke, H. W. 2007, ARA&A, 45, 481